

Connecting the neuronal proteome

Unraveling protein dynamics in neurons
using Mass Spectrometry-based proteomics

Riccardo Stucchi

ISBN: 978-90-393-7133-6

© 2019 Riccardo Stucchi

The studies described in this thesis were performed at the division of Cell Biology and at the division of Biomolecular Mass Spectrometry and Proteomics of Utrecht University, The Netherlands

Cover and layout by: Riccardo Stucchi

Printed by: ProefschriftMaken || www.proefschriftmaken.nl

**Connecting the neuronal proteome:
Unraveling protein dynamics in neurons using
Mass Spectrometry-based proteomics**

Het neuronale proteoom verbinden:

De dynamiek van neuronale eiwitten ontrafeld met behulp van
massaspectrometrie-gebaseerde proteomica

(met een samenvatting in het Nederlands)

Proefschrift

ter verkrijging van de graad van doctor aan de
Universiteit Utrecht
op gezag van de
rector magnificus, prof.dr. H.R.B.M. Kummeling,
ingevolge het besluit van het college voor promoties
in het openbaar te verdedigen op

woensdag 5 juni 2019 des middags te 4.15 uur

door

Riccardo Stucchi

geboren op woensdag 24 april 1985
te Vimercate, Italië

promotoren:

Prof. dr. C.C. Hoogenraad

Prof. dr. A.J.R. Heck

copromotor:

Dr. A.F.M. Altelaar

TABLE OF CONTENTS

Chapter 1 - GENERAL INTRODUCTION - Neuroproteomics: investigating neuronal protein dynamics and protein-protein interaction networks	7
1. Mass Spectrometry (MS)-based proteomics in cell biology	8
2. Proteomics of the nervous system (Neuroproteomics)	10
3. Protein profiling of neuronal proteomes	11
Bottom-up workflows in Neuroproteomics	11
Quantitative proteomics	13
Temporal proteomics	14
Spatial proteomics	16
4. Identification of protein-protein interactions by MS	18
Affinity Purification-mass spectrometry (AP-MS)	18
Protein-protein interaction analysis by chemical cross linking-MS (XL-MS)	21
5. Phosphoproteomics and analysis of post translational modifications (PTMs)	22
6. Scope of this thesis	24
Chapter 2 - Quantitative map of proteome dynamics during neuronal differentiation	33
Chapter 3 - Regulation of KIF1A-driven dense core vesicle (DCVs) transport: Ca²⁺/CaM controls DCV binding and liprin-α and TANC2 recruit DCVs to postsynaptic sites	73
Chapter 4 - Kinesin-3 mediated transport: towards a better understanding of KIF1A and KIF13B regulation	117
Chapter 5 - Fibril formation rewire interactome of the Alzheimer protein Tau by π-stacking	141
Chapter 6 - Proteomic-based approaches to investigate neuronal protein dynamics	167
1. TRIM46 acts as microtubule (MT) bundler at the AIS	170
2. Role of the ER-shaping proteins (RTNs and DP1) in developing neurons	172

3. Characterization of the HAUS/augmin complex in neurons	174
4. SCRNI-VAP1 interaction regulates dynamic endoplasmic reticulum remodeling and presynaptic function	176
Chapter 7 - GENERAL DISCUSSION	183
1. Neurodevelopment of hippocampal neurons <i>in vitro</i>	184
2. The role of kinesin-dependent transport in neurons, the study of KIF1A	186
3. Cargo trafficking into dendritic spines	188
4. The role of KIF1A and KIF13B in vesicle transport into spines	189
5. The importance of LBS and MBS domains in KIF1A and KIF13B regulation respectively	190
6. Open questions about kinesin-3 mediated transport	193
7. Tau fibrils promote co-aggregation of aberrant interactors leading to loss of function mechanisms in Alzheimer's Disease (AD)	195
8. Future perspectives	196
Addendum	203
- Summary	204
- Samenvatting	207
- Curriculum vitae	210
- List of publications	211
- Acknowledgments	213

CHAPTER 1

General Introduction

Neuroproteomics:

Investigating neuronal protein dynamics and protein-protein interaction networks

Riccardo Stucchi^{1,2}

¹Cell Biology, Department of Biology, Faculty of Science, Utrecht University, Padualaan 8, 3584 Utrecht, the Netherlands

²Biomolecular Mass Spectrometry and Proteomics, Bijvoet Center for Biomolecular Research and Utrecht Institute for Pharmaceutical Sciences, Utrecht University, Padualaan 8, 3584 Utrecht, the Netherlands

Neuroproteomics: investigating neuronal protein dynamics and protein-protein interaction networks.

1. Mass Spectrometry (MS)-based proteomics in cell biology

Before discussing and classifying the field of neuroproteomics, it is important to start from the basics and clarifying key concepts of general proteomics. Proteomics is generally described as a branch of science that is focused on the study of the proteome. The term ‘proteome’ was coined in 1994 by Mark Wilkins as an analogy of ‘genome’ and was initially defined as the complete complement of proteins that are expressed by a genome (Wasinger et al., 1995). Therefore, proteomics is currently described as the science that studies the proteome of a particular biological system (organism, tissue, cell type, sub-cellular structure) in a particular state or in an experimental condition. Classical proteomics studies typically investigate changes in protein profiles or in protein interactions as related to diseases and/or environmental stimuli. A proteomic experiment is composed of three major parts: 1) a method to fractionate complex protein or peptide mixtures, 2) mass spectrometry (MS) technology to acquire the data necessary to identify individual proteins, 3) bioinformatics to analyze and assemble the MS data. Decades of technological and instrumental developments have enormously contributed to implement these three major aspects of a proteomic workflow and have strongly contributed to define and re-shape the proteomics field, as we know it, in its current state. Among all the different approaches available to study proteins and their behavior in a biological context, mass spectrometry (MS) based proteomics has increased exponentially in the last few years and now represents a gold standard technology. This is mainly due to the fact that MS-based techniques are becoming more and more accessible and user friendly and MS-data can be more easily processed and analyzed also by non-experts. For this reason, compared to few years ago, MS-based proteomics is now becoming almost an essential tool in the hands of a cell biologist or a neuroscientist through which he can access to a multitude of detailed and reliable information, with the enormous potential to drastically influence several aspects of his/her research. Within the field of proteomics, a great variety of approaches as well as instruments exist. In general terms, Mass Spectrometers use electric and magnetic fields to measure the mass-to-charge ratios (m/z) of charged molecules (typically peptides), allowing for their molecular masses determination and their relative abundances. For most of the experiments, it is not the mass of the proteins, but the mass of peptides derived from protein enzymatic cleavage which is measured (bottom-up proteomics). In a general bottom-up workflow (Figure 1), proteins are first cleaved at distinct sites into a mixture of peptides by proteolytic enzymes (typically trypsin) and then injected into a liquid chromatography (LC) system, coupled to a MS. A full MS spectrum is then

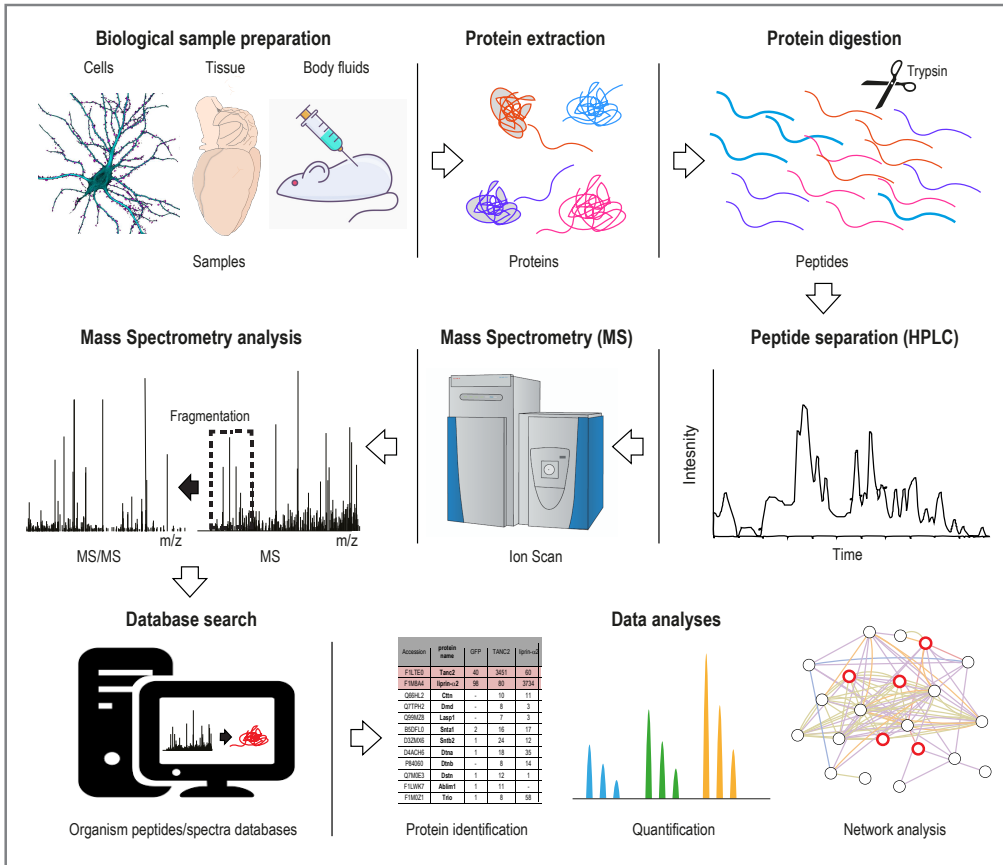


Figure 1. General workflow in bottom-up MS-based proteomics

Proteins are extracted from a biological source, such as from tissues, cells, or body fluids. In standard bottom-up MS, proteins are then digested into a peptide mixture using trypsin. Peptides are then separated by High Performance Liquid Chromatography (HPLC) systems to reduce the complexity of the mixture and analyzed by MS which is coupled to the HPLC through an electrospray ion source. MS analysis is performed by selecting individual peptides (precursor ions) in the mass spectrometer and by fragmenting them by collisions with nitrogen gas molecules at low pressure (Collision-Induced Dissociation, CID) or by radical reactions (Electron Transfer Dissociation, ETD). As results of this, tandem mass spectra (MS/MS) are generated, which contain peptide sequence information. Computer algorithms match these mass spectra to organism specific databases. Matched spectra are used to identify proteins from the corresponding peptide sequence information. Further statistical data analyses are performed *in silico* and allow to filter out false positives from the dataset, to extrapolate quantitative information and to further validate the MS data obtained.

acquired for the peptides eluting from the column at any given time by the Mass Spectrometer. Currently orbitraps are the most common instruments used in MS-based proteomics. The most intense peptides are then subsequently isolated and fragmented, usually by collision with an inert gas (CID, Collision-Induced Dissociation / HCD, Higher-energy collisional dissociation)

or by radical reactions (ETD, Electron Transfer Dissociation). The generated tandem MS (MS/MS) spectrum is composed by a list of m/z ratios for the different fragments. Each spectra produced in the analysis is then used for peptide identification by matching it against a protein database with a search engine (Aebersold and Mann, 2003). Search engine algorithms work by correlating the thousands of experimental spectra generated in each single MS run to theoretical spectra of peptides. Mascot is probably the most popular commercially available search engine on the market (Perkins et al., 1999). Other algorithms have been later developed but they all share the same searching criteria. Initially an *in silico* digestion of a defined protein database is performed, taking into account modifications, miss-cleavages and cleavage specificity of the selected enzyme, and theoretical masses of these *in silico* generated peptides are compared to the precursor masses generated by the experimental data. In the next step, this restricted dataset of matched peptides is further theoretically fragmented, depending on the applied fragmentation technique (CID, HDC, ETD) and compared to the experimental MS/MS spectra, ultimately leading to a defined score for each spectra match. The better the theoretical spectra matches the experimental ones, the higher is the score. Only spectra with scores above a certain threshold are taken into consideration. Due to the large number of spectra generated, there is a chance that some spectra are matched randomly. To correct for this and to distinguish true matches versus false matches, a False Discovery Rate (FDR) filter is applied to the peptide assignment (Steen and Mann, 2004). With this filter, spectra are set against a randomized decoy sequence database. The FDR is usually set to 1%, allowing a maximum of 1% of the matches to be false. Therefore, only true resulting peptide-spectrum-matches are then assigned to each protein, contributing to highly confident protein identification.

2. Proteomics of the nervous system (Neuroproteomics)

The brain is without any doubt the most complex organ of the entire human body. This is only partially reflected by the hundred billion neurons composing it, because the real complexity does not rely in the total number of cells but mainly in the almost infinite ways these single units (neurons) are connected with each other in the central nervous system (CNS). A full understanding of this complicated network of connections still represents one of the main priorities for the scientific community. Over the last decades, huge investments have been made in this sense (Amunts et al., 2016), which ultimately lead to enormous developments in diverse technologies (electron microscopy, super-resolution microscopy, optogenetics, transcriptomics). Super-resolution microscopy (also called Single Molecule Localization Microscopy, SMLM) is a collective term for a number of techniques (PALM, STORM, dSTORM) that allow diffraction-unlimited imaging (Betzig et al., 2006; Heilemann et al., 2008; Rust et al., 2006),

and are therefore well-suited to study the precise localization of proteins in the small neuronal projections (Tas et al., 2017) or in highly compartmentalized neuronal structures such as dendritic spines (MacGillavry and Hoogenraad, 2015). However due the limited amount of fluorophores and channels used in these imaging approaches, it is almost impossible to detect/analyze the multitude of proteins involved in each single molecular mechanism at each given time. In a similar fashion, the recent developments in genomic/transcriptomic techniques, allowing for single cell DNA/RNA sequencing, have greatly contributed to a more detailed characterization of the CNS at the cellular level (McCarroll et al., 2014; Pandey et al., 2018; Shekhar et al., 2016). Unfortunately, although both the transcriptome and proteome of living systems are interconnected with each other, multiple studies have shown that mRNAs levels are relatively poor predictors of protein abundance (Ghazalpour et al., 2011; Gygi et al., 1999; Low et al., 2013; Yeung, 2011). So, despite the great contribution brought by these techniques and taking into account that proteins are the building blocks and the final effectors in neurons, assessing the organization of the nervous system at the protein/molecular level remains one of the more crucial challenges in neuroscience. Moreover, at the moment the application of proteomic-based approaches in brain derived samples (Neuroproteomics) is still in a “preliminary/immature phase” if compared to other fields (cancer proteomics, immunoproteomics). The scarcity of studies in this sector is mainly due to two reasons: a) lack of sensitivity and a certain bias of the most common Mass Spectrometry techniques if compared to next-generation sequencing (NGS); b) technical difficulties in obtaining enough amount of sample when working with post-mitotic dissociated neuronal cells or neuronal differentiated induced pluripotent stem cells (iPSCs). These limitations have been now almost completely overcome due to the maturation of mass spectrometers into more powerful and versatile machines and to new improved protocols for proteins/peptides extraction (Altelaar et al., 2013b). These general improvements have prepared the ground for more reliable and accurate investigations of neuronal proteomes and protein dynamics in the coming years. In the next paragraphs I will shortly discuss about the huge technological improvements on the machines and then I will mainly focus my attention on the methodological advances in sample preparation and sample analysis that might be of particular interest for the neuroscience field.

3. Protein profiling of neuronal proteomes

Bottom-up workflows in Neuroproteomics

Similarly to other -omics approaches which allow the detection of every single mRNA or to map every single gene of genomic DNA in a living cell, the goal of proteomics has always

been the identification of all proteins in a given biological sample. In order to increase the sensitivity of the analysis and consequently the numbers of total proteins successfully identified, pioneering proteomics works with brain-derived samples were all characterized by a first step of protein separation by two-dimensional electrophoresis (2DE) (Jungblut and Klose, 1985; Klose and Feller, 1981). However, numbers of neural proteins were frequently underestimated in these early 2DE experiments. Moreover these electrophoresis-dependent approaches were strongly biased against low-abundant proteins, membrane proteins, proteins with very high or low molecular weight, or again highly acidic or basic proteins. A real game changer in the field was represented by the combined use of chromatographic methods with mass spectrometry (LC-MS-MS). This set-up in association with bioinformatics and the human genome sequence, allowed for a less biased analysis of very complex neural samples (Yates et al., 1996) (Figure 1). This increased sensitivity of LC-MS/MS was directly translated into much higher number of identified proteins in the entire brain (7,792, 34% of the genome) (Wang et al., 2006) and in brain plasma membrane fraction (862 from cortex and 1685 from hippocampus) (Nielsen et al., 2005). These proteomic experiments typically required milligram amounts of starting protein sample, however the situation has drastically changed with the development of more sensitive and powerful high-resolution mass spectrometers that allow in-depth coverage of the proteome starting from sub microgram quantities (Wilhelm et al., 2014). In addition to MS technology improvements, better methods for sample preparation (Switzar et al., 2013) and for sample fractionation at the protein or peptide level enormously improved the coverage of the proteome. MS can only sequence a certain amount of peptides within a certain time window, thereby limiting the amount of proteins detected. Fractionation in modern proteomic workflows is an essential step required to reduce the complexity of the sample and to consequently increase the numbers of positive identifications in the MS analysis. In proteomics pre-fractionation is often done by employing an orthogonal method of LC separation before the LC-reversed phase separation, for example by strong cation exchange or high pH fractionation (Batth et al., 2014; Di Palma et al., 2012; Fournier et al., 2007). Another way of decreasing the complexity of the sample is by enriching for specific PTMs for example using phosphopeptide enrichment strategies (Post et al., 2017) or peptide-centric immunoprecipitations for lysine acetylation or ubiquitination (Choudhary et al., 2009; Xu et al., 2010). Thanks to these new technological advances and improved workflows, it has now become possible to quantify more than 10000 proteins in cell lines and tissues (Kulak et al., 2017; Riley et al., 2016) and fully resolve complete proteomes of specific brain regions or specific sub-neuronal cell types (Frese et al., 2017; Sharma et al., 2015).

Quantitative proteomics

The main historical limitations of proteomics are its slower throughput and its less sensitivity compared to some of the other large-scale technologies. Improved instrumentation and more efficient protocols for sample preparations and data analysis occurred in the last decade, have transformed proteomics from a “pure descriptive technique” into a technology that is capable of accurate measurement of protein dynamics in any sort of biological sample (Focking et al., 2006; Ong and Mann, 2005). In particular, the recent advances in the MS-based quantification techniques and methods have hugely contributed for a more systematic study of the CNS. In proteomics experiments, relative protein quantification can be accomplished by using label free strategies or stable isotope labeling. Both methods have been successfully applied in this thesis. Label free quantification relies on spectral counting (PSMs, peptide-to-spectrum matches) or signal intensities to obtain quantitative information on proteins of interest. Spectral counting (PSMs) reflects the total number of spectra identified for a defined protein and provides a quantitative indication about its abundance (Lundgren et al., 2010). In this thesis, protein quantification based on the number of PSMs was extensively used to infer protein abundance of co-interacting proteins in affinity-purification mass spectrometry (AP-MS) experiments. To make this method more robust and reproducible, multiple measurements, obtained by performing independent experiments, have to be completed. Few limitations are associated with this strategy. For example, number of PSMs could be partially influenced by the type of protease used for digestion, or by the protein size, finally resulting in “partially-biased” measurements of protein abundances. To overcome these problems, more advanced strategies exist that allow relative protein quantification with better accuracy (Bantscheff et al., 2012). These alternative methods make use of stable heavy isotopes to label biological samples at the protein or peptide level. Different isotopes can be then easily distinguished due to their different masses in the MS analysis (Altelaar et al., 2013a). SILAC (stable isotope labeling with amino acids in cell culture) makes use of stable isotopes of lysine and arginine amino acids, which are added directly to the cell growth media (Ong et al., 2002). Although in recent years even whole animals were completely labeled with SILAC (Kruger et al., 2008), this method is mostly restricted to cultured cells making it suitable for dissected neurons (Spellman et al., 2008) but not for tissue samples. Isotopic labeling after sample lysis represents a valuable and less expensive alternative which is suitable to virtually any sort of biological sample, including specific brain areas or tissues. The two most common types of isotopic labeling methods are dimethyl labeling or isobaric tags labeling (TMT, iTRAQ). Both of them have been applied for the investigation of neuronal protein dynamics in this thesis. Dimethyl labeling targets peptides generated after protease digestion converting all the available amines into dimethylamines by

using cyanoborohydride and formaldehyde in their unlabeled and stable isotope-labeled forms. Quantification occurs at the MS1 level, by comparing the ion intensities of heavy, medium or light labeled peptides which are distinguished based on a minimum mass difference of 4Da. One of the major advantage of this approach is that is cheaper compared to other labelling techniques but still is capable of equivalent depths of analysis providing comparable and accurate results (Altelaar et al., 2013a). One of the major technical limitations is represented by the limit in the amount of multiplexing that needs to be compared. Typically dimethyl labeling can be used for a maximum of three conditions (3plex), however recent technological advances in this application now allow relative quantification of up to 5 conditions (5plex) (Wu et al., 2014). To overcome the problems due to the limited multiplexing, isobaric tags, such as TMT or iTRAQ have been developed. These methods represent a valid alternative when multiplexing for more than 3 conditions is required. TMT labeling can now be successfully applied up to 11 different conditions, by combining different isotopic labels. Isobaric tags do not differ in total mass in MS1, but their resulting products present specific reporter ion signatures after fragmentation in MS2. These fragmentation signatures are then used for the identification and quantification of the different tags resulting from differential labeling. One of the major advantages of this technique relies in its potential to analyze large sample set coming from multiple time points, treatments or conditions. Nowadays, in the neuroscience field this reliable quantification method is widely used for temporal proteomics analyses in order to investigate multiple time points during neuronal development or for spatial proteomics to compare protein profiles of multiple brain areas or different neuronal populations (Rauniyar and Yates, 2014).

Temporal proteomics

Our understanding of the development of the nervous system has been enormously ameliorated by our ability to generate *in vitro* cultures of primary rat or mouse neuronal cells. Neurons differentiate and respond to stimuli or external conditions over time by continuously regulating their protein profiles. As we mentioned in the previous chapter, protein dynamics of primary neuronal cultures can nowadays be precisely monitored by several quantitative-based proteomic approaches (SILAC, dimethyl labeling, TMT, iTRAQ). These methods generate in depth information about protein expression throughout development and allow accurate detection of even small quantitative changes in protein (Zhang et al., 2014). They are also becoming increasingly accessible and more accurate. Thanks to their capability of generating in depth quantitative data about protein dynamics over multiple time points, our vision is that within a few years they will replace entirely other protein detection methods such as classical WB-approaches which only allow detection of one single protein per experiment and are strongly dependent on the availability of the antibodies. In their current state they already represent

an essential tool for a neuroscientist who can now directly compare the different proteomes of CNS-derived cells almost in every step of their differentiation (Figure 2A) (Frese et al., 2017; Sharma et al., 2015). These approaches also allow precise monitoring of protein changes during disease progression or upon specific treatments with the final aim to unravel potential biomarkers or identify novel molecular targets for future therapeutic applications (Figure 2A). In particular they can now be directly applied to deeply investigate the proteomes of human-induced Pluripotent Stem Cells (hiPSCs) derived from patients with neurological diseases. These stem cells are raised from human somatic cells with the introduction of specific growth factors and differentiated in various neuronal cell types (Takahashi et al., 2007; Yamanaka, 2007). By comparing protein profiling of neuronal cells derived from healthy and disease patients at critical time points of development it has now become possible to unravel key molecular mechanisms underlying genetic neurological disorders (Brennand et al., 2015; Chae et al., 2012; Singec et al., 2016). Similarly to hiPSCs, patient-derived 3d cultures and organoid technology have been recently shown to recapitulate the *in vivo* features of the original individual's tissue in a three-dimensional *in vitro* culture system (Centeno et al., 2018; Dutta et al., 2017). Therefore, the application of proteome profiling throughout development by using quantitative proteomics on patient-specific tissues or organoids can now contribute to discover new protein targets and contribute to the optimization of patient-specific therapeutic approaches (Cristobal et al., 2017; Dakic et al., 2017). hiPSCs and organoids will definitely represent the future of neuroscience, however they still require further optimization in order to completely substitute the use of neuronal primary cultures. Mouse and rat primary cultures are still the preferred working model by several labs since they are easier to maintain and to be manipulated (by treatments or transfections) and they grow faster.

Most of the research performed in this thesis is therefore based on quantitative proteomics approaches performed on rat dissociated cortical and hippocampal neurons. As we described in chapter 2 the application of quantitative proteomics in hippocampal neurons can now provide reliable protein profiling with short measurement times and with similar precision and effort to routine techniques, such as Western Blotting. Instead of quantifying one or a few proteins, the neuroscientist can obtain a detailed global overview of all the changes associated with the neuronal system within a spatiotemporal dimension. Moreover, these MS-based quantitative approaches are extremely important in specific cases where protein detection by WB or IF is not visible (typically in rat derived or mouse derived neurons) due to the lack of good working antibodies (see Chapter 6). We therefore envision that in the next few years proteomics will be tackling a wide variety of biological questions, especially in the field of neuroscience.

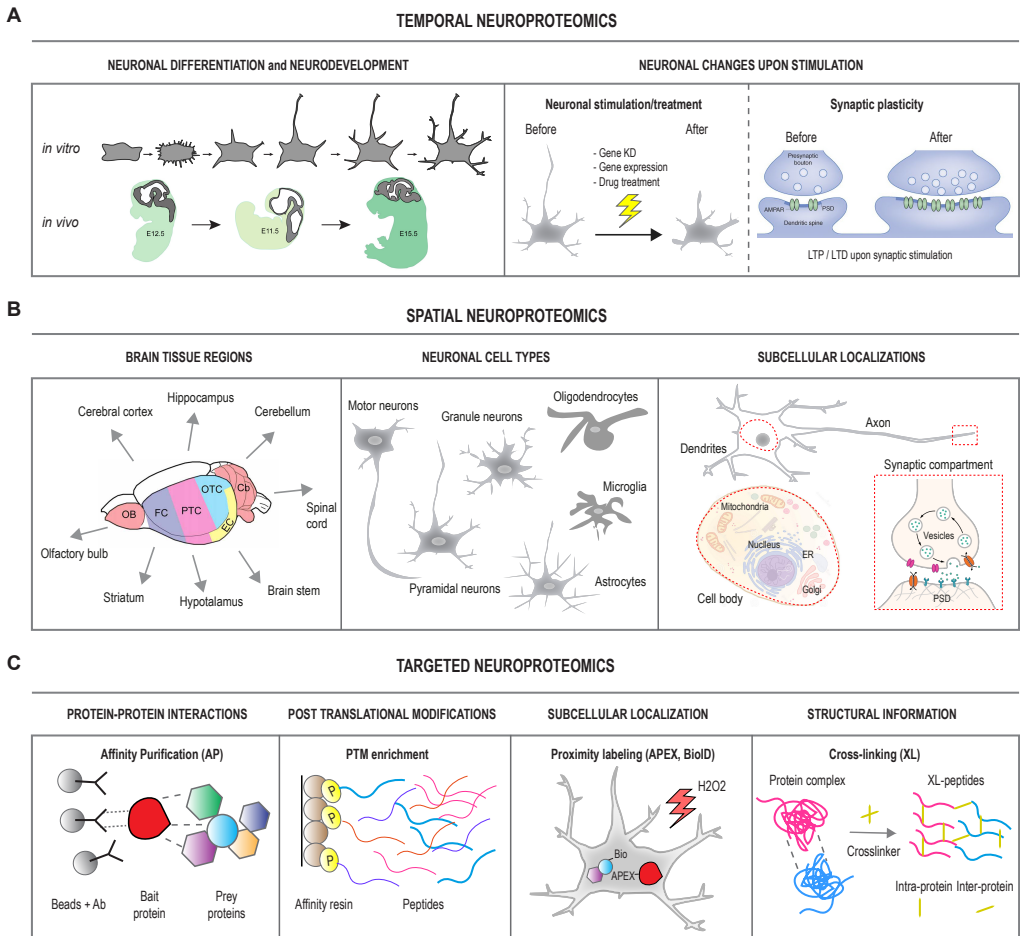


Figure 2. Overview of different neuroproteomics applications

(A) Temporal proteomics is applied for the investigation of temporal changes to the proteome, during neuronal differentiation and development, or in response to specific treatment/stimuli (KD, overexpression, drug treatment) or in response to a specific neuronal adaptation (synaptic plasticity). (B) Spatial proteomics is used to infer the spatial diversity of proteins in specific brain tissue regions and neuronal cell types, as well their subcellular localization within different neuronal compartments. (C) Targeted proteomics is mainly used to identify protein-based interactions (AP-MS), post-translational modifications (PTMs-MS), subcellular localization of proteins and to get structural information about protein complexes (XL-MS).

Spatial proteomics

The nervous system is not only constantly changing throughout development but also at its complete maturation it is organized in different compartmentalized regions, each one characterized by a specific subcellular neuronal population that is more over-represented than

others (Figure 2B). A key application and a future challenge for these MS-based quantitative methods is to define differential proteomes in these different brain regions, in order to pinpoint the minimal variations in protein composition that could underlie the extreme complexity of the human brain. In the past proteomic analyses have already created in depth and quantitative resources for many defined brain areas, similar to other mapping projects, such as the Allan Brain Atlas (Sunkin et al., 2013) or the Connectome project (Glasser et al., 2016). One of the first pioneering proteomic works tackling the protein complexity in the brain was represented by the Human brain Proteome Project (HbPP) which mapped the different proteomes in human brain regions (Hamacher et al., 2008). More recently, a new proteomic brain atlas, consisting of about 13,000 different proteins in different mouse brain regions, became available (Sharma et al., 2015). Specialization at the cell-type level gives rise to characteristic features to each neuronal cell population which can be distinguished by unique morphology, function or staining. Besides characterizing neuronal tissue-proteomic patterns several studies have now provided quantitative information about specific cell-specific proteomes, including those of neurons, glial cells, astrocytes, oligodendrocytes, and their progenitors (Figure 2B) (Chaerkady et al., 2009; Frese et al., 2017; Han et al., 2014; Iwata et al., 2013; Sharma et al., 2015). Recent efforts in neuroproteomics not only allow protein investigation in particular brain areas or neuronal cellular subtypes, which comprise low sample amounts, but also allow detailed characterization of intracellular compartments such as the post synaptic density, synaptosomes, or the pre-synaptic active zone, by achieving a better subcellular resolution (Figure 2B). Several approaches have utilized MS enrichment-based strategies (subcellular fractionation) to isolate the post synaptic density (PSD) and to systematically map the proteomes of these subcellular structures (Bayes et al., 2012; Peng et al., 2004; Sheng and Hoogenraad, 2007). Following similar enrichment approaches, other studies have focused on the MS-based identification and quantification of protein complexes composing the active zone or neuronal vesicles (Boyken et al., 2013; Witzmann et al., 2005). One of the current limitations of these works is that they heavily rely on good purification strategies. At the moment the lack of good protocols for diverse subcellular structures limits their in-depth analysis by MS. In this perspective, the recent application of new technologies which combine quantitative proteomics with proximity-labeling approaches (BioID or APEX) has the potential to become a real game changer in the field (Figure 2C) (Chen and Perrimon, 2017; Rees et al., 2015; Roux et al., 2012). In the BioID method, one protein targeting a cellular compartment is fused to a biotin protein ligase, which labels all the proteins in close proximity in the same compartment, thereby allowing protein investigation in their native environment (Roux et al., 2012). APEX (ascorbate peroxidase labeling) makes use of the same strategy but with faster labeling dynamics (Martell et al., 2012; Rhee et al.,

2013). The main advantage of these techniques is that they do not require any fractionation protocol optimization, therefore in principle they could be applied for the investigation of any sort of neuronal subcellular micro-domain (Han et al., 2018). These methods have already been extensively used to elucidate protein complexes, pathways, and subcellular organelles in cell lines, and they have been recently applied also for the first time in neurons to quantitatively assess the protein composition of excitatory and inhibitory synaptic clefts (Loh et al., 2016).

4. Identification of protein-protein interactions by MS

Affinity Purification-mass spectrometry (AP-MS)

In the previous section we explained how proteomic methods can monitor protein profiling throughout neurodevelopment or can characterize protein composition of specific brain regions or subcellular structures. However to get a full insight on the biological role of a protein of interest the final goal should be the identification of the structural and functional interactions the protein is involved in (Budayeva and Cristea, 2014; Morris et al., 2014). Affinity Purification-Mass Spectrometry (AP-MS) is a highly effective method for isolating and identifying binding partners in any sort of neuronal sample (Figure 2C). AP can be performed using immobilized antibodies, proteins, peptides or ligands to isolate protein complexes. Since a successful MS analysis requires a considerable amount of purified proteins, AP-MS typically relies on the exogenous expression of a target protein linked to an affinity tag. The target protein is usually referred as “bait” protein, which works as an affinity probe able to capture the binding partners, typically described as “prey” proteins (Morris et al., 2014). Most of the affinity tags are made of short hydrophilic peptides (FLAG, HA) and they are often chosen because they do not interfere with the folding of the linked protein thanks to their reduced size. Other types of tags are small proteins (GST, GFP) or small molecules (biotin) and they are sometimes preferred because they could be used in multiple applications such as imaging or other biochemical assays. In this form of AP, these tags are added to protein of interest using recombinant DNA technologies and then expressed in the cellular model system of choice. In this thesis most of the AP-MS experiments were performed using as “bait” GFP-tagged or biotin-tagged proteins. Whenever possible biotin was preferred because of its high binding affinity for streptavidin which allows very efficient protein purifications (Kay et al., 2009). A more straightforward approach that has been less used in this thesis is to make use of an antibody to pull down the endogenous protein of interest without transiently expressing it (Altelaar et al., 2013b), however this alternative is heavily influenced by the limited availability of specific antibodies, which very often do not recognize with high affinity mouse or rat epitopes. Considering these limitations, in order to identify neuronal specific interactors, a “hybrid” approach was applied in this thesis (Chapter

3). Briefly, biotin- or GFP-tagged proteins were firstly expressed and purified from HEK293 cells using streptavidin or anti-GFP beads respectively, and then incubated with brain lysates obtained from adult rats. Once the protein complexes are co-purified, the samples are separated by gel electrophoresis prior to in-gel digestion. By performing in-gel protein digestion it is possible to divide the sample in multiple fractions thus reducing its complexity, ultimately resulting in a higher number of identifications in the MS analysis (Dunham et al., 2012). To exclude interacting proteins from HEK293 cells and to distinguish brain-specific interactors, a control AP-MS experiment is performed in parallel with samples not supplemented with brain extracts. A representative workflow of the AP-MS methodology described is shown in Figure 3.

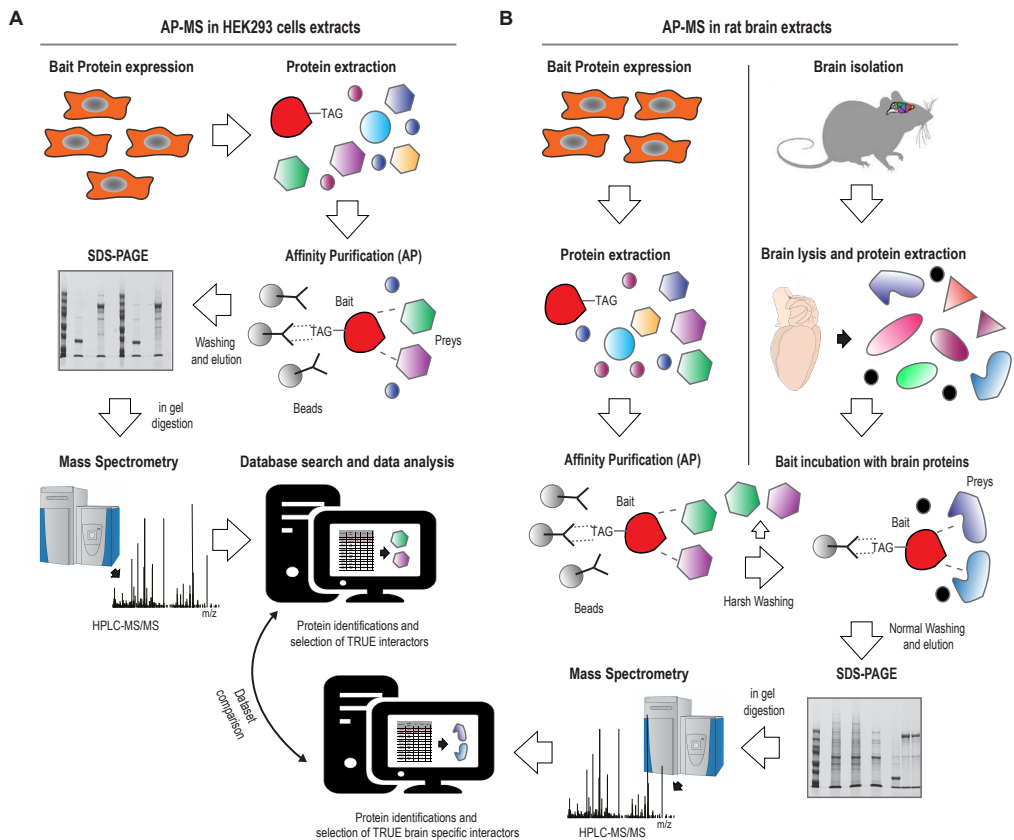


Figure 3. Overview of a typical AP-MS experiment in HEK293 cells and in rat brain extracts

(A-B) The biotinylated-tagged protein of interest is first transiently expressed together with the protein-biotin ligase BirA, in HEK293 cells, next bio-tagged proteins with co-precipitating proteins are purified with streptavidin beads. For the identification of HEK293 interactors, samples are eluted from the beads after few washing steps and directly analyzed by LC-MS/MS (A). To identify brain specific interactions, the “bait” protein is further extensively washed with a buffer containing high salt concentrations to remove HEK293 interactors. The protein is then incubated *in vitro* with protein extracts from adult rat brains and co-purified neuronal proteins are identified by LC-MS/MS (B).

Putative binding partners are then analyzed using the SAINT algorithm for scoring AP-MS data. Neuron specific binding proteins can be distinguished from interactors of HEK293 cells by comparing results of the two parallel AP-MS experiments.

Compared to other techniques, such as for example the “two-hybrid” assay, AP-MS allows the simultaneous identification of several binding proteins of a protein of interest, and can give indications whether multiple proteins are co-precipitating together in complexes, even providing quantitative information about the stoichiometry and the dynamic changes of the protein complex (Gingras et al., 2007; Ngounou Wetie et al., 2013). One potential drawback of this method is represented by the high chances of detecting false positives in the analysis, which is mainly due to the presence of background proteins. This can be minimized by carefully performing negative control AP assays, for instance by using the same support resin without the bait or by using a bait, composed of the affinity tag but not including the protein of interest (Mehta and Trinkle-Mulcahy, 2016; Mellacheruvu et al., 2013). Proteins enriched in samples compared to negative controls can then be discriminated based on the total amount of spectral counts or peptides identified, or in case of quantitative proteomic approaches (SILAC, TMT, iTRAQ) by comparing their relative abundance measured with the isotopic tags (Armean et al., 2013; Vermeulen et al., 2008).

More recently, proximity based labeling approach (such as APEX and BioID previously described in this chapter) are also becoming more popular to study protein-protein interactions in their native environment. Besides identifying specific proteins present in defined organelles or subcellular structures, these methods work perfectly also for the detection of transient and weak interactions (Figure 2C). Once interacting proteins are biotinylated by a promiscuous biotin ligase mutant (BirA) fused to the protein of interest due to their proximity, they can then be subjected to harsh lysis and more stringent enrichment and washing steps which reduce the background binding problem (Chen and Perrimon, 2017; Smits and Vermeulen, 2016).

Cellular aggregates can also be purified and analyzed by MS as physiological protein complexes. Protein aggregates are pathological hallmarks typical of several neurodegenerative diseases. Aggregate formation proceeds following consecutive temporal steps. Initially monomers are transformed into soluble oligomers which then turn into insoluble fibrils or inclusion bodies along with the disease progression. During these pathological processes, normal proteins are also often sequestered into aggregates causing a loss of function phenotype. It is therefore extremely important to investigate the intrinsic nature of these aggregates. In fact, despite their clinical relevance very little is known about their precise protein composition. Optimized protocols for mechanical disruption and solubilization of these aggregates and controlled *in vitro* preparations of these entities allow a spatial and temporal characterization which can be achieved by

advanced proteomics based techniques. For instance, the interactomes of aggregation-prone disease proteins have been successfully characterized by quantitative MS (Hosp et al., 2015) and more recently profiling of Huntington inclusions has been performed (Hosp et al., 2017; Kim et al., 2016). These studies show drastic protein loss due to sequestration into aggregates. Similarly, Chapter 5 of this thesis described in detail the proteomic based approach we used to identify the brain proteins sequestered by Tau pathological oligomers and fibrils at different time points of their aggregation.

Protein-protein interaction analysis by chemical cross linking-MS (XL-MS)

Chemical cross-linking mass spectrometry (XL-MS), similarly to proximity-proteomics could be used as a complementary approach to classical AP-MS, thanks to its enhanced capability of detecting and mapping weak and transient interactions (Figure 2C) (Sinz, 2018; Yang et al., 2015). With this method, two amino acid residues that are in close proximity are covalently bound by a cross-linker, which consists in a reactive molecule composed by two functional lateral groups separated by a space arm. Several types of cross-linkers are currently available. XL-MS uses the characteristic distance constraint provided by each specific cross-linker to detect intra-protein and inter-protein interactions within molecular complexes. The distance constraint is equivalent to the length of the space arm summed to the lengths of the side chains of two cross-linked residues (Liu and Heck, 2015; Sinz, 2014). In standard XL workflows, affinity purification of the protein of interest is performed before the cross-linking reaction and cross-linked residues are identified by MS after enzymatic digestion of the linked proteins. The main advantage of this technique is that not only identifies novel interacting partners but offers meaningful information about their binding interfaces directly involved in the interactions (Liu et al., 2017). Although the resolution of the domain structures resolved by XL-MS is still limited compared to other techniques, such as X-Ray, NMR (Nuclear Magnetic Resonance) or cryo-EM (Cryogenic Electron Microscopy), at the moment XL-MS represents a convenient and attractive solution for gaining structural data without using huge amount of proteins and without dedicated technologies. For example in chapter 3 of this thesis XL-MS was used in combination with classical AP-WB approaches to infer KIF1A intra-molecular interactions underlying KIF1A tail conformation. One other recent alternative of cross-linking is that it can also be applied efficiently *in vivo*, offering the opportunity to investigate protein-protein interactions directly in the cell (Kaake et al., 2014). Boosted by huge advances in data analysis methods, XL-MS can now provide valuable conformational information not only of individual protein complexes but also of the entire proteome (Liu et al., 2015; Lossel et al., 2016). Despite the huge improvements global XL-MS studies are still challenging due to the limited amount of cross-linked peptides detected by MS and to the computational difficulties of the data analysis (Liu and Heck, 2015). In neurobiology another interesting application of cross-linking could be represented by the

detailed characterization of neuro-receptors interactomes. Similar studies have been already proven to be successful in the investigation of receptor protein complexes in different types of cell lines (Deroo et al., 2015; Komolov et al., 2017).

5. Phosphoproteomics and analysis of post translational modifications (PTMs)

Phosphorylation is the most characterized type of PTM. Phosphorylation typically mediates conformational changes in protein structures often resulting into allosteric regulation or modulation of protein-protein interactions. Reversible phosphosites are usually located in crucial positions, for example in proximity of regulatory regions or docking sites, thus controlling activation/inactivation or binding/unbinding of specific proteins involved in cell signaling. Phosphorylation-mediated signaling is extremely important in neuronal synapses. Pioneering proteomics work in the field identified the post synaptic density (PSD) as composed of 466 total proteins (Collins et al., 2006), ~60 of which are kinases phosphorylating ~ 1000/1500 phosphosites in mouse (Collins et al., 2005; Munton et al., 2007; Trinidad et al., 2008). A more recent survey on proteomic studies about protein synaptic composition indicated that more than 2700 different proteins are localized at post- and pre-synaptic sites (Pielot et al., 2012), consequently the number of expected synaptic phospho-sites is expected to be significantly higher.

Learning and memory changes are encoded via synaptic plasticity which is directly correlated with the two main molecular processes modulating synaptic activity, named long-term potentiation (LTP) and long-term depression (LTD). LTP results in a persistent enhancement of synaptic transmission while in the complementary process of LTD the efficacy of synaptic transmission is reduced. Huge reorganization of proteins takes place during LTP and LTD and is usually achieved by changes in the levels or activity of signaling molecules such as kinases and phosphatases within the PSD. Quantitative phospho-proteomics approaches allow to precisely map the dynamics of these phosphorylation events which regulate the main synaptic proteins such as NMDARs, AMPARs, CaMKII, and PSD-95. For example activation of the NMDA receptor leads to changes in the phosphorylation of over 200 sites on 127 proteins (Coba et al., 2009). In a similar fashion, stimulation of dopamine receptor triggers a different combination of phosphorylation events leading to activation of DA-PKA-Rap1-MAPK intracellular signaling pathway (Nagai et al., 2016). Lately, a phospho-proteomic work in the brain, highlighted the importance of the phosphorylation–dephosphorylation cycle of ~80 synaptic proteins in regulating synaptic sleep–wake homeostasis and in maximizing cognitive functions of the brain (Wang et al., 2018).

Despite the importance of this PTM, the stoichiometry of phosphorylated proteins is low in

cells, therefore a dedicated enrichment step is necessary to study this modification (Mann et al., 2002; Zhou et al., 2013). For instance, in Strong Cation Exchange (SCX) chromatography, phosphorylated peptides, containing a negative group, are separated based on their net charge and are typically eluted before the bulk of non-phosphorylated peptides from the SCX column (Alpert et al., 2010; Mant and Hodges, 1985). Other phosphopeptide-enrichment strategies include purification by phosphosite-specific antibodies, chelation, using immobilized metal affinity chromatography (IMAC) resins, where negatively charged phosphopeptides bind to positively charged metal ions, or separation by titanium dioxide (TiO₂) (Figure 2C) (Huang et al., 2014). One of the main problems of these enrichment strategies is that they require a certain amount of sample which can be problematic when working with dissociated cultured neurons, where the yield of harvested proteins is limited. However, new automated phosphopeptide-enrichment methods have been recently optimized allowing high-throughput identifications of PTMs from low sample amounts of primary hippocampal neurons (Post et al., 2017). More targeted approaches can be also applied to map novel phospho-sites on a protein of interest. For these applications, the protein of interest is first separated from the complex mixture (using antibodies or specific tags) and subsequently analyzed by MS to precisely map the position of the phosphate groups on potential phosphorylated residues. The advent of ETD (Electron Transfer Dissociation) based fragmentation in combination with classical HCD and CID has dramatically increased the phosphosite localization scores (Frese et al., 2013; Wiesner et al., 2008).

Although most of the emphasis has been placed on phosphorylation, other PTMs can also be detected by similar kind of proteomic experiments. Just to cite a few, palmitoylation of neuronal integral and peripheral membrane proteins, influences protein function and trafficking (Dejanovic et al., 2014; Tortosa et al., 2017) and can now be investigated in depth by systematic MS studies (Kang et al., 2008). Ubiquitylation is involved in regulating protein turnover and mis-regulation of the ubiquitin-mediated degradation which can lead to multiple neurological diseases (Thompson et al., 2008). High-throughput proteomic technologies can now resolve both the presence and the type of ubiquitin linkage and even providing quantitative values (Ordureau et al., 2015; Ordureau et al., 2018). Glycosylation in the brain can also be precisely monitored using quantitative proteomics. This particular PTM seems to be dynamically modulated by excitatory stimulation in the brain, suggesting a potential role during synaptic plasticity (Khidekel et al., 2007). Altogether these studies show that the latest applications of neuroproteomics can precisely monitor not only global changes in protein expression but also the synchronized modifications and the PTMs cross talks occurring upon different stimulations and/or neuronal maturation.

6. Scope of this thesis

Proteins are highly dynamic entities which can modulate their cellular functions based on their expression level profiles and their intrinsic capabilities of forming complexes and networks in response to differentiation or stimulation. In neurobiology the investigation of protein dynamics has always been challenging due to the vast cellular heterogeneity in the CNS and the small numbers of cells (and consequently proteins) available. Over the last decade neuroproteomics has enormously contributed to the understanding of some of the major challenges in neurobiology. Considering that the combined application of multiple approaches and techniques is often the key for a complete comprehension of a biological event, we envision that MS-based approaches along with other -omics approaches will shortly become routine applications for the neuroscientist aiming to study neurological processes in more detail. In this thesis we applied the latest techniques in proteomics to study neuronal differentiation, kinesin-mediated neuronal transport and protein-interaction networks in the brain.

In **Chapter 2** we perform a systematic and in-depth analysis of proteome dynamics in cultured hippocampal neurons at various developmental stages, including axon outgrowth, dendritogenesis and synapse formation. Using a combination of stable isotope labeling and high-resolution tandem mass spectrometry (MS/MS) we show that almost one third of all 4500 neuronal proteins quantified undergo a more than two-fold expression change during neuronal differentiation, indicating extensive remodeling of the neuron proteome. By using AP-MS and cell biological assays we also reveal an unappreciated role for the classic ‘axon guidance molecule’ neural cell adhesion molecule 1 (NCAM1) in dendritic development. Besides its role in the axon, we show that NCAM1 is strongly upregulated during dendritogenesis and stimulates dendritic arbor development by promoting actin filament stabilization at the dendritic growth cone.

In **Chapter 3** we address the role of the kinesin-3 family member KIF1A in transporting DCVs in dendrites. By performing a systematic AP-MS approach we identify the neuronal KIF1A interactome and focus on three binding partners, the calcium binding protein Calmodulin (CaM) and two synaptic scaffolding proteins: liprin- α and TANC2. We report that calcium, acting via CaM, enhances KIF1A binding to DCVs and increases vesicle motility in dendrites. In addition we show that liprin- α and TANC2 are mainly localized in dendritic spines and help in recruiting KIF1A-driven DCVs to synaptic sites. In general our combined proteomics-cell biological data describe a novel loading and delivery mechanism for KIF1A-driven vesicles.

In **Chapter 4** we identify the interacting binding partners of different domains of the kinesin-3

family members KIF13B and KIF1A using AP-MS. We further investigate the role of these domains in transporting specific cargos in neurons by using a “split kinesin binding assay” previously described by (Jenkins et al., 2012). We discover that specific regions such as the MBS domain on KIF13B and the Liprin Binding Domain (LBD) on KIF1A (and consequently the specific adaptor proteins interacting with these regions, namely DLG and liprin- α respectively) are not directly required for the formation of the motor-cargo complex and therefore are not directly required for cargo transport, as previously hypothesized.

In **Chapter 5** we apply a MS-based approach to characterize the aberrant interacting partners sequestered by Tau pathological aggregates at different time point of aggregation. We also test the effect of the chaperone Hsp-90 on Tau aggregates by analyzing Tau interactome in samples supplemented with Hsp-90. Results suggest that specific MT binding proteins, RNA binders are sequestered into Tau fibrillary aggregates and their abnormal sequestration can be rescued by the activity of the chaperone Hsp-90 which prevents the aggregation of Tau, keeping it in its soluble monomeric conformation.

In **Chapter 6** we apply quantitative MS-based technologies to: i) measure protein expression levels of TRIM related proteins in neurons depleted for the axon initial segment protein TRIM46; ii) verify KD-efficiency for several shRNAs directed against proteins known to shape ER morphology (REEPs, DP1) in neurons. We also use AP-MS in brains and cells to: i) characterize HAUS2 and HAUS6 protein complexes; ii) identify interacting binding proteins of SCRNI (Secernin1) which is a protein we demonstrate is involved in the synaptic vesicle cycle.

In **Chapter 7** we discuss the critical steps required to ensure a correct neuronal differentiation highlighting the importance of microtubule dependent transport in this process. We mainly focus on the regulation of kinesin motors and in the predominant role of kinesin 3 motors (KIF1A and KIF13B) in transport of vesicles in dendrites and into dendritic spines. In the final part we provide an outlook on future research and applications in the study of motor protein regulation.

REFERENCES

- Aebersold, R., and Mann, M. (2003). Mass spectrometry-based proteomics. *Nature* 422, 198-207.
- Alpert, A.J., Petritis, K., Kangas, L., Smith, R.D., Mechtler, K., Mitulovic, G., Mohammed, S., and Heck, A.J. (2010). Peptide orientation affects selectivity in ion-exchange chromatography. *Anal Chem* 82, 5253-5259.
- Altealar, A.F., Frese, C.K., Preisinger, C., Hennrich, M.L., Schram, A.W., Timmers, H.T., Heck, A.J., and Mohammed, S. (2013a). Benchmarking stable isotope labeling based quantitative proteomics. *J Proteomics* 88, 14-26.
- Altealar, A.F., Munoz, J., and Heck, A.J. (2013b). Next-generation proteomics: towards an integrative view of proteome dynamics. *Nat Rev Genet* 14, 35-48.
- Amunts, K., Ebell, C., Muller, J., Telefont, M., Knoll, A., and Lippert, T. (2016). The Human Brain Project: Creating a European Research Infrastructure to Decode the Human Brain. *Neuron* 92, 574-581.
- Armean, I.M., Lilley, K.S., and Trotter, M.W. (2013). Popular computational methods to assess multiprotein complexes derived from label-free affinity purification and mass spectrometry (AP-MS) experiments. *Mol Cell Proteomics* 12, 1-13.
- Bantscheff, M., Lemeer, S., Savitski, M.M., and Kuster, B. (2012). Quantitative mass spectrometry in proteomics: critical review update from 2007 to the present. *Anal Bioanal Chem* 404, 939-965.
- Bath, T.S., Francavilla, C., and Olsen, J.V. (2014). Off-line high-pH reversed-phase fractionation for in-depth phosphoproteomics. *J Proteome Res* 13, 6176-6186.
- Bayes, A., Collins, M.O., Croning, M.D., van de Lagemaat, L.N., Choudhary, J.S., and Grant, S.G. (2012). Comparative study of human and mouse postsynaptic proteomes finds high compositional conservation and abundance differences for key synaptic proteins. *PLoS One* 7, e46683.
- Betzig, E., Patterson, G.H., Sougrat, R., Lindwasser, O.W., Olenych, S., Bonifacino, J.S., Davidson, M.W., Lippincott-Schwartz, J., and Hess, H.F. (2006). Imaging intracellular fluorescent proteins at nanometer resolution. *Science* 313, 1642-1645.
- Boyken, J., Gronborg, M., Riedel, D., Urlaub, H., Jahn, R., and Chua, J.J. (2013). Molecular profiling of synaptic vesicle docking sites reveals novel proteins but few differences between glutamatergic and GABAergic synapses. *Neuron* 78, 285-297.
- Brennand, K., Savas, J.N., Kim, Y., Tran, N., Simone, A., Hashimoto-Torii, K., Beaumont, K.G., Kim, H.J., Topol, A., Ladrán, I., *et al.* (2015). Phenotypic differences in hiPSC NPCs derived from patients with schizophrenia. *Mol Psychiatry* 20, 361-368.
- Budayeva, H.G., and Cristea, I.M. (2014). A mass spectrometry view of stable and transient protein interactions. *Adv Exp Med Biol* 806, 263-282.
- Centeno, E.G.Z., Cimarosti, H., and Bithell, A. (2018). 2D versus 3D human induced pluripotent stem cell-derived cultures for neurodegenerative disease modelling. *Mol Neurodegener* 13, 27.
- Chae, J.I., Kim, D.W., Lee, N., Jeon, Y.J., Jeon, I., Kwon, J., Kim, J., Soh, Y., Lee, D.S., Seo, K.S., *et al.* (2012). Quantitative proteomic analysis of induced pluripotent stem cells derived from a human Huntington's disease patient. *Biochem J* 446, 359-371.
- Chaerkady, R., Kerr, C.L., Marimuthu, A., Kelkar, D.S., Kashyap, M.K., Gucek, M., Gearhart, J.D., and Pandey, A. (2009). Temporal analysis of neural differentiation using quantitative proteomics. *J Proteome Res* 8, 1315-1326.
- Chen, C.L., and Perrimon, N. (2017). Proximity-dependent labeling methods for proteomic profiling in living cells. *Wiley Interdiscip Rev Dev Biol* 6.
- Choudhary, C., Kumar, C., Gnäd, F., Nielsen, M.L., Rehman, M., Walther, T.C., Olsen, J.V., and Mann, M. (2009). Lysine acetylation targets protein complexes and co-regulates major cellular functions. *Science* 325, 834-840.
- Coba, M.P., Pocklington, A.J., Collins, M.O., Kopanitsa, M.V., Uren, R.T., Swamy, S., Croning, M.D., Choudhary, J.S., and Grant, S.G. (2009). Neurotransmitters drive combinatorial multistate postsynaptic density networks. *Sci Signal* 2, ra19.
- Collins, M.O., Husi, H., Yu, L., Brandon, J.M., Anderson, C.N., Blackstock, W.P., Choudhary, J.S., and Grant, S.G. (2006). Molecular characterization and comparison of the components and multiprotein complexes in the postsynaptic proteome. *J Neurochem* 97 Suppl 1, 16-23.
- Collins, M.O., Yu, L., Coba, M.P., Husi, H., Campuzano, I., Blackstock, W.P., Choudhary, J.S., and Grant, S.G. (2005). Proteomic analysis of in vivo

phosphorylated synaptic proteins. *J Biol Chem* 280, 5972-5982.

Cristobal, A., van den Toorn, H.W.P., van de Wetering, M., Clevers, H., Heck, A.J.R., and Mohammed, S. (2017). Personalized Proteome Profiles of Healthy and Tumor Human Colon Organoids Reveal Both Individual Diversity and Basic Features of Colorectal Cancer. *Cell Rep* 18, 263-274.

Dacic, V., Minardi Nascimento, J., Costa Sartore, R., Maciel, R.M., de Araujo, D.B., Ribeiro, S., Martins-de-Souza, D., and Rehen, S.K. (2017). Short term changes in the proteome of human cerebral organoids induced by 5-MeO-DMT. *Sci Rep* 7, 12863.

Dejanovic, B., Semtner, M., Ebert, S., Lamkemeyer, T., Neuser, F., Luscher, B., Meier, J.C., and Schwarz, G. (2014). Palmitoylation of gephyrin controls receptor clustering and plasticity of GABAergic synapses. *PLoS Biol* 12, e1001908.

Deroo, S., Stengel, F., Mohammadi, A., Henry, N., Hubin, E., Krammer, E.M., Aebersold, R., and Raussens, V. (2015). Chemical cross-linking/mass spectrometry maps the amyloid beta peptide binding region on both apolipoprotein E domains. *ACS Chem Biol* 10, 1010-1016.

Di Palma, S., Hennrich, M.L., Heck, A.J., and Mohammed, S. (2012). Recent advances in peptide separation by multidimensional liquid chromatography for proteome analysis. *J Proteomics* 75, 3791-3813.

Dunham, W.H., Mullin, M., and Gingras, A.C. (2012). Affinity-purification coupled to mass spectrometry: basic principles and strategies. *Proteomics* 12, 1576-1590.

Dutta, D., Heo, I., and Clevers, H. (2017). Disease Modeling in Stem Cell-Derived 3D Organoid Systems. *Trends Mol Med* 23, 393-410.

Focking, M., Boersema, P.J., O'Donoghue, N., Lubec, G., Pennington, S.R., Cotter, D.R., and Dunn, M.J. (2006). 2-D DIGE as a quantitative tool for investigating the HUPO Brain Proteome Project mouse series. *Proteomics* 6, 4914-4931.

Fournier, M.L., Gilmore, J.M., Martin-Brown, S.A., and Washburn, M.P. (2007). Multidimensional separations-based shotgun proteomics. *Chem Rev* 107, 3654-3686.

Frese, C.K., Mikhaylova, M., Stucchi, R., Gautier, V., Liu, Q., Mohammed, S., Heck, A.J.R., Altelaar, A.F.M., and Hoogenraad, C.C. (2017). Quantitative Map of Proteome Dynamics during Neuronal Differentiation. *Cell Rep* 18, 1527-1542.

Frese, C.K., Zhou, H., Taus, T., Altelaar, A.F., Mechtler, K., Heck, A.J., and Mohammed, S.

(2013). Unambiguous phosphosite localization using electron-transfer/higher-energy collision dissociation (EThcD). *J Proteome Res* 12, 1520-1525.

Ghazalpour, A., Bennett, B., Petyuk, V.A., Orozco, L., Hagopian, R., Mungrue, I.N., Farber, C.R., Sinsheimer, J., Kang, H.M., Furlotte, N., *et al.* (2011). Comparative analysis of proteome and transcriptome variation in mouse. *PLoS Genet* 7, e1001393.

Gingras, A.C., Gstaiger, M., Raught, B., and Aebersold, R. (2007). Analysis of protein complexes using mass spectrometry. *Nat Rev Mol Cell Biol* 8, 645-654.

Glasser, M.F., Smith, S.M., Marcus, D.S., Andersson, J.L., Auerbach, E.J., Behrens, T.E., Coalson, T.S., Harms, M.P., Jenkinson, M., Moeller, S., *et al.* (2016). The Human Connectome Project's neuroimaging approach. *Nat Neurosci* 19, 1175-1187.

Gygi, S.P., Rochon, Y., Franza, B.R., and Aebersold, R. (1999). Correlation between protein and mRNA abundance in yeast. *Mol Cell Biol* 19, 1720-1730.

Hamacher, M., Hardt, T., van Hall, A., Stephan, C., Marcus, K., and Meyer, H.E. (2008). Inside SMP proteomics: six years German Human Brain Proteome Project (HBPP) - a summary. *Proteomics* 8, 1118-1128.

Han, D., Jin, J., Woo, J., Min, H., and Kim, Y. (2014). Proteomic analysis of mouse astrocytes and their secretome by a combination of FASP and StageTip-based, high pH, reversed-phase fractionation. *Proteomics* 14, 1604-1609.

Han, S., Li, J., and Ting, A.Y. (2018). Proximity labeling: spatially resolved proteomic mapping for neurobiology. *Curr Opin Neurobiol* 50, 17-23.

Heilemann, M., van de Linde, S., Schüttelpe, M., Kasper, R., Seefeldt, B., Mukherjee, A., Tinnefeld, P., and Sauer, M. (2008). Subdiffraction-resolution fluorescence imaging with conventional fluorescent probes. *Angew Chem Int Ed Engl* 47, 6172-6176.

Hosp, F., Gutierrez-Angel, S., Schaefer, M.H., Cox, J., Meissner, F., Hipp, M.S., Hartl, F.U., Klein, R., Dudanova, I., and Mann, M. (2017). Spatiotemporal Proteomic Profiling of Huntington's Disease Inclusions Reveals Widespread Loss of Protein Function. *Cell Rep* 21, 2291-2303.

Hosp, F., Vossfeldt, H., Heinig, M., Vasiljevic, D., Arumughan, A., Wyler, E., Genetic, Environmental Risk for Alzheimer's Disease, G.C., Landthaler, M., Hubner, N., *et al.* (2015). Quantitative interaction proteomics of neurodegenerative disease proteins. *Cell Rep* 11, 1134-1146.

Huang, J., Wang, F., Ye, M., and Zou, H. (2014). Enrichment and separation techniques for large-scale

proteomics analysis of the protein post-translational modifications. *J Chromatogr A* 1372C, 1-17.

Iwata, K., Cafe-Mendes, C.C., Schmitt, A., Steiner, J., Manabe, T., Matsuzaki, H., Falkai, P., Turck, C.W., and Martins-de-Souza, D. (2013). The human oligodendrocyte proteome. *Proteomics* 13, 3548-3553.

Jenkins, B., Decker, H., Bentley, M., Luisi, J., and Banker, G. (2012). A novel split kinesin assay identifies motor proteins that interact with distinct vesicle populations. *J Cell Biol* 198, 749-761.

Jungblut, P., and Klose, J. (1985). Genetic variability of proteins from mitochondria and mitochondrial fractions of mouse organs. *Biochem Genet* 23, 227-245.

Kaake, R.M., Wang, X., Burke, A., Yu, C., Kandur, W., Yang, Y., Novtisky, E.J., Second, T., Duan, J., Kao, A., *et al.* (2014). A new in vivo cross-linking mass spectrometry platform to define protein-protein interactions in living cells. *Mol Cell Proteomics* 13, 3533-3543.

Kang, R., Wan, J., Arstikaitis, P., Takahashi, H., Huang, K., Bailey, A.O., Thompson, J.X., Roth, A.F., Drisdell, R.C., Mastro, R., *et al.* (2008). Neural palmitoyl-proteomics reveals dynamic synaptic palmitoylation. *Nature* 456, 904-909.

Kay, B.K., Thai, S., and Volgina, V.V. (2009). High-throughput biotinylation of proteins. *Methods Mol Biol* 498, 185-196.

Khidekel, N., Ficarro, S.B., Clark, P.M., Bryan, M.C., Swaney, D.L., Rexach, J.E., Sun, Y.E., Coon, J.J., Peters, E.C., and Hsieh-Wilson, L.C. (2007). Probing the dynamics of O-GlcNAc glycosylation in the brain using quantitative proteomics. *Nat Chem Biol* 3, 339-348.

Kim, Y.E., Hosp, F., Frottin, F., Ge, H., Mann, M., Hayer-Hartl, M., and Hartl, F.U. (2016). Soluble Oligomers of PolyQ-Expanded Huntingtin Target a Multiplicity of Key Cellular Factors. *Mol Cell* 63, 951-964.

Klose, J., and Feller, M. (1981). Genetic variability of proteins from plasma membranes and cytosols of mouse organs. *Biochem Genet* 19, 859-870.

Komolov, K.E., Du, Y., Duc, N.M., Betz, R.M., Rodrigues, J., Leib, R.D., Patra, D., Skiniotis, G., Adams, C.M., Dror, R.O., *et al.* (2017). Structural and Functional Analysis of a beta2-Adrenergic Receptor Complex with GRK5. *Cell* 169, 407-421 e416.

Kruger, M., Moser, M., Ussar, S., Thievensen, I., Lubber, C.A., Former, F., Schmidt, S., Zanivan, S., Fassler, R., and Mann, M. (2008). SILAC mouse for quantitative proteomics uncovers kindlin-3 as an

essential factor for red blood cell function. *Cell* 134, 353-364.

Kulak, N.A., Geyer, P.E., and Mann, M. (2017). Loss-less Nano-fractionator for High Sensitivity, High Coverage Proteomics. *Mol Cell Proteomics* 16, 694-705.

Liu, F., and Heck, A.J. (2015). Interrogating the architecture of protein assemblies and protein interaction networks by cross-linking mass spectrometry. *Curr Opin Struct Biol* 35, 100-108.

Liu, F., Rijkers, D.T., Post, H., and Heck, A.J. (2015). Proteome-wide profiling of protein assemblies by cross-linking mass spectrometry. *Nat Methods* 12, 1179-1184.

Liu, Q., Rimmelzwaal, S., Heck, A.J.R., Akhmanova, A., and Liu, F. (2017). Facilitating identification of minimal protein binding domains by cross-linking mass spectrometry. *Sci Rep* 7, 13453.

Loh, K.H., Stawski, P.S., Draycott, A.S., Udeshi, N.D., Lehrman, E.K., Wilton, D.K., Svinikina, T., Deerinck, T.J., Ellisman, M.H., Stevens, B., *et al.* (2016). Proteomic Analysis of Unbounded Cellular Compartments: Synaptic Clefts. *Cell* 166, 1295-1307 e1221.

Lossl, P., van de Waterbeemd, M., and Heck, A.J. (2016). The diverse and expanding role of mass spectrometry in structural and molecular biology. *EMBO J* 35, 2634-2657.

Low, T.Y., van Heesch, S., van den Toorn, H., Giansanti, P., Cristobal, A., Toonen, P., Schafer, S., Hubner, N., van Breukelen, B., Mohammed, S., *et al.* (2013). Quantitative and qualitative proteome characteristics extracted from in-depth integrated genomics and proteomics analysis. *Cell Rep* 5, 1469-1478.

Lundgren, D.H., Hwang, S.I., Wu, L., and Han, D.K. (2010). Role of spectral counting in quantitative proteomics. *Expert Rev Proteomics* 7, 39-53.

MacGillavry, H.D., and Hoogenraad, C.C. (2015). The internal architecture of dendritic spines revealed by super-resolution imaging: What did we learn so far? *Exp Cell Res* 335, 180-186.

Mann, M., Ong, S.E., Gronborg, M., Steen, H., Jensen, O.N., and Pandey, A. (2002). Analysis of protein phosphorylation using mass spectrometry: deciphering the phosphoproteome. *Trends Biotechnol* 20, 261-268.

Mant, C.T., and Hodges, R.S. (1985). Separation of peptides by strong cation-exchange high-performance liquid chromatography. *J Chromatogr* 327, 147-155.

Martell, J.D., Deerinck, T.J., Sancak, Y., Poulos, T.L., Mootha, V.K., Sosinsky, G.E., Ellisman,

- M.H., and Ting, A.Y. (2012). Engineered ascorbate peroxidase as a genetically encoded reporter for electron microscopy. *Nat Biotechnol* 30, 1143-1148.
- McCarroll, S.A., Feng, G., and Hyman, S.E. (2014). Genome-scale neurogenetics: methodology and meaning. *Nat Neurosci* 17, 756-763.
- Mehta, V., and Trinkle-Mulcahy, L. (2016). Recent advances in large-scale protein interactome mapping. *F1000Res* 5.
- Mellacheruvu, D., Wright, Z., Couzens, A.L., Lambert, J.P., St-Denis, N.A., Li, T., Miteva, Y.V., Hauri, S., Sardi, M.E., Low, T.Y., *et al.* (2013). The CRAPome: a contaminant repository for affinity purification-mass spectrometry data. *Nat Methods* 10, 730-736.
- Morris, J.H., Knudsen, G.M., Verschueren, E., Johnson, J.R., Cimermanic, P., Greninger, A.L., and Pico, A.R. (2014). Affinity purification-mass spectrometry and network analysis to understand protein-protein interactions. *Nat Protoc* 9, 2539-2554.
- Munton, R.P., Tweedie-Cullen, R., Livingstone-Zatchej, M., Weinandy, F., Waidelich, M., Longo, D., Gehrig, P., Pothast, F., Rutishauser, D., Gerrits, B., *et al.* (2007). Qualitative and quantitative analyses of protein phosphorylation in naive and stimulated mouse synaptosomal preparations. *Mol Cell Proteomics* 6, 283-293.
- Nagai, T., Nakamuta, S., Kuroda, K., Nakauchi, S., Nishioka, T., Takano, T., Zhang, X., Tsuboi, D., Funahashi, Y., Nakano, T., *et al.* (2016). Phosphoproteomics of the Dopamine Pathway Enables Discovery of Rap1 Activation as a Reward Signal In Vivo. *Neuron* 89, 550-565.
- Ngounou Wetie, A.G., Sokolowska, I., Woods, A.G., Roy, U., Loo, J.A., and Darie, C.C. (2013). Investigation of stable and transient protein-protein interactions: Past, present, and future. *Proteomics* 13, 538-557.
- Nielsen, P.A., Olsen, J.V., Podtelejnikov, A.V., Andersen, J.R., Mann, M., and Wisniewski, J.R. (2005). Proteomic mapping of brain plasma membrane proteins. *Mol Cell Proteomics* 4, 402-408.
- Ong, S.E., Blagoev, B., Kratchmarova, I., Kristensen, D.B., Steen, H., Pandey, A., and Mann, M. (2002). Stable isotope labeling by amino acids in cell culture, SILAC, as a simple and accurate approach to expression proteomics. *Mol Cell Proteomics* 1, 376-386.
- Ong, S.E., and Mann, M. (2005). Mass spectrometry-based proteomics turns quantitative. *Nat Chem Biol* 1, 252-262.
- Ordureau, A., Munch, C., and Harper, J.W. (2015). Quantifying ubiquitin signaling. *Mol Cell* 58, 660-676.
- Ordureau, A., Paulo, J.A., Zhang, W., Ahfeldt, T., Zhang, J., Cohn, E.F., Hou, Z., Heo, J.M., Rubin, L.L., Sidhu, S.S., *et al.* (2018). Dynamics of PARKIN-Dependent Mitochondrial Ubiquitylation in Induced Neurons and Model Systems Revealed by Digital Snapshot Proteomics. *Mol Cell* 70, 211-227 e218.
- Pandey, S., Shekhar, K., Regev, A., and Schier, A.F. (2018). Comprehensive Identification and Spatial Mapping of Habenular Neuronal Types Using Single-Cell RNA-Seq. *Curr Biol* 28, 1052-1065 e1057.
- Peng, J., Kim, M.J., Cheng, D., Duong, D.M., Gygi, S.P., and Sheng, M. (2004). Semiquantitative proteomic analysis of rat forebrain postsynaptic density fractions by mass spectrometry. *J Biol Chem* 279, 21003-21011.
- Perkins, D.N., Pappin, D.J., Creasy, D.M., and Cottrell, J.S. (1999). Probability-based protein identification by searching sequence databases using mass spectrometry data. *Electrophoresis* 20, 3551-3567.
- Pielot, R., Smalla, K.H., Muller, A., Landgraf, P., Lehmann, A.C., Eisenschmidt, E., Haus, U.U., Weismantel, R., Gundelfinger, E.D., and Dieterich, D.C. (2012). SynProt: A Database for Proteins of Detergent-Resistant Synaptic Protein Preparations. *Front Synaptic Neurosci* 4, 1.
- Post, H., Penning, R., Fitzpatrick, M.A., Garrigues, L.B., Wu, W., MacGillavry, H.D., Hoogenraad, C.C., Heck, A.J., and Altelar, A.F. (2017). Robust, Sensitive, and Automated Phosphopeptide Enrichment Optimized for Low Sample Amounts Applied to Primary Hippocampal Neurons. *J Proteome Res* 16, 728-737.
- Rauniyar, N., and Yates, J.R., 3rd (2014). Isobaric labeling-based relative quantification in shotgun proteomics. *J Proteome Res* 13, 5293-5309.
- Rees, J.S., Li, X.W., Perrett, S., Lilley, K.S., and Jackson, A.P. (2015). Selective Proteomic Proximity Labeling Assay Using Tyramide (SPPLAT): A Quantitative Method for the Proteomic Analysis of Localized Membrane-Bound Protein Clusters. *Curr Protoc Protein Sci* 80, 19 27 11-18.
- Rhee, H.W., Zou, P., Udeshi, N.D., Martell, J.D., Mootha, V.K., Carr, S.A., and Ting, A.Y. (2013). Proteomic mapping of mitochondria in living cells via spatially restricted enzymatic tagging. *Science* 339, 1328-1331.
- Riley, N.M., Hebert, A.S., and Coon, J.J. (2016). Proteomics Moves into the Fast Lane. *Cell Syst* 2, 142-143.
- Roux, K.J., Kim, D.I., Raida, M., and Burke, B. (2012). A promiscuous biotin ligase fusion

protein identifies proximal and interacting proteins in mammalian cells. *J Cell Biol* 196, 801-810.

Rust, M.J., Bates, M., and Zhuang, X. (2006). Sub-diffraction-limit imaging by stochastic optical reconstruction microscopy (STORM). *Nat Methods* 3, 793-795.

Sharma, K., Schmitt, S., Bergner, C.G., Tyanova, S., Kannaiyan, N., Manrique-Hoyos, N., Kongi, K., Cantuti, L., Hanisch, U.K., Philips, M.A., *et al.* (2015). Cell type- and brain region-resolved mouse brain proteome. *Nat Neurosci* 18, 1819-1831.

Shekhar, K., Lapan, S.W., Whitney, I.E., Tran, N.M., Macosko, E.Z., Kowalczyk, M., Adiconis, X., Levin, J.Z., Nemesh, J., Goldman, M., *et al.* (2016). Comprehensive Classification of Retinal Bipolar Neurons by Single-Cell Transcriptomics. *Cell* 166, 1308-1323 e1330.

Sheng, M., and Hoogenraad, C.C. (2007). The postsynaptic architecture of excitatory synapses: a more quantitative view. *Annu Rev Biochem* 76, 823-847.

Singec, I., Crain, A.M., Hou, J., Tobe, B.T.D., Talantova, M., Winquist, A.A., Doctor, K.S., Choy, J., Huang, X., La Monaca, E., *et al.* (2016). Quantitative Analysis of Human Pluripotency and Neural Specification by In-Depth (Phospho)Proteomic Profiling. *Stem Cell Reports* 7, 527-542.

Sinz, A. (2014). The advancement of chemical cross-linking and mass spectrometry for structural proteomics: from single proteins to protein interaction networks. *Expert Rev Proteomics* 11, 733-743.

Sinz, A. (2018). Cross-Linking/Mass Spectrometry for Studying Protein Structures and Protein-Protein Interactions: Where Are We Now and Where Should We Go from Here? *Angew Chem Int Ed Engl* 57, 6390-6396.

Smits, A.H., and Vermeulen, M. (2016). Characterizing Protein-Protein Interactions Using Mass Spectrometry: Challenges and Opportunities. *Trends Biotechnol* 34, 825-834.

Spellman, D.S., Deinhart, K., Darie, C.C., Chao, M.V., and Neubert, T.A. (2008). Stable isotopic labeling by amino acids in cultured primary neurons: application to brain-derived neurotrophic factor-dependent phosphotyrosine-associated signaling. *Mol Cell Proteomics* 7, 1067-1076.

Steen, H., and Mann, M. (2004). The ABC's (and XYZ's) of peptide sequencing. *Nat Rev Mol Cell Biol* 5, 699-711.

Sunkin, S.M., Ng, L., Lau, C., Dolbeare, T., Gilbert, T.L., Thompson, C.L., Hawrylycz, M., and Dang, C. (2013). Allen Brain Atlas: an integrated spatio-temporal portal for exploring the central

nervous system. *Nucleic Acids Res* 41, D996-D1008.
Switzar, L., Giera, M., and Niessen, W.M. (2013). Protein digestion: an overview of the available techniques and recent developments. *J Proteome Res* 12, 1067-1077.

Takahashi, K., Tanabe, K., Ohnuki, M., Narita, M., Ichisaka, T., Tomoda, K., and Yamanaka, S. (2007). Induction of pluripotent stem cells from adult human fibroblasts by defined factors. *Cell* 131, 861-872.

Tas, R.P., Chazeau, A., Cloin, B.M.C., Lambers, M.L.A., Hoogenraad, C.C., and Kapitein, L.C. (2017). Differentiation between Oppositely Oriented Microtubules Controls Polarized Neuronal Transport. *Neuron* 96, 1264-1271 e1265.

Thompson, S.J., Loftus, L.T., Ashley, M.D., and Meller, R. (2008). Ubiquitin-proteasome system as a modulator of cell fate. *Curr Opin Pharmacol* 8, 90-95.

Tortosa, E., Adolfs, Y., Fukata, M., Pasterkamp, R.J., Kapitein, L.C., and Hoogenraad, C.C. (2017). Dynamic Palmitoylation Targets MAP6 to the Axon to Promote Microtubule Stabilization during Neuronal Polarization. *Neuron* 94, 809-825 e807.

Trinidad, J.C., Thalhammer, A., Specht, C.G., Lynn, A.J., Baker, P.R., Schoepfer, R., and Burlingame, A.L. (2008). Quantitative analysis of synaptic phosphorylation and protein expression. *Mol Cell Proteomics* 7, 684-696.

Vermeulen, M., Hubner, N.C., and Mann, M. (2008). High confidence determination of specific protein-protein interactions using quantitative mass spectrometry. *Curr Opin Biotechnol* 19, 331-337.

Wang, H., Qian, W.J., Chin, M.H., Petyuk, V.A., Barry, R.C., Liu, T., Gritsenko, M.A., Mottaz, H.M., Moore, R.J., Camp II, D.G., *et al.* (2006). Characterization of the mouse brain proteome using global proteomic analysis complemented with cysteinyl-peptide enrichment. *J Proteome Res* 5, 361-369.

Wang, Z., Ma, J., Miyoshi, C., Li, Y., Sato, M., Ogawa, Y., Lou, T., Ma, C., Gao, X., Lee, C., *et al.* (2018). Quantitative phosphoproteomic analysis of the molecular substrates of sleep need. *Nature*.

Wasinger, V.C., Cordwell, S.J., Cerpa-Poljak, A., Yan, J.X., Gooley, A.A., Wilkins, M.R., Duncan, M.W., Harris, R., Williams, K.L., and Humphery-Smith, I. (1995). Progress with gene-product mapping of the Mollicutes: *Mycoplasma genitalium*. *Electrophoresis* 16, 1090-1094.

Wiesner, J., Premrs, T., and Sickmann, A. (2008). Application of electron transfer dissociation (ETD) for the analysis of posttranslational modifications. *Proteomics* 8, 4466-4483.

Wilhelm, M., Schlegl, J., Hahne, H., Gholami, A.M., Lieberenz, M., Savitski, M.M., Ziegler, E., Butzmann, L., Gessulat, S., Marx, H., *et al.* (2014). Mass-spectrometry-based draft of the human proteome. *Nature* 509, 582-587.

Witzmann, F.A., Arnold, R.J., Bai, F., Hrncirova, P., Kimpel, M.W., Mechref, Y.S., McBride, W.J., Novotny, M.V., Pedrick, N.M., Ringham, H.N., and Simon, J.R. (2005). A proteomic survey of rat cerebral cortical synaptosomes. *Proteomics* 5, 2177-2201.

Wu, Y., Wang, F., Liu, Z., Qin, H., Song, C., Huang, J., Bian, Y., Wei, X., Dong, J., and Zou, H. (2014). Five-plex isotope dimethyl labeling for quantitative proteomics. *Chem Commun (Camb)* 50, 1708-1710.

Xu, G., Paige, J.S., and Jaffrey, S.R. (2010). Global analysis of lysine ubiquitination by ubiquitin remnant immunoaffinity profiling. *Nat Biotechnol* 28, 868-873.

Yamanaka, S. (2007). Strategies and new developments in the generation of patient-specific pluripotent stem cells. *Cell Stem Cell* 1, 39-49.

Yang, J., Wagner, S.A., and Beli, P. (2015). Illuminating Spatial and Temporal Organization of Protein Interaction Networks by Mass Spectrometry-Based Proteomics. *Front Genet* 6, 344.

Yates, J.R., 3rd, McCormack, A.L., Link, A.J., Schieltz, D., Eng, J., and Hays, L. (1996). Future prospects for the analysis of complex biological systems using micro-column liquid chromatography-electrospray tandem mass spectrometry. *Analyst* 121, 65R-76R.

Yeung, E.S. (2011). Genome-wide correlation between mRNA and protein in a single cell. *Angew Chem Int Ed Engl* 50, 583-585.

Zhang, G., Deinhardt, K., and Neubert, T.A. (2014). Stable isotope labeling by amino acids in cultured primary neurons. *Methods Mol Biol* 1188, 57-64.

Zhou, H., Di Palma, S., Preisinger, C., Peng, M., Polat, A.N., Heck, A.J., and Mohammed, S. (2013). Toward a comprehensive characterization of a human cancer cell phosphoproteome. *J Proteome Res* 12, 260-271.



CHAPTER 2

Quantitative map of proteome dynamics during neuronal differentiation

Christian K. Frese^{1,2,*}, Marina Mikhaylova^{3,*},
Riccardo Stucchi^{1,2,3,*}, Violette Gautier^{1,2},
Qingyang Liu^{1,2,3}, Shabaz Mohammed^{1,2}, Albert
J.R. Heck^{1,2}, A.F. Maarten Altelaar^{1,2} and
Casper C. Hoogenraad³

Cell Reports, February 2017, 18(6): 1527-1542

¹Biomolecular Mass Spectrometry and Proteomics, Bijvoet Center for Biomolecular Research and Utrecht Institute for Pharmaceutical Sciences, Utrecht University, Padualaan 8, 3584 Utrecht, the Netherlands

²Netherlands Proteomics Centre, Padualaan 8, 3584 Utrecht, the Netherlands

³Cell Biology, Department of Biology, Faculty of Science, Utrecht University, 3584 Utrecht, the Netherlands

*equal contribution

ABSTRACT

Neuronal differentiation is a multistep process that shapes and re-shapes neurons by progressing through several typical stages, including axon outgrowth, dendritogenesis, and synapse formation. To systematically profile proteome dynamics throughout neuronal differentiation, we took cultured rat hippocampal neurons at different developmental stages and monitored changes in protein abundance using a combination of stable isotope labeling and high-resolution liquid chromatography-tandem mass spectrometry (LC-MS/MS). Almost one third of all 4,500 proteins quantified underwent a more than 2-fold expression change during neuronal differentiation, indicating extensive remodeling of the neuron proteome. To highlight the strength of our resource, we studied the neural-cell-adhesion molecule 1 (NCAM1) and found that it stimulates dendritic arbor development by promoting actin filament growth at the dendritic growth cone. We anticipate that our quantitative map of neuronal proteome dynamics is a rich resource for further analyses of the many identified proteins in various neurodevelopmental processes.

INTRODUCTION

The ability to generate *in vitro* cultures of primary rat or mouse neuronal cells has been fundamental to advancing our understanding of the development and functioning of the nervous system. A major advantage of performing experiments in primary hippocampal culture systems is that neurons resynchronize in culture prior to further differentiation (Dotti et al., 1988). This allows systematic processing and analyses of neuronal populations at the same developmental stage, which is particularly helpful for global system-wide analyses. Pyramidal neurons, the principal neuronal cell type in the hippocampus, account for the vast majority of the total neuronal cell population within these preparations and express many key phenotypic features of various neuronal cell types. The stages of neuron development in culture have been categorized and provide a starting point for studying neurodevelopmental processes, such as neuronal polarity, dendrite development, and synapse formation (Dotti et al., 1988). Directly after plating and attaching to the substrate, the cells develop lamellipodia around the soma (stage 1) that, within a few hours, transform into several short and highly motile neurites (stage 2). Quickly after, the neurons polarize upon which one of the several neurites develops into an axon (stage 3). Around day *in vitro* 4 (DIV4), dendrites start to develop from the minor neurites (stage 4); this process is much slower than axonal outgrowth and specification and lasts for several days. After 1 week in culture, synaptogenesis begins, and neurons form functional synaptic contacts and, in the following weeks, undergo further neuronal maturation (stage 5).

Several studies have been reported monitoring global gene expression changes in developing rodent neurons (Mody et al., 2001; Dabrowski et al., 2003), albeit nearly all at the mRNA transcript level. These studies revealed that large changes in mRNA expression occur across different stages of hippocampal neuronal development (Dabrowski et al., 2003). Several earlier studies have been reporting differential gene expression during the specialization of the axon and dendrites in hippocampal primary culture systems. In more recent studies, also, the expression of non-coding regulatory RNAs has been profiled in developing neurons (van Spronsen et al., 2013). Transcriptome analysis of different brain regions and different cell types, including cortical primary neurons, has been compared with data from large-scale quantitative proteomic screens (Sharma et al., 2015). However, in many cases, the gene expression changes measured with transcriptomics approaches do not completely reflect the changes measured at the protein level. Several studies have shown that the correlation between mRNA and protein expressions can be low due to several factors such as protein turnover, half-lives, and other post-transcription mechanisms (Low et al., 2013). Moreover, a single mRNA can be translated multiple times, introducing another level of complexity in correlating such data. In this context, we argue that applying advanced MS methods and quantitative proteomics approaches to

systematically profile protein expression during neuronal differentiation will provide a better proxy for changes in protein expression.

Here, we perform a systematic and in-depth proteome analysis of hippocampal neurons in culture and established a quantitative map of neuron-specific proteome dynamics during developmental stages 2–3, 4, and 5. Our dataset comprises 6,753 protein identifications, of which more than 4,300 were quantified over all time points, covering crucial neuronal developmental processes, including axon outgrowth, dendrite formation, and synaptogenesis. About one third of the proteins reveal substantial changes in protein expression throughout the neuronal differentiation, clearly highlighting the extensive reprogramming of the proteome. Our analysis revealed an unappreciated role for neural-cell-adhesion molecule 1 isoform 180 (NCAM180) in dendritic development. NCAM180 is strongly upregulated during dendrite outgrowth, is highly enriched in dendritic growth cones, and interacts with a large variety of actin-binding proteins.

RESULTS

Global Proteomic Signatures of Developing Hippocampal Neurons

To profile neuronal proteome alterations during differentiation, primary hippocampal neurons were grown in serum-free neurobasal medium, enabling rapid differentiation and maturation (Dotti et al., 1988). Cells were harvested after DIV1, DIV5, and DIV14, corresponding to neuronal developmental stages 2–3, 4, and 5, respectively, as described recently (van Spronsen et al., 2013). These stages are associated with the distinct neuronal differentiation processes, namely axon formation and specification (stages 2–3/DIV1), dendrite outgrowth (stage 4/DIV5), synaptogenesis, and maturation (stage 5/DIV14). For in-depth quantitative proteome analysis, cell lysates of the three time points were subjected to tryptic digestion (Figure 1A), triplex stable-isotope dimethyl labeling (Boersema et al., 2009), strong cation-exchange (SCX)-based fractionation, and nano-ultra-performance liquid chromatography (nano-UPLC) coupled to high-resolution liquid chromatography-tandem mass spectrometry (LC-MS/MS). Quantification of relative protein expression changes was performed based on the MS signal intensities of the stable isotope-labeled peptide ions (Figure 1A). In total, 46,869 unique peptides from 6,753 unique proteins were identified (median unique peptides per protein = 6.9). Tissue enrichment analysis against the whole *Rattus norvegicus* proteome as background revealed that the dataset covers large parts of hippocampal neuron-specific proteins (Fisher's exact test, adjusted $p = 2.3E-51$; Figure 1B). Overall, 4,354 proteins were quantified across all time points (median ratio count = 14; Table S1). The averaged relative protein abundances span five orders of magnitude (Figure 1C). Within the 25% most abundant proteins, we observed numerous neuron-specific proteins. Gene Ontology (GO) enrichment analysis, with respect to cellular component,

highlights proteins located in the axon and nerve terminal (“neuron projection terminus”) as being among the most abundant proteins, besides more commonly detected nucleosomal proteins and the proteasome (Figure 1C). Scatterplots of the \log_2 -transformed protein ratios (DIV5/DIV1 and DIV14/DIV5) and a heatmap of Pearson correlation scores illustrate the good correlation between biological replicates (Figure 1D; Figure S1A). In total, 1,793 proteins show more than 2-fold (\log_2 scale < -1 and > 1) expression changes, indicating extensive remodeling of at least one third of the neuron proteome during differentiation (Figure S1B).

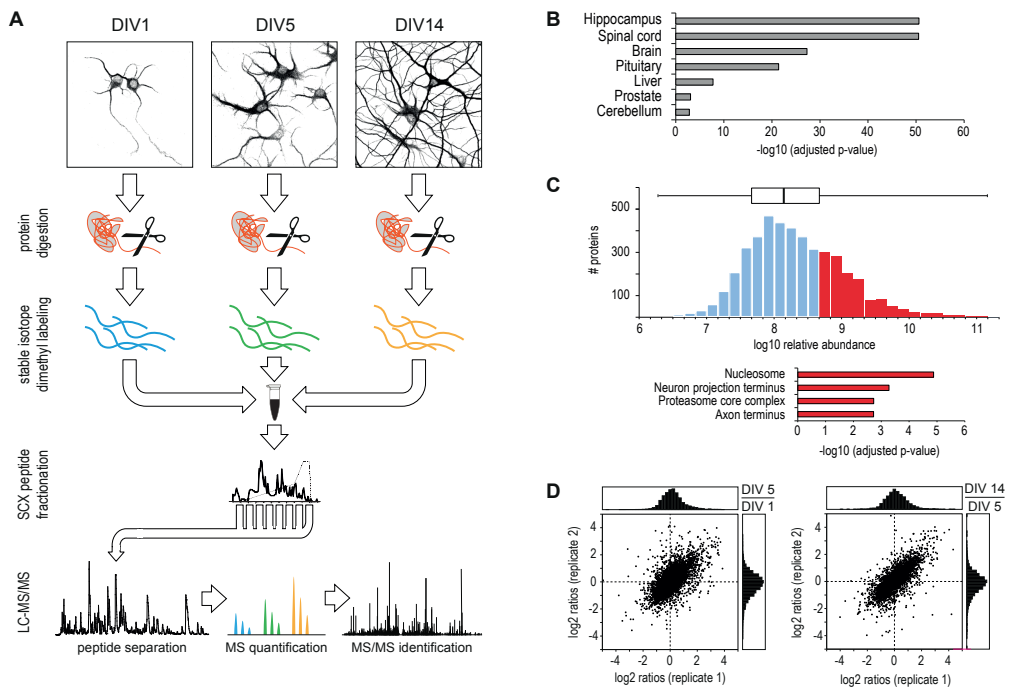


Figure 1. MS-Based Quantitative Proteomic Analysis of Developing Hippocampal Neurons in Culture

(A) Workflow of quantitative neuroproteomic analysis.

(B) Tissue enrichment analysis of all identified proteins using the Database for Annotation, Visualization, and Integrated Discovery (DAVID).

(C) Distribution of protein abundances, spanning five orders of magnitude.

(D) In total, 4,354 proteins were quantified across all time points, and good correlation between biological replicates is observed. See also Table S1.

Quantitative Analysis of Proteome Dynamics during Neuron Differentiation

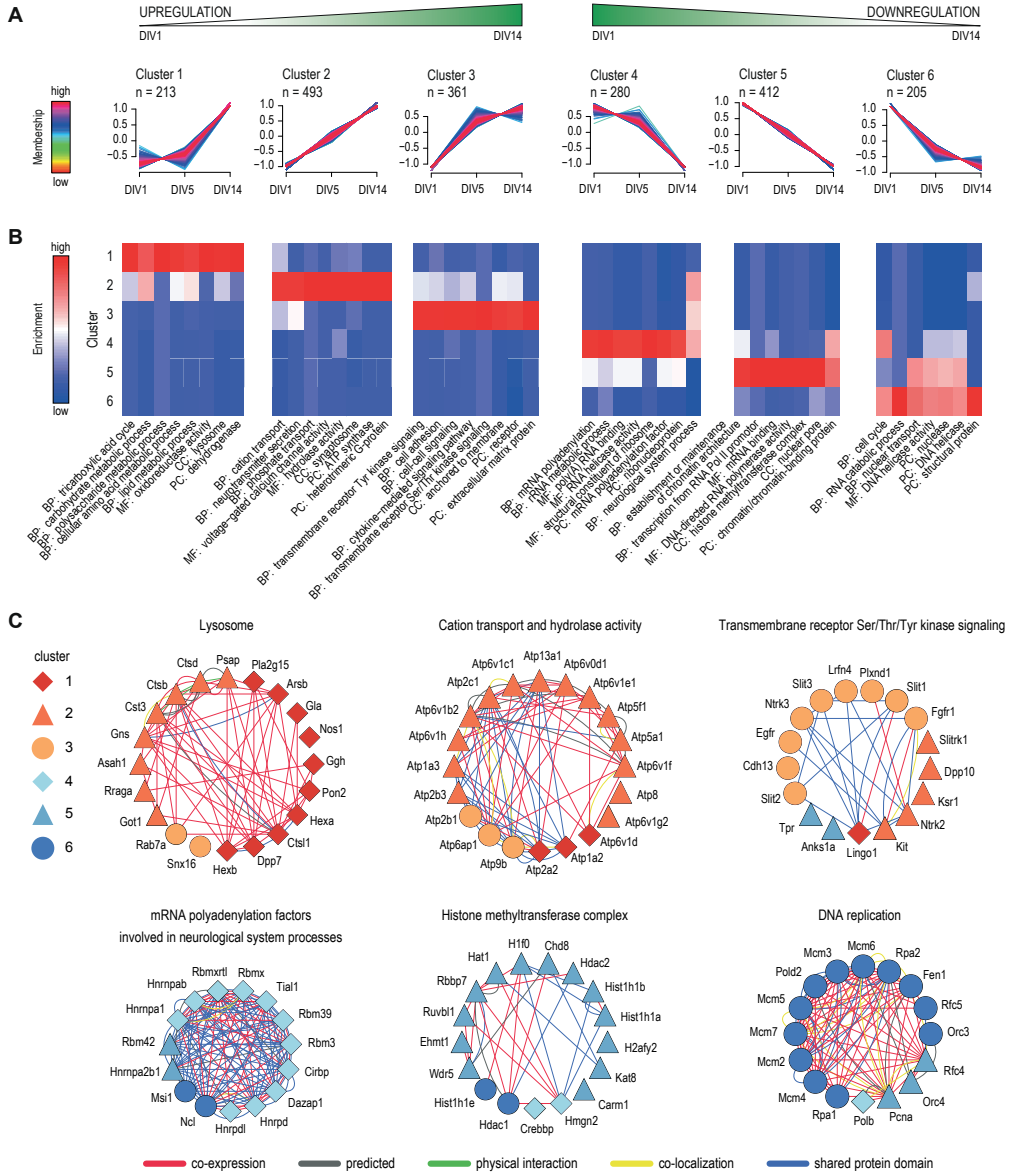
We assessed the global proteome changes of 4,354 proteins quantified across all time points. Close inspection of proteins that were considered not significantly changing (Supplemental Experimental Procedures) revealed general protein metabolism and catabolism as the main processes that are not substantially differentially regulated during neuronal differentiation. This

is reflected by several GO terms, such as “translation” (adjusted p value $9.8E-8$) and “protein catabolic process” ($p = 7.5E-6$), and the Kyoto Encyclopedia of Genes and Genomes (KEGG) terms “ribosome” ($p = 9.9E-5$) and “proteasome” ($p = 6.8E-4$) that were found overrepresented (Figure S1C). Together, these findings imply that the global protein turnover rates are not substantially affected in the course of proteome remodeling during neuronal differentiation.

To obtain an unbiased view of the proteome expression dynamics during neuronal differentiation, we performed unsupervised fuzzy clustering of all significantly changing proteins. This analysis resulted in six clusters of distinct expression profiles (Figure 2A), with proteins upregulated during differentiation in clusters 1, 2, and 3 and proteins downregulated present in clusters 4, 5, and 6. We next investigated whether the clusters revealed proteins with developmental stage-specific expression patterns. Indeed, many proteins within specific clusters shared functionalities related to their cellular component, molecular function, or their contribution to distinct biological processes (Figure 2B). Complete GO annotations for each cluster can be found in Figure S2.

Cluster 6 contains proteins strongly downregulated from DIV1 to DIV5 and, to a lesser extent, from DIV5 to DIV14, indicating a precisely timed downregulation during early neuronal differentiation. Proteins in this cluster are mainly involved in early differentiation processes of post-mitotic neurons, which do not proliferate and remain arrested in G0 phase, exemplified by multiple proteins involved in the regulation of cell cycle and DNA replication, such as DNA helicases. This includes minichromosome maintenance complex proteins (Mcm2–Mcm7) as well as DNA polymerase delta (Pold2), replication factor 5 (Rfc5), and Flap endonuclease 1 (Fen1) (Figure 2C). Downregulation of proteins related to cell cycle and DNA replication have been similarly observed in other terminally differentiating cells (Kristensen et al., 2013). In line with these findings, we detected slight upregulation of cyclin-dependent kinase 5 (Cdk5) (Figure S3A), which is known to be exclusively expressed in post-mitotic neurons and is involved in suppressing cell-cycle reentry (Zhang and Herrup, 2011).

Proteins in cluster 4 exhibit a strong downregulation from DIV5 to DIV14 (Figure 2A). Many proteins in this cluster are associated with RNA metabolism (Figure 2B), exemplified by a highly connected group of mRNA polyadenylation factors (Figure 2C). Interestingly, several transcription factors, which play key roles in neuronal differentiation, are also allocated to this cluster. A prominent example of this subset of proteins is the neuron-specific transcription factor Sox11, which is the most downregulated protein in the total dataset (expression level decreases about 40-fold from DIV1 to DIV14; see also Figures 4A and 4B). The onset of Sox11 expression is known to overlap with decreased expression of Sox2 (not quantified in our data) in neuronal committed proliferating progenitor cells, promoting differentiation into premature neurons (Haslinger et al., 2009).



Likewise, transcription factor *Bcl11a*, which has been identified as a negative regulator of axon branching and dendrite outgrowth (Kuo et al., 2009), follows the expression profile of cluster 4. Other related transcription factors are allocated to cluster 5 (sustained decrease of relative protein levels from DIV1 to DIV14); for instance, *Foxg1* and Sox11-interacting protein *Pou3f2*, both of which play important roles in the early to mid-neurogenesis of postmitotic neurons (Dominguez et al., 2013; Hsieh, 2012). Another transcription factor found in cluster 5 is *Tbr1*, which is expressed in early postmitotic neurons, promotes neurogenesis, and functions as a repressor of astrocyte formation (Mendez-Gomez et al., 2011). Moreover, *Tbr1* has been reported to be involved in regulation of axon pathfinding (Hevner et al., 2006), a process that is part of the major developmental changes from stage 2 to stage 3. Collectively, our data show that neuronal differentiation and maturation from stages 2–3 to stage 5 resonate with a gradual decrease of several transcription factors that are key regulators in the early events of neurogenesis and initial axon formation. Notably, *Sox8*, another member of the SRY-related HMG (high-mobility group)-box gene family, shows a minor increase from DIV1 to DIV5 and an elevated increase from DIV5 to DIV14 (cluster 1). *Sox8* is reportedly involved in the regulation of terminal differentiation of oligodendrocytes (Stolt et al., 2004). Late upregulation from developmental stage 4 to stage 5 suggests that *Sox8* might also be involved in the terminal differentiation of neurons. However, its functional role in the later stages of neuronal development remains to be unveiled.

Cluster 5, representing a constant decrease of relative protein levels over time (Figure 2A), is enriched for proteins associated to chromatin (Figure 2B). Steady downregulation of histone methyltransferases (*Ehmt1* and *Wdr5*), acetyltransferases (*Kat8* and *Hat1*), and histones (*Hist1h1b*, *Hist1h1a*, and *H2afy2*) indicate an ongoing remodeling of the chromatin architecture during neuronal differentiation (Figure 2C). The GO term “mRNA binding” was also found specifically enriched in cluster 5. In fact, 42 out of 103 proteins classified as RNA-binding proteins (RBPs) (Table S2) are allocated to this cluster and undergo, on average, 3-fold downregulation (\log_2 scale = 1.6) from DIV1 to DIV14. Post-transcriptional regulation by RBPs controls gene expression and diversification and is known to accurately coordinate spatiotemporal differentiation of neurons (DeBoer et al., 2013). A prominent member of this cluster is Polypyrimidine tract-binding protein 2 (*Ptbp2*). *Ptbp2* is predominantly expressed in brain tissue during the early stages of neurogenesis, and its main function is the precisely timed negative regulation of alternative splicing events of a distinct set of target genes that play key roles in neuronal differentiation (Sawicka et al., 2008). Therefore, we mined our data for proteins whose transcripts are targets of *Ptbp2* (Licatalosi et al., 2012). We observed that the decrease in *Ptbp2* levels coincides with increased expression of several proteins whose transcripts are

targets of Ptbp2 (including Camk2b, Camk2g, Psd95, Dnm1, Ppp3cb, and Numb). Interestingly, we observed for three other target proteins, whose transcript levels were found elevated in that study, no significant expression changes (Sorbs2 and Pum2) or only a slight decrease (Sympk, cluster 5) in our dataset. Notably, the neuron-specific RBPs Nova1 and Nova2, which are direct interactors of Ptbp2, show no significant expression change from DIV1 to DIV14. Among the upregulated RBPs are Pura and Purb, which, besides their molecular function in RNA binding, are known transcriptionally active DNA binders. Pura and Purb undergo a highly similar expression increase from DIV5 to DIV14 (cluster 1), indicating a specific role in synapse formation and later maturation processes. Indeed, reduced synapse formation was observed in Pura knockout mice (White et al., 2009), supporting a presumed role during synaptogenesis. Notably, a third member of the Pur family, Purg, shows stronger and earlier upregulation compared to Pura and Purb, suggesting involvement in differentiation events preceding synapse formation. Together, these findings support highly coordinated reorganization of the protein network orchestrating post-transcriptional gene expression regulation during neuronal differentiation (Loya et al., 2010).

The proteins in cluster 1 show a substantial increase in relative expression levels from DIV5 to DIV14 (Figure 2A). This expression profile corresponds to stage-specific upregulation during maturation from stage 4 to stage 5. Distinct GO terms, which were found enriched in cluster 1, cover proteins involved in several metabolic processes, including polysaccharide, amino acid, and lipid metabolism (Figure 2B). Closer inspection of the corresponding proteins revealed that most of them function as catalytic enzymes in lysosomes (e.g., cathepsin L1, arylsulfatase B, and dipeptidyl peptidase 2; Figure 2C). Endosomal trafficking is a key control mechanism in synapse formation and modulation of synaptic plasticity. For example, postsynaptic receptor density is governed by the interplay of endosomal recycling and endosome-lysosome trafficking. Therefore, the observed upregulation of lysosomal proteins in the course of neuronal development could reflect an increase in the cellular capacity for the degradation via the lysosomal pathway. Cluster 3 comprises proteins that undergo increased expression from DIV1 to DIV5, while the expression changes from DIV5 to DIV14 are marginal (Figure 2A). Many proteins in this cluster are associated with cell adhesion and cell-cell signaling-related GO terms (Figure 2B). This includes several transmembrane receptor kinases involved in cell adhesion, migration, axon guidance, and dendrite formation. For instance, prominent members of this cluster are growth factor receptors Egfr and Fgfr1; neurotrophin receptor Ntrk3; semaphorin receptor Plxnd1; and axon guidance cues Slit1, Slit2, and Slit3 (Figure 2C). Moreover, numerous cell-adhesion proteins also follow the expression pattern of cluster 3, which will be discussed in detail later. Cluster 2 represents a group of proteins whose expression levels constantly increase from DIV1

to DIV5 and from DIV5 to DIV14 (Figure 2A). GO analysis revealed the enrichment of several terms related to cation transport and neurotransmitter secretion in this cluster (Figure 2B), as exemplified by several highly connected subunits of various ATPases (Figure 2C). Furthermore, the majority of the significantly regulated synaptic proteins belong to this cluster (GO term “synaptosome”), which will be discussed in the following sections.

Coordinated Proteome Dynamics of Proteins in Complexes during Differentiation

We next sought to characterize concerted dynamics of proteins within previously annotated protein complexes. Statistical assessment of the significance of co-regulated proteins revealed coordinated expression changes for proteins involved in several cellular processes during neuronal development (Table S3). This includes, for example, nuclear transport (nuclear pore complex), cell-cycle control (anaphase-promoting complex, APC/C), and DNA replication (MCM complex) (all $p < 0.005$; Figure 3A), providing further evidence for continuous chromatin remodeling during terminal differentiation of post-mitotic neurons. Conversely, the same statistical analysis can reveal proteins that deviate from the expression profile of the corresponding complex or family, indicating a neuron- or developmental stage-specific function. This is nicely illustrated by expression profile analysis of SNARE proteins from the syntaxin family, revealing neuron-specific expression. Syntaxin proteins are important players in vesicle docking and fusion with target membranes. We observed continuous upregulation of Stx1a and Stx1b from DIV1 to DIV14 (Figure 3B; Figure S3B), both of which are specifically expressed in neuronal and secretory cells, playing a key role in neurotransmitter secretion. All other syntaxins undergo no substantial expression changes (Figure 3B; Figure S3B), indicating that syntaxin-mediated intracellular transport processes, including endosomal (Stx7, Stx8, and Stx12), endoplasmic-reticulum (ER)-to-Golgi- (Stx5 and Stx18), and trans-Golgi (Stx6 and Stx16) trafficking, are not regulated by expression changes of syntaxins in the course of neuronal differentiation.

Next, we determined whether this approach was able to resolve neuron-specific isoforms that modulate distinct functions within protein complexes. Adaptor protein (AP) complexes are involved in intracellular vesicular transport and cargo selection by binding to sorting signals. The AP2 complex mainly plays a role in endocytosis from the plasma membrane, whereas AP3 is important for trans-Golgi sorting events (Boehm and Bonifacino, 2001). All subunits of the AP2 adaptor complex show a significant ($p < 0.005$) coordinated upregulation from DIV1 to DIV14 (Figure 3A), following the expression profile of most synaptic proteins (cluster 2; Figure 2A). Strikingly, this does not hold for the AP3 complex ($p = 0.209$), where one isoform of the Ap3b subunit (Ap3b1) diverges from the common expression profile of the other complex proteins, including the neuron-specific isoform Ap3b2 (Figure 3B), implying

functional regulation of the complex activity by Ap3b. It has recently been shown that neuronal AP3 complexes are assembled by one of the two Ap3b isoforms, regulating distinct vesicular sorting processes (Seong et al., 2005). Neuron-specific Ap3b2-containing AP3 mediates cargo sorting preferentially into synaptic vesicles, while ubiquitous Ap3b1-containing AP3 more likely promotes cargo delivery toward the lysosomes (Newell-Litwa et al., 2009). Moreover, neuronal AP3 was shown to be 4-fold more abundant in axons and dendrites than ubiquitous AP3 (Seong et al., 2005). Together, this substantiates our data across developmental stages 2–3 to 5, which are accompanied with dendrite formation, synaptogenesis, and maturation. The richness of the neuron-specific proteome allowed us to further explore expression profiles of several other protein families. We observed distinct regulation of members of the tyrosine-protein phosphatase family, where receptor-type tyrosine phosphatases (Ptp_r) undergo upregulation during neuronal differentiation, whereas most non-receptor-type tyrosine phosphatases (Ptp_n) showed no expression changes (Figure 3B; Figure S3B).

Hierarchical clustering further supports this observation by clearly separating the two subclasses. Ptps are important in signal transduction via a highly coordinated interplay with kinases (Tonks, 2013), and both classes are involved in cell-adhesion processes. Upregulation of the receptor-type Ptps implies an increased demand for cell-adhesion molecules in the course of dendrite outgrowth and synapse formation. Similar observations were made for members of proteins from the Atp1- and Ca²⁺/calmodulin-dependent protein kinase families. The main function of the Na/K-ATPase complex in neurons is to maintain the resting potential by using large amounts of the total cellular ATP supply. Interestingly, we observed that expression levels of Atp1b3 remain unchanged during neuronal differentiation, whereas all other subunits undergo upregulation, indicating a potential functional regulation through a stoichiometric change of the complex (Figure 3B; Figure S3B) (Ori et al., 2016). The ratio between the a and b subunit is 1:1 during assembly in the ER; however, the degradation rate of b subunits is known to be significantly higher. Moreover, each b isoform confers a different ATPase activity; thus, a change in stoichiometry indicates a potential cellular mechanism to regulate pump activity according to changes in Na⁺ or K⁺ concentrations, allowing maintenance of the resting potential or adjustment for changes in cell volume during neuronal differentiation. For the Ca²⁺/calmodulin-dependent protein kinase family, we observed that Camk2 proteins, overall, upregulated during neuronal differentiation, whereas expression levels of the members of the Camk cascade (Camkk, Camk1, and Camk4) remained unchanged (Figure 3B; Figure S3B). The various Cam kinases differ in their subcellular localization. Camk2 predominantly localizes in dendrites, whereas Camkk and Camk1 are ubiquitous cytoplasmic proteins, and Camk4 is nuclear (Wayman et al., 2008). Camkk phosphorylates and activates Camk1 and Camk4,

which act on further downstream targets in the MEK/Erk (mitogen-activated protein kinase/extracellular-signal-related kinase) pathway (Camk1) or modulate CREB (cAMP response element binding protein)-mediated transcription (Camk4) (Wayman et al., 2008). In contrast, Camk2 is one of the major constituents of the post-synaptic density (PSD) and is a key player in mediating Ca^{2+} -influx-triggered signal transduction, modulation of synaptic plasticity, and induction of long-term potentiation. Notably, Camk2a is the most upregulated protein in our dataset. Our data clearly show an increased demand for PSD-localized Camk2 in growing and developing neurons.

Synaptic and Cell-Adhesion Protein Profiling during Neuronal Development

Next, we assessed the proteome dynamics during synaptogenesis, a key event in neuronal development that requires the coordinated assembly of a highly connected protein network that includes scaffolding proteins, receptors, and their downstream targets, signaling molecules, and cell-adhesion proteins. In our hippocampal neuron cultures, dividing non-neuronal cells are mostly represented by astrocytes. They expand after DIV5 (Figure S4A), thus promoting synapse formation and transmission. Indeed, synapse formation during the neuronal development of hippocampal neurons in culture occurs from stage 4 (DIV5) to stage 5 (DIV14) (Figure 4A). Interestingly, the majority of all differentially expressed synaptic proteins are allocated to cluster 2 (Table S4), which corresponds to a steady increase in relative protein levels from DIV1 to DIV14 (Figure 2A). This cluster includes important presynaptic proteins involved in vesicle trafficking (Syn and Syt1), cytoskeleton organization and protein anchoring (Cask, Pclo, Bsn), and neurotransmitter release (Syn1, Vamp2, Snap25, Sv2a, and Sv2b) (Figure 4C). Prominent members of the upregulated postsynaptic proteins are scaffold and anchoring proteins (Shank2, Psd95, Grip1, Homer1), and several glutamate and GABA receptors (Figure 4D; Figure S4B). To validate our quantitative proteomics data, we additionally plotted the relative expression of several proteins where we do not expect large changes (Figure 4F) and confirmed expression of several depicted proteins by western blot analysis (Figures 4G–4I) of lysates from the corresponding time points. These results were paralleled by immunoblotting of embryonic and adult rat hippocampal tissue, Hip.(E) and Hip.(A), respectively (Figure 4G), substantiating the observation of higher expression levels at later developmental stages. Presynaptic markers such as Bassoon (Bsn) and Synaptophysin (Syn) (Figure 4C) are known to accumulate at new synapses before postsynaptic proteins such as Psd95 (Friedman et al., 2000; Okabe et al., 2001). This is supported by our data, which show a later expression increase of Psd95 (Figure 4D). However, for the majority of postsynaptic proteins, we do not observe a timely delayed expression increase, which is also evident from hierarchical clustering analysis of all synaptic

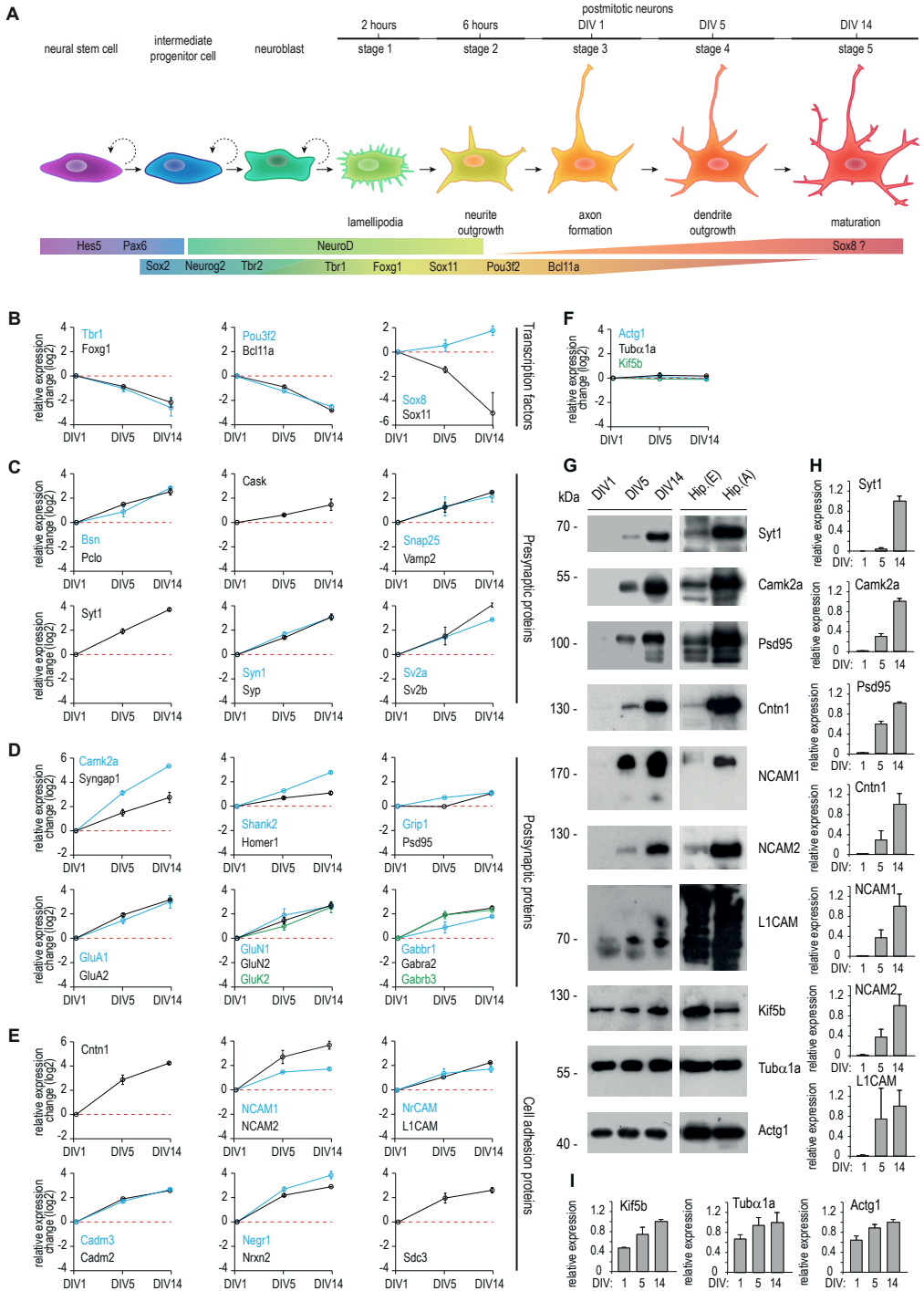


Figure 4. Protein Expression Changes during Neuronal Differentiation

(A) Schematic overview of neurogenesis, illustrating the distinct developmental stages and representative transcription factors involved.

(B) Expression profiles for representative transcription factors including the most downregulated protein in this dataset, Sox11.

(C–F) Expression profiles of selected presynaptic proteins (C), postsynaptic proteins (D), cell-adhesion proteins (E) and proteins with no relative expression change over the developmental stages (F).

(G) Change in the protein expression during neuronal development shown by western blot analysis from cultured hippocampal neurons, embryonic tissue (Hip.(E)), and adult brain tissue (Hip.(A)).

(H and I) Graphs showing the quantifications of relative intensities of the western blot analysis in (G), shown in (H), and control proteins, shown in (I). $n = 3$ experiments per condition. Error bars indicate mean \pm SEM.

In (B)–(F), error bars represent SD.

proteins (Figure S4D). This is likely because the temporal resolution of this study is limited by the experimental design. Nevertheless, our dataset demonstrates the substantial upregulation of many synaptic proteins already at early developmental stages, long before synaptogenesis takes place. Similar expression profiles are observed for subunits of various neurotransmitter receptors and voltage-gated ion channels (Figures S4B and S4C).

Cell-adhesion molecules are another important class of proteins with a key role in neuronal development. They mediate axon pathfinding and axon-dendrite contact formation, and they further modulate dendritic spine morphology and synaptic plasticity. In total, 82 cell-adhesion proteins were quantified in our dataset (Table S5), including Cntn1, NrCAM, Nrnx2, NCAM1, and NCAM2 (Figure 4E). Interestingly, 24 of these are allocated to cluster 3 (Figure 2A), highlighting that their major expression increase proceeds during the transition from stage 2–3 to stage 4, indicating an important role in dendrite formation. Neural cell-adhesion molecule 1 (NCAM1) is a prominent member of the cell-adhesion proteins that share the expression profile of cluster 3 (Figure 2A).

NCAM1 Is Highly Enriched in Dendritic Growth Cones

NCAM1 belongs to the immunoglobulin-like family of cell-adhesion molecules and is one of the most abundant neuronal adhesion proteins (Sharma et al., 2015). NCAM1 expresses in three main isoforms produced by alternative splicing of the NCAM1 gene. Two of the isoforms (NCAM140 and NCAM180) are transmembrane proteins, while NCAM120 is glycosylphosphatidylinositol (GPI) anchored (Figure 5A). We first analyzed by western blot isotype-specific protein expression levels in cultured rat hippocampal neurons extracts from DIV2 to DIV21 (Figure 5B). In agreement with previous observations, NCAM180 is the main isoform expressed in neurons (Noble et al., 1985). Quantification revealed that NCAM180 shows two main peaks of protein expression at DIV5 and DIV16 (Figure 5C), confirming our quantitative MS data and indicating that, in addition to its well-known role in synaptic plasticity

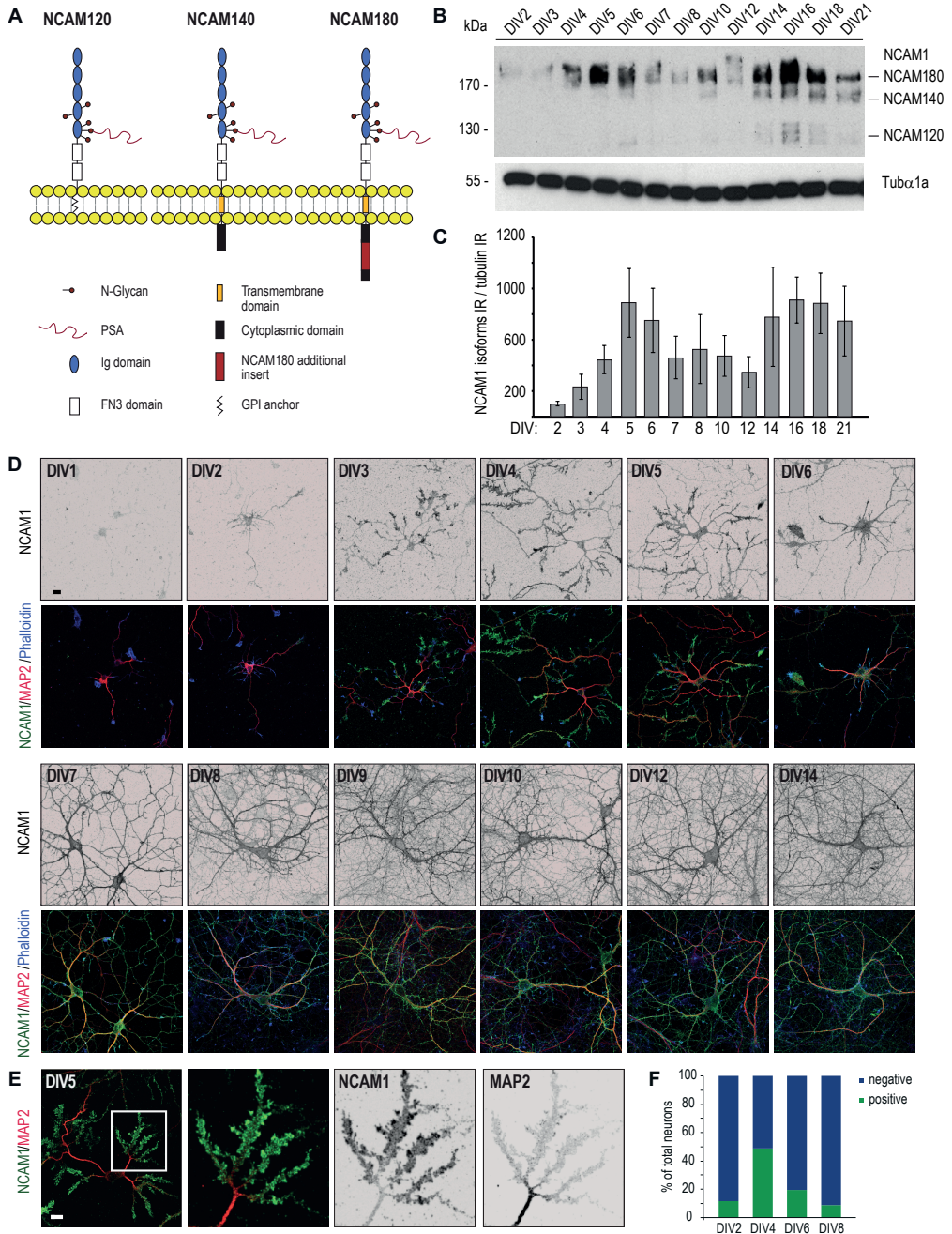


Figure 5. The Cell-Adhesion Molecule NCAM1 and Its Expression throughout Neuronal Development

(A) Schematic overview of the three main NCAM1 isoforms. Ig, immunoglobulin.

(B and C) Western blot analysis (B) and quantification (C) of developmental expression of NCAM1 in DIV2–DIV21 rat hippocampal neurons. Error bars indicate mean \pm SEM.

- (D) Representative images of rat hippocampal neurons from DIV1 to DIV14, stained for NCAM1 (green), MAP2 (red), and phalloidin (blue). Scale bar, 20 μm .
- (E) Representative rat hippocampal neuron at DIV5 stained for NCAM1 (green) and MAP2 (red). Scale bar, 20 μm .
- (F) Quantification of the percentage of neurons characterized by the NCAM1 dendritic staining shown in (D) and (E). n = 100 cells per DIV.

(Doherty et al., 1995), NCAM1 may be important at earlier stages of neuronal development (DIV5). To further investigate NCAM1 distribution in developing neurons (DIV1–DIV14), we performed triple-labeling immunofluorescence experiments using a NCAM1-specific antibody, the dendritic microtubule marker MAP2, and the F-actin marker phalloidin (Figure 5D). As reported previously, NCAM1 showed some staining in stage 2–3 cells (DIV1), which was mainly present in the axonal growth cones. Interestingly, at DIV4–DIV5, many neurons displayed strong accumulation of NCAM1 in dendritic growth cones. Here, NCAM1-rich dendritic growth cones are positive for F-actin but not for the microtubule marker MAP2, which is more restricted to the dendritic shaft (Figure 5E). Dendritic NCAM1 accumulations are present in approximately 40% of the neurons counted at DIV4, and during later stages (DIV6–DIV8), it gradually disappears (Figure 5F). At later developmental stages, NCAM1 was found diffusely distributed over the dendritic plasma membrane. Similar results were obtained with the mouse primary hippocampal culture, although here, NCAM1 was already localized in dendrites at DIV3 (Figure S5).

NCAM1 Is Required for Both Axonal and Dendritic Outgrowth and Branching

Since NCAM1 accumulates in dendritic growth cones, we further investigated the role of NCAM1 during dendritic development. Therefore, three specific short hairpin RNA (shRNA) sequences were designed and generated, based on the NCAM180 mRNA rat sequence, to perform knockdown experiments. All three shRNAs (shRNA_NCAM1#1, shRNA_NCAM1#2, and shRNA_NCAM1#3) reduced protein levels by ~80%, as revealed from both western blot analysis and immunostaining (Figures 6A–6C; Figure S6). We next examined the effect of NCAM1 knockdown on outgrowth of axon and dendrites (Figure 6D). Quantification revealed that both the length of the axon (Figure 6E) and length of the dendrites (Figure 6F) were significantly reduced compared to that of control neurons. The observed reduction of axon length in NCAM1-depleted neurons is consistent with that reported in previous works (Pollerberg et al., 2013). Apart from the axonal phenotype, NCAM1 depletion in young neurons also caused a marked reduction in dendrite development. Quantification indicated that knockdown of NCAM1 using three different shRNAs reduces the length of primary dendrites, total dendrites, and dendritic branches by 40% compared to control neurons (Figure 6F).

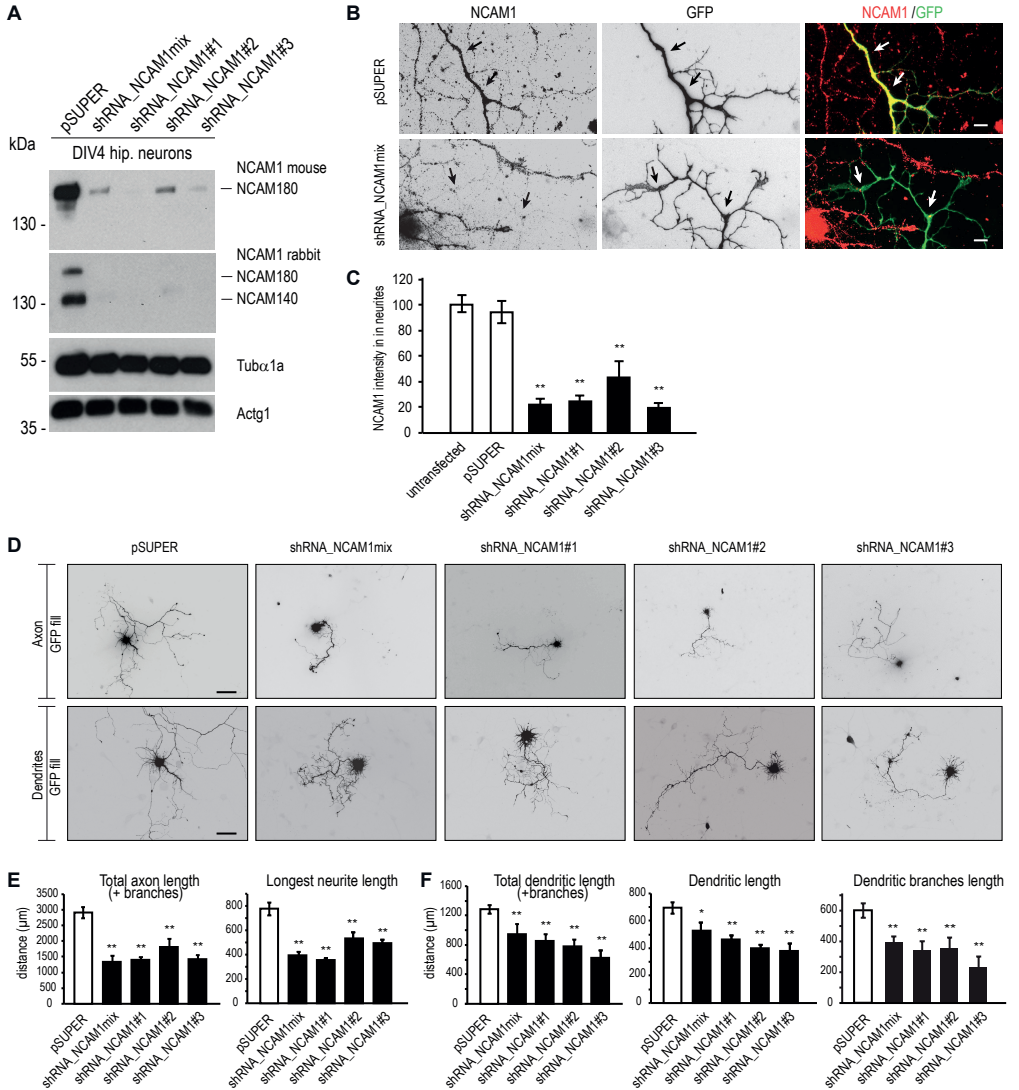


Figure 6. shRNA-Mediated Knockdown of NCAM1 in Neurons

(A) Knockdown of NCAM1 by indicated shRNA constructs and analyzed by western blot in DIV4 cortical neurons. (B) Representative images of hippocampal neurons at DIV4 co-transfected with indicated constructs and stained with NCAM1 monoclonal antibody. Arrows indicate transfected neurites. (C) Quantification of NCAM1 fluorescent-staining intensities in neurites of hippocampal neurons co-transfected at DIV4 with indicated constructs. (D) Representative images of primary hippocampal neurons co-transfected with indicated constructs (DIV1–DIV7) to visualize axon (top) and dendrite (bottom) morphology. (E and F) Quantification of axon (E) and dendrite (F) morphological parameters. Error bars indicate mean ± SEM. * $p < 0.5$, t test; ** $p < 0.01$, t test. Scale bars, 10 μm in (B), 100 μm for the top of (D), and 50 μm for the bottom of (D).

Actin Stabilization Rescues NCAM1 Knockdown Phenotype

To investigate the mechanism by which NCAM1 influences dendritic development, we searched for NCAM180-binding partners in neurons and used the other two isoforms as controls. The GFP-tagged NCAM1 isoforms were expressed in neurons to check their proper localization and their correct insertion in the cell membranes (Figures S7A and S7B). Subsequently, constructs of all three GFP-NCAM1 isoforms and GFP (as control) were transiently expressed in HEK293 cells; GFP proteins were isolated with GFP beads and incubated with either young (postnatal day 5; P5) or adult rat brain extracts, and then co-isolated proteins were analyzed in an affinity purification (AP)-MS experiment. To identify true NCAM1-binding partners (in adult or young brains), we used the “Significance Analysis of INTeractome (SAINT)” for probabilistic scoring of our AP-MS data (Choi et al., 2011). Among the entire list of putative interacting proteins identified (Table S6), only those with a SAINT probability > 0.75 (false discovery rate [FDR] = 0.1) were considered as true interactors and were then represented as spheres of different size and color according to their relative abundance and obtained p value, respectively (Figure 7A). Interestingly, several members of actin-binding, -stabilizing and/or -polymerizing proteins such as spectrin (Spt) and myosin (Myo/Myh); actin-related proteins (Arps), tropomyosins (Tpms); F-actin-capping proteins (Capzas); and actinins (Actn) are the main neuronal interactors of NCAM1, ubiquitously enriched in young brains and, to a lesser extent, in adult brains. The interaction between the NCAM140 and NCAM180 intracellular tails and actin-cytoskeleton-related proteins (Spt, α -Actn, and Tpm) has been already reported and characterized in previous studies (Pollerberg et al., 2013). In our AP-MS experiments, it is interesting to notice that the length of each NCAM1 isoform used as bait directly correlates with the relative abundance of each specific actin-binding protein identified (as indicated by the amount of peptides and peptide spectrum matches [PSMs] measured), thus corroborating the hypothesis that NCAM180 (with its longer C terminus) might be the main player involved in the regulation of actin dynamics in dendrites (Figure 7A; Table S6). By drawing a protein interaction network (Cytoscape, Genemania plugin), using as input the actin-binding proteins identified in the NCAM180 pull-down, it becomes evident how these proteins are tightly connected (Figure 7B). Similarly to NCAM1, most actin-interacting proteins are grouped in the earlier defined cluster 3 (Figure 2A) and upregulated at DIV5 (Figure 7C), suggesting that they may strongly cooperate in NCAM1 signaling. To investigate the potential relationship between NCAM1 and the actin cytoskeleton (Figure 7D), we tested whether the dendritic phenotype caused by NCAM1 depletion can be reversed by jasplakinolide-forced F-actin stabilization. Jasplakinolide is a drug known to stabilize actin fibers and to facilitate actin polymerization. Thus, neurons were first transfected with the two most efficient NCAM1 shRNAs (ShRNA_NCAM1#1 and ShRNA_NCAM1#3),

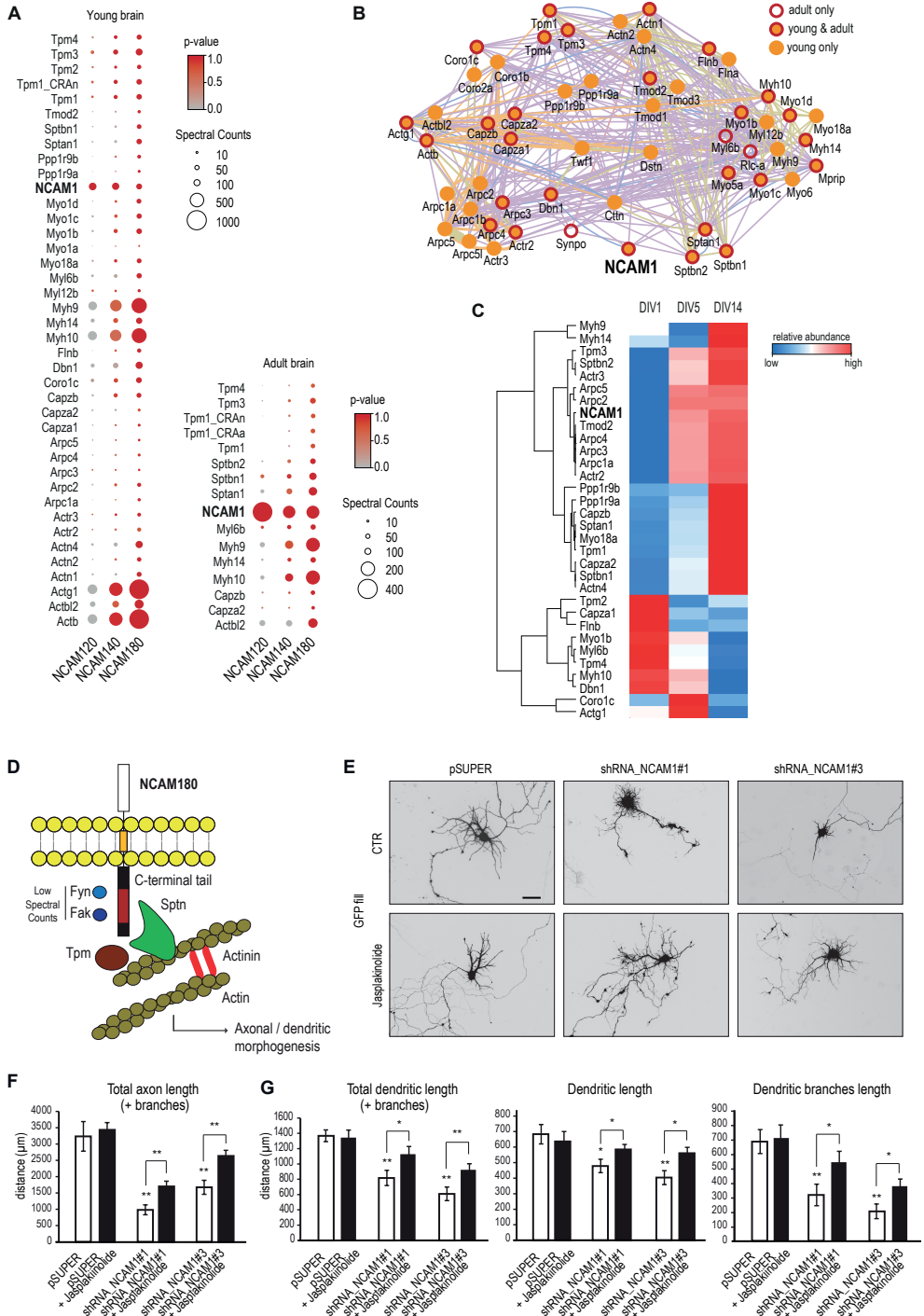


Figure 7. NCAM1 and Its Role in Actin Cytoskeleton Stabilization

(A) Selected candidates of putative NCAM1 interactors identified in young and adult rat brains by AP-MS experiments (see Table S6 for the complete list of proteins). SAINT probability cutoff > 0.75 corresponds to an average FDR of 0.1. The p values and spectral counts are graphically represented by colors and spheres, respectively.

(B) Network analysis on selected NCAM180-binding proteins linked to actin cytoskeleton. Edge color coding: blue, co-localization; orange, predicted interaction; green, shared protein domain; purple, co-expression.

(C) Heatmap and hierarchical clustering of the expression profiles of selected NCAM1-interacting proteins.

(D) Schematic representation of NCAM180 associated with actin-stabilizing proteins.

(E) Representative images of primary hippocampal neurons co-transfected with indicated constructs (DIV1–DIV7) and treated 24 hr later with DMSO or 10 nM jasplakinolide. Scale bar, 50 μm .

(F and G) Quantification of axon (F) and dendrite (G) morphological parameters.

Error bars indicate mean \pm SEM. * $p < 0.5$, t test; ** $p < 0.01$, t test.

2

and 24 hr later, a low dose of jasplakinolide (10nM) was added to the growth medium for 6 days. The addition of jasplakinolide partially rescues the neuronal developmental defects caused by NCAM1 depletion, as demonstrated by the quantification of the axonal and dendritic parameters (Figures 7E–7G). Total dendritic length, primary dendrite length, and dendritic branch length were significantly increased in jasplakinolide-treated neurons compared to control neurons (Figure 7G). Together, the presented data indicate actin stabilization as a mechanism for NCAM1-mediated dendritic growth.

DISCUSSION

The in-depth analysis of neuronal proteins that are abundantly and differentially expressed during the well-defined stages of differentiation is a promising strategy for understanding neurodevelopment- regulated processes. We provide proof of concept by applying this strategy to identify and characterize the role of NCAM1 in dendritic outgrowth.

A Quantitative Map of Proteome Dynamics during Neuronal Differentiation

In neurons, like in all other cells, proteins are the main functional components, but how the proteomes differ in developing neurons is not known. To resolve the global neuronal proteome and to determine the basis for cellular differentiation, we performed a quantitative analysis of protein levels by combining triplex stable-isotope dimethyl labeling coupled to high-resolution LC-MS/MS of hippocampal neurons in culture. Here, we found that 1,793 proteins show more than 2-fold expression changes during the different developmental steps, indicating extensive remodeling of the neuron proteome during early differentiation. This analysis revealed six clusters of distinct expression profiles, with proteins upregulated during differentiation in clusters 1, 2, and 3 and proteins downregulated present in clusters 4, 5, and 6. We mainly focused our attention on cluster 3, which contains proteins whose expression levels are highly upregulated between stages 2–3 and stage 4 of in vitro neuronal development. According to GO classification,

2

most of the proteins present in this cluster are transmembrane proteins that could play a role by modulating dendritic outgrowth and branching. It is interesting to notice that, during these stages of neuronal development, a very specific group of NCAM-adhesion molecules (NCAM1, NCAM2, NRCAM, and L1CAM) is characterized by exactly the same pattern of protein-level regulation (Figure 4E), suggesting that these proteins may act synergistically. On the other hand, pre- and postsynaptic proteins are highly represented in cluster 2, indicating that their expression levels increase throughout neuronal development. These data strongly support a model in which specific synaptic scaffolding proteins such as Bassoon, Piccolo (pre-synaptic proteins), Shank, and Camk2A (post-synaptic proteins) are expressed prior to synapse formation. The full datasets are available in Tables S1, S2, S3, S4, and S5.

NCAM1 Plays an Important Role in Dendritic Outgrowth

To demonstrate the strength of our resource, we focused on NCAM1 as a regulator for dendritic outgrowth. NCAM1 is best known for its role in axonal wiring through interactions with various ligands via its extracellular domain (Pollerberg et al., 2013). NCAM1 is unique among the adhesion molecules because it carries a polysialic acid (Togashi et al., 2009), which can be reversibly attached to extracellular domains, reducing its homophilic interactions and thereby controlling clustering and downstream signaling of NCAM1 (Pollerberg et al., 2013). The cytosolic part of the longer NCAM1 isoform (NCAM180) interacts with several cytoskeletal elements and signaling molecules. NCAM1 is reportedly involved in neurite outgrowth and axon pathfinding (Walsh and Doherty, 1997). For example, in mice lacking NCAM1, hippocampal axons show abnormal pathfinding (Cremer et al., 1997). Our data suggest that NCAM1 not only plays a role in axon outgrowth and guidance but is also required for proper dendritic outgrowth during first days of neuronal development. We speculate that NCAM180 is the specific isoform playing a role in dendrites based on the developmental expression pattern. Consistently, NCAM180 is strongly upregulated during dendrite outgrowth and highly enriched in dendritic growth cones. Interestingly, other NCAM family proteins have been reported to be involved in dendritic branching and morphology in *C. elegans* (Dong et al., 2013). It is likely that, similar to its role in axonal growth cones, NCAM1 at the tips of dendrites may sense various types of extrinsic signals, such as other CAMs or various diffusible factors that determine their general orientation and outgrowth (Pollerberg et al., 2013). The extracellular signals may come from crossing axons, dendrites from the same cell, and neighboring arbors and together regulate the immense complexity of dendrite morphology.

Actin Stabilization as a Mechanism for NCAM1-Mediated Dendritic Growth

Our AP-MS experiments revealed that NCAM180 interacts with several members of actin-

binding, -stabilizing and/or -polymerizing proteins in young and adult brains. These data are consistent with the previously reported interactions between the NCAM1 intracellular tails and actin-related proteins (Buttner et al., 2003; Leshchyn'ska and Sytnyk, 2016). These observations suggest that NCAM1 can act as a scaffold for multiple cytoskeleton components and that multiple actin-binding proteins can amplify the interaction between NCAM1 with the actin cytoskeleton. However, it is also possible that these interactions do not occur simultaneously but are rather highly regulated in response to the extracellular signals (Leshchyn'ska and Sytnyk, 2016). Interestingly, inducing actin polymerization by jasplakinolide treatment partially rescues the dendritic phenotype of NCAM1 depletion. These results indicate that forced actin stabilization can compensate for the absence of NCAM1 and is one of the driving forces that act during dendrite morphogenesis. These data suggest a model in which NCAM1 stimulates dendritic arbor development by promoting actin filament stabilization at the dendritic growth cone.

In summary, the analysis of proteins differentially expressed at each specific stage of hippocampal neuron development constitutes a fundamental research tool that may be used in the future for a better understanding of any specific molecular mechanism involved in neurodevelopment. Our quantitative proteomics results give a comprehensive overview of protein abundances in time, thereby providing a unique database regarding protein expression patterns in cultured neurons. Furthermore, thanks to the recent technological advances in MS-based proteomics (tandem mass tags [TMTs] or iTRAQ isobaric mass tags would allow relative quantification of up to ten different time points), this analysis could also constitute an excellent starting point for other studies that aim to further complement our understanding of neuronal protein dynamics.

EXPERIMENTAL PROCEDURES

Animals

All experiments with animals were performed in compliance with the guidelines for the welfare of experimental animals issued by the Government of The Netherlands, and were approved by the Animal Ethical Review Committee (DEC) of the Utrecht University.

Expression vectors, shRNA constructs and antibodies

The NCAM120, NCAM140, and NCAM180 constructs were kindly provided by Dr. Landmesser. The following NCAM1 shRNAs were designed and used in this study: NCAM1#1 (5'-GGATCTCATCTGGACTTTG), NCAM1#2 (5'-GATCTTCCAGAAGCTCATG) and NCAM1#3 (CGTTGGAGAGTCCAAATTC) targeting rat NCAM1 mRNA (NM_031521.1). NCAM1 mouse (Millipore) and NCAM1 rabbit (Proteintech) antibodies were used for Western blot, immunocytochemistry experiments. For further details, see Supplemental Experimental Procedures.

Primary hippocampal neuron cultures

Primary hippocampal and cortical cultures were isolated from embryonic day 18 (E18) rat brains. Cells were plated on coverslips coated with poly-L-lysine (30µg/ml) and laminin (2µg/ml) at a density of 100,000/well. Hippocampal neurons were transfected at DIV1 using Lipofectamine 2000 (Invitrogen). Cortical neurons Cells were transfected using

the Amaxa Rat Neuron Nucleofector kit (Lonza). For further details, see Supplemental Experimental Procedures.

Statistical Methods

Analysis of significance of proteins changing between developmental stages was carried out using Significance analysis of microarrays (SAM). Clustering was performed using unsupervised fuzzy clustering. Gene ontology enrichment analyses were performed using a Fisher's exact test. Co-regulation of proteins within complexes or families was assessed using the R package *protein.profiles*. Co-IP data were analyzed using Significance Analysis of INteractions. For morphometric analyses of hippocampal neurons, statistical significance was determined using student's *t* test assuming a two-tailed variation. The graphs represent mean \pm s.e.m. For further details, see Supplemental Experimental Procedures.

DATA AND SOFTWARE AVAILABILITY

The mass spectrometry proteomics data have been deposited to the ProteomeXchange Consortium via the PRIDE partner repository with the dataset identifier PXD005031 (Vizcaino et al., 2016).

SUPPLEMENTAL INFORMATION

Supplemental Information includes Supplemental Experimental Procedures, seven figures, and six tables and can be found with this article online at: <http://dx.doi.org/10.1016/j.celrep.2017.01.025>.

ACKNOWLEDGEMENTS

We thank Dr. L.T. Landmesser for sharing NCAM120, NCAM140, NCAM180 constructs. This work was supported by the Netherlands Organization for Scientific Research (NWO-ALW-VICI, CCH), (NWO-CW-VIDI (723.012.102), AFMA) and Proteins@Work, a program of NWO as part of the National Roadmap Large-scale Research Facilities of the Netherlands (project number 184.032.201), the Foundation for Fundamental Research on Matter ((FOM) CCH), which is part of the NWO, the Netherlands Organization for Health Research and Development (ZonMW-TOP, CCH), the European Research Council (ERC) (ERC-consolidator, CCH). Marie-Curie Actions (MC-IEF, MM) and DFG Emmy-Noether Programm (MI 1923/1-1, MM).

AUTHOR CONTRIBUTIONS

C.K.F. designed and performed the quantitative proteomics experiments and analyzed the data; Q.L. conducted proteomics samples preparation; M.M. and R.S. designed and performed immunohistochemistry experiments, biochemical experiments and analyzed the data. R.S. and V.G. performed AP/MS experiments, C.K.F. and R.S. analyzed the results. S.M. and A.J.R.H. supervised the quantitative proteomics experimental set-up and the Mass-Spectrometry data; the figures were designed and assembled by C.K.F., M.M., R.S., A.F.M.A., and C.C.H.; the manuscript was written by C.K.F., M.M., R.S., A.F.M.A., C.C.H. with input from A.J.R.H.; A.F.M.A. and C.C.H. supervised the project and coordinated the study.

REFERENCES

- Boehm, M., and Bonifacino, J.S. (2001). Adaptins: the final recount. *Mol. Biol. Cell* 12, 2907–2920.
- Boersema, P.J., Raijmakers, R., Lemeer, S., Mohammed, S., and Heck, A.J.R. (2009). Multiplex peptide stable isotope dimethyl labeling for quantitative proteomics. *Nat. Protoc.* 4, 484–494.
- Buttner, B., Kannicht, C., Reutter, W., and Horstkorte, R. (2003). The neural cell adhesion molecule is associated with major components of the cytoskeleton. *Biochem. Biophys. Res. Commun.* 310, 967–971.
- Choi, H., Larsen, B., Lin, Z.Y., Breitreutz, A., Mellacheruvu, D., Fermin, D., Qin, Z.S., Tyers, M., Gingras, A.C., and Nesvizhskii, A.I. (2011). SAINT: probabilistic scoring of affinity purification-mass spectrometry data. *Nat. Methods* 8, 70–73.
- Cremer, H., Chazal, G., Goridis, C., and Represa, A. (1997). NCAM is essential for axonal growth and fasciculation in the hippocampus. *Mol. Cell. Neurosci.* 8, 323–35.
- Dabrowski, M., Aerts, S., Van Hummelen, P., Craessaerts, K., De Moor, B., Annaert, W., Moreau, Y., and De Strooper, B. (2003). Gene profiling of hippocampal neuronal culture. *J. Neurochem.* 85, 1279–1288.
- DeBoer, E.M., Kraushar, M.L., Hart, R.P., and Rasin, M.R. (2013). Post-transcriptional regulatory elements and spatiotemporal specification of neocortical stem cells and projection neurons. *Neuroscience* 248, 499–528.
- Doherty, P., Fazeli, M.S., and Walsh, F.S. (1995). The neural cell adhesion molecule and synaptic plasticity. *J. Neurobiol.* 26, 437–446.
- Dominguez, M.H., Ayoub, A.E., and Rakic, P. (2013). POU-III transcription factors (Brn1, Brn2, and Oct6) influence neurogenesis, molecular identity, and migratory destination of upper-layer cells of the cerebral cortex. *Cereb. Cortex* 23, 2632–2643.
- Dong, X., Liu, O.W., Howell, A.S., and Shen, K. (2013). An extracellular adhesion molecule complex patterns dendritic branching and morphogenesis. *Cell* 155, 296–307.
- Dotti, C.G., Sullivan, C.A., and Banker, G.A. (1988). The establishment of polarity by hippocampal neurons in culture. *J. Neurosci.* 8, 1454–1468.
- Friedman, H.V., Bresler, T., Garner, C.C., and Ziv, N.E. (2000). Assembly of New Individual Excitatory Synapses: Time Course and Temporal Order of Synaptic Molecule Recruitment. *Neuron* 27, 57–69.
- Haslinger, A., Schwarz, T.J., Covic, M., and Lie, D.C. (2009). Expression of Sox11 in adult neurogenic niches suggests a stage-specific role in adult neurogenesis. *Eur. J. Neurosci.* 29, 2103–2114.
- Hevner, R.F., Hodge, R.D., Daza, R.A.M., and Englund, C. (2006). Transcription factors in glutamatergic neurogenesis: Conserved programs in neocortex, cerebellum, and adult hippocampus. *Neurosci. Res.* 55, 223–233.
- Hsieh, J. (2012). Orchestrating transcriptional control of adult neurogenesis. *Genes Dev* 26, 1010–1021.
- Kristensen, A.R., Gspöner, J., and Foster, L.J. (2013). Protein synthesis rate is the predominant regulator of protein expression during differentiation. *Mol. Syst. Biol.* 9, 689.
- Kuo, T.Y., Hong, C.J., and Hsueh, Y.P. (2009). Bcl11A/CTIP1 regulates expression of DCC and MAP1b in control of axon branching and dendrite outgrowth. *Mol. Cell. Neurosci.* 42, 195–207.
- Leshchyn'ska, I., and Sytnyk, V. (2016). Reciprocal Interactions between Cell Adhesion Molecules of the Immunoglobulin Superfamily and the Cytoskeleton in Neurons. *Front. cell Dev. Biol.* 4, 9.
- Licaltosi, D.D., Yano, M., Fak, J.J., Mele, A., Grabinski, S.E., Zhang, C., and Darnell, R.B. (2012). Ptpb2 represses adult-specific splicing to regulate the generation of neuronal precursors in the embryonic brain. *Genes Dev.* 26, 1626–1642.
- Low, T.Y., van Heesch, S., van den Toorn, H., Giansanti, P., Cristobal, A., Toonen, P., Schafer, S., Hübner, N., van Breukelen, B., Mohammed, S., et al. (2013). Quantitative and qualitative proteome characteristics extracted from in-depth integrated genomics and proteomics analysis. *Cell Rep.* 5, 1469–1478.
- Loya, C.M., Van Vactor, D., and Fulga, T.A. (2010). Understanding neuronal connectivity through the post-transcriptional toolkit. *Genes Dev.* 24, 625–635.
- Méndez-Gómez, H.R., Vergaño-Vera, E., Abad, J.L., Bulfone, A., Moratalla, R., de Pablo, F., and Vicario-Abejón, C. (2011). The T-box brain 1 (Tbr1) transcription factor inhibits astrocyte formation in the olfactory bulb and regulates neural stem cell fate.

Mol. Cell. Neurosci. 46, 108–121.

Mody, M., Cao, Y., Cui, Z., Tay, K.Y., Shyong, A., Shimizu, E., Pham, K., Schultz, P., Welsh, D., and Tsien, J.Z. (2001). Genome-wide gene expression profiles of the developing mouse hippocampus. *Proc Natl Acad Sci U S A* 98, 8862–8867.

Newell-Litwa, K., Salazar, G., Smith, Y., and Faundez, V. (2009). Roles of BLOC-1 and Adaptor Protein-3 Complexes in Cargo Sorting to Synaptic Vesicles. *Mol. Biol. Cell* 20, 1441–1453.

Noble, M., Albrechtsen, M., Møller, C., Lyles, J., Bock, E., Goridis, C., Watanabe, M., and Rutishauser, U. (1985). Glial cells express N-CAM/D2-CAM-like polypeptides in vitro. *Nature* 316, 725–728.

Okabe, S., Miwa, A., and Okado, H. (2001). Spine formation and correlated assembly of presynaptic and postsynaptic molecules. *J. Neurosci.* 21, 6105–6114.

Ori, A., Iskar, M., Buczak, K., Kastritis, P., Parca, L., Andrés-Pons, A., Singer, S., Bork, P., and Beck, M. (2016). Spatiotemporal variation of mammalian protein complex stoichiometries. *Genome Biol.* 17, 47.

Pollerberg, G.E., Thelen, K., Theiss, M.O., and Hochlehnert, B.C. (2013). The role of cell adhesion molecules for navigating axons: Density matters. *Mech. Dev.* 130, 359–372.

Sawicka, K., Bushell, M., Spriggs, K.A., and Willis, A.E. (2008). Polypyrimidine-tract-binding protein: a multifunctional RNA-binding protein. *Biochem. Soc. Trans.* 36, 641–647.

Seong, E., Wainer, B.H., Hughes, E.D., Saunders, T.L., Burmeister, M., and Faundez, V. (2005). Genetic analysis of the neuronal and ubiquitous AP-3 adaptor complexes reveals divergent functions in brain. *Mol. Biol. Cell* 16, 128–140.

Sharma, K., Schmitt, S., Bergner, C.G., Tyanova, S., Kannaiyan, N., Manrique-Hoyos, N., Kongi, K., Cantuti, L., Hanisch, U.K., Philips, M.A., et al. (2015). Cell type- and brain region-resolved mouse brain proteome. *Nat. Neurosci.* 18, 1819–1831.

Stolt, C.C., Lommes, P., Friedrich, R.P., and Wegner, M. (2004). Transcription factors Sox8 and Sox10 perform non-equivalent roles during oligodendrocyte development despite functional redundancy. *Development* 131, 2349–2358.

Togashi, H., Sakisaka, T., and Takai, Y. (2009). Cell adhesion molecules in the central nervous system. *Cell Adh. Migr.* 3, 29–35.

Tonks, N.K. (2013). Protein tyrosine phosphatases - From housekeeping enzymes to master regulators of signal transduction. *FEBS J.* 280, 346–378.

van Spronsen, M., van Battum, E.Y., Kuijpers, M., Vangoor, V.R., Rietman, M.L., Pothof, J., Gummy, L.F., van IJcken, W.F.J., Akhmanova, A., Pasterkamp, R.J., et al. (2013). Developmental and Activity-Dependent miRNA Expression Profiling in Primary Hippocampal Neuron Cultures. *PLoS One* 8, e74907.

Vizcaino, J.A., Csordas, A., Del-Toro, N., Dianes, J.A., Griss, J., Lavidas, I., Mayer, G., Perez-Riverol, Y., Reisinger, F., Ternent, T., et al. (2016). 2016 update of the PRIDE database and its related tools. *Nucleic Acids Res.* 44, D447–D456.

Walsh, F.S., and Doherty, P. (1997). Neural cell adhesion molecules of the immunoglobulin superfamily: role in axon growth and guidance. *Annu. Rev. Cell Dev. Biol.* 13, 425–456.

Wayman, G.A., Lee, Y.S., Tokumitsu, H., Silva, A., and Soderling, T.R. (2008). Calmodulin-Kinases: Modulators of Neuronal Development and Plasticity. *Neuron* 59, 914–931.

White, M.K., Johnson, E.M., and Khalili, K. (2009). Multiple roles for Puralpha in cellular and viral regulation. *Cell Cycle* 8, 1–7.

Zhang, J., and Herrup, K. (2011). Nucleocytoplasmic Cdk5 is involved in neuronal cell cycle and death in post-mitotic neurons. *Cell Cycle* 10, 1208–1214.

SUPPLEMENTARY FIGURES

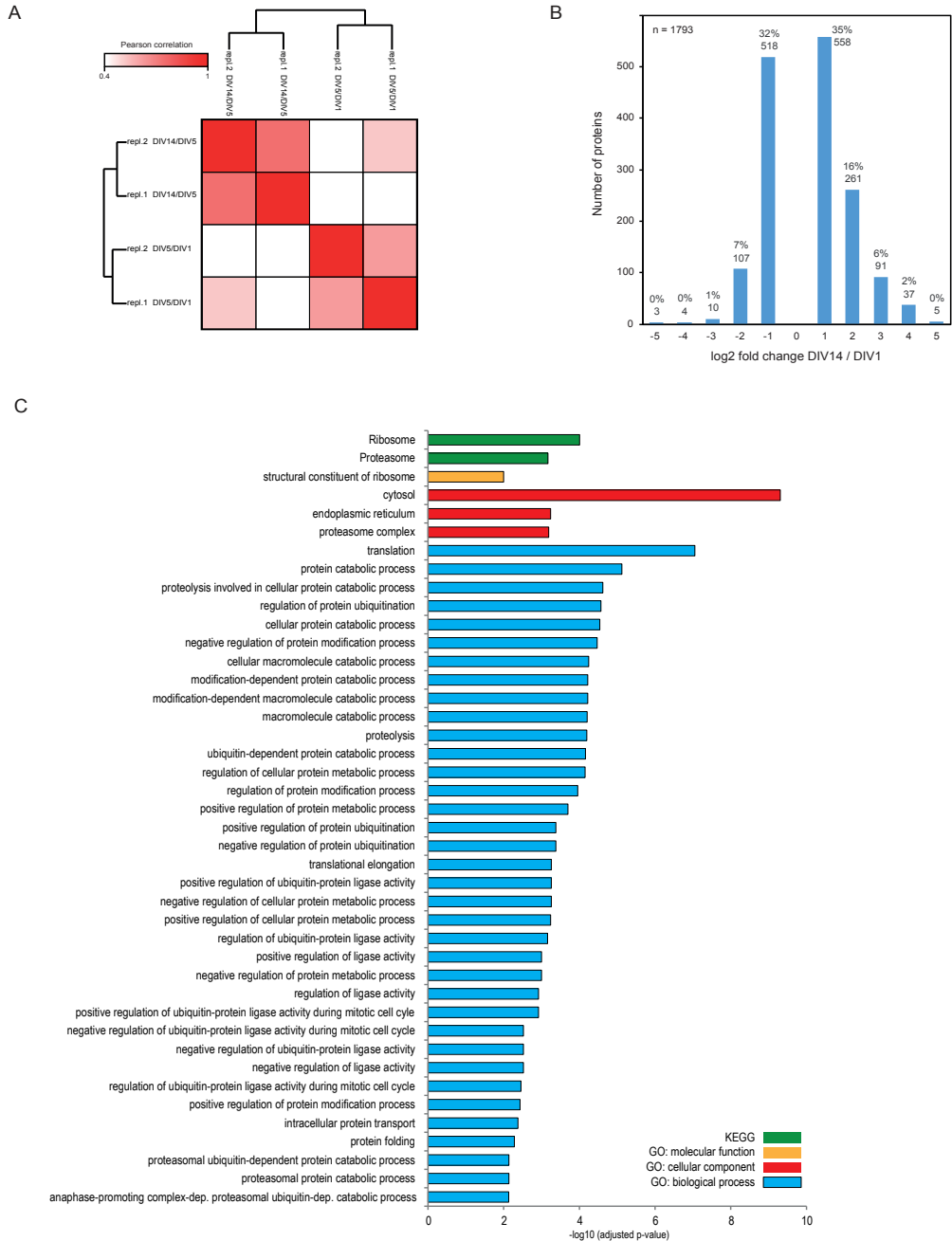


Figure S1. Related to Figure 1. Reproducibility and statistical analysis of differentially expressed proteins

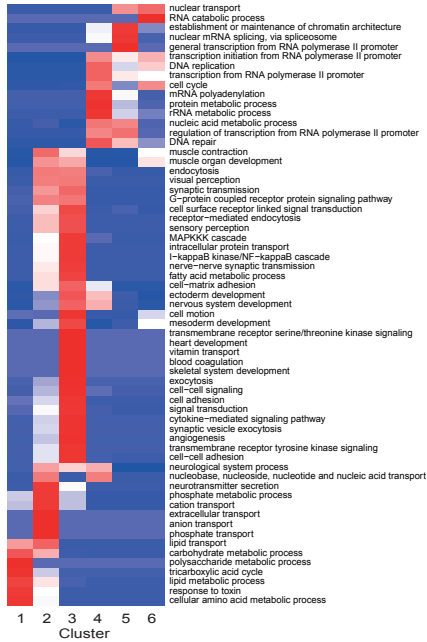
(A) Heat map showing Pearson correlation scores for the two independent biological replica.

(B) Distribution of fold changes calculated on all the quantified proteins.

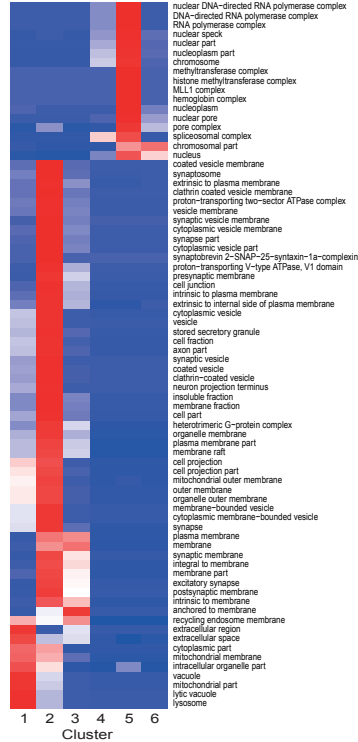


(C) Gene ontology (GO) and KEGG pathway enrichment analysis. All quantified proteins were subjected to enrichment analysis with respect to biological process, molecular function, cellular component, and protein class (KEGG).

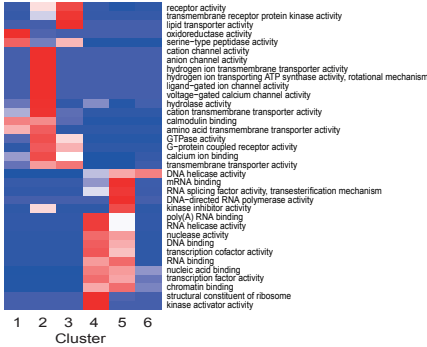
GO Biological Process



GO Cellular Component



GO Molecular Function



Protein Class

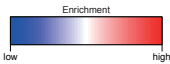
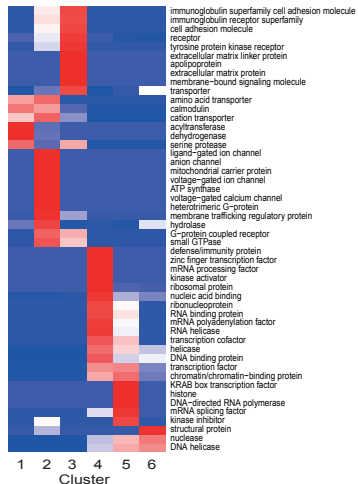


Figure S2. Related to Figure 2. Gene ontology classification of regulated proteins

For all proteins of each cluster (see Figure 2) enrichment analysis with respect to biological process, molecular function, cellular component and protein class (KEGG) was performed. Overrepresentation was tested against all not regulated proteins. The heat maps show the overrepresentation /underrepresentation of each group in each specific cluster.

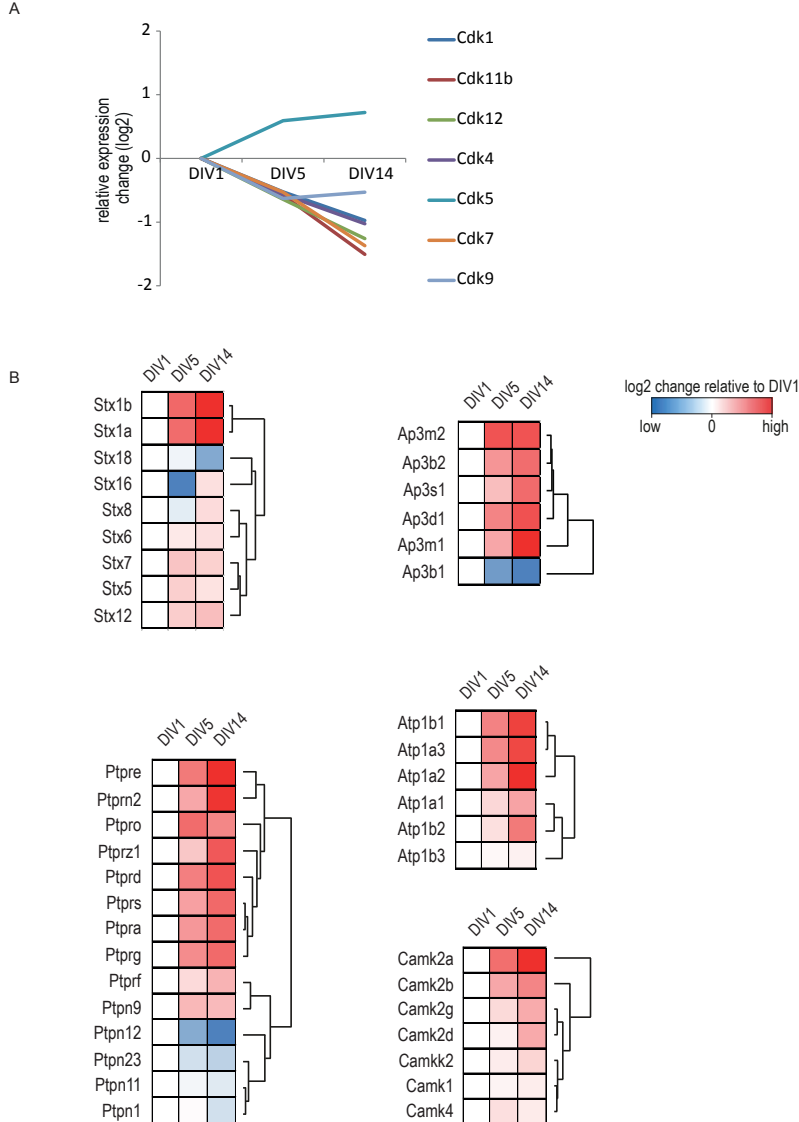


Figure S3. Related to Figure 3. Expression profiles of protein families/complexes

(A) Expression profiles of proteins from the cyclin-dependent kinase family.

(B) Heat maps of expression profiles of proteins showed in Figure 3B. Ap3b1 (6 unique peptides used for the quantification) does not follow the expression profile of the other AP3 complex proteins. Similar trend has been measured for Atp1b3 (7 unique peptides used for the quantification) that does not change over time while other subunits of the complex are upregulated.

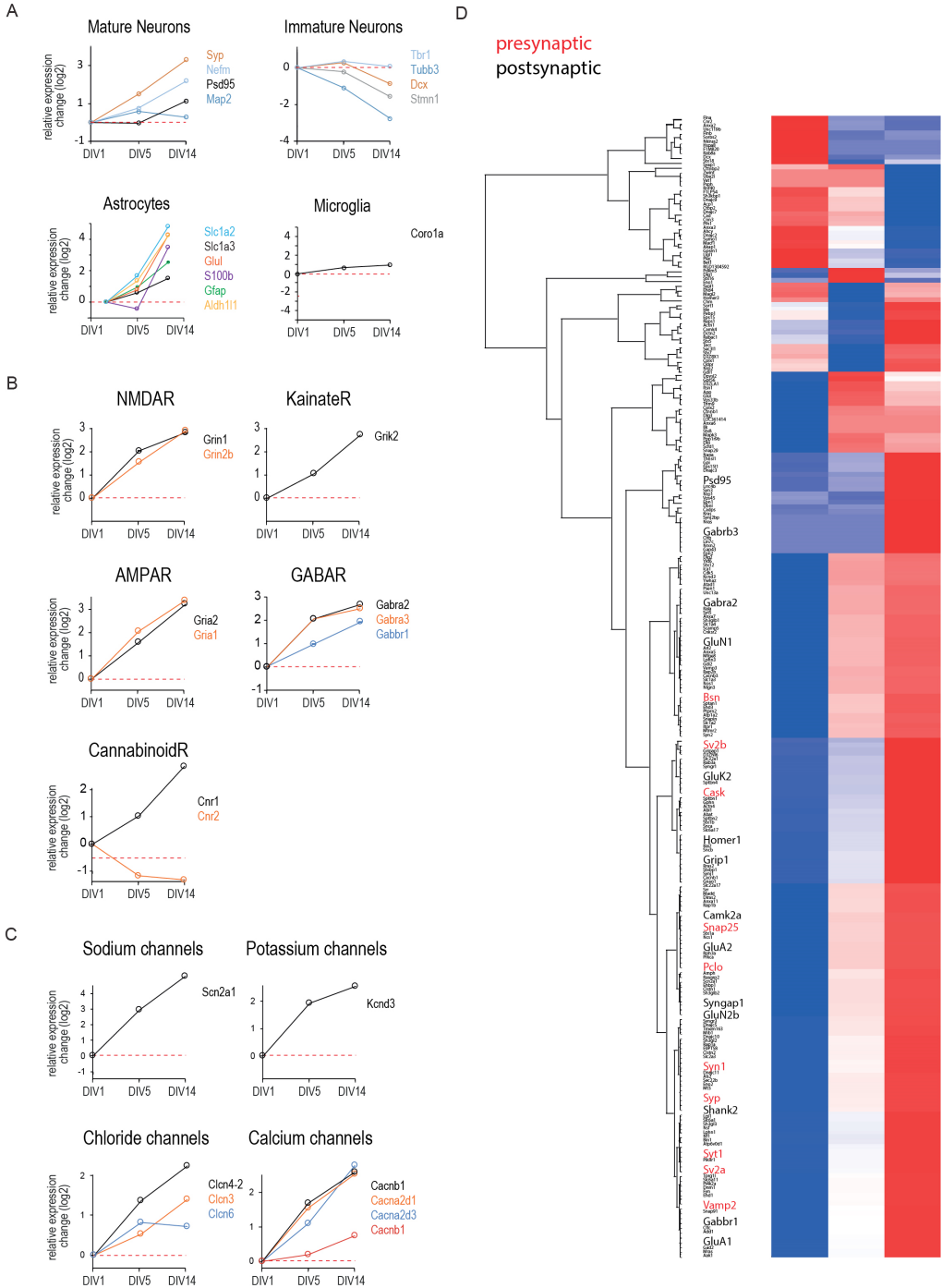


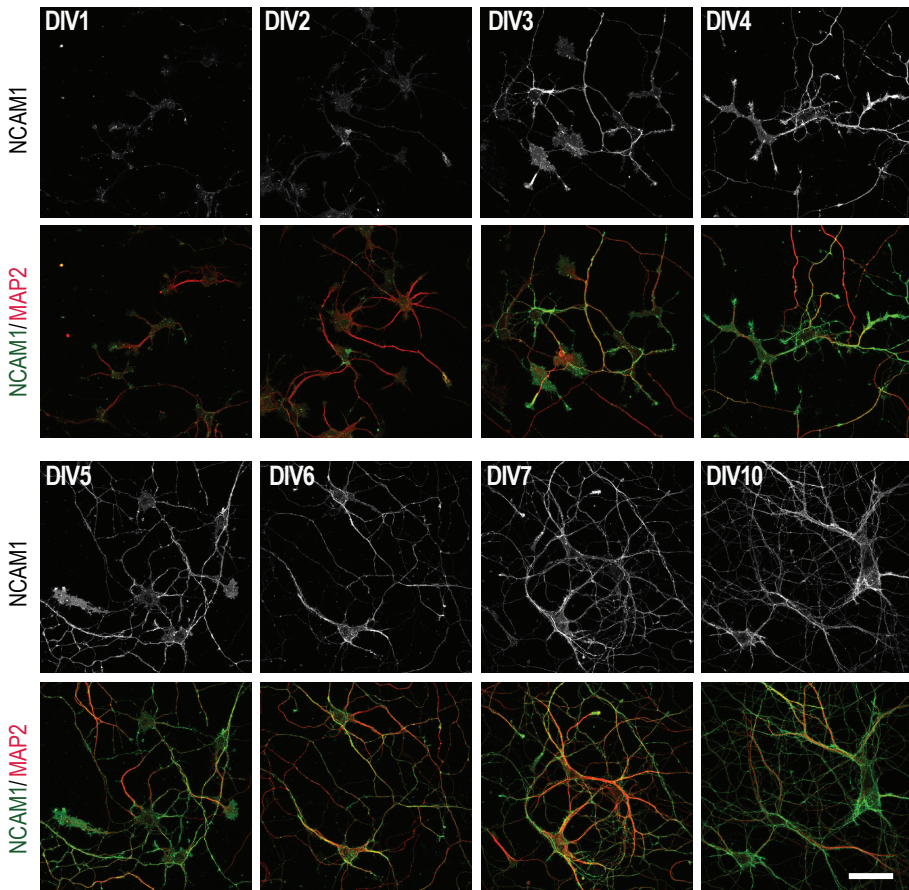
Figure S4. Related to Figure 4. Expression profiles of cell-type protein markers and proteins with similar function/localization

(A) Expression profiles of selected protein markers for mature neurons, immature neurons, astrocytes and microglia. Astrocytes specific proteins are highly up-regulated after DIV5.

(B) Expression profiles of selected neurotransmitter receptors.

(C) Expression profiles of selected voltage-gated ion channels.

(D) Hierarchical clustering of all synaptic proteins (based on Euclidian distance). Proteins known to be located either pre- or postsynaptic are highlighted in bold. Evidently, the expression profiles of these two subclasses are not distinguishable by hierarchical clustering.

**Figure S5. Related to Figure 5. NCAM1 localization in mouse hippocampal primary neurons**

Representative images of mouse hippocampal neurons from DIV1 to DIV10, stained for NCAM1 (green), MAP2 (red). Scale bar, 50 μ m.

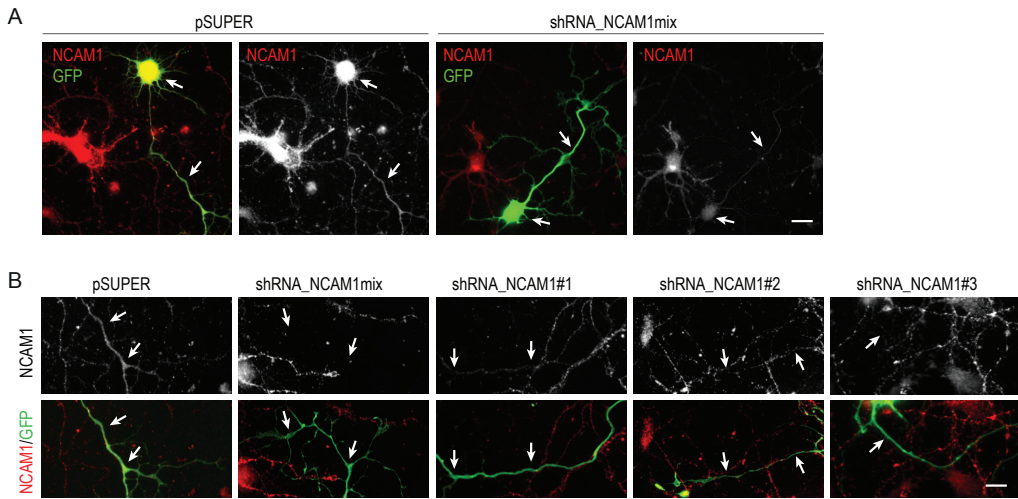


Figure S6. Related to Figure 6. NCAM1 downregulation in rat hippocampal primary neurons

(A) Representative images of neurons transfected with pSUPER or shRNA NCAM1mix, filled with GFP (1DIV for 3 days) and stained with NCAM1 monoclonal antibody. Scale bar, 20 μ m.

(B) Higher magnifications of representative images of neurons co-transfected with pSUPER, shRNA NCAM1mix, shRNA NCAM1#1, shRNA NCAM1#2, shRNA NCAM1#3 and GFP. Arrows point to representative neurites. Scale bar, 10 μ m.

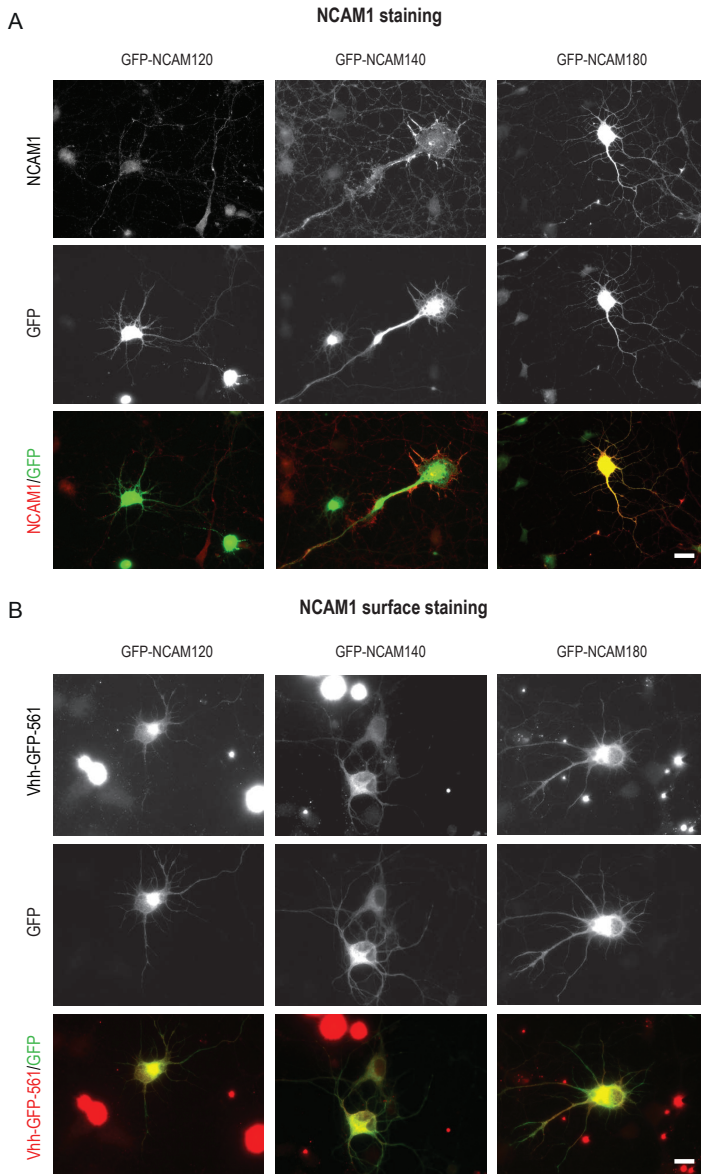


Figure S7. Related to Figure 7. Characterization of N-terminal GFP tagged NCAM1 isoforms

(A) Representative images of neurons transfected with GFP-NCAM120, GFP-NCAM140 or GFP-NCAM180 and stained with NCAM1 mouse antibody. The NCAM1 antibody recognizes the C-terminal tail of NCAM1 and as expected the signal is completely overlapping with the GFP only when the longer NCAM1 isoform (NCAM180) is expressed. Scale bar, 20 μ m.

(B) Representative images of neurons transfected with GFP-NCAM120, GFP-NCAM140 or GFP-NCAM180 and live stained with Vhh-GFP-568 nanobodies. Cells were not permeabilized before the staining and the GFP-targeted-nanobodies were added directly in the medium at 37°C, so only NCAM1 molecules efficiently expressed on the neuronal surface can be detected. Scale bar, 10 μ m.

SUPPLEMENTAL EXPERIMENTAL PROCEDURES

Animals

All experiments with animals were performed in compliance with the guidelines for the welfare of experimental animals issued by the Government of The Netherlands, and were approved by the Animal Ethical Review Committee (DEC) of the Utrecht University.

Antibodies and reagents

The following primary and secondary antibodies were used in this study: NCAM1 mouse (Millipore), NCAM1 rabbit (Proteintech), Syt1, Camk2a mouse (Sigma), PSD95, Cntn1, NCAM2, L1CAM, Kif5B, Actg mouse (Millipore) and Tubα1a rabbit (Abcam), MAP2 rabbit (Cell Signaling), Vhh-GFP-Alexa 561 nanobodies (Yau et al., 2014). Alexa 488-, Alexa 568- and Alexa 594-conjugated secondary antibodies (Invitrogen). Other reagents used in this study include: Jaspilakinolide (2792, Tocris Bioscience), n-Dodecyl β-D-maltoside (A0819, Applichem).

Expression vectors and shRNA constructs

The following mammalian expression plasmids have been described: pGW1-GFP (Hoogenraad et al, 2005), pCDNA3.1-RFP-NCAM120, pCDNA3.1-RFP-NCAM140, pCDNA3.1-RFP-NCAM180, pCDNA3.1-eGFP-NCAM120, pCDNA3.1-eGFP-NCAM140, pCDNA3.1-eGFP-NCAM180 (Hata et al., 2007) the expression and targeting of each isoform and its relationship to distinct forms of synaptic vesicle cycling before and after synapse formation was previously unknown. By transfecting chick motoneurons with fluorescently tagged mouse 180, 140 and 120 isoforms, we show that before myotube contact the 180 and 140 isoforms are expressed in distinct puncta along the axon which are sites of an immature form (Brefeldin A sensitive, L-type Ca²⁺ channel mediated). The following shRNA sequences are used in this study. NCAM1#1 (5'-GGATCTCATCTGGACTTTG), NCAM1#2 (5'-GATCTCCAGAAGCTCATG) and NCAM1#3 (CGTTGGAGAGTCCAAATTC) targeting rat NCAM1 mRNA (NM_031521.1) were designed using the siRNA selection program at the Whitehead Institute for Biomedical Research (jura.wi.mit.edu/bioc/siRNAext) (Yuan et al., 2004). The complementary oligonucleotides were annealed and inserted into a pSuper vector (Hoogenraad et al., 2005). The control pSuper vector contained a scrambled sequence.

Primary hippocampal neuron cultures and transfection

Rat primary hippocampal cultures were prepared from embryonic day 18 rat brains. Cells were plated on coverslips coated with poly-L-lysine (30 μg/ml) and laminin (2 μg/ml) at a density of 100,000/well as previously (Kapitein et al., 2010). Hippocampal cultures were grown in Neurobasal medium (NB) supplemented with B27, 0.5 μM glutamine, 12.5 μM glutamate and penicillin/streptomycin. Mouse primary hippocampal cultures were prepared from embryonic day 18 mouse brains then plated and cultured in the same conditions as rat primary neurons.

Hippocampal neurons were transfected at DIV1 using Lipofectamine 2000 (Invitrogen). Briefly, DNA (1.8 μg/well, for a 12 wells plate) was mixed with 3.3 μl of Lipofectamine 2000 in 200 μl NB, incubated for 30 min, and then added to the neurons in NB at 37°C in 5% CO₂ for 45 min. Next, neurons were washed with NB and transferred in their original medium at 37°C in 5% CO₂ for 3-7 days. For forced actin-stabilization experiments, young neurons co-transfected at day1 were treated 24 hours later (DIV2) with 10 nM Jaspilakinolide and cells were then incubated for 6 days at 37°C in the presence of the drug (Swiech et al., 2011).

Primary cortical neuron nucleofection

Primary cortical neurons were isolated from E18 rat brain. Cells (1x10⁶) were transfected using the Amaxa Rat Neuron Nucleofector kit (Lonza) with 3 μg of plasmid DNA (pSUPER, ShRNA-NCAM1mix, ShRNA-NCAM1#1, ShRNA-NCAM1#2, ShRNA-NCAM1#3) and plated on coverslips coated with poly-L-lysine (37.5 μg/ml) and laminin (5 μg/ml) in 12-wells plates (2-6 x10⁴ cells/well) containing DMEM supplemented with 10% FBS (Kaeck and Banker, 2006). Cells were allowed to recover and adhere to the surface at 37°C in 5% CO₂, after 4 hours the medium was replaced

with Neurobasal medium supplemented with 2% B27, 0.5mM glutamine, 15.6 μ M glutamate, and 1% penicillin/streptomycin. After 4 days cells were lysed in hot denaturing sample buffer.

Sample preparation for Mass spectrometry

At three time points (DIV1, DIV5, DIV14) neurons were washed 4x with 500 μ L pre-warmed PBS. For lysis 500 μ L lysis buffer (8 M Urea, 1 tablet Complete Mini EDTA-free protease inhibitor Cocktail (Roche) in 10 mL 50 mM triethylammonium bicarbonate (Sigma)) was added to each well. Following sonication, samples were cleared by centrifugation at 20,000 \times g for 20 min. Proteins were reduced (5 mM DTT, 55°C, 30 min), alkylated (10 mM Iodoacetamide, 30 min in the dark) and sequentially digested by LysC (Protein-enzyme ratio 1:50, 37°C, 4 h) and trypsin (Protein-enzyme ratio 1:50, 37°C, 16 h) according to the standard filter-aided sample preparation protocol (Wiśniewski et al., 2009). Resulting peptides from each time point were desalted using C18 solid phase extraction cartridges (Waters) and subjected to stable isotope triplex dimethyl labeling on column (Boersema et al., 2009). Labels were swapped between biological replicates. Differentially labeled peptides were mixed in a 1:1:1 ratio based on LC-MS base peak intensity of the separate channels, dried in a vacuum concentrator and reconstituted in 10% formic acid for subsequent fractionation.

Peptide Fractionation

Peptides were fractionated using strong cation exchange chromatography (SCX), as previously described (Frese et al., 2012) ISBN: 1520-6882 (Electronic). Briefly, peptides were loaded onto a Zorbax BioSCX-Series II column (0.8 mm \times 50 mm, 3.5 μ m) in 100% solvent A (0.05% formic acid in 20% acetonitrile). Solvent B consisted of 0.05% formic acid and 0.5 M NaCl in 20% acetonitrile. Fractionation was conducted using the following gradient: 0–0.01 min (0–2% B); 0.01–8.01 min (2–3% B); 8.01–14.01 min (3–8% B); 14.01–28 min (8–20% B); 28–38 min (20–40% B); 38–48 min (40–90% B); 48–54 min (90% B); 54–60 min (0% B). Collected fractions were dried in vacuo, reconstituted in 10% formic acid/5% DMSO and stored at -80°C prior MS analysis.

Affinity Purification-Mass Spectrometry (AP-MS) using GFP pull-down

Human Embryonic Kidney 293 cells (HEK293) cells were cultured in DMEM/Ham's F10 (50%/50%) containing 10% Fetal Calf Serum (FCS) and 1% penicillin/streptomycin at 37°C and 5% CO₂. HEK293 cells were transfected with pGW1-GFP, eGFP-NCAM120, eGFP-NCAM140 and eGFP-NCAM180 constructs with polyethylenimine (PEI, Polysciences) according to the manufacturer instructions. Cells were lysed 48 hours later in a lysis buffer for transmembrane proteins (20mM TrisHCl, 100mM NaCl, 10mM EDTA (pH8.0), 10mM Na₄P₂O₇, 10% Glycerol, 50mM NaF, 1% n-Dodecyl β -D-maltoside, and protease inhibitors (Roche)), centrifuged at 13000 rpm for 15 min and the supernatants were incubated with GFP-trap beads (Chromotek) for 1 hour at 4°C. Beads were then separated using a magnet (Dyna; Invitrogen) and washed five times in washing buffer (20mM Tris HCl, 150mM KCl, 0.1% TritonX-100). Brains were obtained from female adult rats or P5 rat pups and homogenized in 10x volume/weight in tissue lysis buffer (50mM TrisHCl, 150mM NaCl, 0.1% SDS, 0.2% NP-40, and protease inhibitors (Roche)). Brain lysates were centrifuged at 16,000 g for 15 min at 4°C and the supernatant was incubated with the Dynabeads containing GFP or GFP-NCAM120/140/180 for 2 hrs at 4°C and washed with lysis buffer for five times. For MS analysis, the beads were resuspended in 15 μ l of 4x Laemmli Sample buffer (Biorad) and supernatants were loaded on a 12% Criterion XT Bis-Tris precast gel (Biorad). The gel was stained with 0.1% Coomassie Brilliant Blue G250 (Sigma-Aldrich, Steinheim, Germany) in 25% methanol and 10% acetic acid (Merck, Darmstadt, Germany). Each lane from the gel was cut in 3 slices, destained and digested using trypsin, as described in (Ekkebus et al., 2013). Briefly, each lane from the gel was cut into three pieces and placed in 0.5-ml tubes. They were washed with 250 μ l of water, followed by 15-min dehydration in acetonitrile. Proteins were reduced (10 mM dithiothreitol, 1h at 56°C), dehydrated and alkylated (55 mM iodoacetamide, 1h in the dark). After two rounds of dehydration, trypsin was added to the samples (20 μ l of 0.1 mg/ml trypsin in 50 mM Ammoniumbicarbonate) and incubated overnight at 37°C. Peptides were extracted with ACN, dried down and reconstituted in 10% formic acid prior MS analysis.

Mass spectrometry analysis

All samples were analyzed on an ETD enabled LTQ-Orbitrap Elite or Q-Exactive mass spectrometer (Thermo Fisher Scientific, Bremen, Germany) that was coupled to Proxeon EASY-nLC 1000 (Thermo Fisher Scientific, Odense, Denmark). Peptides were loaded onto a trap column (Reprosil C18, 3 μm , 2 $\text{cm} \times 100 \mu\text{m}$; Dr. Maisch) with solvent A (0.1% formic acid in water) at a maximum pressure of 800 bar and chromatographically separated over the analytical column (Zorbax SB-C18, 1.8 μm , 50 $\text{cm} \times 75 \mu\text{m}$; Agilent) using a 60 min, 90 min or 150 min linear gradient from 7-30% solvent B (0.1% formic acid in acetonitrile) at a flow rate of 150 nL/min. The mass spectrometer was operated in the data-dependent acquisition mode. After a survey scan from 350-1500 m/z the 10 or 20 most abundant peptides were subjected to either HCD or decision tree-guided CID/ETD fragmentation (ddDT) (Frese et al., 2011) in a 2D or 3D ion trap, respectively. Product ions were detected in the Orbitrap (HCD methods; Resolution 7,500) and linear ion trap (ddDT methods), respectively. Normalized collision energy was set to 35% and 32% for CID and HCD, respectively. Charge state dependent ETD reaction time and supplemental activation were enabled. Charge state screening was enabled and ions with charge states $<2+$ were excluded from analysis. Samples from in-gel digestion were analyzed using a 90 min gradient.

Mass spectrometry data analysis

All mass spectrometric raw data were processed with Proteome Discoverer (version 1.3, Thermo Scientific, Bremen, Germany), as described in (Frese et al., 2012) "ISBN" : "1520-6882 (Electronic. Peak lists were generated using a standard workflow. The non-fragment filter was used to simplify ETD spectra. HCD spectra were deisotoped and charge deconvoluted. The TopN filter node was used to filter CID and ETD spectra and to retain the 10 most abundant peaks per 100 Da window. Peptide identification was performed by searching individual peak lists of HCD, ETD-IT and CID-IT against the Uniprot rat database (version 2013_01) concatenated with a list of common contaminants using Mascot (version 2.3, Matrix Science, UK). Trypsin was set as cleavage specificity, allowing a maximum of 2 missed cleavages. Precursor ion mass tolerance was set to 15 ppm. Product ion mass tolerance was set to 0.02 Da (Orbitrap detection) and 0.5 Da (ion trap detection), respectively. Carbamidomethylation (C) was used as fixed modification. Oxidation (M) and dimethylation (light, intermediate or heavy) of lysine residues and the peptide N-termini, respectively, were set as variable modification. The percolator algorithm was used to filter the data to $<1\%$ false-discovery-rate on peptide level. Additionally, only peptides that pass the following filters were retained: mascot ion score ≥ 20 , minimum peptide length 6, precursor mass tolerance 10 ppm, and search engine rank 1. Only unique peptides were used for quantification and the obtained ratios were normalized to the median. AP-MS data was analyzed using Proteome Discoverer and the aforementioned settings. Common contaminant proteins including immunoglobulins were removed from the list.

Bioinformatic analysis

Gene ontology (GO) classification was obtained via PANTHER (Mi et al., 2005) using human expertise. These subfamilies model the divergence of specific functions within protein families, allowing more accurate association with function (ontology terms and pathways and Perseus (version 1.3.0.4, within MaxQuant) (Cox et al., 2009; Huang et al., 2009). Hierarchical clustering was performed within Perseus using Euclidian distance. Network analysis was performed using the GeneMania plugin (Montejo et al., 2010) within Cytoscape (Shannon et al., 2003). Significance analysis of microarrays (SAM) (Roxas and Li, 2008) was used to assess significance of obtained protein ratios, as described in (Munoz et al., 2011). Briefly, \log_2 -transformed ratios of proteins that were quantified in all time points and in both replicates were subjected to a one-class test using 1000 permutations and an S_0 value based on the method by (Tusher et al., 2001). Proteins with a SAM q -value ≤ 0.15 (corresponding to a median \log_2 fold-change of >1.5 between DIV14 and DIV1) were considered significantly regulated and subjected to unsupervised fuzzy clustering using GProX 1.1.9 (Rigbolt et al., 2011) the analysis of data has become the bottleneck of proteomics experiment. To provide the proteomics community with a user-friendly platform for comprehensive analysis, inspection and visualization of quantitative proteomics data we developed the Graphical Proteomics Data Explorer (GProX). Briefly, the relative abundance of all proteins from each time point was \log_{10} transformed, Z -scored and clustered using a fuzzification

value of 2, 100 iterations and a minimum membership value of 0.35. Gene ontology enrichment for each cluster was performed using a Fisher's exact test within GProX (min. occurrences 5 for GOMF, GOBP and protein class, and 1 for GOCC; Benjamini-Hochberg corrected p-value <0.05). Significance of expression profile similarities within groups of interest was determined using the R package "proteinProfiles" (Julian Gehring [2011], <https://bioconductor.org/packages/devel/bioc/html/proteinProfiles.html>) within R/Bioconductor (Gentleman et al., 2004), as reported elsewhere (Hansson et al., 2012). The heatmap in Figure 7 was generated by subjecting log₁₀-transformed and z-scored relative abundances of all proteins from each time point (DIV 1, 5, 14) to hierarchical clustering using Euclidean distance. Statistical assessment of the AP-MS data was performed based on spectral counts using the SAINT (Significance Analysis of INteractions, version 2.3.2) algorithm (Choi et al., 2011). The SAINT parameters were set as follows: nburn=4000, niter=20000, lowmode=0, minfold=1, and norm=1. Bait proteins with a SAINT probability score >0.75 were considered putative protein interaction partners.

Cell extracts and Western blotting

HEK293 cell extracts were prepared by resuspending cells in equal amounts of lysis buffer containing 25mM Tris-HCl pH 8.0, 50mM NaCl, 0.5% Triton X-100 supplemented with 1x protease inhibitors cocktail (Roche). The soluble fraction was separated by centrifugation at 13000 rpm for 15 minutes and supplemented with sample buffer 4x (8% SDS, 25% glycerol, 0.05M Tris pH 6.8, 400mM DTT and 40mg/l bromophenol blue). Rat primary hippocampal neurons (E18) were plated on 24 mm coverslips in 6 well plates and harvested at DIV 1, 5 and 14 days in vitro (DIV), or at DIV2, 4, 6, 8, 10, 12, 14, 16, 18 and 21. Cells were lysed in hot denaturing sample buffer. Lysates prepared from individual wells were pooled together (3 wells each stage, 3 independent preparations) and equal protein concentrations were adjusted before supplementing with 4x sample buffer. Samples were boiled at 99°C for 10 minutes before being analyzed by SDS PAGE. Proteins were transferred on PVDF membranes (Millipore) using a semi-dry blotting system. Membranes were blocked and incubated with primary antibodies (overnight at 4°C) in PBS or PBST (0.1% Tween-20, 2% BSA). Peroxidase-coupled secondary antibodies were applied for 1 hour at RT. Following primary NCAM1 antibodies have been used for detection: NCAM1 mouse antibody (Millipore 1:1000), NCAM1 rabbit antibody (Proteintech 1:1000). For quantifying NCAM1 expression levels, the relative intensities of NCAM1 for each sample (n=3) were obtained by normalization to the tubulin loading control. The relative percentage of NCAM1 expression levels was obtained by normalization of the relative intensities with the relative intensity of NCAM1 at DIV2. For quantifying Syt1, Camk2a, PSD95, Cntn1, NCAM1, NCAM2, L1CAM expression levels, the relative intensities of each band (n=3) were measured together with 3 different loading controls such as Kif5B, Actg and Tuba1a. Quantifications were performed with ImageJ.

Immunohistochemistry

For general immunohistochemistry, neurons were fixed for 10 min with 4% paraformaldehyde (PFA)/4% sucrose in phosphate buffered saline (PBS) at room temperature. After fixation cells were washed 3 times for 10 min in PBS at room temperature, incubated for 10 min with permeabilization buffer (0.25% TritonX-100 in PBS) and then blocked for 1 hour with blocking buffer (2% BSA, 2% Glycin, 0.2% Gelatin, 50mM NH₄Cl, in PBS). Neurons were then incubated with primary antibodies in blocking buffer overnight at 4°C, washed three times in PBS for 10 min at room temperature and then incubated with the Alexa-conjugated secondary antibodies in blocking buffer for 1 hour at room temperature. Neurons were then washed 3 times for 5 min in PBS at room temperature and subsequently mounted on slides in Vectashield mounting medium (Vector Laboratories). For labeling of F-actin neurons were incubated with Phalloidin-647 (1:100 in PBS; Molecular Probes) for 30 min at room temperature, washed 3 times in PBS and mounted on slides in Mowiol. Images were acquired using a Nikon upright or Olympus BX53 upright fluorescent microscopes with a 10x, 20x or 40x objective. Confocal images were acquired using a Leica SP5 microscope (Wetzlar, Germany) equipped with a Krypton-Argon-Ion laser (488/568/647 nm) and an acousto-optic-tunable filter (AOTF) for selection and intensity adaptation of laser lines. Images and were taken with 63x oil objective as z-stacks (300 nm z-step) and maximum intensity projections were calculated from each fluorescence channel of the image-stack.

Analyzing NCAM1 knockdown efficiency by immunostaining

Efficiency of NCAM1 shRNA knock down was verified by immunostaining of endogenous NCAM1 protein in hippocampal neurons co-transfected at DIV1 with 0.45 $\mu\text{g}/\text{well}$ GFP and 1,35 $\mu\text{g}/\text{well}$ of different NCAM1-shRNAs or a mixture of all of them, and fixed 3 days later. NCAM1 staining was measured in neurites of GFP positive neurons and was compared to NCAM1 staining in neurites of GFP negative surrounding cells. Quantifications were performed with Image J software (<http://rsb.info.nih.gov/ij>).

Quantification of fluorescent intensity. For the quantification of antibody staining, images were acquired with a 40x oil objective with the same settings and the exposure time and ImageJ was used to manually draw specific regions of interest (ROI) located in primary neurites. From the ROIs the mean intensity was measured. To prevent selection bias during quantification, in NCAM1-KD neurons the neurites segments were selected in one channel (GFP) and blindly quantified in the other channel (NCAM1 intensity). Intensities were measured in at least three neurites per neuron, in segments of approximately the same size, both in GFP positives and GFP negatives neurons within the image. To remove the background signal, the intensity near the selected neurites (same segment size) was measured and subtracted to the neurites measured intensities within the same image. Intensities were averaged over multiple cells, normalized and a statistical analysis was performed with student's t test assuming a two-tailed and unequal variation. For Figure 6C, n=9+9 neurons for pSUPER, n=13+13 neurons for shNCAM1 mix, n=7+7 neurons for shNCAM1#1, #2 and #3. n is derived from two independent experiments.

Morphometric analyses of hippocampal neurons

To analyze axonal and dendritic morphology of NCAM1 knockdown neurons, GFP was used as an unbiased cell-fill in combination with different NCAM1-shRNAs or a mixture of all of them. Hippocampal neurons were co-transfected at DIV1 using the same concentrations of plasmid DNA previously reported, and fixed 7 days later. The morphometric analysis and quantification were performed with ImageJ. The axonal parameters, such as axonal total length and longest neurite length, were measured in images acquired with a dry 10x objective whereas quantification of the dendrites total length, primary dendrites length and branches length was done with images acquired with an 20x dry or 40x oil objective. For axon and dendrite length, all neurites of a single neuron were traced in ImageJ and the number of pixels was then converted to distance in μm . Morphological characteristics and MAP2 staining were used as parameters to distinguish axon and dendrites. Data were averaged over multiple cells and experiments, and a statistical analysis was performed with student's t-test assuming a two-tailed and unequal variation. For Figure 6E (axon morphology): n=18 neurons for pSUPER, n=25 neurons for shNCAM1mix, n=17 neurons for shNCAM1#1, n=16 neurons for shNCAM1#2, n=18 neurons for shNCAM1#3. For Figure 6F (dendrites morphology): n=9 neurons for pSUPER, n=10 neurons for shNCAM1mix, n=8 neurons for shNCAM1#1, n=8 neurons for shNCAM1#2, n=9 neurons for shNCAM1#3. For Figure 7F (axon morphology): n=9+9 neurons for pSUPER, n=9+9 neurons for shNCAM1#1, n=11+11 neurons for shNCAM1#3. For Figure 7G (dendrites morphology): n=12+12 neurons for pSUPER, n=12+12 neurons for shNCAM1#1, n=13+13 neurons for shNCAM1#3. n is derived from two independent experiments.

SUPPLEMENTAL REFERENCES

- Boersema, P.J., Raijmakers, R., Lemeer, S., Mohammed, S., and Heck, A.J.R. (2009). Multiplex peptide stable isotope dimethyl labeling for quantitative proteomics. *Nat. Protoc.* *4*, 484–494.
- Choi, H., Larsen, B., Lin, Z.Y., Breitkreutz, A., Mellacheruvu, D., Fermin, D., Qin, Z.S., Tyers, M., Gingras, A.C., and Nesvizhskii, A.I. (2011). SAINT: probabilistic scoring of affinity purification-mass spectrometry data. *Nat. Methods* *8*, 70–73.
- Cox, J., Matic, I., Hilger, M., Nagaraj, N., Selbach, M., Olsen, J. V., and Mann, M. (2009). A practical guide to the MaxQuant computational platform for SILAC-based quantitative proteomics. *Nat. Protoc.* *4*, 698–705.
- Ekkebus, R., Van Kasteren, S.I., Kulathu, Y., Scholten, A., Berlin, I., Geurink, P.P., De Jong, A., Goerdalay, S., Neeffjes, J., Heck, A.J.R., et al. (2013). On terminal alkynes that can react with active-site cysteine nucleophiles in proteases. *J. Am. Chem. Soc.* *135*, 2867–2870.
- Frese, C.K., Altalear, A.F.M., Hennrich, M.L., Nolting, D., Zeller, M., Griep-Raming, J., Heck, A.J.R., and Mohammed, S. (2011). Improved Peptide Identification by Targeted Fragmentation Using CID, HCD and ETD on an LTQ-Orbitrap Velos. *J. Proteome Res.* *10*, 2377–2388.
- Frese, C.K., Altalear, A.F.M., Van Den Toorn, H., Nolting, D., Griep-Raming, J., Heck, A.J.R., and Mohammed, S. (2012). Toward full peptide sequence coverage by dual fragmentation combining electron-transfer and higher-energy collision dissociation tandem mass spectrometry. *Anal. Chem.* *84*, 9668–9673.
- Gentleman, R.C., Carey, V.J., Bates, D.M., Boltstad, B., Dettling, M., Dudoit, S., Ellis, B., Gautier, L., Ge, Y., Gentry, J., et al. (2004). Bioconductor: open software development for computational biology and bioinformatics. *Genome Biol.* *5*, R80.
- Hansson, J., Rafiee, M.R., Reiland, S., Polo, J.M., Gehring, J., Okawa, S., Huber, W., Hochedlinger, K., and Krijgsveld, J. (2012). Highly Coordinated Proteome Dynamics during Reprogramming of Somatic Cells to Pluripotency. *Cell Rep.* *2*, 1579–1592.
- Hata, K., Polo-Parada, L., and Landmesser, L.T. (2007). Selective targeting of different neural cell adhesion molecule isoforms during motoneuron myotube synapse formation in culture and the switch from an immature to mature form of synaptic vesicle cycling. *J. Neurosci.* *27*, 14481–14493.
- Hoogenraad, C.C., Milstein, A.D., Ethell, I.M., Henkemeyer, M., and Sheng, M. (2005). GRIP1 controls dendrite morphogenesis by regulating EphB receptor trafficking. *Nat. Neurosci.* *8*, 906–915.
- Huang da, W., Sherman, B.T., and Lempicki, R.A. (2009). Systematic and integrative analysis of large gene lists using DAVID bioinformatics resources. *Nat. Protoc.* *4*, 44–57.
- Kapitein, L.C., Yau, K.W., and Hoogenraad, C.C. (2010). Microtubule Dynamics in Dendritic Spines. *Methods Cell Biol.* *97*, 111–132.
- Mi, H., Lazareva-Ulitsky, B., Loo, R., Kejariwal, A., Vandergriff, J., Rabkin, S., Guo, N., Muruganujan, A., Doremieux, O., Campbell, et al. (2005). The PANTHER database of protein families, subfamilies, functions and pathways. *Nucleic Acids Res.* *33*, D284–288.
- Montejo, J., Zuberi, K., Rodriguez, H., Kazi, F., Wright, G., Donaldson, S.L., Morris, Q., and Bader, G.D. (2010). GeneMANIA cytoscape plugin: Fast gene function predictions on the desktop. *Bioinformatics* *26*, 2927–2928.
- Munoz, J., Low, T.Y., Kok, Y.J., Chin, A., Frese, C.K., Ding, V., Choo, A., and Heck, A.J.R. (2011). The quantitative proteomes of human-induced pluripotent stem cells and embryonic stem cells. *Mol. Syst. Biol.* *7*, 1–13.
- Rigbolt, K.T.G., Vanselow, J.T., and Blagoev, B. (2011). GProX, a user-friendly platform for bioinformatics analysis and visualization of quantitative proteomics data. *Mol. Cell. Proteomics* *10*, O110.007450.
- Roxas, B.A., and Li, Q. (2008). Significance analysis of microarray for relative quantitation of LC/MS data in proteomics. *BMC Bioinformatics* *9*, 187.
- Shannon, P., Markiel, A., Ozier, O., Baliga, N.S., Wang, J.T., Ramage, D., Amin, N., Schwikowski, B., and Ideker, T. (2003). Cytoscape: A software Environment for integrated models of biomolecular interaction networks. *Genome Res.* *13*, 2498–2504.
- Swiech, L., Blazejczyk, M., Urbanska, M., Pietruszka, P., Dortland, B.R., Malik, A.R., Wulf, P.S., Hoogenraad, C.C., and Jaworski, J. (2011). CLIP-170 and IQGAP1 cooperatively regulate dendrite morphology. *J. Neurosci.* *31*, 4555–4568.
- Tusher, V.G., Tibshirani, R., and Chu, G. (2001). Significance analysis of microarrays applied to the ionizing radiation response. *Proc. Natl. Acad. Sci. USA* *98*, 5116–5121.

Wiśniewski, J.R., Zougman, A., Nagaraj, N., and Mann, M. (2009). Universal sample preparation method for proteome analysis. *Nat. Methods* 6, 359–362.

Yuan, B., Latek, R., Hossbach, M., Tuschl, T., and Lewitter, F. (2004). siRNA selection server: An automated siRNA oligonucleotide prediction server. *Nucleic Acids Res.* 32, W130-134.

CHAPTER 3

Regulation of KIF1A-driven Dense Core Vesicle transport: Ca^{2+} /CaM controls DCV binding and Liprin- α /TANC2 recruits DCVs to postsynaptic sites

Riccardo Stucchi^{1,2,3}, Gabriela Plucinska¹,
Jessica J.A. Hummel¹, Eitan E. Zahavi¹, Irune
Guerra San Juan¹, Oleg Klykov^{2,3}, Richard A.
Scheltema^{2,3}, A.F. Maarten Altelaar^{2,3} and
Casper C. Hoogenraad^{1,4}

Cell Reports, July 2018, 24(3):685-700

¹Cell Biology, Department of Biology, Faculty of Science, Utrecht University, Padualaan 8, 3584 Utrecht, the Netherlands

²Biomolecular Mass Spectrometry and Proteomics, Bijvoet Center for Biomolecular Research and Utrecht Institute for Pharmaceutical Sciences, Utrecht University, Padualaan 8, 3584 Utrecht, the Netherlands

³Netherlands Proteomics Centre, Padualaan 8, 3584 Utrecht, the Netherlands

ABSTRACT

Tight regulation of neuronal transport allows for cargo binding and release at specific cellular locations. The mechanisms by which motor proteins are loaded on vesicles and how cargoes are captured at appropriate sites remain unclear. To better understand how KIF1A-driven dense core vesicle (DCV) transport is regulated, we identified the KIF1A interactome and focused on three binding partners, the calcium binding protein calmodulin (CaM) and two synaptic scaffolding proteins: liprin- α and TANC2. We showed that calcium, acting via CaM, enhances KIF1A binding to DCVs and increases vesicle motility. In contrast, liprin- α and TANC2 are not part of the KIF1A-cargo complex but capture DCVs at dendritic spines. Furthermore, we found that specific TANC2 mutations, reported in patients with different neuropsychiatric disorders, abolish the interaction with KIF1A. We propose a model in which Ca^{2+} /CaM regulates cargo binding and liprin- α and TANC2 recruit KIF1A-transported vesicles.

INTRODUCTION

Kinesins and dyneins are motor proteins responsible for cargo transport and delivery along microtubule tracks. Microtubule-based cargo transport is particularly important in cells with complex geometry, such as neurons (Hirokawa et al., 2010). The neuronal transport machinery delivers proteins, lipids, mRNA, and organelles to the distal sites, as well as controlling cargo degradation and recycling of building blocks. Various cargoes that are transported along microtubules move bidirectionally, exhibiting periods of rapid movements, pauses, and directional switches. The identification of mutations in genes encoding tubulin isoforms, motor proteins, or other components of the trafficking machinery in human patients strongly supports the view that defective cargo transport can directly trigger neurodegeneration (Millecamps and Julien, 2013). It is therefore important to understand how cargo trafficking is initiated and how cargoes are captured at their final destinations. In addition, transport deficits might arise through various indirect mechanisms. For example, the stalling of vesicles could trigger the formation of aggregates within axons that may result in neuronal dysfunction.

Several molecular mechanisms related to microtubules, motors, and cargo interactions were shown to regulate cargo pick-up and delivery (Maeder et al., 2014; Schlager and Hoogenraad, 2009). On one hand, microtubule orientation, length, and spacing in axons and dendrites can control cargo sorting and transport efficiency (Kapitein et al., 2010; Yogev et al., 2016). Additional motor-microtubule mechanisms include tubulin posttranslational modifications (PTMs), microtubule-associated proteins (MAPs), and tubulin isoforms (Gumy et al., 2017; Sirajuddin et al., 2014). On the other hand, transport is regulated on the site of motor-cargo interaction through motor interaction with phospholipids, receptors or integral membrane proteins, scaffolding proteins, and small Rab guanosine triphosphatase (GTPases) and their effector proteins (Maeder et al., 2014; Schlager and Hoogenraad, 2009). Moreover, local subcellular specializations and compartmentalization of specific structures can control local cargo trafficking. For instance, the axon initial segment (AIS) functions as a cargo filter that selectively prevents passage of dendritic vesicles while allowing the entry of axonal cargoes (Leterrier and Dargent, 2014). Furthermore, evidence suggests that during transient microtubule polymerization into dendritic spines, kinesin motors transport cargoes along microtubules (MTs) into spines (Esteves da Silva et al., 2015; McVicker et al., 2016). Despite growing evidence of transport regulation, little is known about how vesicles are loaded on motors and captured at the dendritic spines.

KIF1A, named UNC-104 in *Caenorhabditis elegans* (*C. elegans*) and *Drosophila*, was identified as the primary motor protein first for synaptic vesicles (SVs) (Niwa et al., 2008; Okada et al., 1995) and later for dense core vesicles (DCVs) (Barkus et al., 2008; Lo et al., 2011; Zahn et

al., 2004). DCVs, also called secretory vesicles or post-Golgi vesicles, are transported from the Golgi apparatus to the plasma membrane in both axons and dendrites, unlike SVs (de Wit et al., 2006; Lochner et al., 2008). DCVs contain secretory proteins such as brain-derived neurotrophic factor (BDNF) and neuropeptide Y (NPY) and do not coincide with membrane protein transferrin receptor (TfR) (Lipka et al., 2016). The integral membrane protein synaptotagmin 4 (Syt4) is also present on DCVs (Dean et al., 2009). The scaffolding protein liprin- α interacts with the tail region of KIF1A (Shin et al., 2003), and liprin- α mutants in *Drosophila* impair cargo trafficking, suggesting that liprin- α is part of the KIF1A-cargo complex (Miller et al., 2005). However, in *C. elegans*, liprin- α is mainly localized to synaptic sites, and its distribution is not affected in KIF1A mutants (Sieburth et al., 2005). An additional model suggests that liprin- α can play an active role in clustering KIF1A transported SVs (Wagner et al., 2009; Wu et al., 2013). Thus, whether liprin- α is a cargo adaptor linking KIF1A to vesicles or captures KIF1A-driven cargo to synaptic sites remains an open question.

To better understand how KIF1A-driven vesicle trafficking is controlled in neurons, we performed an interactome analysis of KIF1A. Based on those results, we focused on three KIF1A binding partners, the calcium binding protein calmodulin (CaM) and two synaptic scaffolding proteins: liprin- α and TANC2 (tetratricopeptide repeat, ankyrin repeat, and coiled coil containing 2). TANC2 was originally identified as a postsynaptic density (PSD)-95-interacting protein, regulating dendritic spine and synapse function (Han et al., 2010). TANC2 gene mutations are identified in patients with neurological disorders ranging from autism to schizophrenia (de Ligt et al., 2012; Fromer et al., 2014; Iossifov et al., 2012). To gain insights into the role of these three proteins in KIF1A-mediated transport, we used a combination of live-cell imaging and biochemical-proteomic methodology. This approach allowed us to demonstrate that calcium, acting via CaM, enhances KIF1A binding to DCVs and increases vesicle motility. In addition, we show that liprin- α and TANC2 are mainly localized in dendritic spines and recruit KIF1A-driven DCVs to synaptic sites. Altogether, our findings reveal a mechanism for pick-up and delivery of DCVs in dendrites.

RESULTS

Kinesin-3 Family Member KIF1A Interacts with Liprin- α and TANC2

KIF1A contains a classical N-terminal motor domain, followed by three coiled coils, a stalk domain in the middle part, and a pleckstrin homology (PH) domain in the tail region, which in *C. elegans* is crucial for recognition of phosphatidylinositol 4,5-bisphosphate (PIP₂) in cargo vesicle membranes (Figure 1A) (Klopfenstein et al., 2002). To identify KIF1A interactome, we set up a systematic affinity purification-mass spectrometry (AP-MS) screening using different

KIF1A tail fragments (Figure 1A). BioGFP-KIF1A fragments were expressed in HEK293 cells, purified with streptavidin beads, and incubated with brain lysates. Co-isolated proteins were then analyzed by mass spectrometry (MS). Among the list of putative interacting proteins detected with this approach, we classified candidate KIF1A binding partners with a probability > 0.98 , using SAINT (Significance Analysis of INteractome) to score our AP-MS data (Figure S1A; Tables S1 and S2) (Choi et al., 2011). Most identified binding partners are associated with the stalk domain of KIF1A (amino acid 657-1105), and most of them belong to the postsynaptic density (PSD) ($7.82 = \log_{10}[\text{corrected } p \text{ value}]$ Gene Ontology [GO], cellular component) (Figures S1A and S1B). This stalk region is highly similar to MAGUK binding sites (MBSs) found in other kinesin-3 motors, such as KIF13B (Zhu et al., 2016). MBS regions mediate binding with the guanylate kinase (GK) domain, and in the case of KIF13B, MBS is required for the formation of a complex with the GK of the synaptic protein DLG1 (Hanada et al., 2000; Yamada et al., 2007). Although MBS regions are highly conserved, small amino acid sequence variations could drastically change their binding specificities for different scaffolding proteins. In line with this, our results indicate that the MBS domain of KIF1A interacts with a different group of postsynaptic scaffolds compared to KIF13B, confirming high selectivity of these domains (Figure S1A; Tables S1 and S2). As part of the interactome, we detected well-known interactors of KIF1A, such as liprin- α family proteins (Shin et al., 2003), as well as interactors such as TANC2. We observed a highly significant enrichment of TANC2 total spectral counts (Figure 1B) but not of counts for its homolog TANC1 (Figure 1C). Similarly, we found KIF1A associated only with TANC2 in our AP-MS experiment in which we immunoprecipitated TANC1 or TANC2 from rat brain extracts (Figure 1D). To validate our proteomic results, we performed affinity purification-Western blot (AP-WB) experiments in cells co-expressing bioGFP-KIF1A fragments (657-1105 and 657-1698), along with a HA-tagged version of TANC1 and TANC2. As expected, both TANC2 and liprin- α bound the KIF1A middle fragment (657-1105), but not TANC1 (Figures 1E and 1F). Surprisingly, neither TANC2 nor liprin- α was able to bind a longer KIF1A fragment including the PH domain (Figures 1E and 1F), as shown by MS data (Figure 1B; Tables S1 and S2), indicating an auto-inhibitory role of the C-terminal portion of KIF1A. As final evidence, reverse AP-WB experiments confirmed that TANC2 and liprin- α are binding partners of KIF1A (Figures 1G and 1H), and in vitro competition assays showed that TANC2 and liprin- α 2 partially compete for the same binding site on KIF1A (Figures S1C and S1D). In addition, we pinpointed their N-terminal domains as the regions mainly involved in the binding (Figures 1I and 1J; Figure S1F). We also found a potential association between TANC2 and liprin- α (Figures S1G and S1H); however, it is quite likely that the two proteins only indirectly interact by binding KIF1A within a macromolecular complex. Overall, these results identify the

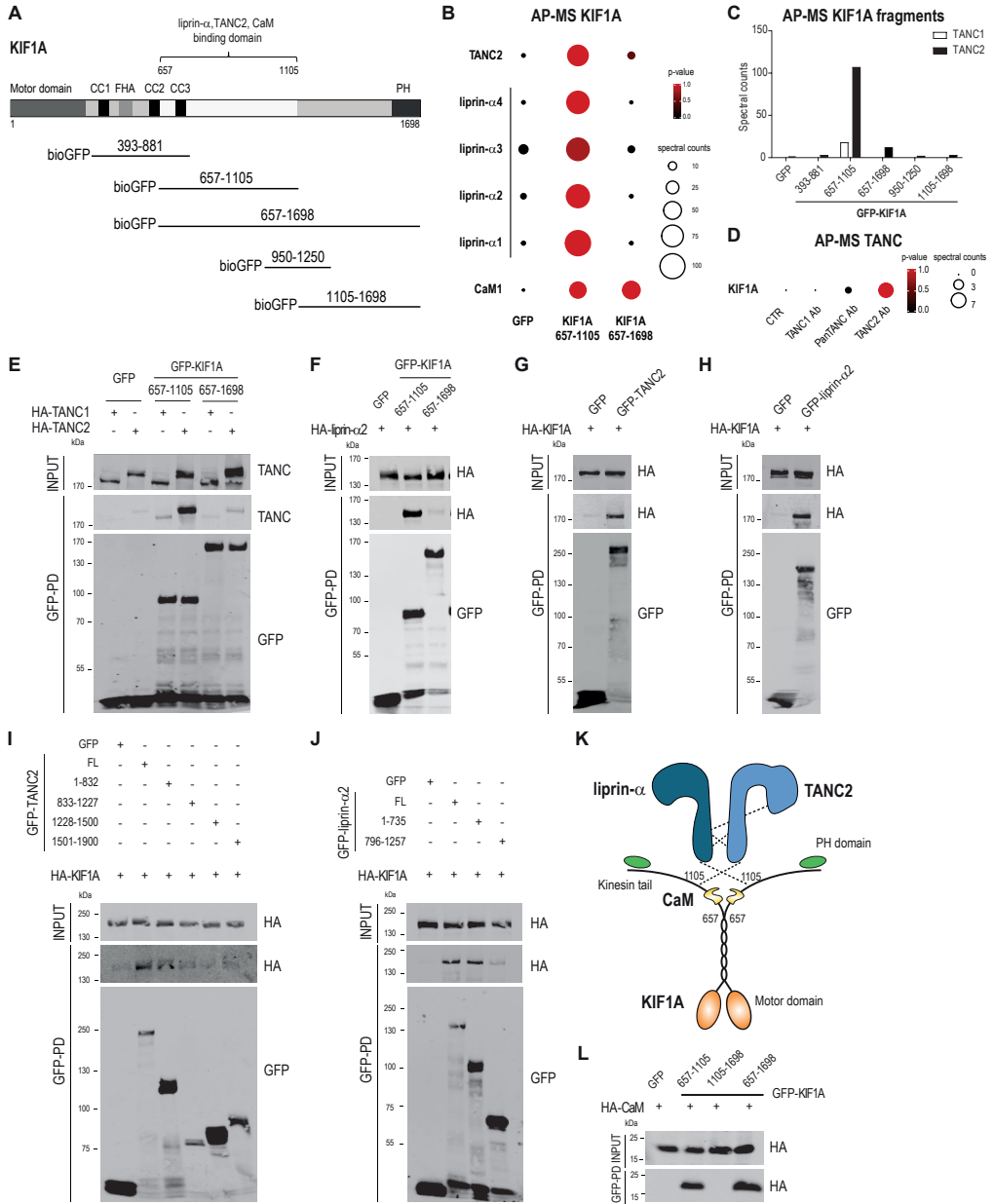


Figure 1. KIF1A Binds to TANC2, Liprin- α , and CaM

(A) bioGFP-KIF1A(383-881, 657-1105, 657-1698, 950-1250, 1105-1698) used to perform AP-MS experiments.

(B) KIF1A interactors identified by MS. p values and spectral counts are graphically represented by colors and spheres, respectively. See also Figures S1A and S1B and Tables S1 and S2.

(C) TANC1 and TANC2 spectral counts detected by MS.

(D) TANC (TANC1 Ab, PanTANC Ab, and TANC2 Ab) immunoprecipitation-MS experiments. p values and spectral counts of KIF1A are graphically represented by colors and spheres, respectively.

- (E) Western blots (WBs) of HA-TANC proteins and liprin- α 1 in AP experiments of bioGFP-KIF1A(657-1105, 657-1698) from co-transfected HEK293 cells.
- (F) WB of HA-liprin- α 2 in AP of bioGFP-KIF1A(657-1105, 657-1698).
- (G and H) WB of HA-KIF1A in AP of bioGFP-TANC2 (G) or bioGFP-liprin- α 2 (H).
- (I) WB of HA-KIF1A in AP of full-length GFP-TANC2 and GFP-TANC2 fragments (1-832, 833-1227, 1228-1500, and 1501-1900).
- (J) WB of HA-KIF1A in AP of full-length GFP-liprin- α 2 and GFP-liprin- α 2 fragments (1-735 and 796-1257).
- (K) Schematic representation of KIF1A in association with the PSD scaffolding proteins TANC2 and liprin- α 2 and with the calcium sensor CaM.
- (L) WB of HA-CaM in AP of bioGFP-KIF1A fragments (657-1105, 1105-1698, and 657-1698).

PSD proteins liprin- α and TANC2 as interactors of KIF1A (Figure 1K).

Kinesin-3 Family Member KIF1A Interacts with CaM

Among other identified candidate KIF1A interactors, we decided to further characterize the calcium regulator CaM. As suggested by the number of CaM spectra detected by MS (Figure 1B) and confirmed by subsequent AP-WB (Figure 1L), CaM is one of the few proteins capable of binding both the KIF1A middle tail region (657-1105) and the full tail (657-1698). Combined with CaM being calcium regulated, it represents an ideal modulator of KIF1A-based cargo trafficking (Figure 1K). Typically, calcium binding to the EF hands of CaM induces a conformational switch, which exposes the hydrophobic pockets present in the two lobes of CaM, allowing binding to target proteins (Zhang et al., 1995). To assess the ability of CaM to bind to KIF1A in response to calcium, we performed *in vitro* affinity purification (AP) assays using bioGFP-KIF1A fragments and HA-CaM in the presence of excessive calcium (2 mM) or EDTA (2 mM) (Wang and Schwarz, 2009). Western blot (WB) analysis revealed that the amount of CaM bound to KIF1A increased by ~50% in calcium-supplemented samples (Figures 2A and 2B), indicating a stronger association between motor protein and CaM upon calcium addition. The structure of Ca²⁺-bound CaM is flexible and dynamic, allowing it to recognize and modulate the activity of its substrates. As a consequence, the consensus sequence for CaM binding motifs is not well defined. Most Ca²⁺/CaM binding substrates can be broadly characterized by a short stretch of amino acids containing a high density of positively charged and hydrophobic residues (Yamniuk and Vogel, 2004). In search of potential CaM binding sites, we used two separate databases: the Calmodulin Target Database (<http://calcium.uhnres.utoronto.ca>) (Yap et al., 2000) and the Calmodulation Database and Meta-Analysis website (<http://cam.umassmed.edu>) (Mruk et al., 2014). This analysis revealed the existence of a conserved binding motif for CaM spanning residues 710–740 of KIF1A (Figure 2C). Therefore, we generated different KIF1A fragments of ~60 amino acids each (Figure 2C) and found that KIF1A(691-752) interacted with CaM (Figure 2D). Consequently, we made a CaM binding-deficient bioGFP-KIF1A(657-1105)

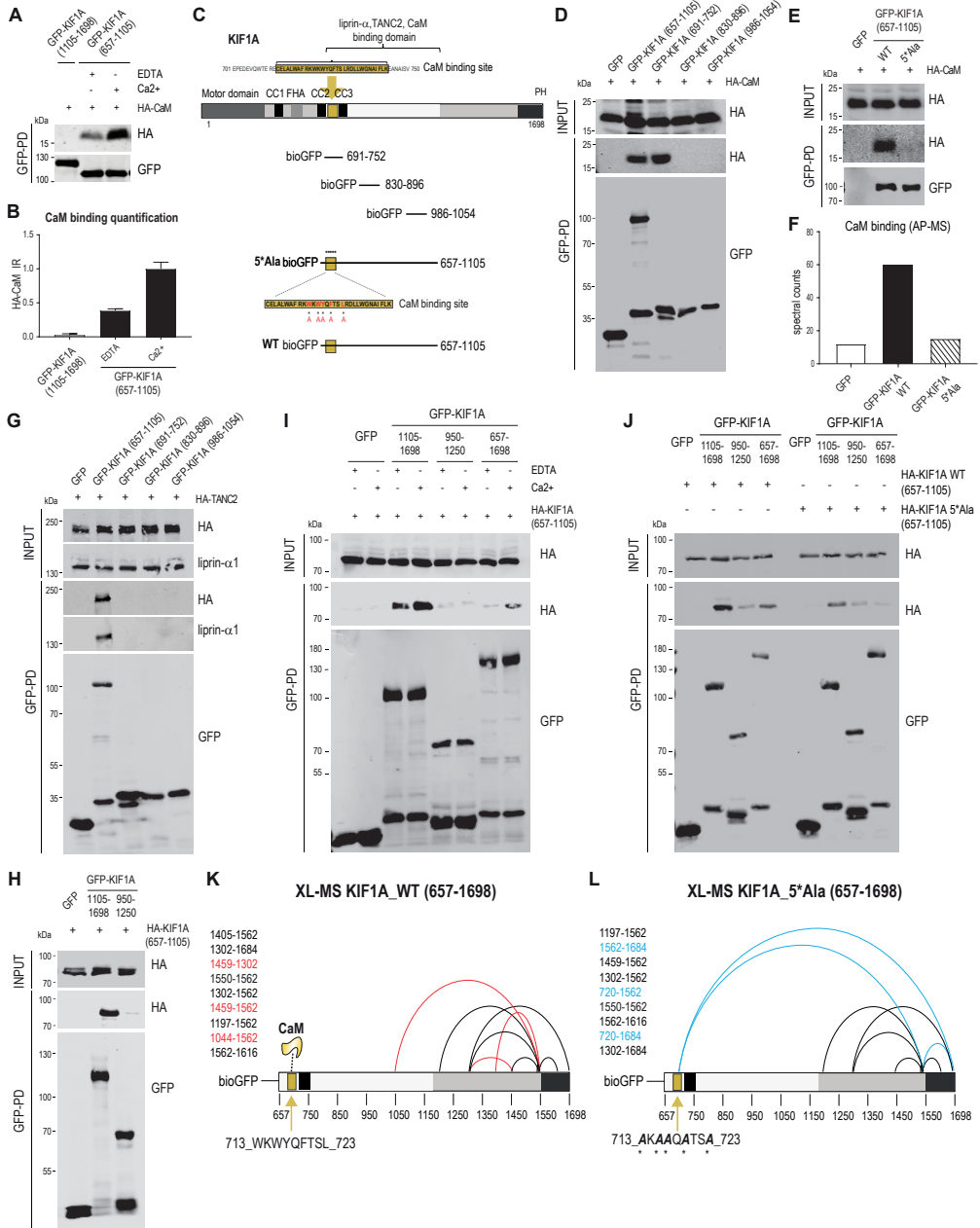


Figure 2. Ca^{2+} Promotes CaM-KIF1A Binding and Ca^{2+} /CaM Modulates KIF1A Tail Conformation

(A) bioGFP-KIF1A(657-1105) was expressed in HEK293 cells, purified using streptavidin pull-downs, and incubated with protein extracts of cells expressing HA-CaM in the presence of 2 mM EDTA or 2 mM Ca^{2+} . bioGFP-KIF1A(1105-1698) was used as negative control. Western blot detection was performed using HA and GFP antibodies. (B) Quantification of CaM relative intensities shown in (A), calculated as the ratio of HA-CaM signals normalized on the affinity-purified bioGFP-KIF1A signals. n = 3 experiments per condition. The bars show mean \pm SEM.

- (C) bioGFP-KIF1A fragments (691-752, 800-896, and 986-1054) and mutant bioGFP-KIF1A(657-1105_5*Ala) (W714A, W716A, Y717A, F719A, and L722A).
- (D) WB of HA-CaM in AP experiments of bioGFP-KIF1A truncations (657-1105, 691-752, 800-896, and 986-1054) from co-transfected HEK293 cells.
- (E) WB of HA-CaM in AP of bioGFP-KIF1A(657-1105_WT) or bioGFP-KIF1A(657-1105_5*Ala).
- (F) CaM spectral counts detected by MS in AP of bioGFP-KIF1A(657-1105_WT) or bioGFP-KIF1A(657-1105_5*Ala).
- (G) WB of HA-TANC2 and liprin- α 1 in AP of bioGFP-KIF1A(657-1105, 691-752, 800-896, 986-1054).
- (H) WB of HA-KIF1A(657-1105) in AP of bioGFP-KIF1A(1105-1698, 950-1250).
- (I) bioGFP-KIF1A(1105-1698, 950-1250, 657-1698) were incubated with protein extracts of cells expressing HA-KIF1A(657-1105) in the presence of 2 mM EDTA or 2 mM Ca^{2+} . WB detection was performed using HA and GFP antibodies. Ca^{2+} increases binding affinity between KIF1A fragments.
- (J) bioGFP-KIF1A(1105-1698, 950-1250, 657-1698) were incubated with protein extracts of cells expressing HA-KIF1A(657-1105_WT) or HA-KIF1A(657-1105_5*Ala). WB detection was performed using HA and GFP antibodies. Mutant KIF1A(657-1105_5*Ala) shows reduced binding to KIF1A C-terminal fragments compared to WT.
- (K and L) Crosslinking-mass spectrometry (XL-MS)-based analysis of purified bioGFP-KIF1A(657-1698_WT) (K) or bioGFP-KIF1A(657-1698_5*Ala) (L). Schematic maps of intra-protein crosslinks are identified. Crosslinks detected in both WT and 5*Ala are represented as black lines, WT-specific crosslinks are represented as red lines, and 5*Ala-specific crosslinks are represented as blue lines.

fragment by substituting five hydrophobic amino acids with alanine residues, as reported previously (Figure 2C) (Li and Sacks, 2003). The absence of HA-CaM signal and of CaM spectra in the bioGFP-KIF1A_5*Ala pull-downs indicates that the hydrophobic residues are required for CaM recognition (Figures 2E and 2F). Altogether, these results indicate that CaM interacts with a short KIF1A fragment (691-752), in contrast to TANC2 and liprin- α , which require the entire region (657-1105) to associate with KIF1A (Figure 2G) and do not compete with CaM for KIF1A binding (Figures S1C–S1E).

CaM Binding to KIF1A Changes Intramolecular Interactions

Next, we wanted to address the question of the loss of KIF1A binding partners in the full-length fragment. As described earlier, TANC2 and liprin- α are able to bind to KIF1A(657-1105), but not to the longer fragment KIF1A(657-1698) (Figures 1B, 1E, and 1F; Figure S1A). One possible explanation is the presence of an inhibitory mechanism caused by the intramolecular interactions. To assess this, we performed AP-WB experiments using different bioGFP-KIF1A truncations, in combination with HA-KIF1A(657-1105). We only detected binding between HA-KIF1A(657-1105) and bioGFP-KIF1A(1105-1698), confirming an intramolecular interaction between the C terminus and the middle part of the tail (Figure 2H). This interaction is regulated by Ca^{2+} /CaM binding (Figures 2I and 2J). To further characterize these intramolecular interactions, we applied crosslinking-mass spectrometry (XL-MS) to KIF1A(657-1698_WT) and mutant KIF1A(657-1698_5*Ala). We detected nine intramolecular crosslinked peptides, of which 6 peptides were shared between the two proteins (in black) (Figures 2K and 2L).

Three of those crosslinks were specific for either KIF1A-wild-type (WT) (highlighted in red) or KIF1A_5*Ala (in blue). In the KIF1A_5*Ala mutant, crucial intramolecular interactions were disturbed compared to the WT protein. In particular, crosslink 1044-1562 was not present in the absence of CaM and aberrant intramolecular crosslinks 720-1562 and 720-1684 were detected, confirming that the backfolding of the tail is governed by CaM binding.

Ca²⁺/CaM Regulates the Binding of KIF1A with DCVs

Altogether, our results highlight the importance of Ca²⁺/CaM in regulating KIF1A molecular dynamics. In the following steps, we decided to repeat our initial KIF1A AP-MS experiments in rat brain extracts, this time supplemented with either calcium or EDTA (Figures 3A–3C). The number of spectra detected for co-precipitated liprin- α and TANC2 markedly decreased in samples treated with calcium when compared to the EDTA condition (Figures 3A and 3C; Figure S2A), suggesting that calcium negatively affects the binding affinity of KIF1A for these scaffolds. Consistent with the *in vitro* AP data (Figures 2A and 2B), we detected more CaM spectra in the presence of calcium compared to the EDTA condition (Figures 3A–3C). Only in the presence of calcium KIF1A(657-1698) associated with specific DCV-related proteins such as Syt4 and synaptotagmin 11 (Syt11) (Figures 3B and 3C; Figure S2B). We obtained the same results for other proteins involved in PIP₂ and phosphoinositide metabolism (Figure 3C; Figures S2C–S2E). Based on these results, we can conclude that calcium increases the binding between KIF1A and DCVs. These proteomic findings were confirmed by *in vitro* AP-WB experiments (Figures 3D–3I). Using a CaM binding-deficient KIF1A mutant (657-1698_5*Ala), revealed a reduction in the amounts of co-precipitated Syt4 (Figure 3J) or Syt11 (Figure 3K), confirming a role for CaM in promoting the interaction between KIF1A tail and DCV proteins (Figure 3L). Our proteomic data did not allow us to derive any conclusion about SV-related proteins, because the number of spectra identified was not sufficient to show enrichment.

Based on these considerations and taking into account that KIF1A(657-1105) was found associated with proteins enriched in the PSD (Figures S1A and S1B), we decided to further investigate the role of KIF1A in DCV trafficking in dendrites. First, we assess the role of CaM in the KIF1A-DCV interaction in hippocampal neurons. To this end, we co-expressed GFP-KIF1A_WT or GFP-KIF1A_5*Ala with DCV proteins: NPY-RFP (Figures 4A and 4B) or mCherry-Syt4 (Figures 4C and 4D). KIF1A-WT co-localized with NPY and Syt4 on vesicles, whereas mutant KIF1A, which is unable to bind CaM, showed a diffuse cytoplasmic localization that did not coincide with DCVs (Figures 4A–4E). Because CaM-KIF1A binding affinity is already stimulated at low micromolar concentrations of calcium (Figures 4F and 4G) (comparable to physiological Ca²⁺ concentrations *in vivo*), we next wondered whether increasing calcium in neurons could activate KIF1A-mediated DCV transport. To test this, we increased intracellular

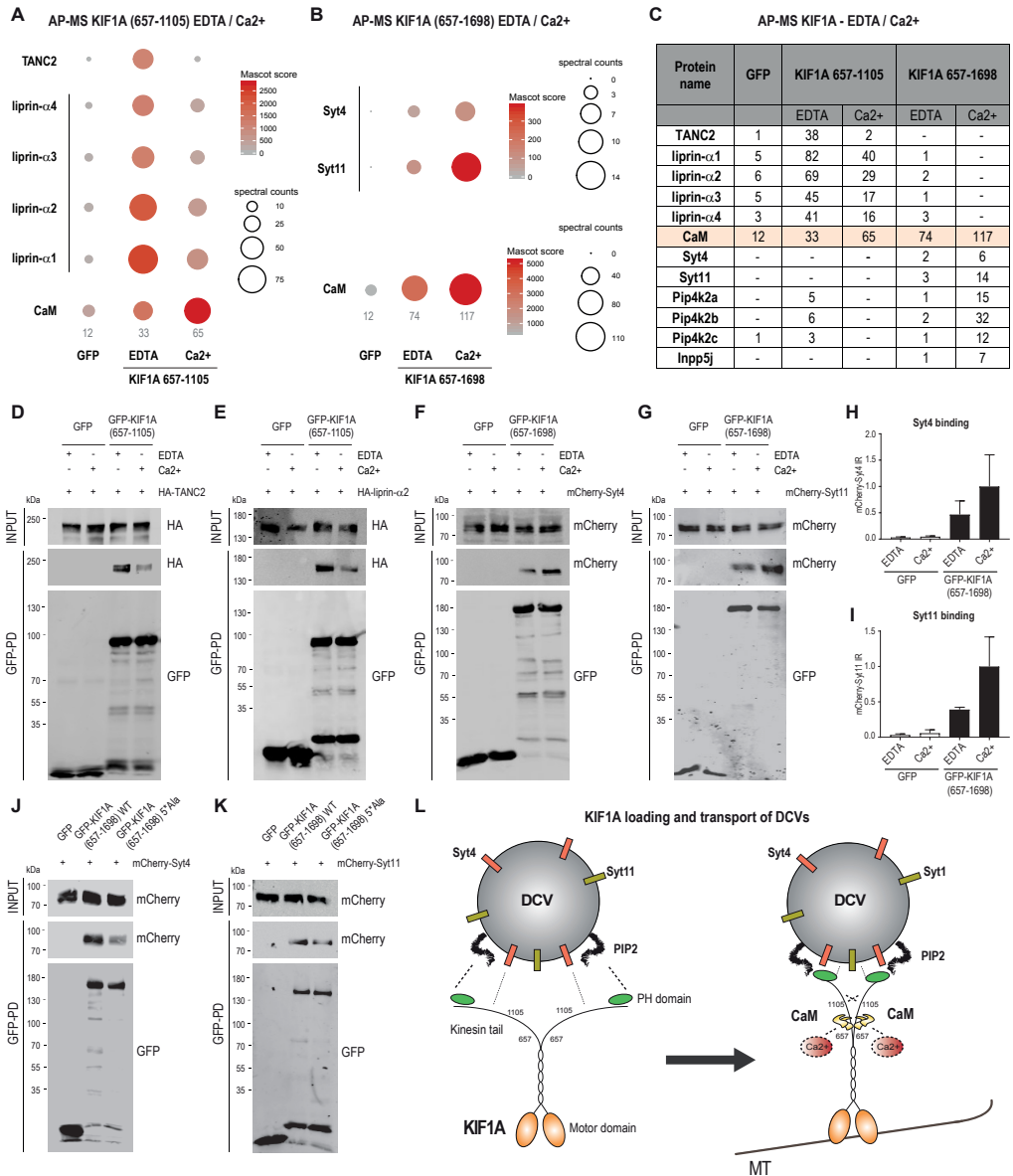


Figure 3. KIF1A Binds DCVs in a Ca²⁺/CaM-Dependent Manner

(A) bioGFP-KIF1A(657-1105) was purified using streptavidin pull-downs and incubated with rat brain extracts in the presence of 2 mM EDTA or 2 mM Ca²⁺.

KIF1A(657-1105) interactors were identified by MS. Mascot scores and spectral counts of selected proteins (TANC2, liprin-α, and CaM) are graphically represented by colors and spheres, respectively. See also (C) and Figure S2A.

(B) bioGFP-KIF1A(657-1698) was incubated with rat brain extracts in the presence of 2 mM EDTA or 2 mM Ca²⁺. KIF1A(657-1698) interactors were identified by MS. Mascot scores and spectral counts of selected proteins (Syt4, Syt11, and CaM) are graphically represented by colors and spheres, respectively. See also (C) and Figures S2B–S2E.

(C) Table represents the number of spectral counts detected in AP-MS experiments of bioGFP-KIF1A(657-1105) and

bioGFP-KIF1A(657-1698) in the presence of 2 mM EDTA or 2 mM Ca^{2+} for selected co-purified proteins: TANC2, liprin- α , calmodulin (CaM), synaptotagmin (Syt), phosphatidylinositol 5-phosphate 4-kinase (Pip4k2), and inositol polyphosphate 5-phosphatase (Inpp5).

(D and E) bioGFP-KIF1A(657-1105) was incubated with protein extracts of cells expressing HA-TANC2 (D) or HA-liprin- α 2 (E) in the presence of 2 mM EDTA or 2 mM Ca^{2+} . WB detection was performed using HA and GFP antibodies. (F and G) bioGFP-KIF1A(657-1698) was incubated with protein extracts of cells expressing mCherry-Syt4 (F) or mCherry-Syt11 (G) in the presence of 2mM EDTA or 2 mM Ca^{2+} . WB detection was performed using mCherry and GFP antibodies.

(H and I) Quantifications of Syt4 (H) and Syt11 (I) relative intensities shown in (F) and (G), calculated as the ratio of co-purified mCherry signals normalized on the bioGFP-KIF1A. $n = 3$ experiments per condition. The bars show mean \pm SEM.

(J and K) bioGFP-KIF1A(657-1698_WT) or bioGFP-KIF1A(657-1698_5*Ala) was incubated with protein extracts of cells expressing mCherry-Syt4 (J) or mCherry-Syt11 (K). WB detection was performed using mCherry and GFP antibodies.

(L) Schematic model illustrating the Ca^{2+} /CaM mechanism acting on the KIF1A tail, leading to DCV loading and mobilization.

concentration of calcium by treating neurons with bicuculline, which acutely enhances neuronal activity by inhibiting g-aminobutyric acid (GABA) receptor activity. Bicuculline induced clustering of KIF1A and increased motility of KIF1A-NPY complexes within minutes (Figures 4H–4M). In addition, we examined the effect of calcium deprivation (BAPTA-AM treatment) on DCV motility, and BAPTA-AM-treated neurons showed lower motility of KIF1A, NPY, and Syt4 vesicles (Figures 4N–4P). These data strongly support a role for calcium in the regulation of KIF1A-DCV loading and motility in neurons. Altogether, these results indicate that binding of Ca^{2+} /CaM to the KIF1A tail regulates DCV pick-up and trafficking (Figure 3L).

KIF1A-Mediated DCV Trafficking Is Independent of TANC2 and Liprin- α

Next, we were interested whether KIF1A, TANC2, and/or liprin- α can also control DCV motility. We first systematically quantified the co-localization of KIF1A with DCV markers (NPY, Syt4, and Syt11) in hippocampal neurons (Figure 5A; Figures S3A and S3B). KIF1A showed $\sim 50\%$ co-localization with NPY-, Syt4-, and Syt11-positive vesicles (Figures 5B and 5C). Next, we tested whether NPY and synaptotagmins label the same DCV population. Only 10% of the NPY-positive vesicles coincided with Syt4 or Syt11 (Figures 5D–5F; Figures S3C and S3D). In contrast, Syt4 and Syt11 showed $\sim 70\%$ co-localization (Figures 5G–5I; Figures S3E and S3F), indicating that NPY and synaptotagmins label different subpopulations of DCVs. Second, using live-cell imaging, we assessed whether NPY and DCVs are transported by KIF1A. Kymographs of those recordings showed robust co-movement of GFP-KIF1A and NPY-RFP, as well as mCherry-Syt4-labeled vesicles (Figures 5J and 5K). Next, we tested the effect of KIF1A knockdown on NPY or Syt4 vesicle motility. DCV motility was severely affected in neurons depleted of KIF1A, with $\sim 50\%$ reduction of mobile NPY-GFP- or Syt4-Cherry-positive

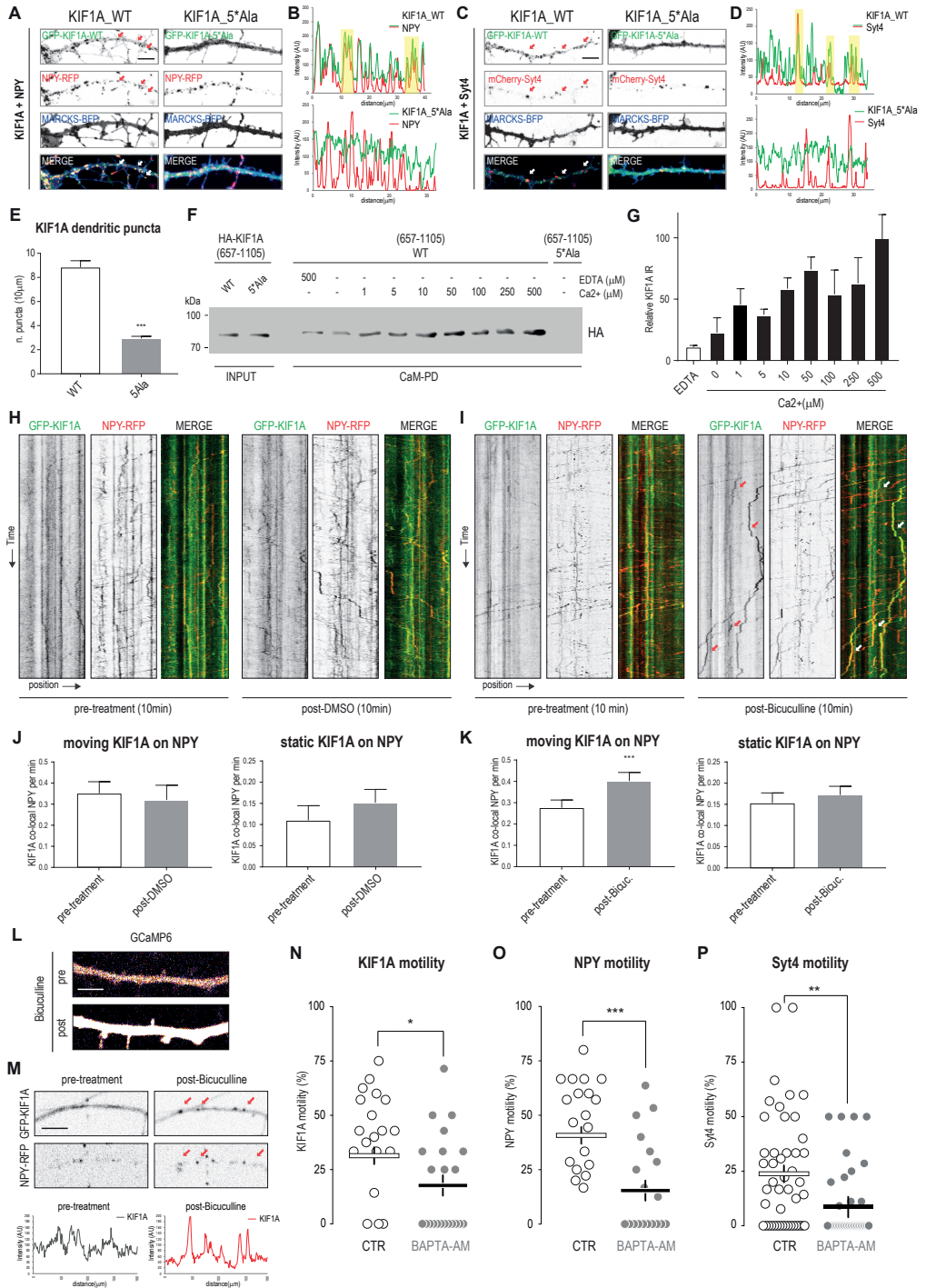


Figure 4. KIF1A-Driven DCVs Transport Is Regulated by Ca²⁺/CaM

- (A) Representative dendrites of rat hippocampal neurons (11–14 DIV) co-transfected with GFP-KIF1A_WT or GFP-KIF1A_5*Ala (green) with NPY-RFP (red). Arrows point to co-localizing puncta. Scale bar, 5 μ m.
- (B) Line scans of fluorescence intensity of GFP-KIF1A and NPY-RFP channels shown in (A).
- (C) Dendrites of neurons co-transfected with GFP-KIF1A_WT or GFP-KIF1A_5*Ala (green) with mCherry-Syt4 (red). Arrows point to co-localizing puncta. Scale bar, 5 μ m.
- (D) Line scans of fluorescence intensity of GFP-KIF1A and mCherry-Syt4 channels shown in (C).
- (E) Quantifications of GFP-KIF1A_WT and GFP-KIF1A_5*Ala puncta in dendrites. The bars show mean \pm SEM (n = 20–28 dendrites; ***p < 0.001, t test).
- (F) Ca²⁺ dependence of the *in vitro* binding of CaM to KIF1A. AP of CaM (anti-CaM beads) from lysates of cells transfected with HA-KIF1A(657-1105_WT) or HA-KIF1A(657-1105_5*Ala). WB detection was performed using anti-HA antibody.
- (G) Quantification of KIF1A binding to CaM shown in (F). The percentage of maximal binding to CaM was defined as the intensity of the co-precipitated band of KIF1A and set at 100% in 2 mM Ca²⁺. n = 3 experiments per condition. The bars show mean \pm SEM.
- (H and I) Representative kymographs showing trajectories of GFP-KIF1A and NPY-RFP vesicles in selected neurites of co-transfected neurons pre- and post-treatment with DMSO (H) or with 40 μ M of bicuculline (I).
- (J and K) Quantifications of trajectories of GFP-KIF1A co-localizing with NPY-RFP (see H and I) pre- and post-treatment with DMSO (J) or with bicuculline (K). The bars show mean \pm SEM (n = 12 dendrites in J and n = 34 dendrites in K; ***p < 0.001, paired t test).
- (L) Intracellular calcium levels in a representative dendrite treated with bicuculline and visualized with the calcium indicator GCaMP6. Scale bar, 5 μ m.
- (M) GFP-KIF1A clustering in a representative dendrite treated with bicuculline. Scale bar, 5 μ m.
- (N–P) Quantifications of the percentage of mobile GFP-KIF1A (N), NPY-GFP vesicles (O), or mCherry-Syt4 vesicles (P) in neurons (11–14 DIV) treated with DMSO (CTR) or 10 μ M of BAPTA-AM. Bars show the mean (n = 21–29 dendrites in N, n = 20–28 dendrites in O, and n = 41–50 dendrites in P; *p < 0.05, **p < 0.001, ***p < 0.001, t test).

vesicles compared to pSuper control (Figures 5L–5O). We confirmed the specificity of this result with a rescue experiment in which expression of full-length KIF1A (but not of KIF1A lacking the C-terminal PH domain) restored NPY motility (Figure 5M). These data are in line with a previously described role for KIF1A in transporting DCVs (Arthur et al., 2010; Lipka et al., 2016; Lo et al., 2011; McVicker et al., 2016).

Finally, we assessed whether the depletion of TANC2 and/or liprin- α also affects DCV motility. We used previously described short hairpin RNAs (shRNAs) targeting liprin- α (Spangler et al., 2013) and generated TANC2-specific shRNAs, whose efficacy was tested by quantifying the intensity of the staining of endogenous TANC2 in neurons (Figures S3G–S3I). TANC2 or liprin- α knockdowns did not influence DCV motility, as shown by live-cell imaging of NPY or Syt4 (Figures 5N and 5O). In addition, other transport parameters, such as pausing frequency and duration, were not affected by this treatment (Figures S3J–S3L). These data suggest that TANC2 and liprin- α are not part of the KIF1A-DCV transport complex and do not work as classical cargo-adaptor proteins.

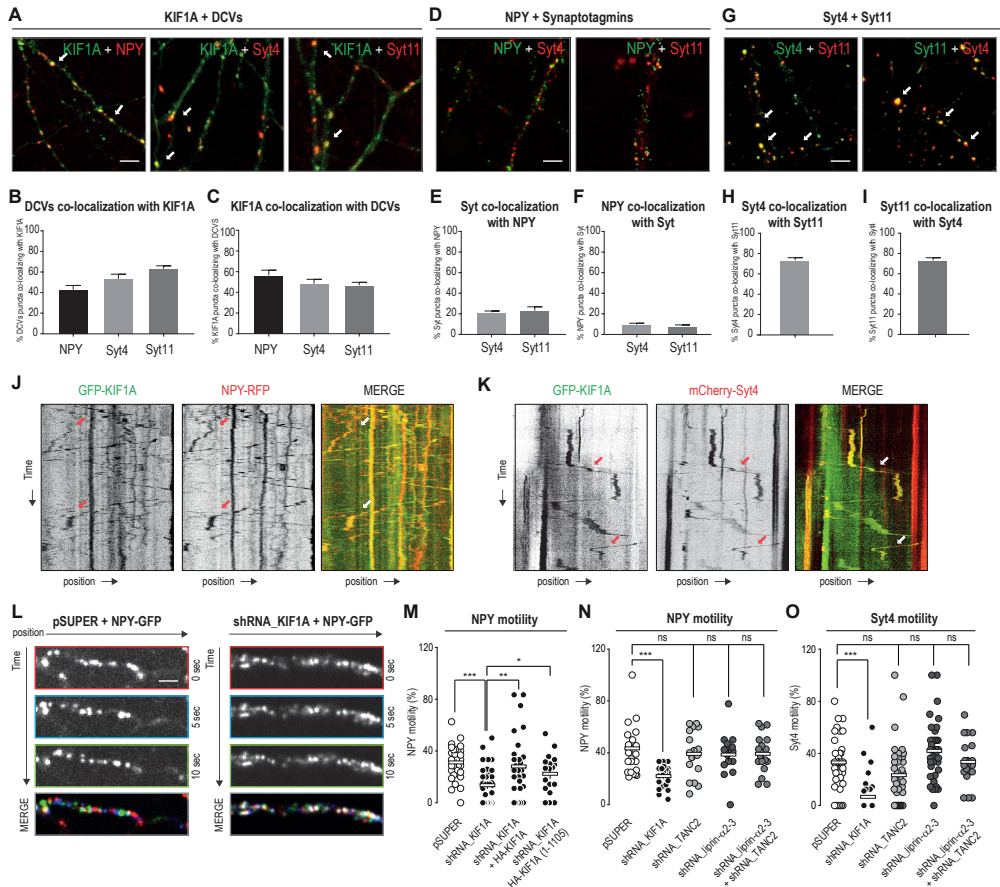


Figure 5. DCV Dendritic Trafficking Is KIF1A Dependent and TANC2/Liprin- α Independent

(A) Neurons (11–14 DIV) co-transfected with GFP-KIF1A (green), in combination with NPY-RFP, mCherry-Syt4, or mCherry-Syt11 (red). Arrows point to co-localizing puncta. Scale bar, 5 μ m. See also Figures S3A and S3B.

(B and C) Percentage of co-localizing puncta between DCV proteins and KIF1A (B), and vice versa (C). The bars show mean \pm SEM (n = 19–23 dendrites).

(D) NPY-GFP (green), in combination with mCherry-Syt4 or mCherry-Syt11 (red). Scale bar, 5 μ m. See also Figures S3C and S3D.

(E and F) Co-localizing puncta between NPY and Syt4 or Syt11 (E), and vice versa (F). The bars show mean \pm SEM (n = 21–31 dendrites).

(G) Phluorin-Syt4 (green) with mCherry-Syt11 (red) or Phluorin-Syt11 (green) with mCherry-Syt4 (red). Arrows point to co-localizing puncta. Scale bar, 5 μ m. See also Figures S3E and S3F.

(H and I) Co-localizing puncta between Syt4 and Syt11 (H), and vice versa (I). The bars show mean \pm SEM (n = 20–27 dendrites).

(J and K) Representative kymographs showing trajectories of NPY-RFP vesicles (J) or mCherry-Syt4 vesicles (K) (red) moving with GFP-KIF1A (green).

(L) Representative images acquired at 10s intervals showing NPY-GFP motility in dendrites of neurons transfected with pSuper (right) or shRNA_KIF1A (left). In the merged images, red corresponds to 0s, blue corresponds to 10s, and green corresponds to 20s. Scale bar, 5 μ m.

(M) Quantification of the percentage of mobile NPY vesicles in neurons (11–14 DIV) co-transfected with NPY-GFP, in combination with pSuper, shRNA_KIF1A, shRNA_KIF1A + FL-HA-KIF1A, or shRNA_KIF1A + HA-KIF1A(1-1105). The bars show mean (n = 18–32 dendrites; *p < 0.05, **p < 0.001, ***p < 0.001, t test).

(N and O) Quantification of the percentage of mobile DCVs in neurons (11–14 DIV) co-transfected with NPY-GFP (N) or mCherry-Syt4 (O), in combination with pSuper, shRNA_KIF1A, shRNA_TANC2, shRNA_liprin- α 2-3, or shRNA_liprin- α 2-3 + shRNA_TANC2. The bars show mean (n = 17–58 dendrites in N and n = 17–39 dendrites in O; ***p < 0.001, t test). See also Figures S3J–S3L.

TANC2 and Liprin- α Are Scaffolding Proteins in Dendritic Spines

To better understand the roles of TANC2 and liprin- α in KIF1A-dependent cargo trafficking, we investigated their distribution in neurons. Both proteins localized in dendrites (Figure 6A), were enriched in dendritic protrusions, and co-localized with the postsynaptic markers PSD-95 and Homer (Figures 6B–6D). When co-expressed, TANC2 and liprin- α co-clustered in dendritic spines (Figure 6E). Analysis of the truncated isoforms revealed that the C-terminal part of TANC2 (1501-1900), which includes the PDZ binding domain, is responsible for the synaptic localization (Figure S4A). In contrast, for liprin- α , the N-terminal part (1-735) is required for the synaptic localization (Figure S4B). We followed those observations and characterized the interactomes of TANC2 and liprin- α (Tables S3 and S4). Based on this analysis, we identified postsynaptic density proteins (GO classification, cellular component), such as PSD-95(DLG4), SAP-97(DLG1), CASK, Scribble, Centaurin gamma 2 and 3 (AGAP1 and AGAP3), and various subunits of the NMDA receptor (Grin1 and Grin2B), as the main interactors of TANC2 (Figure S4C; Table S3). These results are in line with previous findings that describe TANC2 as a synaptic scaffold, interacting and co-localizing with the synaptic anchoring proteins PSD-95 and Homer (Han et al., 2010) and with other PDZ domain proteins (Gasparini et al., 2017). Among the interacting partners of liprin- α 2, we picked up both postsynaptic (Grip1, Grip2, Lin7, Trio, and CASK) (Wyszynski et al., 2002) and pre-synaptic proteins (Rims1/2, ERC1/2, and Munc13-1/2) involved in the maturation, docking and secretion of SVs and known to form macromolecular protein complexes with liprin- α in the axonal active zone (Figure S4D; Table S4) (Olsen et al., 2005; Spangler et al., 2013). Altogether, we can conclude that TANC2 and liprin- α are enriched in dendritic spines and interact with various synaptic proteins.

TANC2, KIF1A, and Liprin- α Depletion Affects Spine Density and Morphology

Spine morphology is largely controlled by actin dynamics. Identifying TANC2 and liprin- α as enriched in dendritic spines led us to speculate that their distribution and accumulation may also be regulated by actin. Therefore, we transfected neurons with GFP-TANC2 or GFP-liprin- α 2 and treated them with either latrunculin B to depolymerize the actin cytoskeleton or jasplakinolide to stabilize actin (Figures S4E and S4F). Latrunculin B treatment reduced the

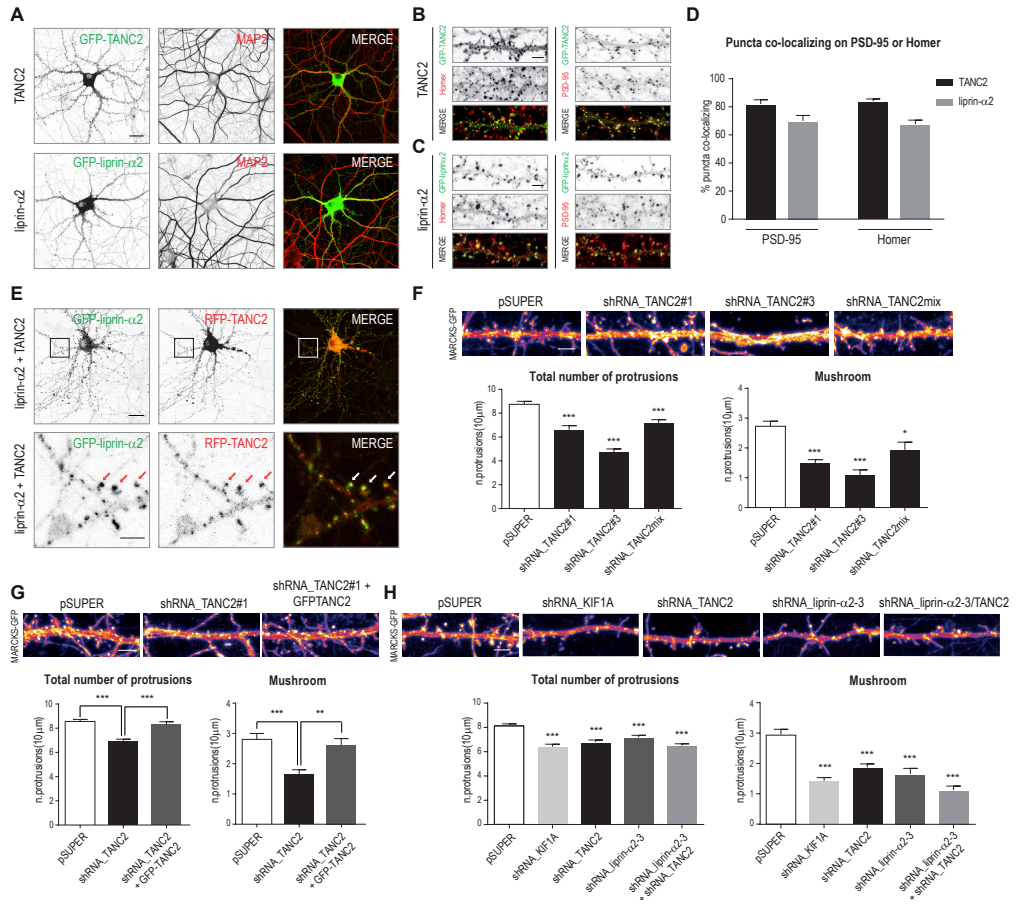


Figure 6. TANC2 and Liprin- α 2 Are PSD Scaffolds that Localize in Dendritic Spines

(A) Hippocampal neurons (11–14 DIV) transfected with GFP-TANC2 or GFP-liprin- α 2 (green) and stained for MAP2 (red). Scale bar, 20 μ m.

(B and C) GFP-TANC2 (B) or GFP-liprin- α 2 (C) (green) co-localization with Homer and PSD-95 (red) in dendritic spines. Scale bar, 5 μ m.

(D) Quantifications corresponding to the percentage of GFP-TANC2 (B) or GFP-liprin- α 2 (C) puncta co-localizing with PSD-95 or Homer. The bars show mean \pm SEM ($n = 24$ –36 dendrites).

(E) Neurons co-expressing GFP-liprin- α 2 and RFP-TANC2. Scale bar, 20 μ m. Bottom panels correspond to higher magnification showing TANC2 and liprin- α 2 co-localization in dendritic spines. Arrows point to co-localizing puncta. Scale bar, 5 μ m.

(F) Dendritic protrusions of pSuper or TANC2-KD (knockdown) neurons (shRNA_TANC2#1, shRNA_TANC2#3, and shRNA_TANC2mix) co-transfected with MARCKS-GFP to visualize membrane morphology. Scale bar, 5 μ m. Graphs show quantifications of protrusion density (number of protrusions per 10 μ m) for total number of protrusions (left) or mushroom-shaped protrusions (right). The bars show mean \pm SEM ($n = 30$ –33 dendrites; * $p < 0.05$, *** $p < 0.001$, t test).

(G) Dendritic protrusions in neurons co-transfected with pSuper, shRNA_TANC2#1, or shRNA_TANC2#1 + GFP-TANC2, in combination with MARCKS-GFP. Scale bar, 5 μ m. The bars show mean \pm SEM ($n = 54$ –75 dendrites, ** $p < 0.01$, *** $p < 0.001$, t test).

(H) Dendritic protrusions in neurons transfected with pSuper, shRNA_KIF1A, shRNA_TANC2, shRNA_liprin- α 2-3, or shRNA_liprin- α 2-3 + shRNA_TANC2, together with MARCKS-GFP. Scale bar, 5 μ m. The bars show mean \pm SEM ($n = 30\text{--}36$ dendrites, *** $p < 0.001$, t test).

number of TANC2 and liprin- α 2 clusters in spines by $\sim 30\%$, whereas jasplakinolide treatment resulted in an opposite phenotype, with $\sim 30\%$ increase of clusters in spines (Figures S4G and S4H). These data suggest that the localization and clustering of TANC2 and liprin- α 2 are affected by the actin cytoskeleton in dendritic spines. This hypothesis is strengthened by the ability of several TANC2- and liprin- α -interacting proteins to directly or indirectly associate with the actin cytoskeleton (Figure S4I). To get further insights into the roles of TANC2, KIF1A and liprin- α in dendritic spine morphology, we performed knockdown experiments. TANC2 depletion caused a significant reduction in the total number of protrusions, particularly of mushroom spines (Figure 6F), and the effect was rescued by re-introducing full-length TANC2 (Figure 6F). KIF1A and liprin- α depletion showed a similar phenotype, severely affecting the total number of dendritic protrusions (Figure 6H). These data are consistent with previous findings (Han et al., 2010; McVicker et al., 2016) and show that TANC2, KIF1A, and liprin- α depletion affects spine number and morphology.

TANC2 and Liprin- α 2 Act as Immobile Postsynaptic Posts Able to Recruit KIF1A in a Subset of Dendritic Spines

Based on the preceding results, we further examined the functional relationship between KIF1A and TANC2 or liprin- α in dendritic spines. Co-expression of HA-KIF1A with GFP-TANC2 or GFP-liprin- α 2 showed that $\sim 10\%$ KIF1A-FL co-clustered with TANC2 and liprin- α 2 in dendritic spines (Figure 7A). In contrast, KIF1A(1-1105), lacking the PH domain but containing the TANC2 and liprin- α binding region, showed a rather diffuse cytoplasmic pattern (Figure 7B). Nevertheless, we noticed accumulation of KIF1A(1-1105) in dendritic spines that co-localized with TANC2 and liprin- α 2 (Figure 7B), suggesting that KIF1A can co-localize with TANC2 and liprin- α 2 in spines even without cargo binding. This effect was exacerbated when these proteins were expressed in COS7 cells (Figures S5A–S5F). Because KIF1A is a motor protein, we next examined the spatial and temporal dynamics of KIF1A, DCVs (by imaging NPY and Syt4), TANC2, and liprin- α . As we described earlier, KIF1A-, NPY-, and Syt4-positive vesicles showed high motility along the dendritic shaft. This was not the case for TANC2 and liprin- α , which were relatively static in dendritic spines (Figures 7C–7E). This finding supports our claim that TANC2 and liprin- α are not part of the KIF1A-DCV transport complex. Closer analysis of the vesicle dynamics revealed that DCVs frequently paused and stopped near TANC2- or liprin- α -positive clusters (Figures 7C–7E) and the number of DCV pauses at TANC2/liprin- α 2 clusters

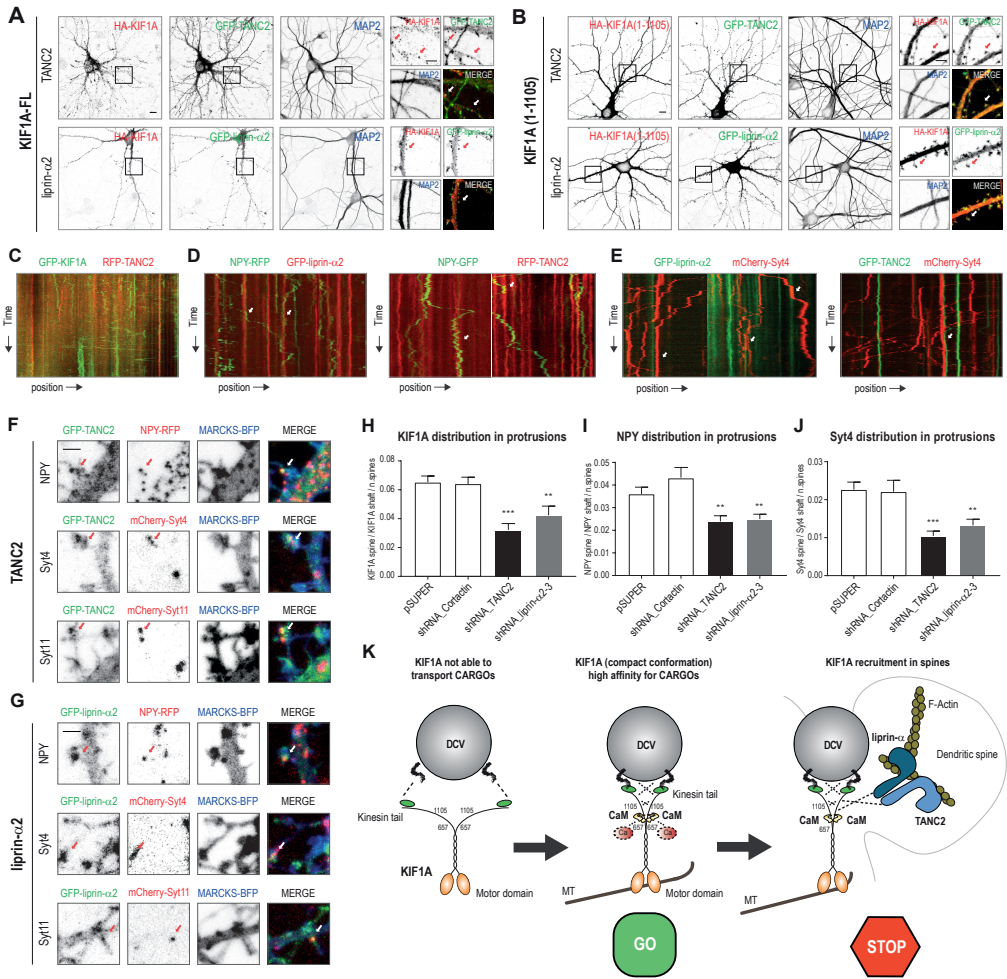


Figure 7. TANC2 and Liprin-α Recruit KIF1A-Driven DCVs in Dendritic Spines

(A and B) Neurons co-expressing GFP-TANC2 or GFP-liprin-α2 (green), in combination with HA-KIF1A (A) or HA-KIF1A(1-1105) (B) (red) and stained for MAP2 (blue). Scale bar, 10 μm. Panels on the right correspond to higher magnifications showing dendritic TANC2 and liprin-α2 puncta co-localizing with KIF1A. Scale bar, 5 μm.

(C) Kymographs showing trajectories of GFP-KIF1A and RFP-TANC2 in a selected dendritic region of transfected hippocampal neurons (11–14 DIV).

(D) Trajectories of NPY-RFP (green) vesicles pausing at GFP-liprin-α2 (red) clusters (left panel); trajectories of NPY-GFP (green) vesicles pausing at RFP-TANC2 (red) clusters (right panel).

(E) mCherry-Syt4 (red) vesicles pausing at GFP-liprin-α2 (green) clusters (left panel) or at GFP-TANC2 (green) clusters (right panel).

(F and G) GFP-TANC2 (F) or GFP-liprin-α2 (G) co-localizing with NPY-RFP, mCherry-Syt4, or mCherry-Syt11 puncta in dendritic protrusions visualized with MARCKS-BFP. Scale bar, 2 μm.

(H–J) Quantifications showing the percentage of GFP-KIF1A (H), NPY-GFP (I), and mCherry-Syt4 (J) puncta in dendritic protrusions, measured in neurons transfected with pSuper, shRNA_Cortactin, shRNA_TANC2, and shRNA_liprin-α2-3 (11–14 DIV) and filled with MARCKS-BFP. The bars show mean ± SEM (n = 30–57 dendrites in H, n =

35–71 dendrites in I, and $n = 43$ –90 dendrites in J; * $p < 0.05$, ** $p < 0.01$, *** $p < 0.001$, t test).

(K) Hypothetical model of KIF1A-dependent transport of DCVs in dendritic spines. KIF1A, in low Ca^{2+} , is in an auto-inhibited conformation, unable to efficiently bind any cargo. In the presence of high Ca^{2+} , KIF1A interacts with CaM, resulting in a conformational change of its C-terminal tail. Upon Ca^{2+} /CaM binding, KIF1A is activated, allowing for DCV loading and motility. KIF1A-driven DCVs are recruited in dendritic spines by liprin- α and TANC2, which ensure a precise mechanism of synaptic tagging for the vesicles.

was higher in mature neurons (17 days in vitro [DIV]) in which TANC2 and liprin- $\alpha 2$ were more accumulated in spines (Figures S5G–S5K). We also found DCV accumulation in dendritic spines, and in ~10% of the spines, DCVs co-localized with TANC2 and liprin- $\alpha 2$ (Figures 7F and 7G). To gain additional functional insight, we analyzed the distribution of DCVs in TANC2- or liprin- α -depleted neurons. TANC2 and liprin- α knockdown, but not Cortactin knockdown, caused a reduction of KIF1A, NPY, and Syt4 clusters in spines by ~40% compared to control (Figures 7H–7J). Based on these results, we propose that TANC2 and liprin- α recruit KIF1A-driven DCVs to dendritic spines (Figure 7K).

TANC2 Disease Mutations Abolish the Interaction with KIF1A and Affect KIF1A-DCV Recruitment

The preceding findings on the role of TANC2 in DCV transport turned our interest into potential consequences for neuronal dysfunction. TANC2 gene mutations R760C and R1066X (nonsense mutation) were found in patients with intellectual disorders and autism spectrum disorder, respectively (de Ligt et al., 2012; Iossifov et al., 2012). In the last part, we wanted to test whether those mutants may be affecting TANC2 localization to dendritic spines and/or its ability to bind KIF1A. While the localization of TANC2-R760C was similar to the WT TANC2, TANC2-R1066X failed to accumulate at the dendritic spines (Figures S6A and S6B). These results are in agreement with an important role of the C-terminal PDZ binding domain for TANC2 synaptic localization (Figure S4A). Furthermore, AP-WB experiments revealed strongly reduced binding between both TANC2 mutants and KIF1A (Figure S6C). To directly assess the effect of TANC2 point mutation (R760C) on KIF1A and DCV transport, we next produced chimeric proteins, which are the result of the fusion between NF186 (Neurofascin) and TANC2(1-832_WT) or TANC2(1-832_R760C). As expected, both Neurofascin-fusion proteins mis-accumulate TANC2 at the AIS (Figures S6D and S6E). Neurons co-expressing a WT TANC2 chimera showed reduced run length (Figure S6F), speed (Figure S6G), and run duration (Figure S6H) of anterograde-transported DCVs at the AIS compared to a control NF186, whereas in the presence of a mutant R760C, DCV motility was not affected (Figures S6F–S6H). These data suggest that a single point mutation (within the N-terminal part of TANC2) found in patients with intellectual disorders, apart from being detrimental for binding

with KIF1A (Figure S6C), drastically impairs the recruitment of KIF1A-transported vesicles in neurons. Altogether, these data suggest that the aberrant localization, the abolished interaction with KIF1A, and the deficient recruitment of KIF1A-driven vesicles of TANC2 mutants may contribute to the underlying molecular mechanisms that lead to neurological defects observed in patients.

DISCUSSION

Ca²⁺/CaM Interacts with KIF1A and Allows DCV Binding and Motility

In neurons, calcium is a regulatory factor for multiple elements of the trafficking machinery. Calcium and calcium-activated proteins control motor protein processivity and motor-cargo binding (Hirokawa et al., 2010; Schlager and Hoogenraad, 2009). For example, Ca²⁺/CaM allows activation of actin-based motors, such as myosin Va (Krementsov et al., 2004), myosin VI (Batters et al., 2016), and myosin 1C (Lu et al., 2015). In those cases, calcium is required for an initial activation of the myosin motor protein, allowing the transition from a backfolded conformation to an active status. Another example is the activation of Ca²⁺/CaM-dependent protein kinase II (CaMKII) by calcium, which in turn phosphorylates KIF17, leading to the release of NMDA receptor- containing vesicles (Guillaud et al., 2008). Finally, the regulation of mitochondrial trafficking depends on calcium. Upon calcium binding, the adaptor protein Miro interacts with the motor domain of KIF5 motors, thereby preventing its microtubule interaction and inhibiting the transport of mitochondria (Macaskill et al., 2009; Wang and Schwarz, 2009). Similar to this mechanism, cytoplasmic KIF1A is in an auto-inhibited state and becomes active only upon cargo binding (Hammond et al., 2009; Niwa et al., 2016). In this study, we were able to decipher the role of calcium in KIF1A-dependent vesicle trafficking. We show that Ca²⁺/CaM-dependent modulation on KIF1A allows for binding to vesicular cargo. Our results indicate that at low calcium concentrations, the tail domain of KIF1A does not bind to vesicular cargo, whereas at high calcium concentrations, CaM binds KIF1A, allowing for subsequent DCV motility. Thus, we propose a mechanism in which Ca²⁺/CaM regulates the loading of DCVs. This model potentially represents a more general paradigm for other kinesins and cargoes in response to calcium. For example, KIF1B β contains a predicted CaM binding site in a highly conserved region and therefore could undergo similar Ca²⁺/CaM-dependent dynamics.

TANC2 and Liprin- α Capture KIF1A-Driven DCVs

Syt4 is present on DCVs and is transported by KIF1A along microtubules in the dendritic shaft (Arthur et al., 2010). Microtubule entry into dendritic spines was proposed as a mechanism of local delivery of KIF1A-mediated DCVs (McVicker et al., 2016). Our data point to two

scaffolding proteins, TANC2 and liprin- α , present in dendritic spines as important players in the mechanism behind KIF1A-transported DCV capture. First, TANC2 and liprin- α bind the stalk domain of KIF1A. Second, they are stably present in dendritic spines while not being part of the KIF1A-cargo complex. Third, although TANC2 and liprin- α do not directly affect the motility of KIF1A-transported DCVs, they influence the cargo distribution in dendritic spines. Based on those points, we speculate that TANC2 and liprin- α , interacting with KIF1A, are able to stop and capture KIF1A-bound DCVs upon dendritic spine entry. In this model, TANC2 and liprin- α act as local signposts tethering KIF1A-transported DCVs. Consistent with our model, neurons lacking KIF1A show spine morphology defects, which can be directly caused by an altered transport of DCVs within the dendritic spines. In this study, we focused on KIF1A-dependent DCV transport in dendrites; however, the same general principles might be applied to the transport of SVs in the axonal compartment. Similar mechanisms have been described at the pre-synaptic axonal boutons, where static clusters of liprin- α can capture KIF1A-transported SVs (Olsen et al., 2005; Wu et al., 2013, 2016) or where actin pre-synaptic pools locally recruit DCVs (Bharat et al., 2017). Based on our biochemical results, DCV recruitment is favored by low calcium concentrations, thereby working as an opposing mechanism counteracting the Ca^{2+} /CaM-induced DCV mobility. Myosin motors may play an additional role in trafficking DCVs into spines. Specifically, it was proposed that myosin V modulates DCV transport and delivery (Bittins et al., 2010) and myosin V activity is regulated by a similar Ca^{2+} /CaM mechanism (Lu et al., 2006; Nguyen and Higuchi, 2005). Thus, local Ca^{2+} concentrations have an important role in the modulation of DCV trafficking and delivery in and out of dendritic spines.

In summary, we propose that Ca^{2+} /CaM regulates cargo pick-up and scaffolding proteins liprin- α and TANC2 recruit KIF1A-driven DCVs into spines. Our findings reveal a potential general mechanism that depends on two basic elements: calcium to load motors to cargo and specific signposts to unload cargo. Given that alterations in cargo trafficking pathways were described in several neurological diseases, our findings that some TANC2 disease mutants do not interact with KIF1A are bringing to light additional molecular targets to investigate the trafficking machinery in neuropathological disease models.

EXPERIMENTAL PROCEDURES

Animals

All experiments were approved by the DEC Dutch Animal Experiments Committee (Dier Experimenten Commissie), performed in line with institutional guidelines of Utrecht University and were conducted in agreement with Dutch law (Wet op de Dierproeven, 1996) and European regulations (Directive 2010/63/EU). For details see Supplemental Experimental Procedures. Female pregnant Wistar rats were obtained from Janvier Laboratories. Hippocampal neurons were obtained from embryos of both genders at E18 stage of development.

Expression vectors, shRNA constructs.

pebioGFP-KIF1A(657-1105, 657-1698) correspond to truncated versions of the KIF1A rat variant 2 (XM_003750741). HA- and GFP-TANC2 were generated using as template FLAG-TANC2 described in (Han et al., 2010). The following shRNA sequences are used in this study: TANC2#1 (5'-CCTCAGTCAAGGGTCATAT-3') targeting rat TANC2 mRNA (XM_008768351.1), shRNA_KIF1A (Kevenaer et al., 2016), shRNA_liprin- α 2/ α 3 (Spangler et al., 2013). All other constructs were created using PCR-based strategies. For details, see Supplemental Experimental Procedures.

Hippocampal Neuron Cultures, Transfections, Treatments.

Primary hippocampal cultures were prepared from embryonic day 18 rat brains. Cells were plated on coverslips coated with poly-L-lysine (30 μ g/ml) and laminin (2 μ g/ml) at a density of 100,000/well. Hippocampal neurons were transfected using lipofectamine (Invitrogen). Neuron cultures were treated with 10 μ M latrunculin B, 10 μ M jaspalakinolide, 10 μ M BAPTA-AM or 40 μ M bicuculline and fixed or imaged from 0 to 1h after addition of the drugs. For details, see Supplemental Experimental Procedures.

Affinity Purification-Mass spectrometry (AP-MS) using biotin or GFP pull-down on rat brain extracts

Brains were obtained from female adult rats and homogenized in tissue lysis buffer (50mM TrisHCl, 150mM NaCl, 0.1% SDS, 0.2% NP-40, and protease inhibitors). Brain lysates were centrifuged at 16,000g for 15min at 4°C and the supernatant was then incubated for 1h at 4°C with beads previously conjugated with the protein of interest. For details, see Supplemental Experimental Procedures.

Sample preparation, peptide fractionation, mass spectrometry and data analysis

All samples were analyzed on an ETD enabled LTQ-Orbitrap Elite coupled to Proxeon EASY-nLC 1000 (Thermo Fisher Scientific) or on an Orbitrap Q-Exactive mass spectrometer (Thermo Fisher Scientific) coupled to an Agilent 1290 Infinity LC (Agilent Technologies). The full MS methods are available in the Supplemental Experimental Procedures.

Live-Cell Imaging Microscopy and analysis

Live-cell imaging experiments were performed in an inverted spinning disk confocal microscope equipped with a Plan Apo VC 100x/60x NA 1.40 oil objective, and an incubation chamber mounted on a motorized XYZ stage which were all controlled using MetaMorph (Molecular Devices) software. For details, see Supplemental Experimental Procedures.

Statistical Methods

AP-MS data were analyzed using SAINT (Significance Analysis of INteractions, version 2.3.2) algorithm. Statistical significance was determined using Student's t test assuming a two-tailed variation. The graphs represent mean \pm s.e.m. For details, see Supplemental Experimental Procedures.

DATA AND SOFTWARE AVAILABILITY

The mass spectrometry proteomics data have been deposited to the ProteomeXchange Consortium via the PRIDE partner repository with the dataset identifier PXD010080.

SUPPLEMENTAL INFORMATION

Supplemental Information includes Supplemental Experimental Procedures, six figures, and four tables and can be found with this article online at: <https://doi.org/10.1016/j.celrep.2018.06.071>.

ACKNOWLEDGMENTS

We thank Gary Banker for sharing bioGFP-KIF1A constructs, Camin Dean for sharing Syt4/Syt11 constructs, Mike Boxem for sharing human-CAM1 cDNA, Eunjoon Kim for sharing FLAG-TANC constructs and panTANC antibody, and Philipp Schatzle for cloning advice. This work was supported by the Netherlands Organisation for Scientific Research (865.10.010, NWO-ALWVICI, CCH), the Netherlands Organisation for Health Research and Development (91215084, ZonMW-TOP, CCH), and the European Research Council (ERC) (617050, ERC-consolidator, CCH). G.B. was supported by the Deutsche Forschungsgemeinschaft Research Fellowship (807223).

AUTHOR CONTRIBUTIONS

R.S. cloned the constructs, designed and performed proteomics, biochemical, imaging experiments and analyzed the data; G.P. and E.Z. conducted live imaging experiments and analyzed the data; J.H. and I.G.S.J. cloned DNA constructs and performed biochemical/imaging experiments; O.K. performed XL-MS experiments; R.A.S. supervised the XL-MS part; A.F.M.A supervised the proteomics part; the figures were designed and assembled by R.S.; the manuscript was written by R.S. and C.C.H with inputs from G.P.; C.C.H. supervised and coordinated the study.

REFERENCES

- Arthur, C.P., Dean, C., Pagratis, M., Chapman, E.R., and Stowell, M.H. (2010). Loss of synaptotagmin IV results in a reduction in synaptic vesicles and a distortion of the Golgi structure in cultured hippocampal neurons. *Neuroscience* 167, 135-142.
- Barkus, R.V., Klyachko, O., Horiuchi, D., Dickson, B.J., and Saxton, W.M. (2008). Identification of an axonal kinesin-3 motor for fast anterograde vesicle transport that facilitates retrograde transport of neuropeptides. *Mol Biol Cell* 19, 274-283.
- Batters, C., Brack, D., Ellrich, H., Averbeck, B., and Veigel, C. (2016). Calcium can mobilize and activate myosin-VI. *Proc Natl Acad Sci U S A* 113, E1162-1169.
- Bharat, V., Siebrecht, M., Burk, K., Ahmed, S., Reissner, C., Kohansal-Nodehi, M., Steubler, V., Zweckstetter, M., Ting, J.T., and Dean, C. (2017). Capture of Dense Core Vesicles at Synapses by JNK-Dependent Phosphorylation of Synaptotagmin-4. *Cell Rep* 21, 2118-2133.
- Bittins, C.M., Eichler, T.W., Hammer, J.A., 3rd, and Gerdes, H.H. (2010). Dominant-negative myosin Va impairs retrograde but not anterograde axonal transport of large dense core vesicles. *Cell Mol Neurobiol* 30, 369-379.
- Choi, H., Larsen, B., Lin, Z.Y., Breitreutz, A., Mellacheruvu, D., Fermin, D., Qin, Z.S., Tyers, M., Gingras, A.C., and Nesvizhskii, A.I. (2011). SAINT: probabilistic scoring of affinity purification-mass spectrometry data. *Nat Methods* 8, 70-73.
- de Ligt, J., Willemsen, M.H., van Bon, B.W., Kleefstra, T., Yntema, H.G., Kroes, T., Vulto-van Silfhout, A.T., Koolen, D.A., de Vries, P., Gilissen, C., et al. (2012). Diagnostic exome sequencing in persons with severe intellectual disability. *N Engl J Med* 367, 1921-1929.
- de Wit, J., Toonen, R.F., Verhaagen, J., and Verhage, M. (2006). Vesicular trafficking of semaphorin 3A is activity-dependent and differs between axons and dendrites. *Traffic* 7, 1060-1077.
- Dean, C., Liu, H., Dunning, F.M., Chang, P.Y., Jackson, M.B., and Chapman, E.R. (2009). Synaptotagmin-IV modulates synaptic function and long-term potentiation by regulating BDNF release. *Nat Neurosci* 12, 767-776.
- Esteves da Silva, M., Adrian, M., Schatzle, P., Lipka, J., Watanabe, T., Cho, S., Futai, K., Wierenga, C.J., Kapitein, L.C., and Hoogenraad, C.C. (2015). Positioning of AMPA Receptor-Containing Endosomes Regulates Synapse Architecture. *Cell Rep* 13, 933-943.
- Fromer, M., Pocklington, A.J., Kavanagh, D.H., Williams, H.J., Dwyer, S., Gormley, P., Georgieva, L., Rees, E., Palta, P., Ruderfer, D.M., et al. (2014). De novo mutations in schizophrenia implicate synaptic networks. *Nature* 506, 179-184.
- Gasparini, A., Tosatto, S.C.E., Murgia, A., and Leonardi, E. (2017). Dynamic scaffolds for neuronal signaling: in silico analysis of the TANC protein family. *Sci Rep* 7, 6829.
- Guillaud, L., Wong, R., and Hirokawa, N. (2008). Disruption of KIF17-Mint1 interaction by CaMKII-dependent phosphorylation: a molecular model of kinesin-cargo release. *Nat Cell Biol* 10, 19-29.
- Gumy, L.F., Katrukha, E.A., Grigoriev, I., Jaarsma, D., Kapitein, L.C., Akhmanova, A., and Hoogenraad, C.C. (2017). MAP2 Defines a Pre-axonal Filtering Zone to Regulate KIF1- versus KIF5-Dependent Cargo Transport in Sensory Neurons. *Neuron* 94, 347-362 e347.
- Hammond, J.W., Cai, D., Blasius, T.L., Li, Z., Jiang, Y., Jih, G.T., Meyhofer, E., and Verhey, K.J. (2009). Mammalian Kinesin-3 motors are dimeric in vivo and move by processive motility upon release of autoinhibition. *PLoS Biol* 7, e72.
- Han, S., Nam, J., Li, Y., Kim, S., Cho, S.H., Cho, Y.S., Choi, S.Y., Choi, J., Han, K., Kim, Y., et al. (2010). Regulation of dendritic spines, spatial memory, and embryonic development by the TANC family of PSD-95-interacting proteins. *J Neurosci* 30, 15102-15112.
- Hanada, T., Lin, L., Tibaldi, E.V., Reinherz, E.L., and Chishti, A.H. (2000). GAKIN, a novel kinesin-like protein associates with the human homologue of the *Drosophila* discs large tumor suppressor in T lymphocytes. *J Biol Chem* 275, 28774-28784.
- Hirokawa, N., Niwa, S., and Tanaka, Y. (2010). Molecular motors in neurons: transport mechanisms and roles in brain function, development, and disease. *Neuron* 68, 610-638.
- Iossifov, I., Ronemus, M., Levy, D., Wang, Z., Hakker, I., Rosenbaum, J., Yamrom, B., Lee, Y.H., Narzisi, G., Leotta, A., et al. (2012). De novo gene disruptions in children on the autistic spectrum. *Neuron* 74, 285-299.
- Kapitein, L.C., Schlager, M.A., Kuijpers, M., Wulf, P.S., van Spronsen, M., MacKintosh, F.C., and Hoogenraad, C.C. (2010). Mixed microtubules steer

- dynein-driven cargo transport into dendrites. *Curr Biol* 20, 290-299.
- Kevenaar, J.T., Bianchi, S., van Spronsen, M., Olieric, N., Lipka, J., Frias, C.P., Mikhaylova, M., Harterink, M., Keijzer, N., Wulf, P.S., et al. (2016). Kinesin-Binding Protein Controls Microtubule Dynamics and Cargo Trafficking by Regulating Kinesin Motor Activity. *Curr Biol* 26, 849-861.
- Klopfenstein, D.R., Tomishige, M., Stuurman, N., and Vale, R.D. (2002). Role of phosphatidylinositol(4,5)bisphosphate organization in membrane transport by the Unc104 kinesin motor. *Cell* 109, 347-358.
- Krementsov, D.N., Kremntsova, E.B., and Trybus, K.M. (2004). Myosin V: regulation by calcium, calmodulin, and the tail domain. *J Cell Biol* 164, 877-886.
- Letierrier, C., and Dargent, B. (2014). No Pasaran! Role of the axon initial segment in the regulation of protein transport and the maintenance of axonal identity. *Semin Cell Dev Biol* 27, 44-51.
- Li, Z., and Sacks, D.B. (2003). Elucidation of the interaction of calmodulin with the IQ motifs of IQGAP1. *J Biol Chem* 278, 4347-4352.
- Lipka, J., Kapitein, L.C., Jaworski, J., and Hoogenraad, C.C. (2016). Microtubule-binding protein doublecortin-like kinase 1 (DCLK1) guides kinesin-3-mediated cargo transport to dendrites. *EMBO J* 35, 302-318.
- Lo, K.Y., Kuzmin, A., Unger, S.M., Petersen, J.D., and Silverman, M.A. (2011). KIF1A is the primary anterograde motor protein required for the axonal transport of dense-core vesicles in cultured hippocampal neurons. *Neurosci Lett* 491, 168-173.
- Lochner, J.E., Spangler, E., Chavarha, M., Jacobs, C., McAllister, K., Schuttner, L.C., and Scalettar, B.A. (2008). Efficient copackaging and cotransport yields postsynaptic colocalization of neuromodulators associated with synaptic plasticity. *Dev Neurobiol* 68, 1243-1256.
- Lu, H., Kremntsova, E.B., and Trybus, K.M. (2006). Regulation of myosin V processivity by calcium at the single molecule level. *J Biol Chem* 281, 31987-31994.
- Lu, Q., Li, J., Ye, F., and Zhang, M. (2015). Structure of myosin-1c tail bound to calmodulin provides insights into calcium-mediated conformational coupling. *Nat Struct Mol Biol* 22, 81-88.
- Macaskill, A.F., Rinholm, J.E., Twelvetrees, A.E., Arancibia-Carcamo, I.L., Muir, J., Fransson, A., Aspenstrom, P., Attwell, D., and Kittler, J.T. (2009). Miro1 is a calcium sensor for glutamate receptor-dependent localization of mitochondria at synapses. *Neuron* 61, 541-555.
- Maeder, C.I., Shen, K., and Hoogenraad, C.C. (2014). Axon and dendritic trafficking. *Curr Opin Neurobiol* 27, 165-170.
- McVicker, D.P., Awe, A.M., Richters, K.E., Wilson, R.L., Cowdrey, D.A., Hu, X., Chapman, E.R., and Dent, E.W. (2016). Transport of a kinesin-cargo pair along microtubules into dendritic spines undergoing synaptic plasticity. *Nat Commun* 7, 12741.
- Millecamps, S., and Julien, J.P. (2013). Axonal transport deficits and neurodegenerative diseases. *Nat Rev Neurosci* 14, 161-176.
- Miller, K.E., DeProto, J., Kaufmann, N., Patel, B.N., Duckworth, A., and Van Vactor, D. (2005). Direct observation demonstrates that Liprin-alpha is required for trafficking of synaptic vesicles. *Curr Biol* 15, 684-689.
- Mruk, K., Farley, B.M., Ritacco, A.W., and Kobertz, W.R. (2014). Calmodulation meta-analysis: predicting calmodulin binding via canonical motif clustering. *J Gen Physiol* 144, 105-114.
- Nguyen, H., and Higuchi, H. (2005). Motility of myosin V regulated by the dissociation of single calmodulin. *Nat Struct Mol Biol* 12, 127-132.
- Niwa, S., Lipton, D.M., Morikawa, M., Zhao, C., Hirokawa, N., Lu, H., and Shen, K. (2016). Autoinhibition of a Neuronal Kinesin UNC-104/KIF1A Regulates the Size and Density of Synapses. *Cell Rep* 16, 2129-2141.
- Niwa, S., Tanaka, Y., and Hirokawa, N. (2008). KIF1Bbeta- and KIF1A-mediated axonal transport of presynaptic regulator Rab3 occurs in a GTP-dependent manner through DENN/MADD. *Nat Cell Biol* 10, 1269-1279.
- Okada, Y., Yamazaki, H., Sekine-Aizawa, Y., and Hirokawa, N. (1995). The neuron-specific kinesin superfamily protein KIF1A is a unique monomeric motor for anterograde axonal transport of synaptic vesicle precursors. *Cell* 81, 769-780.
- Olsen, O., Moore, K.A., Fukata, M., Kazuta, T., Trinidad, J.C., Kauer, F.W., Streuli, M., Misawa, H., Burlingame, A.L., Nicoll, R.A., and Brecht, D.S. (2005). Neurotransmitter release regulated by a MALS-liprin-alpha presynaptic complex. *J Cell Biol* 170, 1127-1134.
- Schlager, M.A., and Hoogenraad, C.C. (2009). Basic mechanisms for recognition and transport of synaptic cargos. *Mol Brain* 2, 25.
- Shin, H., Wyszynski, M., Huh, K.H., Valtschanoff, J.G., Lee, J.R., Ko, J., Streuli, M., Weinberg, R.J., Sheng, M., and Kim, E. (2003).

Association of the kinesin motor KIF1A with the multimodular protein liprin-alpha. *J Biol Chem* 278, 11393-11401.

Sieburth, D., Ch'ng, Q., Dybbs, M., Tavazoie, M., Kennedy, S., Wang, D., Dupuy, D., Rual, J.F., Hill, D.E., Vidal, M., et al. (2005). Systematic analysis of genes required for synapse structure and function. *Nature* 436, 510-517.

Sirajuddin, M., Rice, L.M., and Vale, R.D. (2014). Regulation of microtubule motors by tubulin isotypes and post-translational modifications. *Nat Cell Biol* 16, 335-344.

Spangler, S.A., Schmitz, S.K., Kevenaer, J.T., de Graaff, E., de Wit, H., Demmers, J., Toonen, R.F., and Hoogenraad, C.C. (2013). Liprin-alpha2 promotes the presynaptic recruitment and turnover of RIM1/CASK to facilitate synaptic transmission. *J Cell Biol* 201, 915-928.

Wagner, O.I., Esposito, A., Kohler, B., Chen, C.W., Shen, C.P., Wu, G.H., Butkevich, E., Mandalapu, S., Wenzel, D., Wouters, F.S., and Klopfenstein, D.R. (2009). Synaptic scaffolding protein SYD-2 clusters and activates kinesin-3 UNC-104 in *C. elegans*. *Proc Natl Acad Sci U S A* 106, 19605-19610.

Wang, X., and Schwarz, T.L. (2009). The mechanism of Ca²⁺-dependent regulation of kinesin-mediated mitochondrial motility. *Cell* 136, 163-174.

Wu, G.H., Muthaiyan Shanmugam, M., Bhan, P., Huang, Y.H., and Wagner, O.I. (2016). Identification and Characterization of LIN-2(CASK) as a Regulator of Kinesin-3 UNC-104(KIF1A) Motility and Clustering in Neurons. *Traffic* 17, 891-907.

Wu, Y.E., Huo, L., Maeder, C.I., Feng, W., and Shen, K. (2013). The balance between capture and dissociation of presynaptic proteins controls the spatial distribution of synapses. *Neuron* 78, 994-1011.

Wyszynski, M., Kim, E., Dunah, A.W., Passafaro, M., Valtschanoff, J.G., Serra-Pages, C., Streuli, M., Weinberg, R.J., and Sheng, M. (2002). Interaction between GRIP and liprin-alpha/SYD2 is required for AMPA receptor targeting. *Neuron* 34, 39-52.

Yamada, K.H., Hanada, T., and Chishti, A.H. (2007). The effector domain of human Dlg tumor suppressor acts as a switch that relieves autoinhibition of kinesin-3 motor GAKIN/KIF13B. *Biochemistry* 46, 10039-10045.

Yamniuk, A.P., and Vogel, H.J. (2004). Calmodulin's flexibility allows for promiscuity in its interactions with target proteins and peptides. *Mol Biotechnol* 27, 33-57.

Yap, K.L., Kim, J., Truong, K., Sherman, M., Yuan, T., and Ikura, M. (2000). Calmodulin target

database. *J Struct Funct Genomics* 1, 8-14.

Yogev, S., Cooper, R., Fetter, R., Horowitz, M., and Shen, K. (2016). Microtubule Organization Determines Axonal Transport Dynamics. *Neuron* 92, 449-460.

Zahn, T.R., Angleson, J.K., MacMorris, M.A., Domke, E., Hutton, J.F., Schwartz, C., and Hutton, J.C. (2004). Dense core vesicle dynamics in *Caenorhabditis elegans* neurons and the role of kinesin UNC-104. *Traffic* 5, 544-559.

Zhang, M., Tanaka, T., and Ikura, M. (1995). Calcium-induced conformational transition revealed by the solution structure of apo calmodulin. *Nat Struct Biol* 2, 758-767.

Zhu, J., Shang, Y., Xia, Y., Zhang, R., and Zhang, M. (2016). An Atypical MAGUK GK Target Recognition Mode Revealed by the Interaction between DLG and KIF13B. *Structure* 24, 1876-1885.

SUPPLEMENTARY FIGURES

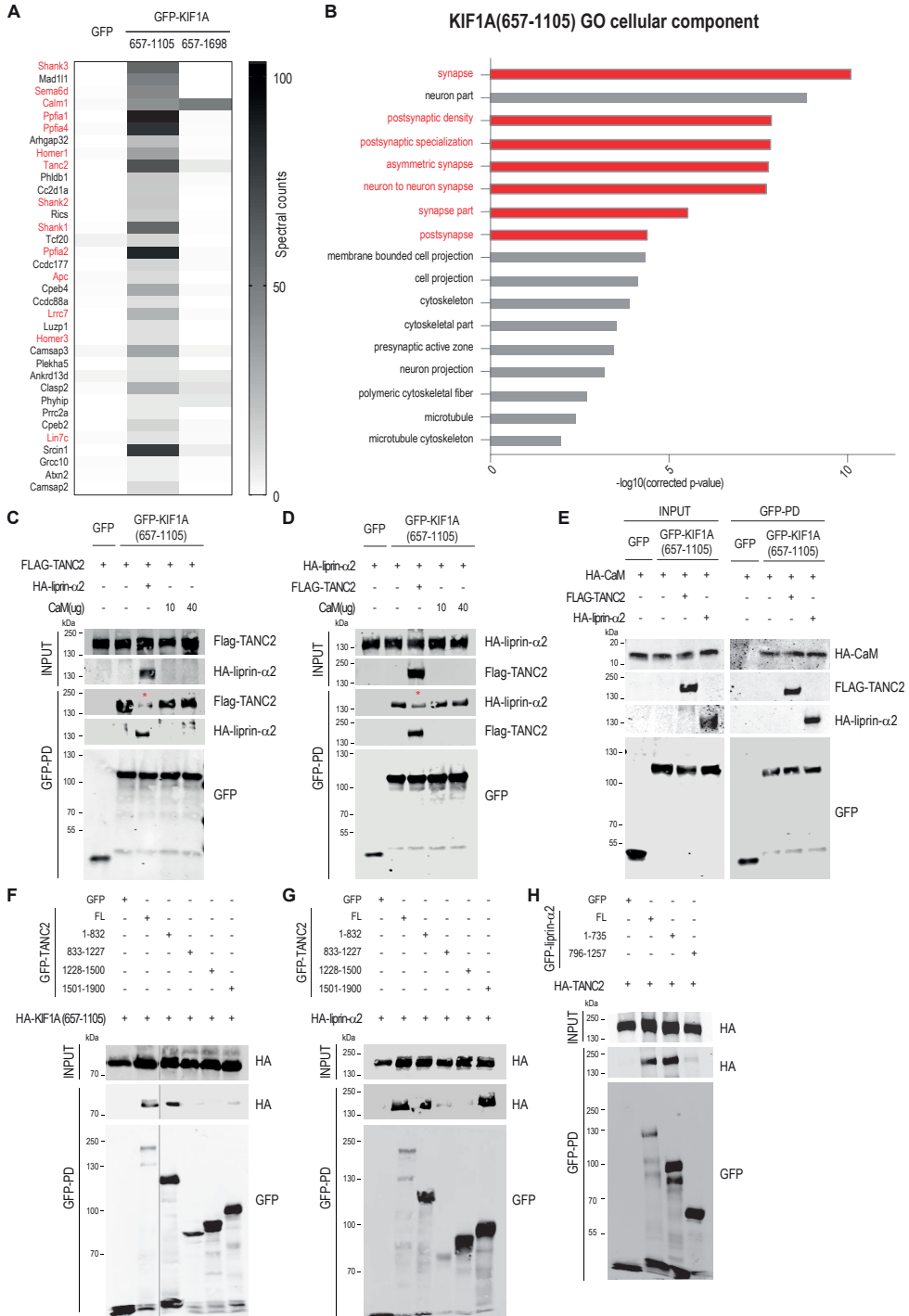


Figure S1. Related to Figure 1. KIF1A(657-1105) interacts with TANC2, liprin- α 2, CaM and shows high binding affinity for a restricted group of post synaptic density (PSD) proteins

(A) List of KIF1A (657-1105) interactors identified by LC/MS-MS in rat brain affinity purification (AP) experiments. BioGFP-CTR and bioGFP-KIF1A truncated isoforms (657-1105; 657-1698) were firstly expressed in HEK293 cells, purified using streptavidin-pulldowns and then incubated with rat brain extracts. Candidate proteins identified by MS are considered true KIF1A(657-1105) interactors when their probability >0.98 using the SAINT algorithm. Heat map shows total spectral counts detected for each protein candidate in AP-MS experiments of bioGFP, bioGFP-KIF1A(657-1105) or bioGFP-KIF1A(657-1698). Selected candidates shown in the graph are neuronal specific interacting partners not detected in a control bioGFP-KIF1A(657-1105) AP-MS experiment performed in HEK293 cells. See also Table S1.

(B) Gene ontology analysis (cellular component) of KIF1A(657-1105) interacting proteins (P-value >0.98). See also Figure S1A and Table S1.

(C) bioGFP-KIF1A(657-1105) was expressed in HEK293 cells, purified using streptavidin-pulldowns and incubated with protein extracts of cells expressing FLAG-TANC2 alone, or in combination with extracts of cells expressing HA-liprin- α 2 or in combination with 10 or 40 μ g of purified calmodulin (Sigma). Western blot detection was performed using FLAG, HA and GFP antibodies.

(D) bioGFP-KIF1A(657-1105) was expressed in HEK293 cells, purified and incubated with protein extracts of cells expressing HA-liprin- α 2 alone, or in combination with extracts of cells expressing FLAG-TANC2 or in combination with 10 or 40 μ g of purified calmodulin (Sigma). Western blot detection was performed using HA, FLAG and GFP antibodies.

(E) bioGFP-KIF1A(657-1105) was expressed in HEK293 cells, purified using streptavidin-pulldowns and incubated with protein extracts of cells expressing HA-CaM alone, or in combination with extracts of cells expressing FLAG-TANC2 or in combination with extracts of cells expressing HA-liprin- α 2. Western blot detection was performed using HA, FLAG and GFP antibodies.

(F) Western blots of HA-KIF1A(657-1105) in AP experiments of full length GFP-TANC2 and GFP-TANC2 fragments (1-832, 833-1227, 1228-1500, 1501-1900) from co-transfected HEK293 cells.

(G) Western blots of HA-liprin- α 2 in AP experiments of GFP, full length GFP-TANC2, or GFP-TANC2 fragments (1-832, 833-1227, 1228-1500, 1501-1900).

(H) Western blots of HA-TANC2 in AP experiments of GFP, full length GFP-liprin- α 2, GFP-liprin- α 2(1-735) or GFP-liprin- α 2(796-1257).

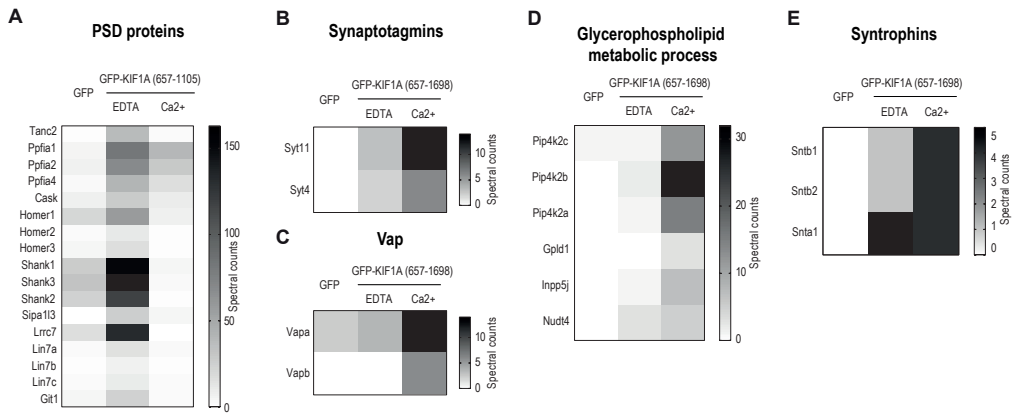


Figure S2. Related to Figure 3. KIF1A interactome is modulated by calcium

(A) BioGFP-KIF1A(657-1105) was incubated with rat brain extracts in presence of 2mM EDTA or 2mM Ca^{2+} . Heat map shows selected post synaptic density (PSD) proteins co-purified with KIF1A(657-1105)_EDTA and identified by MS. Relative abundance of each protein is represented as total spectral counts detected in bioGFP (ctr), bioGFP-KIF1A(657-1105)_EDTA or bioGFP-KIF1A(657-1105)_ Ca^{2+} .

(B-E) BioGFP-KIF1A(657-1698) was incubated with rat brain extracts in presence of 2mM EDTA or 2mM Ca^{2+} . Relative abundance of each protein is represented as total spectral counts detected in bioGFP (ctr), bioGFP-KIF1A(657-1698)_EDTA or bioGFP-KIF1A(657-1698)_ Ca^{2+} . Heat maps show selected co-purified proteins with KIF1A(657-1698) _ Ca^{2+} : Synaptotagmin4 (Syt4) and synaptotagmin11 (Syt11) (B); Vapa and Vapb(C); phosphatidylinositol 5-phosphate 4-kinase (Pip4k2), phosphatidylinositol-glycan-specific phospholipase D (Gpld1), inositol polyphosphate 5-phosphatase (Inpp5), diphosphoinositol polyphosphate phosphohydrolase 2 (Nudt4) (D); syntrophins (Snt) (E).

Figure S3. Related to Figure 5. KIF1A transports DCVs in dendrites but DCV motility is not influenced by TANC2 and liprin- α

(A) Representative images of rat hippocampal neurons (DIV11-DIV14) co-transfected with GFP-KIF1A (green) in combination with NPY-RFP (red), mCherry-Syt4 (red) or mCherry-Syt11 (red) and stained for MAP2 (blue). Scale bar, 10 μm .

(B) Images correspond to higher magnifications of the selected areas highlighted in the nearby figures. Arrows point to co-localizing puncta. Scale bar, 5 μm .

(C) Neurons co-transfected with NPY-GFP (green) in combination with mCherry-Syt4 (red) or mCherry-Syt11 (red) and stained for MAP2 (blue). Scale bar, 10 μm .

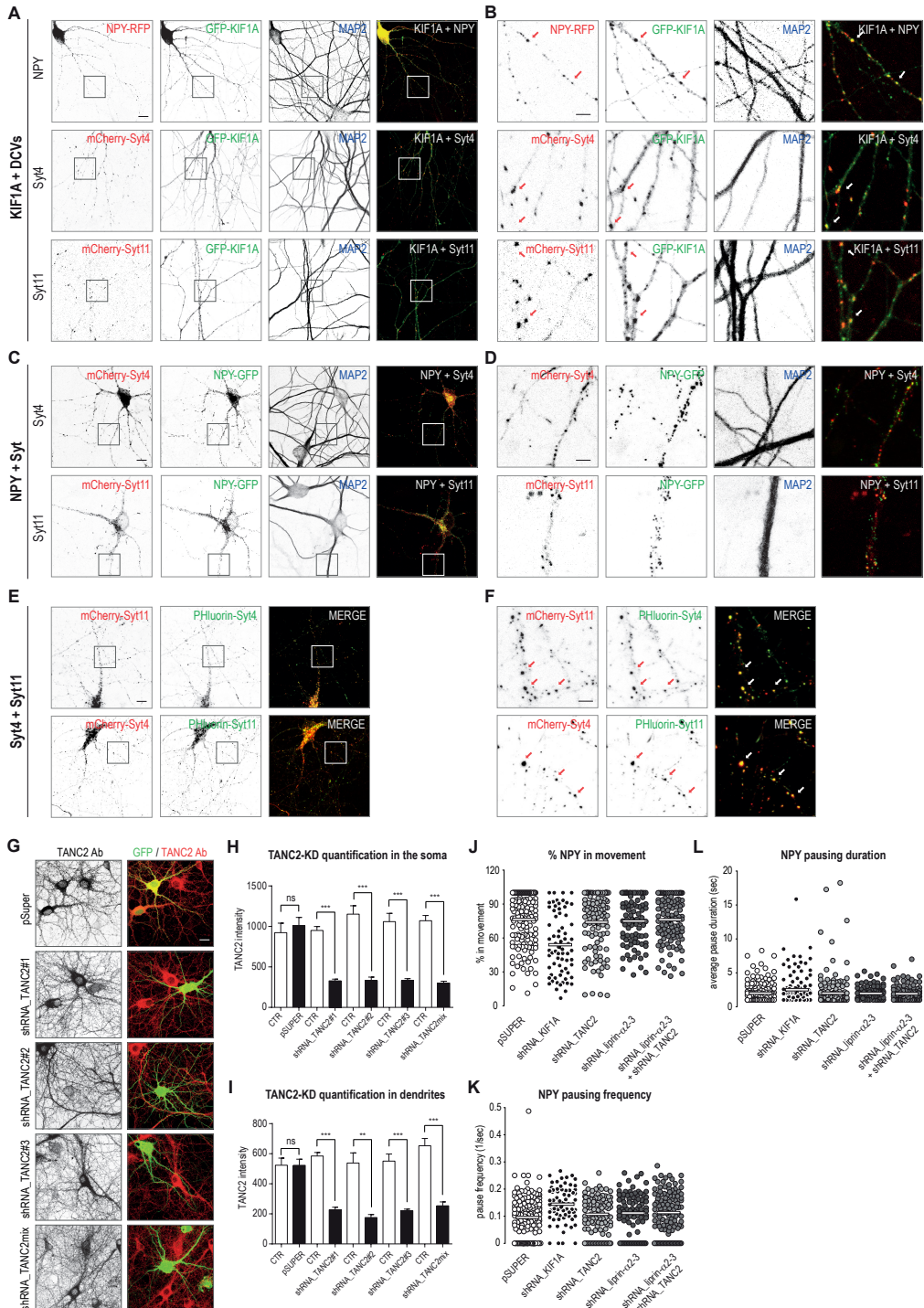
(D) Images correspond to higher magnifications of the selected areas highlighted in the nearby figures. Scale bar, 5 μm .

(E) Neurons co-transfected with Phluorin-Syt4 (green) in combination with mCherry-Syt11 (red), or with Phluorin-Syt11 (green) in combination with mCherry-Syt4 (red). Scale bar, 10 μm .

(F) Images correspond to higher magnifications of the selected areas highlighted in the nearby figures. Arrows point to co-localizing puncta. Scale bar, 5 μm .

(G) Representative images of hippocampal neurons (DIV11-14) knockdown for TANC2 with indicated shRNA constructs (shRNA_TANC2#1, shRNA_TANC2#2, shRNA_TANC2#3, shRNA_TANC2mix), filled with GFP (green) and stained with TANC2 polyclonal antibody (red). Scale bar, 20 μm .

(H-I) Quantifications of TANC2 fluorescent-staining intensities in KD-neurons shown in Figure S3G. (H) TANC2 staining intensity in the soma of transfected KD-neurons is compared to TANC2 intensity in the soma of non-transfected neurons within the same images; (I) TANC2 staining intensity in neurites of transfected KD-neurons is compared to



TANC2 intensity in neurites of non-transfected neurons within the same images. The bars show mean±s.e.m. (n=9-13 neurons (H), n=27-39 neurites (I)); ***P*<0.01, *paired t*-test; ****P*<0.001, *paired t*-test).

(J-L) Quantifications of NPY trafficking parameters in dendrites of neurons (DIV11-14) co-transfected with NPY-GFP in combination with pSuper, shRNA_KIF1A, shRNA_TANC2, shRNA_liprin-α2-3, shRNA_liprin-α2-3 + shRNA_TANC2; percentage of NPY vesicles in movement (J), NPY pause frequency (K), NPY average pause duration (L). Bars show the mean; (n=17-58 dendrites).

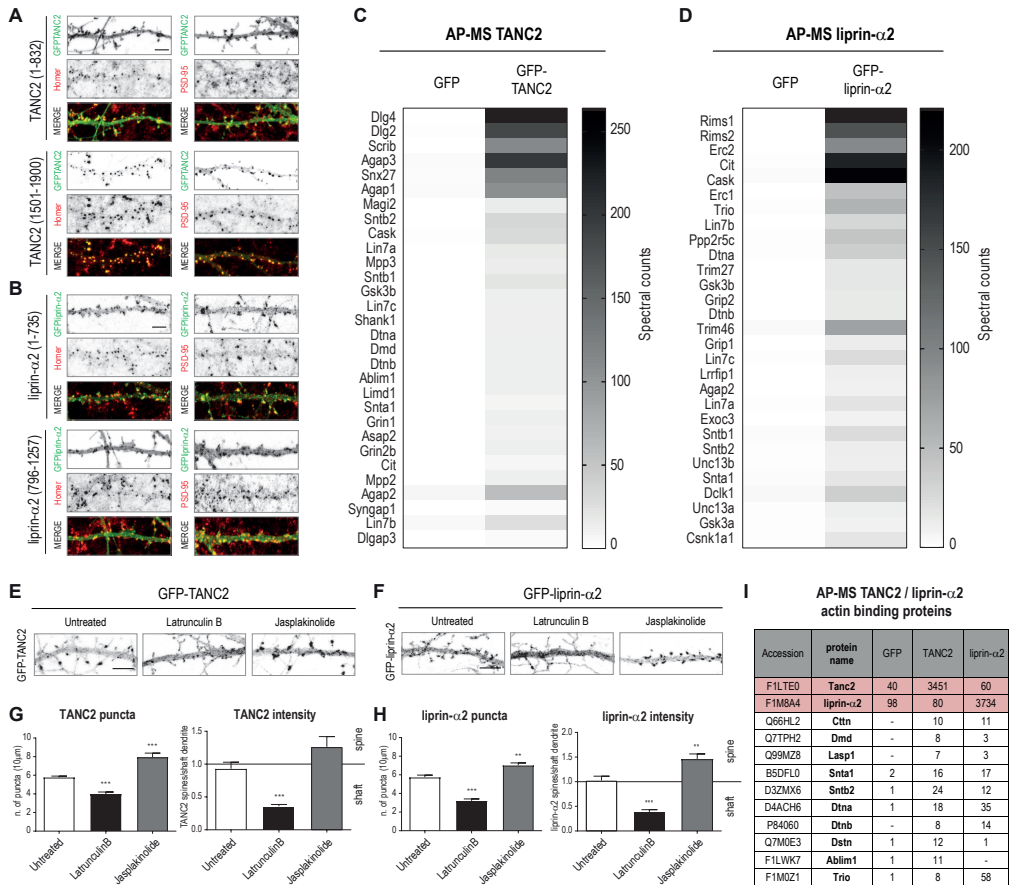


Figure S4. Related to Figure 6. TANC2 and liprin-α2 are scaffolding proteins in the post synaptic density (PSD)

(A) Representative dendritic protrusions of neurons (DIV14-17) expressing GFP-TANC2 n-terminal (1-832) or GFP-TANC2 c-terminal fragment (1501-1900) and stained for the post-synaptic proteins Homer or PSD-95 (red). Scale bar, 5µm.

(B) Representative dendritic protrusions of neurons (DIV14-17) expressing GFP-liprin-α2 n-terminal (1-735) or GFP-liprin-α2 c-terminal fragment (796-1257) and stained for the post-synaptic proteins Homer or PSD-95 (red). Scale bar, 5µm.

(C) List of significant TANC2 interactors identified by MS in AP experiments using bioGFP-TANC2 as bait. BioGFP-CTR and bioGFP-TANC2 were expressed in HEK293 cells, purified using streptavidin-pull-downs and then incubated with rat brain extracts. Co-purified proteins have been identified by AP-MS and have been classified as TANC2

interactors if probability >0.90 using the SAINT algorithm. Heat map shows total spectral counts in bioGFP-CTR and bioGFP-TANC2. See also Table S3.

(D) List of significant liprin- $\alpha 2$ interactors identified by LC/MS-MS in AP experiments using bioGFP-liprin- $\alpha 2$ as bait. BioGFP-CTR and bioGFP-liprin- $\alpha 2$ were purified using streptavidin-pulldowns and then incubated with rat brain extracts. Co-purified proteins have been identified by AP-MS and have been classified as putative liprin- $\alpha 2$ interactors if probability >0.90 using the SAINT algorithm. Heat map shows total spectral counts in bioGFP-CTR and bioGFP-liprin- $\alpha 2$. See also Table S4.

(E) Dendritic protrusions of neurons (DIV14-17) expressing GFP-TANC2 and treated with DMSO (Untreated), LatrunculinB or Jasplakinolide for 1h. Scale bar, $5\mu\text{m}$.

(F) Dendritic protrusions of neurons (DIV14-17) expressing GFP-liprin- $\alpha 2$ and treated with DMSO (Untreated), LatrunculinB or Jasplakinolide for 1h. Scale bar, $5\mu\text{m}$.

(G) Quantifications of total GFP-TANC2 puncta in dendrites (left panel) and of TANC2 intensity in spines/dendritic shaft (right panel) in DMSO (Untreated), Latrunculin B or Jasplakinolide treated neurons (Figure S4E). The bars show mean \pm s.e.m. (n=27-30 dendrites; *** $P<0.001$, *t*-test).

(H) Quantifications of total GFP-liprin- $\alpha 2$ puncta in dendrites (left panel) and of liprin- $\alpha 2$ intensity in spines/dendritic shaft (right panel) in DMSO (Untreated), Latrunculin B or Jasplakinolide treated neurons (Figure S4F). The bars show mean \pm s.e.m. (n=24-31 dendrites, ** $P<0.01$, *t*-test, *** $P<0.001$, *t*-test).

(I) Table represents selected actin binding proteins co-purified with bioGFP-TANC2 or bioGFP-liprin- $\alpha 2$ and identified by MS (Ctn=Cortactin, Dmd=Dystrophin, Lasp1=LIM and SH3 domain protein 1, Snt=Syntrophin, Dtn=Dystrobrevin, Dstn=Destrin, Ablim=Actin-binding LIM protein, Trio=Triple functional domain protein). Relative abundance of each protein is represented as total spectral counts. See also Table S3-4.

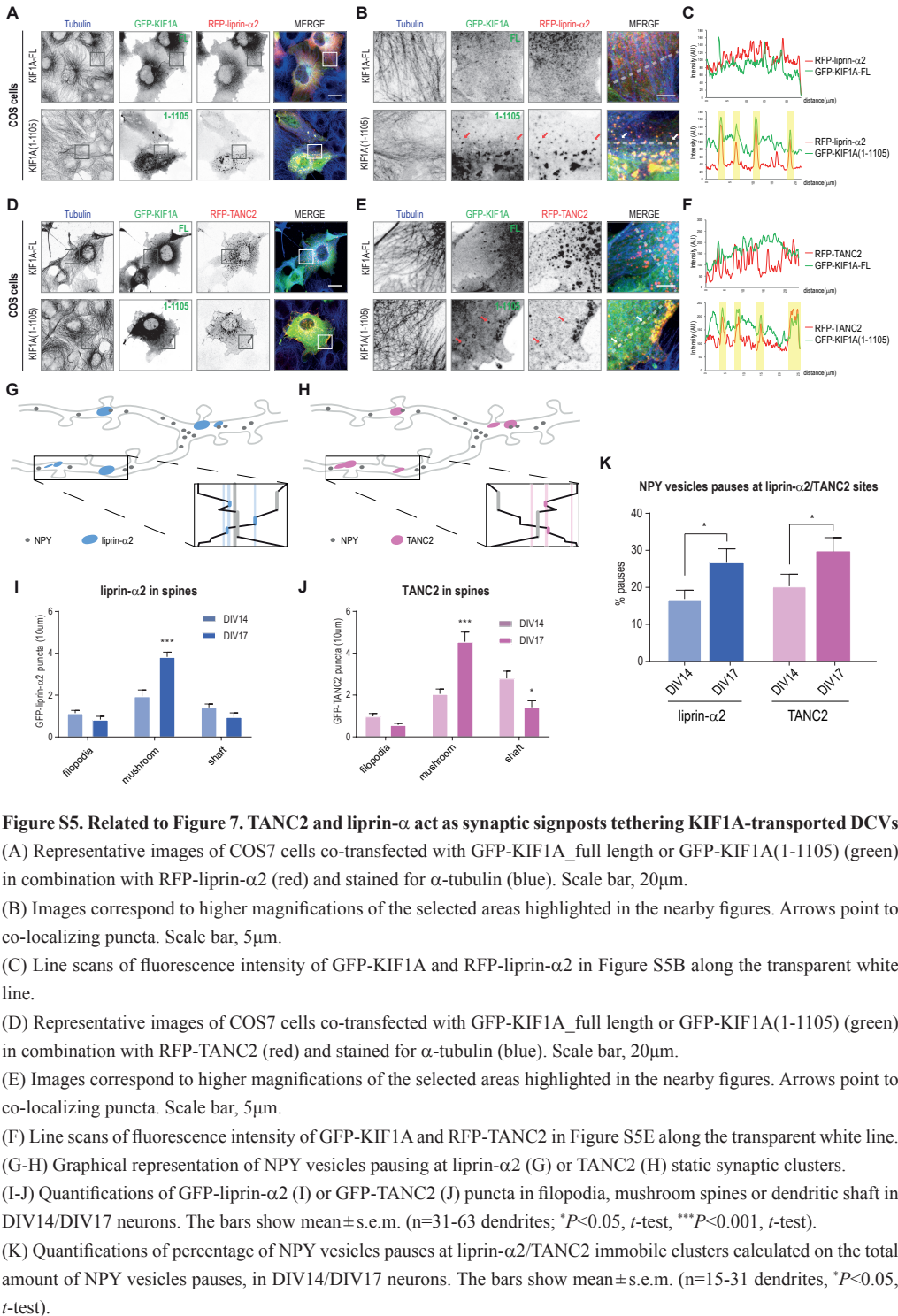


Figure S5. Related to Figure 7. TANC2 and liprin- α act as synaptic signposts tethering KIF1A-transported DCVs

(A) Representative images of COS7 cells co-transfected with GFP-KIF1A_{full length} or GFP-KIF1A(1-1105) (green) in combination with RFP-liprin- α 2 (red) and stained for α -tubulin (blue). Scale bar, 20 μ m.

(B) Images correspond to higher magnifications of the selected areas highlighted in the nearby figures. Arrows point to co-localizing puncta. Scale bar, 5 μ m.

(C) Line scans of fluorescence intensity of GFP-KIF1A and RFP-liprin- α 2 in Figure S5B along the transparent white line.

(D) Representative images of COS7 cells co-transfected with GFP-KIF1A_{full length} or GFP-KIF1A(1-1105) (green) in combination with RFP-TANC2 (red) and stained for α -tubulin (blue). Scale bar, 20 μ m.

(E) Images correspond to higher magnifications of the selected areas highlighted in the nearby figures. Arrows point to co-localizing puncta. Scale bar, 5 μ m.

(F) Line scans of fluorescence intensity of GFP-KIF1A and RFP-TANC2 in Figure S5E along the transparent white line.

(G-H) Graphical representation of NPY vesicles pausing at liprin- α 2 (G) or TANC2 (H) static synaptic clusters.

(I-J) Quantifications of GFP-liprin- α 2 (I) or GFP-TANC2 (J) puncta in filopodia, mushroom spines or dendritic shaft in DIV14/DIV17 neurons. The bars show mean \pm s.e.m. (n=31-63 dendrites; * P <0.05, t -test, *** P <0.001, t -test).

(K) Quantifications of percentage of NPY vesicles pauses at liprin- α 2/TANC2 immobile clusters calculated on the total amount of NPY vesicles pauses, in DIV14/DIV17 neurons. The bars show mean \pm s.e.m. (n=15-31 dendrites, * P <0.05, t -test).

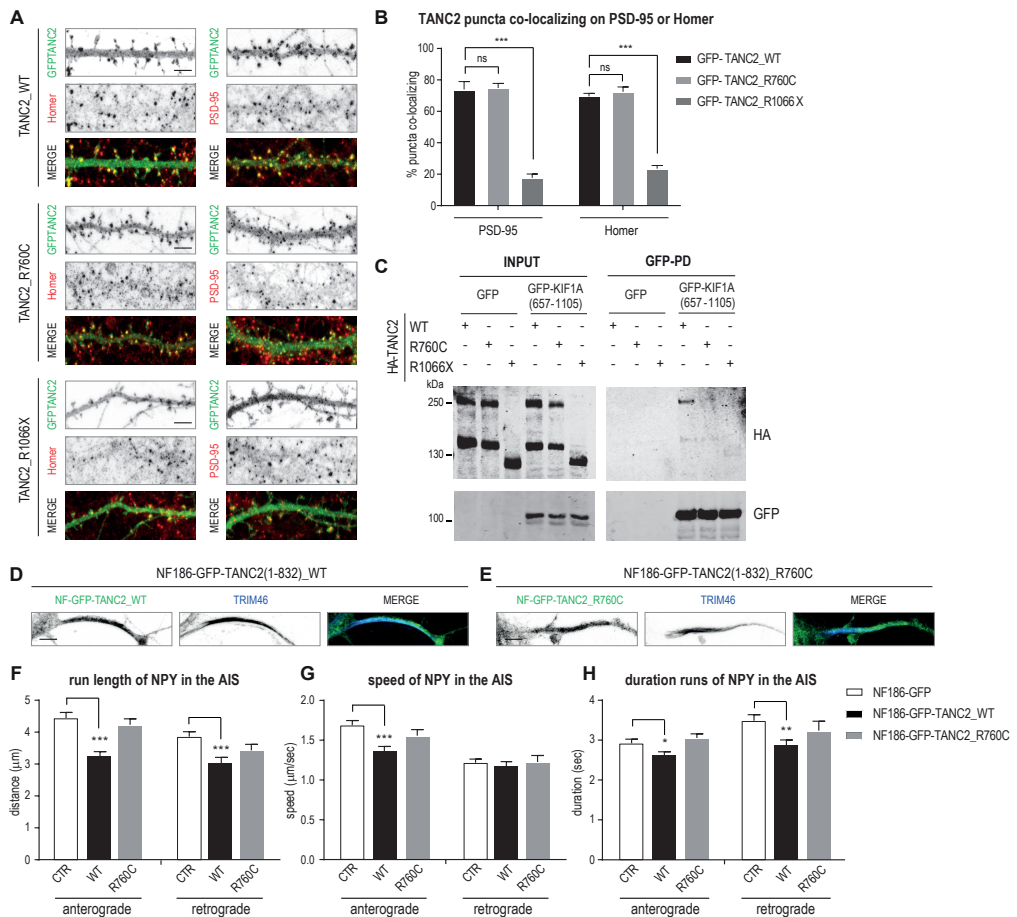


Figure S6. Related to Figure 7. TANC2 disease mutations affect KIF1A binding and DCV recruitment

(A) Representative dendritic protrusions of neurons (DIV14-17) expressing GFP-TANC2_WT, GFP-TANC2_R760C or GFP-TANC2_R1066X (green) and stained for the post-synaptic markers Homer or PSD-95 (red). Scale bar, 5 μ m.

(B) Quantifications corresponding to the percentage of GFP-TANC2 co-localizing puncta with endogenous Homer or PSD-95 shown in Figure S6A. The bars show mean \pm s.e.m. ($n=20-33$ dendrites, *** $P<0.001$, t-test).

(C) Western blots of HA-TANC2_WT, HA-TANC2_R760C and HA-TANC2_R1066X in AP experiments of bioGFP or bioGFP-KIF1A(657-1105) from co-transfected HEK293 cells.

(D-E) Zoom of the proximal axon in DIV11 hippocampal neurons transfected with NF186-GFP-TANC2(1-832_WT) (WT) (D) or NF186-GFP-TANC2(1-832_R760C) (R760C) (E) and stained for TRIM46 (blue). Scale bar, 5 μ m.

SUPPLEMENTAL EXPERIMENTAL PROCEDURES

Animals

All experiments were approved by the DEC Dutch Animal Experiments Committee (Dier Experimenten Commissie), performed in line with institutional guidelines of Utrecht University and conducted in agreement with the Dutch law (Wet op de Dierproeven, 1996) and European regulations (Directive 2010/63/EU). Female pregnant Wistar rats were obtained from Janvier Laboratories. Upon delivery, rats were kept in a controlled 12h light-dark cycle with a temperature of 22°C and were given unrestricted access to food and water. The animals were housed with companions in transparent Plexiglas cages with wood-chip bedding and paper tissue for nest building and cage enrichment. Hippocampal neurons were obtained from embryos of both genders at E18 stage of development. None of the parameters analyzed in this study are reported to be affected by embryo gender. Pregnant female rats and embryos have not been involved in previous procedures.

Antibodies and reagents

The following primary and secondary antibodies were used in this study: Homer rabbit (SySy), PSD-95 mouse (NeuroMab), TRIM46 rabbit (van Beuningen et al., 2015), Tub α 1a rabbit (Abcam), GFP rabbit (Abcam), MAP2 mouse (Sigma), MAP2 rabbit (Cell Signaling), mCherry mouse (Clontech), HA mouse (Covance), HA rabbit (Santa Cruz), FLAG mouse (Sigma), TANC1 rabbit (Abcam), TANC2 rabbit (Abcam), PanTANC (Han et al., 2010), and liprin- α 1 (Spangler et al., 2013). Alexa405-, Alexa 488-, Alexa 568- and Alexa 594-conjugated secondary antibodies (Invitrogen). Other reagents used in this study include: jasplakinolide (2792, Trocis Bioscience), latrunculinB (SC-203318, Bioconnect), BAPTA-AM (SC-202488, Santa Cruz), bicuculline (Sigma), Streptavidin Dynabeads M-280 (Thermo Scientific), GFP-Trap® beads (ChromoTek), Calmodulin-Sepharose beads (Biovision), recombinant Calmodulin (C4874, Sigma).

Expression vectors and shRNA constructs

The following mammalian expression plasmids have been previously described: BirA coding vector and pebioGFP (van der Vaart et al., 2013), pGW1-GFP (Jaworski et al., 2009), pSuper vector (Brummelkamp et al., 2002), pGW2-MARCKS-GFP (Schatzle et al., 2011), pGW1-HA-liprin- α 2, pGW1-GFP-liprin- α 2, pGW1-GFP-liprin- α 2(1-735), pGW1-GFP-liprin- α 2(796-1257) and peBioGFP-liprin- α 2 (Spangler et al., 2013), pGW1-HA-KIF1A (Kevenaar et al., 2016), pGW1-GFP-KIF1A (Lee et al., 2003), pGW2-NPY-GFP and pGW2-NPY-RFP (Schlager et al., 2010). pGW2-MARCKS-BFP was cloned by replacing GFP with cDNA encoding for BFP using BamHI and XbaI sites. pAAV-mCherry-Syt4, pAAV-mCherry-Syt11, pAAV-Syt4-phluorin, pAAV-Syt11-phluorin were kindly given us by Camin Dean. HA-CaM was generated by PCR on human-CAM1 cDNA kindly given us by Mike Boxem and cloned into a pGW2-HA linearized backbone using AscI and BamHI.

PebioGFP-KIF1A(657-1105), pebioGFP-KIF1A(393-881), pebioGFP-KIF1A(1105-1698), pebioGFP-KIF1A (950-1250), pebioGFP-KIF1A(657-1698) correspond to truncated versions of the KIF1A rat variant 2 (XM_003750741) and were kindly given us by Gary Banker; pebioGFP-KIF1A(691-752), (830-896), (986-1054) were produced by PCRs using pebioGFP-KIF1A(657-1105) as template and cloned using BamHI and XbaI sites; pebioGFP-KIF1A(657-1105_5*Ala) mutant was generated by gibson cloning (New England Biolabs) using 3 fragments: 1) gene blocks (IDT) to introduce 5 point mutations within the predicted CaM binding site (W714A, W716A, Y717A, F719A and L722A) (360b), 2) PCR product of pebioGFP-KIF1A657-1105 and 3) peBioGFP backbone digested with BamHI and AscI; pebioGFP-KIF1A(657-1698_5*Ala) mutant was generated with the same strategy but using the pebioGFP-KIF1A657-1698 as substrate for PCR of fragment 2; pGW1-HA-KIF1A(657-1105), pGW1-HA-KIF1A(657-1105_5*Ala), pGW1-HA-KIF1A(657-1698), pGW1-HA-KIF1A(657-1698_5*Ala) were created using PCR based strategies and cloned into pGW1-HA vector using AscI and EcoRI sites; pGW1-GFP-KIF1A_5*Ala was created by Gibson cloning using 3 fragments: 1) pGW1-GFP-KIF1A digested with KpnI and BamHI 2-3) PCR products obtained using degenerated primers to introduce 5 point mutations in the CaM binding site; pGW1-HA-KIF1A(1-1105) was generated by PCR on

pGW1-HA-KIF1A and cloned using *AscI* and *EcoRI*.

pGW2-HA-TANC1 and pGW2-HA-TANC2 were generated using FLAG-TANC1 and FLAG-TANC2 (Han et al., 2010) as templates respectively and gene blocks (IDT) for the N-terminal part of the proteins and cloned into a pGW2-HA backbone using *AscI* and *BamHI* sites; peBioGFP-TANC2, b-actin-GFP-TANC2, b-actin-myc-tagRFP-TANC2 were generated using as template pGW2-HA-TANC2; b-actin-GFP-TANC2(1-832, 833-1227, 1228-1500, 1501-1900) were created by PCR strategies and cloned into b-actin-GFP vector using *AscI* and *BamHI* sites; pGW2-HA-TANC2_R760C and pGW2-HA-TANC2_R1066X were generated by Gibson cloning using pGW2-HA-TANC2_WT as template for PCRs and a pGW2-HA linearized backbone; b-actin-GFP-TANC2_R760C and b-actin-GFP-TANC2_R1066X were generated by PCR based strategies using b-actin-GFP-TANC2 as backbone and pGW2-HA-TANC2_R760C and pGW2-HA-TANC2_R1066X as templates for PCR reactions. pGW1-NF186-GFP-TANC2(1-832_WT) and (1-832_R760C) were produced by PCRs based strategies using b-actin-GFP-TANC2_WT or _R760C as templates and by cloning these PCRs products into a pGW1-NF186 (Kuijpers et al., 2016) backbone using *AscI/XbaI* sites.

The following shRNA sequences are used in this study: TANC2#1 (5'-CCTCAGTCAAGGGTCATAT-3'), TANC2#2 (5'-GGAGCTGAAACCGAAATCT-3') and TANC2#3 (5'-GGCCAGTAAATACCAATCT-3') targeting rat TANC2 mRNA (XM_008768351.1) were designed using the siRNA selection program at the Whitehead Institute for Biomedical Research (jura.wi.mit.edu/bioc/siRNAext) (Yuan et al., 2004) and the complementary oligonucleotides were annealed and inserted into a pSuper vector (Brummelkamp et al., 2002; Hoogenraad et al., 2005). ShRNA_KIF1A has been already described (Kevenaar et al., 2016) as well as shRNA_liprin- α 2, shRNA_liprin- α 3 (Spangler et al., 2013) and shRNA_cortactin (Jaworski et al., 2009). The control pSuper vector contains a scrambled sequence.

Primary hippocampal neuron cultures, transfections and drug treatments

Primary hippocampal cultures were prepared from embryonic day 18 rat brains. Cells were plated on coverslips coated with poly-L-lysine (30 μ g/ml) and laminin (2 μ g/ml) at a density of 100.000/well as previously described (Goslin and Banker, 1989; Kapitein et al., 2010). Hippocampal cultures were grown in Neurobasal medium (NB) supplemented with B27, 0.5 mM glutamine, 12.5 μ M glutamate and penicillin/streptomycin. Hippocampal neurons at DIV 11-14 / 14-17 were transfected using Lipofectamine 2000 (Invitrogen). Briefly, DNA (1.8 μ g/well, for a 12 wells plate) was mixed with 3.3 μ l of Lipofectamine 2000 in 200 μ l NB, incubated for 30 min, and then added to the neurons in NB at 37°C in 5% CO₂ for 45 min. Next, neurons were washed with NB and transferred in their original medium at 37°C in 5% CO₂ for 2-3 days. 10 μ M latrunculin B, 10 μ M jasplakinolide, 10 μ M BAPTA-AM or 40 μ M bicuculline were added to neuron cultures and fixed or imaged from 0 to 1h after addition.

Affinity Purification-Western blot (AP-WB) using biotin or GFP pull-down

Human Embryonic Kidney 293 cells (HEK293) cells were cultured in DMEM/Ham's F10 (50%/50%) containing 10% Fetal Calf Serum (FCS) and 1% penicillin/streptomycin at 37°C and 5% CO₂. HEK293 cells were transfected with pe-Biotin-GFP constructs in combination with BirA or with GFP tagged constructs using polyethylenimine (PEI, Polysciences) according to the manufacturer instructions. Cells were lysed 48h later in lysis buffer (50mM TrisHCl (PH 7.4-7.8), 100mM NaCl, 0.5% TX-100, 5mM MgCl₂, protease inhibitors (Roche)), centrifuged at 13.000 rpm for 15 min and the supernatants were incubated with either Streptavidin Dynabeads M-280 (Thermo Scientific) or GFP-trap beads (Chromotek) for 1h at 4°C. Beads were then separated using a magnet (Dyna, Invitrogen) and washed five times in washing buffer (20mM Tris HCl, 150mM KCl, 0.1% TritonX-100). Proteins were eluted from the beads by adding a 4x dilution of the sample buffer (8% SDS, 25% glycerol, 0.05M Tris pH 6.8, 400mM DTT and 40mg/l bromophenol blue). Samples were then boiled at 99°C for 10 minutes before being analyzed by SDS PAGE. Proteins were transferred on nitrocellulose membranes (Millipore) using a semi-dry blotting system. Membranes were blocked with 3% BSA in PBS-T (0.1% Tween-20) and incubated with primary antibodies (overnight at 4°C) in 3% BSA PBS-T. IRdye680 or IRdye800-conjugated secondary antibodies (Li-Cor) were diluted 1:20.000 in 3%BSA-PBST and applied for 1h at RT. Blots were acquired using a LICOR Odyssey scanner at 680nm or 800nm. To quantify the relative amount of a specific co-precipitated protein, the intensity of each band was measured and then normalized to the intensities

of the corresponding INPUT loading control band and to the intensity of the band relative to the purified bait protein. Quantifications were performed with Image J software (Universal Imaging Corporation).

Affinity Purification-Mass spectrometry (AP-MS) using biotin or GFP pull-down on rat brain extracts

Human Embryonic Kidney 293 cells (HEK293) cells were cultured in DMEM/Ham's F10 (50%/50%) containing 10% Fetal Calf Serum (FCS) and 1% penicillin/streptomycin at 37°C and 5% CO₂. HEK293 cells were transfected with pe-Biotin-GFP constructs in combination with BirA or with GFP-constructs using polyethylenimine (PEI, Polysciences) according to the manufacturer instructions. Cells were lysed 48h later in RIPA lysis buffer (50mM TrisHCl pH 7.4-7.8, 150mM NaCl, 1% Triton X-100, 0.1% SDS, 0.5% Sodium Deoxycholate and Protease inhibitors (Roche)), centrifuged at 13,000 rpm for 15 min and the supernatants were incubated for 1h at 4°C with either Streptavidin Dynabeads M-280 (Thermo Scientific) or GFP-trap beads (Chromotek), previously blocked in chicken egg albumin (Life Technologies). Beads were then separated using a magnet (Dyna, Invitrogen) washed twice in low salt washing buffer (20mM Tris-HCl pH 7.4-7.8, 100 mM KCl, 0.1% Triton X-100), followed by two washing steps in high salt wash buffer (20mM Tris-HCl pH 7.4-7.8, 500 mM KCl, 0.1% Triton X-100) and two final steps in low salt washing buffer (20mM Tris-HCl pH 7.4-7.8, 100 mM KCl, 0.1% Triton X-100) to remove binding proteins from HEK293 cells. Brains were obtained from female adult rats and homogenized in 10x volume/weight in tissue lysis buffer (50mM TrisHCl, 150mM NaCl, 0.1% SDS, 0.2% NP-40, and protease inhibitors). Brain lysates were centrifuged at 16,000 g for 15 min at 4°C and the supernatant was then incubated for 1h at 4°C with beads previously conjugated with either the biotinylated or the GFP-tagged proteins of interest. Beads were then separated using a magnet (Dyna; Invitrogen) and washed in normal washing buffer (20mM Tris HCl, 150mM KCl, 0.1% TritonX-100) for five times. For MS analysis, the beads were resuspended in 15 µl of Laemmli Sample buffer (Biorad), boiled at 99°C for 10 minutes and supernatants were loaded on 4-12% Criterion XT Bis-Tris precast gel (Biorad). The gel was fixed with 40% methanol and 10% acetic acid and then stained for 1h using colloidal coomassie dye G-250 (Gel Code Blue Stain Reagent, Thermo Scientific). Each lane from the gel was cut in 3 slices, destained and digested using trypsin, as described in (Ekkebus et al., 2013). Briefly, each lane from the gel was cut into three pieces and placed in 0.5-ml tubes. Gel pieces were then washed with 250 µl of water, followed by 15 min dehydration in acetonitrile. Proteins were reduced (10 mM dithiothreitol, 1h at 56°C), dehydrated and alkylated (55 mM iodoacetamide, 1h in the dark). After two rounds of dehydration, trypsin (Promega) was added to the samples (20 µl of 0.1 mg/ml trypsin in 50 mM Ammoniumbicarbonate) and incubated overnight at 37°C. Peptides were extracted with ACN, dried down and reconstituted in 10% formic acid prior MS analysis.

***In vitro* Co-purification of KIF1A using sepharose CaM beads**

Equal amounts of lysates from HEK293 cells transfected with KIF1A(657-1105_WT) or KIF1A(657-1105_5*Ala) were incubated for 4h at 4°C with Calmodulin-Sepharose beads (Biovision) with increasing µM concentration of Ca²⁺ or EDTA. Beads were then washed with normal washing buffer (20mM Tris HCl, 150mM KCl, 0.1% TritonX-100) for 3 times by centrifuging them at 1500g for 3min. Proteins were eluted from the beads by adding a 4x dilution of the sample buffer (8% SDS, 25% glycerol, 0.05M Tris pH 6.8, 400mM DTT and 40mg/l bromophenol blue). Samples were then boiled at 99°C for 10 minutes before being analyzed by SDS PAGE.

Immunoprecipitation on rat brain extracts

Rat brain extracts were obtained from female adult rats and homogenized in 10x volume/weight in tissue lysis buffer (50mM TrisHCl, 150mM NaCl, 0.1% SDS, 0.2% NP-40, and protease inhibitors). Brain lysates were centrifuged at 16,000 g for 15 min at 4°C and the supernatant was used for the immunoprecipitations. IPs were performed using Pierce Crosslink IP kit (Thermo Scientific) according to manufacturer recommended protocol. TANC1 rabbit (Abcam), TANC2 rabbit (Abcam), PanTANC (Han et al., 2010) were the antibodies used for the IP experiments.

Mass spectrometry analysis

All samples were analyzed on an ETD enabled LTQ-Orbitrap Elite coupled to Proxeon EASY-nLC 1000 (Thermo

Fisher Scientific, Odense, Denmark) or on an Orbitrap Q-Exactive mass spectrometer (Thermo Fisher Scientific, Bremen, Germany) coupled to an Agilent 1290 Infinity LC (Agilent Technologies). Peptides were loaded onto a trap column (Reprosil pur C18, Dr. Maisch, 100 μm x 2 cm, 3 μm ; constructed in-house) with solvent A (0.1% formic acid in water) at a maximum pressure of 800 bar and chromatographically separated over the analytical column (Poroshell 120 EC C18, Agilent Technologies, 50 μm x 50 cm, 2.7 μm) using 90 min linear gradient from 7-30% solvent B (0.1% formic acid in acetonitrile) at a flow rate of 150 nL/min. The mass spectrometers were used in a data-dependent mode, which automatically switched between MS and MS/MS. After a survey scan from 350-1500 m/z the 10 or 20 most abundant peptides were subjected to either CID or HCD fragmentation depending on the MS-spectrometer used. MS spectra were acquired in high-resolution mode ($R > 30,000$), whereas MS2 was in high-sensitivity mode ($R > 15,000$). For data analysis, raw files were processed using Proteome Discoverer 1.4 (version 1.4.1.14, Thermo Scientific, Bremen, Germany). Database search was performed using the Uniprot rat database and Mascot (version 2.5.1, Matrix Science, UK) as the search engine. Carbamidomethylation of cysteines was set as a fixed modification and oxidation of methionine was set as a variable modification. Trypsin was set as cleavage specificity, allowing a maximum of 2 missed cleavages. Data filtering was performed using a percolator (Kall et al., 2007), resulting in 1% false discovery rate (FDR). Additional filters were search engine rank 1 and mascot ion score >20 . The mass spectrometry proteomics data have been deposited to the ProteomeXchange Consortium via the PRIDE (Vizcaino et al., 2016) partner repository with the dataset identifier PXD010080.

Cross linking Mass Spectrometry (XL-MS)

For crosslinking experiment, the beads with affinity-precipitated proteins were incubated with 2 mM disuccinimidyl sulfoxide (DSSO; ThermoFischer Scientific) crosslinker for 1h at room temperature (Kao et al., 2011). The crosslinking reaction was quenched with 20 mM Tris-HCl for 20 min at room temperature. On-beads crosslinked proteins were denatured with 2 mM Urea, reduced with 4 mM dithiothreitol at 56°C for 30 min and then alkylated with 8mM iodoacetamide for 30 min in the dark. Proteins were partially digested using trypsin (Promega) at 37°C for 2h. The supernatant was removed from the beads, fresh aliquot of trypsin was added and further digested overnight at 37°C. Crosslinked protein digests were subsequently desalted and enriched with Strong Cation Exchange (SCX) Stage Tips. Obtained fractions were dried and stored at -80°C for further use.

Crosslinked peptide mixtures were reconstituted in DMSO/FA/HOH 5%/10%/85% (v/v/v) mixture and analyzed on an Orbitrap Fusion Lumos (ThermoFisher Scientific) coupled online to an Agilent UPLC 1290 system (Agilent Technologies). Crosslinked peptide digest was trapped on a pre-column (Reprosil pur C18, Dr. Maisch, 100 μm x 2 cm, 3 μm ; constructed in-house) for 10 min with buffer A (0.1% formic acid) and separated on an analytical column (Poroshell 120 EC C18, Agilent Technologies, 50 μm x 50 cm, 2.7 μm) over 65 min with a linear gradient from 10% to 40% B (B: 0.1% formic acid, 80% acetonitrile). MS data acquisition was performed using MS2_MS3 acquisition strategy: at the MS¹ level survey scan was recorded in Orbitrap (OT) at 60,000 resolution. For selected precursors collisional-induced dissociation (CID) was applied and signature peaks for the crosslinkers were recorded at 30000 resolution. Fragments exhibiting patterns associated to the DSSO cleavable crosslinker were further subjected to low-resolution MS³ scan in the ion trap (IT) (Kao et al., 2011; Liu et al., 2017). Raw data files were processed in Proteome Discoverer 2.2 with in-house developed nodes for crosslink analysis (Liu et al., 2015). The mass spectrometry proteomics data have been deposited to the ProteomeXchange Consortium via the PRIDE (Vizcaino et al., 2016) partner repository with the dataset identifier PXD010080.

Bioinformatic analysis

Gene ontology (GO) classification was obtained via PANTER (Mi et al., 2005). Statistical assessment of the AP-MS data was performed based on spectral counts using the SAINT (Significance Analysis of INTeractome, version 2.3.2) algorithm (Choi et al., 2011). The SAINT parameters were set as follows: nburn=2000, niter=20,000, lowmode=0, minfold=0, and norm=1. Bait proteins with a SAINT probability score >0.90 were considered putative protein interaction partners.

Immunofluorescent staining

Neurons were fixed for 10 min with 4% formaldehyde/4% sucrose in phosphate-buffered saline (PBS) at room temperature. After fixation cells were washed three times for 10 min in PBS, incubated for 10 min with permeabilization buffer (0.25% TritonX-100 in PBS) and then blocked for 1h with blocking buffer (2% BSA, 2% Glycin, 0.2% Gelatin, 50mM NH_4Cl , in PBS). Neurons were then incubated with primary antibodies diluted in blocking buffer overnight at 4°C, washed three times in PBS for 10 min and then incubated with Alexa-conjugated secondary antibodies in blocking buffer for 1h at room temperature. Neurons were then washed 3 times for 5 min in PBS at room temperature and subsequently mounted on slides in Vectashield mounting medium (Vector Laboratories). Confocal images were acquired using a LSM 700 confocal laser-scanning microscope (Zeiss) with a 40×1.3 N.A or 63×1.4 N.A. oil objective (Zeiss). Each image was a z-series of ~7-10 images, each averaged 2 times and was chosen to cover the entire region of interest from top to bottom. The resulting z-stack was “flattened” into a single image using maximum projection. Images were not further processed and were of similar high quality to the original single planes. The confocal settings were kept the same for all scans when fluorescence intensity was compared. Morphometric analysis, quantification, and co-localization were performed using ImageJ software (Universal Imaging Corporation). See for details the methods section: Image analysis and quantification.

Image analysis and quantification

Quantification of TANC2 knockdown efficiency by immunostaining in cultured hippocampal neurons

Efficiency of TANC2 shRNAs knock down was verified by immunostaining of endogenous TANC2 protein in hippocampal neurons co-transfected at DIV11 with 0.45 $\mu\text{g}/\text{well}$ GFP and 1.35 $\mu\text{g}/\text{well}$ of different TANC2-shRNAs or a mixture of all of them, and fixed 3 days later (DIV14). TANC2 staining (rabbit polyclonal anti-TANC2 antibody, Abcam) was measured both in the soma and in the neurites of GFP positive neurons and was compared to TANC2 corresponding staining in GFP negative surrounding cells within the same image. Images were acquired using a LSM 700 confocal laser-scanning microscope (Zeiss) using a plan-apo 40×1.3 N.A with the same settings and the exposure time and taking series of stacks from the bottom to the top. Maximum intensity projections were created using ZEN 2014 software (Zeiss) and later used for the analyses. ImageJ was used to manually draw specific regions of interest (ROI) located in the soma and in at least three primary neurites. From the ROIs the mean intensity was then measured. To prevent selection bias during quantification, the regions of interest in TANC2-KD neurons were selected in one channel (GFP) and blindly quantified in the other channel (TANC2 intensity). Intensities were measured in segments of approximately the same size, both in GFP positives and GFP negatives neurons. To remove the background signal, the intensity near the selected areas (same segment size) was measured and subtracted to the measured intensities within the same image. Normalized intensities were averaged over multiple cells and a statistical analysis was performed with student's t test assuming a two-tailed and unequal variation.

Dendritic protrusions analysis

To highlight protrusions morphology, neurons were transfected at DIV11 and fixed at DIV14 using MARCKS-GFP as an unbiased cell-fill in combination with our constructs of interest up to a maximum of 1.8 μg of total DNA/well. Confocal images were acquired using a LSM700 confocal laser-scanning microscope (Zeiss) with a 63x oil objective. The confocal laser intensity settings were optimized for each neuron. The resulting z-stack used for the spine counting was a single image processed by using the maximum projection function of ZEN2014 software (Zeiss). Images were not further processed and were of similar high quality to the original single planes. Morphological analysis and quantification were performed using ImageJ. For each neuron three dendrites were selected and boxes of 20 μm of length were placed 20 μm from the soma. Within these boxes the number of mushroom, filopodia-like and stubby spines were counted manually by using the Cell Counter plugin.

Quantification of fluorescent intensity in neurons

For the quantification of fluorescent intensity, images were acquired on a LSM700 confocal microscope (Zeiss) using a plan-apo 40×1.3 N.A objective and intensity of signals in the cell body and neurites were measured using ImageJ software. Because neurites often crossed several z planes, series of stacks were taken from the bottom to the top and the

ZEN 2014 software (Zeiss) was used to generate image projections for quantitative analyses. To prevent selection bias during quantification, the neurites segments were selected in one channel (GFP, RFP or BFP to visualize neuronal morphology) and quantified in the other channel. To control for background signals the intensity of an area of the same size was measured near the selected neuron and the measured random fluorescent intensity was subtracted in these images. Intensities were averaged over multiple cells and normalized.

Quantification of KIF1A and DCV distribution in dendritic spines

To highlight protrusions morphology, neurons were transfected at DIV14 and fixed at DIV17 using MARCKS-BFP as an unbiased cell-fill in combination with our constructs of interest (KIF1A, NPY, Syt4) up to a maximum of 1.8 μg of total DNA/well. Confocal images were acquired using a LSM700 confocal laser-scanning microscope (Zeiss) with a 63x oil objective. The confocal laser intensity settings were optimized for each neuron. The resulting z-stack used for the counting was a single image processed with the maximum projection function of ZEN2014 software (Zeiss). To prevent selection bias during quantification, the selected dendritic fragments were selected in the BFP channel. For each neuron three dendrites were selected and boxes of 20 μm of length were placed approximately 20 μm from the soma; then KIF1A, NPY or Syt4 puncta were counted in each single spine along 20 μm as well as in the dendritic shaft. Ratios of puncta spines/shaft were then normalized for the total number of spines along 20 μm to correct for different spines densities in different conditions.

Live cell imaging and imaging processing

Live-cell imaging experiments were performed in an inverted microscope Nikon Eclipse Ti-E (Nikon), equipped with a Plan Apo VC 100x NA 1.40 oil or a 60x NA 1.40 oil, a Yokogawa CSU-X1-A1 spinning disk confocal unit (Roper Scientific), a Photometrics Evolve 512 EMCCD camera (Roper Scientific) and an incubation chamber (Tokai Hit) mounted on a motorized XYZ stage (Applied Scientific Instrumentation) which were all controlled using MetaMorph (Molecular Devices) software. Neurites that were in close proximity to the soma were selected for imaging.

Imaging and analysis of motility of NPY and Syt4 motility

Time-lapses were acquired with 1 sec intervals for 5min, later analyzed for motility of vesicles. Motility was analyzed by pseudocoloring 1st frame in green and 10th frame in red. Merging those frames revealed vesicles non-colocalizing (motile), partially and fully co-localizing (immotile).

Imaging and analysis of motility of KIF1A, NPY, Syt4 upon BAPTA treatment

For motility analyses, time-lapses were acquired with 1 sec intervals for 5min, later analyzed for motility of vesicles. BAPTA-AM or DMSO were pipetted to the sample at a final concentration of 10 μM . Motility was analyzed by pseudocoloring 1st frame in green and 10th frame in red. Merging those frames revealed vesicles non-colocalizing (motile), partially and fully co-localizing (immotile).

Imaging and analysis of motility of KIF1A, NPY upon bicuculline treatment

Time lapse images in GFP and RFP channels were carried at 1 frame per second intervals, for 10 minutes before addition of DMSO or bicuculline. Treatments were pipetted to the sample and imaging of the same field of view was carried for another 10 minutes. To analyze the mobility of KIF1A and NPY along neurites, 3-5 neurite segments were selected from each field of view. The same segments were selected from the time lapse taken before and after addition of treatments. Only segments that were of at least 15 μm in length and with minimal crossings by other neurites were selected for kymographs based analysis. Using Fiji software, segments were traced with a line-ROI and kymographs were separately created using the Multi Kymograph plugin. The number of KIF1A and co-localized, mobile KIF1A and NPY traces of each kymograph were manually counted.

Imaging and analysis of motility of KIF1A, NPY, Syt4 in combination with the scaffolding proteins liprin- α 2 and TANC2.

Time-lapses were acquired with 1 sec intervals for 5min, in neurons (DIV14, DIV17) co-transfected with GFP- or RFP-tagged TANC2 or liprin- α 2 in combination with GFP-, RFP- or mCherry-tagged KIF1A, NPY or Syt4. To analyze the mobility of DCVs along neurites, 3-5 neurite segments were selected from each field of view. To calculate the percentage of DCV pausing within or outside static TANC2/liprin- α 2 spots, kymographs were obtained and subsequently analyzed.

NPY was used as marker for DCVs. NPY pausing was calculated as percentage of the ratio of NPY pauses at TANC2/liprin- α 2 positive clusters on the total amount of NPY pauses.

Imaging and analysis of NPY motility in the axon initial segment (AIS) of neurons transfected with Neurofascin-TANC2 fusion proteins.

Time lapse images in GFP and RFP channels were carried at 5 frames per second intervals, for 50 seconds. Neurons (DIV11) were co-transfected with NPY-RFP in combination with NF186-GFP or NF186-GFP-TANC2(1-832_WT) or NF186-GFP-TANC2(1-832_R760C). The AIS of transfected neurons was clearly detectable in the green channel because of the accumulation of NF186 and NF186 chimeric proteins in this region. After the AIS was visualized in green, the RFP channel was used for the imaging of NPY vesicles in the same region. For the analysis, a z-projection of the average intensity of the movie was made and subtracted from the original movie to background fluorescence and non-moving particles. A line of approximately 10-20 μ m in each AIS was drawn. Kymographs of these lines were then created using KymoResliceWide plugin. Clearly visible anterograde and retrograde traces were traced on the kymos by drawing straight lines. Length and angle of the lines were measured and used to calculate velocity, run length and duration.

SUPPLEMENTAL REFERENCES

- Brummelkamp, T.R., Bernards, R., and Agami, R. (2002). Stable suppression of tumorigenicity by virus-mediated RNA interference. *Cancer Cell* 2, 243-247.
- Choi, H., Larsen, B., Lin, Z.Y., Breikreutz, A., Mellacheruvu, D., Fermin, D., Qin, Z.S., Tyers, M., Gingras, A.C., and Nesvizhskii, A.I. (2011). SAINT: probabilistic scoring of affinity purification-mass spectrometry data. *Nat Methods* 8, 70-73.
- Ekkebus, R., van Kasteren, S.I., Kulathu, Y., Scholten, A., Berlin, I., Geurink, P.P., de Jong, A., Goerdal, S., Neefjes, J., Heck, A.J., *et al.* (2013). On terminal alkynes that can react with active-site cysteine nucleophiles in proteases. *J Am Chem Soc* 135, 2867-2870.
- Goslin, K., and Banker, G. (1989). Experimental observations on the development of polarity by hippocampal neurons in culture. *J Cell Biol* 108, 1507-1516.
- Han, S., Nam, J., Li, Y., Kim, S., Cho, S.H., Cho, Y.S., Choi, S.Y., Choi, J., Han, K., Kim, Y., *et al.* (2010). Regulation of dendritic spines, spatial memory, and embryonic development by the TANC family of PSD-95-interacting proteins. *J Neurosci* 30, 15102-15112.
- Hoogenraad, C.C., Milstein, A.D., Ethell, I.M., Henkemeyer, M., and Sheng, M. (2005). GRIP1 controls dendrite morphogenesis by regulating EphB receptor trafficking. *Nat Neurosci* 8, 906-915.
- Jaworski, J., Kapitein, L.C., Gouveia, S.M., Dortland, B.R., Wulf, P.S., Grigoriev, I., Camera, P., Spangler, S.A., Di Stefano, P., Demmers, J., *et al.* (2009). Dynamic microtubules regulate dendritic spine morphology and synaptic plasticity. *Neuron* 61, 85-100.
- Kall, L., Canterbury, J.D., Weston, J., Noble, W.S., and MacCoss, M.J. (2007). Semi-supervised learning for peptide identification from shotgun proteomics datasets. *Nat Methods* 4, 923-925.
- Kao, A., Chiu, C.L., Vellucci, D., Yang, Y., Patel, V.R., Guan, S., Randall, A., Baldi, P., Rychnovsky, S.D., and Huang, L. (2011). Development of a novel cross-linking strategy for fast and accurate identification of cross-linked peptides of protein complexes. *Mol Cell Proteomics* 10, M110 002212.
- Kapitein, L.C., Yau, K.W., and Hoogenraad, C.C. (2010). Microtubule dynamics in dendritic spines. *Methods Cell Biol* 97, 111-132.
- Kevenaar, J.T., Bianchi, S., van Spronsen, M., Olieric, N., Lipka, J., Frias, C.P., Mikhaylova, M., Harterink, M., Keijzer, N., Wulf, P.S., *et al.* (2016). Kinesin-Binding Protein Controls Microtubule Dynamics and Cargo Trafficking by Regulating Kinesin Motor Activity. *Curr Biol* 26, 849-861.
- Kuijpers, M., van de Willige, D., Freal, A., Chazeau, A., Franker, M.A., Hofen, J., Rodrigues, R.J., Kapitein, L.C., Akhmanova, A., Jaarsma, D., and Hoogenraad, C.C. (2016). Dynein Regulator NDEL1 Controls Polarized Cargo Transport at the Axon Initial Segment. *Neuron* 89, 461-471.

- Lee, J.R., Shin, H., Ko, J., Choi, J., Lee, H., and Kim, E. (2003). Characterization of the movement of the kinesin motor KIF1A in living cultured neurons. *J Biol Chem* 278, 2624-2629.
- Liu, F., Lossl, P., Scheltema, R., Viner, R., and Heck, A.J.R. (2017). Optimized fragmentation schemes and data analysis strategies for proteome-wide cross-link identification. *Nat Commun* 8, 15473.
- Liu, F., Rijkers, D.T., Post, H., and Heck, A.J. (2015). Proteome-wide profiling of protein assemblies by cross-linking mass spectrometry. *Nat Methods* 12, 1179-1184.
- Mi, H., Lazareva-Ulitsky, B., Loo, R., Kejariwal, A., Vandergriff, J., Rabkin, S., Guo, N., Muruganujan, A., Doremieux, O., Campbell, M.J., *et al.* (2005). The PANTHER database of protein families, subfamilies, functions and pathways. *Nucleic Acids Res* 33, D284-288.
- Schatzle, P., Ster, J., Verbich, D., McKinney, R.A., Gerber, U., Sonderegger, P., and Mateos, J.M. (2011). Rapid and reversible formation of spine head filopodia in response to muscarinic receptor activation in CA1 pyramidal cells. *J Physiol* 589, 4353-4364.
- Schlager, M.A., Kapitein, L.C., Grigoriev, I., Burzynski, G.M., Wulf, P.S., Keijzer, N., de Graaff, E., Fukuda, M., Shepherd, I.T., Akhmanova, A., and Hoogenraad, C.C. (2010). Pericentrosomal targeting of Rab6 secretory vesicles by Bicaudal-D-related protein 1 (BICDR-1) regulates neuritogenesis. *EMBO J* 29, 1637-1651.
- Spangler, S.A., Schmitz, S.K., Kevenaar, J.T., de Graaff, E., de Wit, H., Demmers, J., Toonen, R.F., and Hoogenraad, C.C. (2013). Liprin-alpha2 promotes the presynaptic recruitment and turnover of RIM1/CASK to facilitate synaptic transmission. *J Cell Biol* 201, 915-928.
- van Beuningen, S.F.B., Will, L., Harterink, M., Chazeau, A., van Battum, E.Y., Frias, C.P., Franker, M.A.M., Katrukha, E.A., Stucchi, R., Vocking, K., *et al.* (2015). TRIM46 Controls Neuronal Polarity and Axon Specification by Driving the Formation of Parallel Microtubule Arrays. *Neuron* 88, 1208-1226.
- van der Vaart, B., van Riel, W.E., Doodhi, H., Kevenaar, J.T., Katrukha, E.A., Gumy, L., Bouchet, B.P., Grigoriev, I., Spangler, S.A., Yu, K.L., *et al.* (2013). CFEOM1-associated kinesin KIF21A is a cortical microtubule growth inhibitor. *Dev Cell* 27, 145-160.
- Vizcaino, J.A., Csordas, A., Del-Toro, N., Dienes, J.A., Griss, J., Lavidas, I., Mayer, G., Perez-Riverol, Y., Reisinger, F., Ternent, T., *et al.* (2016). 2016 update of the PRIDE database and its related tools. *Nucleic Acids Res* 44, 11033.
- Yuan, B., Latek, R., Hossbach, M., Tuschl, T., and Lewitter, F. (2004). siRNA Selection Server: an automated siRNA oligonucleotide prediction server. *Nucleic Acids Res* 32, W130-134.



CHAPTER 4

Kinesin-3 mediated transport: towards a better understanding of KIF1A and KIF13B regulation

Riccardo Stucchi^{1,2,3}, Jessica J.A. Hummel¹,
A.F. Maarten Altelaar^{2,3}
and Casper C. Hoogenraad¹

¹ Cell Biology, Department of Biology, Faculty of Science, Utrecht University, Padualaan 8, 3584 Utrecht, the Netherlands

² Biomolecular Mass Spectrometry and Proteomics, Bijvoet Center for Biomolecular Research and Utrecht Institute for Pharmaceutical Sciences, Utrecht University, Padualaan 8, 3584 Utrecht, the Netherlands

³ Netherlands Proteomics Centre, Padualaan 8, 3584 Utrecht, the Netherlands

ABSTRACT

The ability of a cell to transport cargo vesicles to their correct destination is called selective transport. Neurons, being cells of complex architecture, heavily rely on MT-based transport to develop and function properly. Kinesin-mediated transport is implicated in the anterograde transport of vesicles both in the axon and in dendrites. The focus of this work is to understand the mechanisms responsible for kinesin-driven vesicle transport in neurons. For this reason we investigated the role of two kinesin-3 family members – KIF1A and KIF13B – in binding and transporting neuronal vesicle populations. To this end, we first tested their capability to interact with specific brain adaptor proteins by performing affinity purification – Mass Spectrometry (AP-MS) experiments using a series of kinesin tail domains. KIF1A and KIF13B are characterized by a similar structural domain organization, nevertheless they bind distinct groups of proteins, suggesting different selectivity towards different adaptors. Next, by using these C-terminal tail fragments in combination with the axon-selective KIF5C motor domain (KIF5C(1-560)) we performed a split kinesin assay in hippocampal neurons to investigate their potential association with different populations of dendritic vesicles. When the split kinesins are assembled, only the bound vesicles are misdirected into the axon. Results show that the Dense Core Vesicle (DCV) related protein NPY is selectively transported by KIF1A, while the endocytic marker Transferrin Receptor (TfR) shows positive association only with KIF13B. The C-terminal regions of both kinesins (1105-1698 for KIF1A and 832-1826 for KIF13B) are essential in kinesin-driven transport. On the contrary, middle regions (657-1105 for KIF1A and 442-832 for KIF13B) are not directly involved in the interaction with vesicles. These data indicate that the post synaptic scaffolds associated with KIF13B and KIF1A middle regions (MBS, MAGUK binding stalk, and LBS, liprin binding site, respectively) are not required for motor-cargo transport. Based on these findings, we conclude that disc-large proteins (DLGs) and liprin- α proteins might play different regulatory roles on the motors and/or might affect the distribution and delivery of vesicles by acting as immobile signposts in neurons.

INTRODUCTION

Kinesins are the motor proteins able to transport vesicles to the plus end of microtubules (MTs). Kinesins are typically composed of two general modules: the motor domain, which binds MTs and the tail domain which is responsible for cargo binding. Kinesin tail domains contains specialized regions responsible for the interaction with adaptor proteins, which are supposed to mediate the association with vesicle cargos (Hirokawa et al., 2010). Several studies have successfully described which kinesin interacts with which cargo (Schlager and Hoogenraad, 2009), however, these works do not investigate in detail which are the functional domains required for the kinesin-cargo loading and which adaptor proteins are essential in facilitating the motor-cargo interaction.

The kinesin-3 family (KIF) consists of five subfamilies in mammals (KIF1, KIF13, KIF14, KIF16, and KIF28). KIF1A is characterized by the presence of a C-terminal Pleckstrin Homology (PH) domain capable of binding to PIP₂ containing vesicles (Klopfenstein et al., 2002; Klopfenstein and Vale, 2004). However, it is unclear whether this interaction has a supporting role in stabilizing the kinesin-cargo interaction or it is actually how KIF1A interacts with vesicles. KIF1A was originally shown to be involved in the transport of synaptic precursor proteins (Hall and Hedgecock, 1991; Okada et al., 1995). The regulatory molecular mechanism at the base of this transport was described few years later and relies on the capability of KIF1A to bind selectively only the GTP-bound form of Rab3 on synaptic vesicles (SVs) through the adaptor protein DENN/MADD (Niwa et al., 2008). At the same time this kinesin can also transport dendritically polarized cargos (Jenkins et al., 2012; Karasmanis et al., 2018; Stucchi et al., 2018). Dense Core Vesicles (DCVs) can be specifically transported by this kinesin-3 family member both in the axon and in dendrites (Barkus et al., 2008; de Wit et al., 2006; Lo et al., 2011; Lochner et al., 2008; Zahn et al., 2004). KIF1A stalk domain was also shown to associate with liprin- α , which is a scaffolding protein for AMPA receptors in dendrites (Shin et al., 2003). Besides interacting with liprin- α , KIF1A co-precipitated with GRIP, GluR2/3, synaptotagmin, RIM, which are proteins enriched in the post-synaptic compartment (Shin et al., 2003). Despite these biochemical evidences, currently there are no direct evidences of KIF1A transporting liprin- α associated vesicles. In this perspective, further investigations are required to understand whether this protein complex directly modulates DCV trafficking or recruits DCVs at synaptic sites.

KIF13B is another kinesin-3 family member (Lawrence et al., 2004) which similarly to KIF1A, has been reported to act in axonal and dendritic transport in neurons (Horiguchi et al., 2006; Jenkins et al., 2012). KIF13B was originally named GAKIN (guanylate kinase-associated kinesin) (Asaba et al., 2003; Hanada et al., 2000) and is known to transport PIP₃-containing

vesicles through the interaction with the adaptor protein centaurin- α 1 (Horiguchi et al., 2006). Interestingly, centaurin- α 1 is a regulator of dendritic branching and dendritic spine formation in neurons (Miyazaki et al., 2005; Moore et al., 2007). The tail domain of KIF13B is also capable of binding to vesicles that contain Transferrin Receptor (TfR), a dendritically polarized protein (Jenkins et al., 2012). The middle region of KIF13B contains a MAGUK binding site (MBS) domain responsible for the interaction with the guanylate kinase (GUK) domain of DLG1 (SAP-97) (Hanada et al., 2000), as well as with the GUK domain of DLG4 (PSD-95) (Mok et al., 2002; Zhu et al., 2016). PSD-95 and SAP-97 are scaffolding proteins in the post-synaptic compartment and are suggested to regulate AMPA and NMDA receptors trafficking in dendritic spines (Mauceri et al., 2007; Rumbaugh et al., 2003; Sans et al., 2001; Schluter et al., 2006). In neurons SAP-97 can also act as an endocytic scaffold, forming a complex with Myo6 and AP-2, favoring the internalization of AMPARs (Osterweil et al., 2005). As in the case of liprin- α in relationship with KIF1A, currently there is not a clear consensus whether these DLG proteins operate by directly coupling KIF13B to cargos, such as AMPARs/NMDARs and other membrane components, or work as synaptic posts by tethering KIF13B-driven cargos to the plasma membrane.

In this context, we performed a systematic Affinity Purification (AP) proteomic screening using different KIF1A and KIF13B fragments in search for novel binding proteins. This MS-based approach allowed us to successfully identify their complete interactomes in cells and rat brains and pinpoint the functional domains involved in the interactions. To get further insights into the biological relevance of these data we then used the same kinesin truncations in a split kinesin assay in hippocampal neurons (Jenkins et al., 2012). Results indicate that the KIF1A binding proteins (liprin- α and TANC2) and the KIF13B binding proteins (DLGs) are not directly required for the transport of NPY and TfR positive vesicles, respectively. Therefore we conclude that these PSD proteins are not mobile adaptor proteins for KIF1A- and KIF13B-driven vesicles but work as immobile synaptic clusters, recruiting vesicles at specific sites, as we previously hypothesized ((Stucchi et al., 2018), Chapter 3). Taken together, our findings clarify the role of these kinesin-3 interactors in respect to DCV (NPY) and endocytic vesicle (TfR) transport in neurons.

RESULTS

Characterization of KIF1A and KIF13B neuronal interactomes

The kinesin-3 family protein KIF1A is a neuron specific motor protein characterized by a motor domain, a Forkhead-Associated (FHA) domain, three coiled-coils, a stalk domain and a C-terminal PH domain responsible for lipid binding (Klopfenstein et al., 2002; Soppina

et al., 2014) (Figure 1A). The regulatory regions in the middle part have been reported to be important for the dimerization and for the consequent relief of KIF1A auto-inhibition (Hammond et al., 2009; Soppina et al., 2014). Furthermore, cargo binding has been shown to favor KIF1A dimerization and processivity (Huo et al., 2012). However it is not clear which KIF1A regulatory adaptor proteins play direct roles in cargo loading and cargo-induced kinesin activation. Similarly KIF13B comprises an N-terminal motor domain, a FHA domain, a MBS domain, a Cytoskeleton-Associated Protein-Glycine-rich (CAP-Gly) domain and several coiled coils, whose functions are still unclear (Figure 1B).

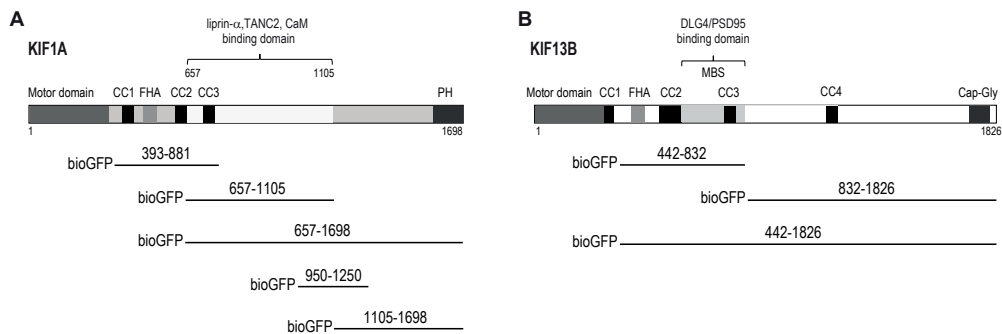


Figure 1. KIF1A and KIF13B fragments

(A) Schematic representation of KIF1A domains and bioGFP-KIF1A(393-881, 657-1105, 657-1698, 950-1250, 1105-1698) fragments used for AP-MS.

(B) Schematic representation of KIF13B domains and bioGFP-KIF13B(442-832, 832-1826, 442-1826) fragments used for AP-MS.

Several proteins have been found associated with KIF13B (in particular with the MBS domain) but despite extensive biochemical characterization still little is known about their possible roles in recruiting KIF13B to exocytotic and/or endocytotic carriers. To get a better understanding into these aspects we performed AP-MS on different KIF1A and KIF13B tail domains (FIGURE 1A-B). Briefly, we transiently expressed 5 bioGFP-KIF1A (383-881, 657-1105, 657-1698, 950-1250, 1105-1698), 3 bioGFP-KIF13B fragments (442-832, 832-1828, 442-1832) and bioGFP control, together with the protein-biotin ligase BirA in HEK293 cells. The bioGFP tagged proteins were purified with streptavidin beads and incubated with rat brain lysates. Co-isolated proteins were then analyzed by MS. Among the list of putative interacting proteins, we selected candidate KIF1A or KIF13B binding partners with a probability >0.95 using the SAINT algorithm for scoring our AP-MS data (Choi et al., 2011) (Table 1-2). To distinguish brain-specific interactors, complementary AP-MS experiments were performed in HEK293 samples not supplemented with brain extracts (Table 3-4). The KIF1A interactome was already described

in (Stucchi et al., 2018, Chapter 3, Figure 1). These data clearly indicate that a subgroup of PSD scaffolding proteins (liprin- α , TANC2, Shank and Homer) mainly binds KIF1A middle region (657-1105) (Table 1). Similarly, our MS analysis of KIF13B interactome, allowed us to identify several KIF13B neuronal interactors and precisely map their binding sites (Table 2). In this case, very distinct groups of proteins bind specifically either the middle part (442-832) or the C-terminus of the protein (832-1826). As expected, PSD proteins such as PSD-95, PSD-93 and SAP-97 were categorized among the most significant interactors of the MBS middle region (Yamada et al., 2007; Zhu et al., 2016). Other SAP-97 interaction partners such as LIN7 and CASK were also co-precipitated (Bohl et al., 2007; Lee et al., 2002), indicating that these scaffolds can form a protein complex together with KIF13B in the brain as well. From these data we could conclude that KIF1A LBS domain (657-1105) and KIF13 MBS (44-832) show a high degree of selectivity towards different sub-class of PSD and dendritic proteins (Table 1-2). Brain centaurin- α 1 (Adap1) was found in association only with full tail of KIF13B (Table 2), further confirming their direct interaction (Tong et al., 2010; Venkateswarlu et al., 2005) and supporting a role for this protein in accumulating KIF13B at the actin cytoskeleton at the leading edges of cells (Kanai et al., 2014; Venkateswarlu et al., 2004). Centaurin- α 1 binds PIP₃ and filamentous actin and interacts with the clathrin coat adaptor AP-3 (Bendor et al., 2010; Nie and Randazzo, 2006), which interestingly was also found enriched in KIF13B AP (Ap3m1, Ap3m2; Table 2). An interactor that specifically binds the C-terminal part of KIF13B tail (832-1826) is Utrophin (Utrn). Utrophin is a large cytoskeletal scaffolding protein, which was recently shown to bind to KIF13B in a complex that mediates endocytosis of the low density Lipoprotein Receptor-related Protein 1 (LRP1) (Kanai et al., 2014). Apart from utrophin, the coiled-coils C-terminal region of KIF13B could also co-precipitate Syntrophin (Snt) and Dystrobrevins (Dtn) (Table 2), which are direct binding partners of this scaffold at the plasma membrane (Kramarcy et al., 1994; Peters et al., 1997). These proteins are part of the Dystrophin Associated Protein Complex (DAPC) which has been recently shown to act as a linker between actin cytoskeleton and MTs. Similarly, DAPC have been identified as main binding partners of the C-terminal region of KIF1A (657-1698) (Table 1). In accordance with these results we can conclude that synaptic PSD proteins bind the MBS and LBS (middle regions) of these kinesins, while Dystrophin associated proteins tightly associate with their C-terminal parts. It is therefore tempting to speculate that the two kinesins, by using similar domains to interact with similar protein groups might be subjected to similar regulations. Besides distinct similarities, their association with different sub-class of PSD and dendritic proteins might underlie their selectivity towards different types of cargos and their specialized different functions in neurons.

KIF13B and KIF1A have similar MBS domains that mediate binding to different PSD proteins

In order to identify putative structural similarities between the two motors we then decided to search for conserved amino acid sequences. Interestingly the MBS of KIF13B shows high degree of homology with a region included in the stalk domain (675-1105) of KIF1A, the LBS (Figure 3A). By using I-TASSER (Iterative Threading ASSEMBly Refinement) (Yang et al., 2015), we applied a homology modelling approach superimposing KIF1A on the structure of KIF13B MBS (Figure 2A), which was previously resolved by X-Ray crystallography in complex with DLG4/PSD-95 (Zhu et al., 2016) (Figure 2B). This *in silico* analysis allowed us to infer the structure of a similar MBS-like domain on KIF1A, with high confidence (TmScore=0.94) (Figure 2C). We then confirmed that a KIF13B minimal fragment, spanning residues 663-862 and including the MBS domain, was sufficient for binding PSD-95 (Figure 2D), as also previously reported by (Zhu et al., 2016). Similarly to this association between PSD-95 and KIF13B, we recently demonstrated that other PSD scaffolding proteins such as liprin- α and TANC2 directly interact with the stalk domain (657-1105) of KIF1A (Stucchi et al., 2018). As next step, we experimentally verified our *in silico* structural predictions by producing a smaller KIF1A fragment, spanning residues 657-864, and homologous to KIF13B MBS (663-862) and by testing its ability of binding liprin- α and TANC2. As expected, AP-WB results show that this shorter KIF1A fragment (657-864) can co-precipitate with both liprin- α and TANC2 (Figure 2E). These data demonstrate that KIF1A uses a domain structurally related to the MBS of KIF13B for the interaction with PSD proteins. Furthermore our results indicate that PSD-95 interacts specifically with the MBS domain of KIF13B but not with KIF1A (Figure 2D). Similarly, liprin- α binds the predicted MBS-like domain of KIF1A but not KIF13B (Figure 2E), confirming the high selectivity of these regions. Altogether these data suggest that although these MBS regions are highly conserved, small amino acid sequence variations could drastically change their binding specificities for different scaffolding proteins. Based on the above findings and on the recently characterized molecular structure of KIF13B in complex with PSD-95 (Figure 2F), we generated a homology based model of KIF1A in complex with the predicted binding regions of liprin- α and TANC2 (Figure 2G-H). These structures highlight the importance of specific coiled-coil regions within the MBS of KIF13B and the LBS of KIF1A in mediating the binding with their substrates (PSD-95 and liprin- α /TANC2, respectively). Our hypothesis is that small amino acid variations within these structurally folded coiled-coil regions have been allowed by evolution in order to achieve selectivity towards different groups of scaffolding proteins. As proof of that, altogether our results indicate that different members of the kinesin-3 family have very unique and characteristic binding affinities for their

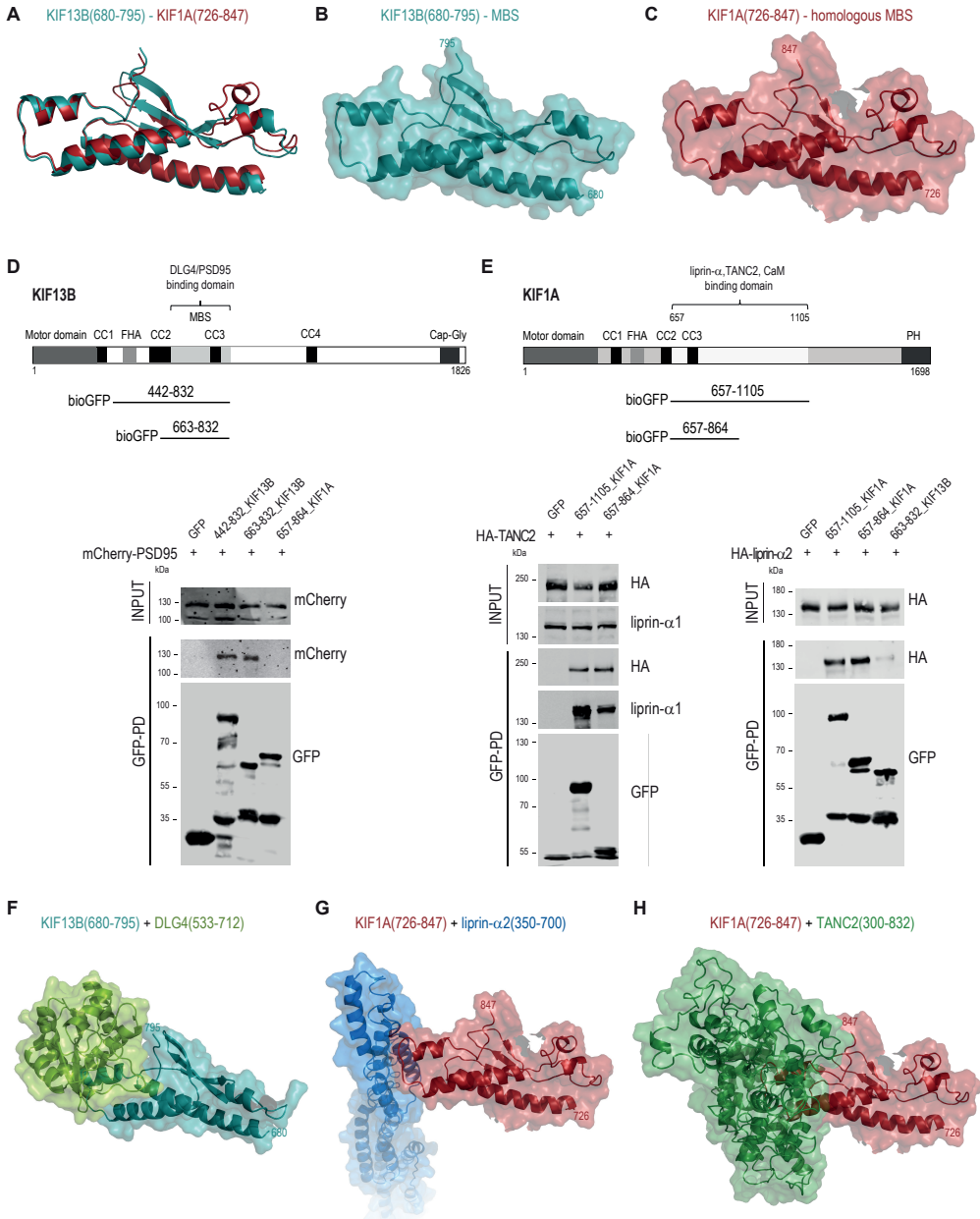


Figure 2. The MBS of KIF13B and a similar MBS “like” domain of KIF1A bind to specific PSD proteins

(A) Superimposed ribbon structures of KIF13B(680-795) (cyan) and KIF1A(726-847) (red).

(B) Ribbon and surface structure of KIF13B-MBS domain(680-795) (PDB: 5B64).

(C) Ribbon and surface structure of KIF1A-MBS”like” domain(726-847).

(D) Schematic representation of bioGFP-KIF13B fragments (442-832, 663-832) used to map the minimal binding site to PSD-95 (top panel). Western Blots of mCherry-PSD-95 in AP of bioGFP-KIF13B(442-832, 663-832) and bioGFP-KIF1A(657-864) (bottom panel).

(bottom panel).

(C) Schematic representation (top panel) and corresponding ribbon structures (bottom) of bioGFP-KIF1A(657-864, 657-813) fragments used for AP-WB. Western Blots of HA-TANC2 and liprin- α in AP of bioGFP-KIF1A(657-864, 657-813) (bottom panel).

interacting synaptic scaffolds. Interestingly, both minimal binding regions, besides being quite homologous with each other, contain well-defined coiled-coil motifs within their sequences (KIF1A CC3=802-825; KIF13B CC3=752-772). When part of this coiled-coil motif (CC3) was removed from the KIF13B MBS region (663-832), the binding between KIF13B (663-762) and the GUK domain of PSD-95 was completely abolished (Figure 3B). These data are consistent with a previous work which hypothesized a critical role for the second alpha helix of this CC region in mediating the interaction with GUK substrates (Zhu et al., 2016). Key residues located on this specific alpha helix, which have been demonstrated to be critical for the PSD-95/KIF13B interaction are not conserved among the kinesin-3 family proteins (Zhu et al., 2016), further supporting the selectivity and specificity of this binding. Consistent with this observation, when the homologous alpha helix (part of the CC3) was removed from the KIF1A LBS (657-864) the binding between KIF1A (657-813) and the scaffolds TANC2 and liprin- α was not affected (Figure 3C). These data contribute to further narrow the interfaces involved in the binding and clearly indicate that an alpha helical region in the CC3 is the motif directly required to mediate the association between KIF13B and PSD-95. In the case of KIF1A, the presence of alternative alpha helical regions downstream in the sequence might be sufficient to stabilize the interaction with the scaffolds.

KIF1A and KIF13B do not require liprin- α and DLG proteins to transport DCVs and TfR respectively

To verify the net effect of each single KIF1A and KIF13B domain on vesicle transport we decided to use several kinesin-3 fragments in a split kinesin assay in neurons. The split kinesin assay was firstly optimized by the Banker lab (Jenkins et al., 2012) and in its original version consists of an imaging based approach to identify kinesins interacting with different fluorescently labeled vesicle population. In brief, two separate constructs are simultaneously expressed, one encoding a kinesin tail domain and the other a kinesin motor domain that can be assembled together into a fully functional kinesin using a linker drug. In our experiments different KIF1A and KIF13B tail fragments were tested (Figure 4A-B) in combination with the motor domain of KIF5C (KIF5C(1-559)) which has a strong bias for transport into the axon. The KIF5C motor domain walks constitutively along microtubules in the axon but it is incapable of transporting vesicles which require regions included in the tail domain for their movement. KIF5C(1-559) is fused to the FK506 binding protein (FKBP) and the KIF1A/KIF13B tail domains are fused

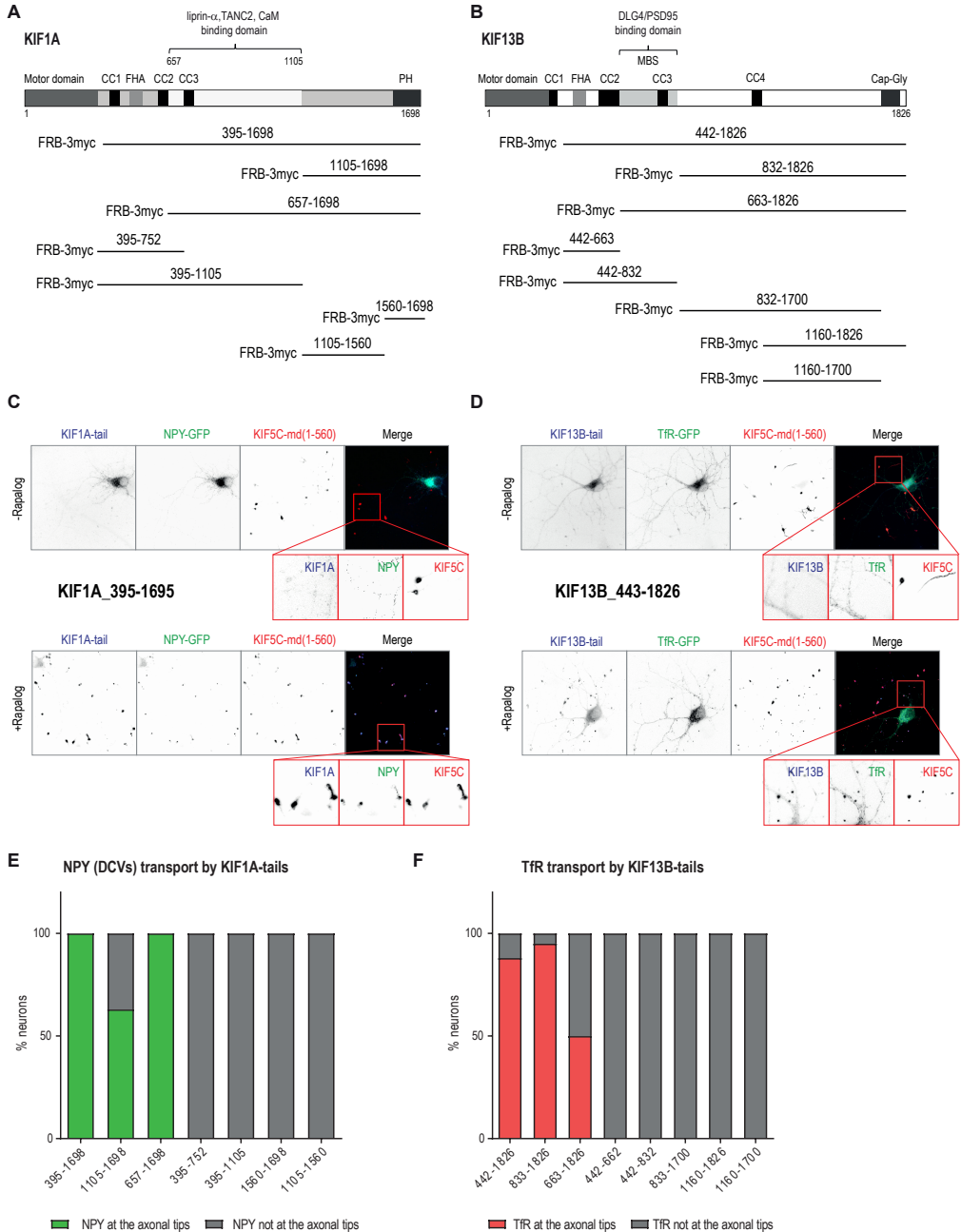


Figure 4. KIF1A and KIF13B do not require their MBS domains to transport DCV and TfR respectively

A) Schematic representation of FRB-KIF1A(395-1698, 1105-1698, 657-1698, 393-752, 395-1105, 1560-1698, 1105-1560) fragments used for the split kinesin assay in combination with KIF5C(1-560)-FKBP.

B) Schematic representation of FRB-KIF13B (442-1826, 832-1826, 663-1826, 442-663, 442-832, 832-1700, 1160-1826, 1160-1700) fragments used for the split kinesin assay in combination with KIF5C(1-560)-FKBP.

C) Representative pictures showing NPY-GFP (green) accumulation at the axonal tips after addition of Rapalog in neurons co-transfected with FRB-KIF1A(396-1698) full tail (blue) and KIF5C(1-560)-FKBP (red). KIF1A-tail specifically transports NPY but failed in transporting TfR.

D) Representative pictures showing TfR-GFP (green) accumulation at the axonal tips after addition of Rapalog in neurons co-transfected with FRB-KIF13B(442-1826) full tail (blue) and KIF5C(1-560)-FKBP (red). KIF13B-tail specifically transports TfR but failed in transporting NPY.

E) Bar graph shows quantifications relative of the percentage of transfected neurons showing NPY accumulation at the axon tips upon Rapalog addition. KIF1A(395-1698, 1105-1698, 657-1698) show positive association between the motor-tail complex and NPY, resulting into vesicle transport in the axon.

F) Bar graph shows quantifications relative of the percentage of transfected neurons showing TfR accumulation at the axon tips upon Rapalog addition. KIF13B(442-1826, 833-1826, 663-1826) show positive association between the motor-tail complex and TfR, resulting into vesicle transport in the axon.

to the FKBP12-rapamycin binding (FRB) domain. Only upon addition of the drug Rapalog, the FKBP and FRB domains can be efficiently linked together (Kapitein et al., 2010) resulting in motor-tail assembly. This assembly is expected to cause a rapid and profound change in the trafficking pattern of the vesicles binding the kinesin tail domain. NPY-GFP was used as marker for DCVs and TfR, as marker for endocytotic vesicles. In our experiments, NPY or TfR were redistributed from dendrites and soma to the axonal tips only in case of positive association with a kinesin tail domain. In a test experiment, NPY positive vesicles were redistributed to the axon and accumulated at the tips specifically by the full tail of KIF1A (395-1698) (Figure 4C) but not by KIF13B while TfR could be redistributed by KIF13B tail (443-1826) (Figure 4D) but not by KIF1A, after addition of the drug. These results confirm previous findings which described KIF1A as the primary motor protein for DCVs (Barkus et al., 2008; Lipka et al., 2016; Lo et al., 2011) and KIF13B as the main motor for endocytic vesicles (Jenkins et al., 2012). After demonstrating the reliability of this technique with the full length tails, we performed a systematic screening using shorter fragments based on functional domains of KIF1A and KIF13B (Figure 4A-B). To quantify the net effect of each single KIF1A domain on DCV trafficking, we decided to count the number of transfected cells showing a distinct accumulation of NPY at the axonal tips upon Rapalog addition in each condition. Results clearly indicate that only KIF1A(657-1698) and KIF1A(1106-1698) (and full tail-KIF1A(395-1698)) showed a positive assembly in the assay, resulting in NPY accumulation at the axonal tips (Figure 4E). Interestingly, KIF1A(1106-1698), despite missing the liprin- α /TANC2 binding domain, is capable of transporting DCVs, though with less efficacy (65% positive cells) compared to the longer fragment (Figure 3E). These results reveal that the C-terminal portion of the protein containing the PH domain is the essential region necessary and sufficient to recruit vesicles. A smaller fragment including the PH domain only (1560-1698) does not show any interaction with DCVs. This implies that additional spanning regions are required to stabilize the PH domain-

vesicle association. In agreement with these findings, KIF1A fragments containing the stalk domain but not the PH domain (395-1105, 395-752, 1106-1559) can not transport vesicles indicating that these middle domains are not sufficient for driving transport and strongly supporting a possible role for them in the regulation of kinesin activity. Altogether, these data bring us to the conclusion that liprin- α and TANC2, which are associated with a defined MBS-like region (657-864) in the stalk domain (657-1105) (Figure 2E), are not directly implicated in the transport.

An identical approach was used to test the ability of different KIF13B tail fragments to redistribute and accumulate TfR-GFP at the axonal tips. Quantifications show that apart KIF13B full tail (443-1826), only KIF13B (663-1826) and KIF13B (833-1826) could efficiently bind and transport TfR vesicles (Figure 3F). Similarly to KIF1A, these results indicate that the C-terminal of KIF13B is the region required to associate with vesicles, while the middle portions of the tail including the MBS or the FHA, failed in transporting TfR. Taken together these data suggest that DLG proteins which bind the MBS of KIF13B (663-862) (Figure 2D) are not directly required in the formation of the kinesin-cargo complex. Our conclusions have been taken using DCVs and TfR vesicles as KIF1A and KIF13B cargos respectively, however further investigations are needed to understand whether this is also true in the case of other type of kinesin-3 transported vesicles.

DISCUSSION

Defining how specific motors are selectively linked to their vesicular cargoes remains a challenging open question. Here we applied a combination of MS-based and imaging assays to identify potential new regulatory adaptor proteins of two kinesin-3 family members and understand their roles in relationship to cargo trafficking. AP-MS results clearly indicated the direct link between different KIF1A/KIF13B domains and specific binding partners. However this technique cannot elucidate the functional role of these newly identified interactions. In this perspective, the combined application of a systematic reliable and fast imaging approach as the split kinesin assay can enormously contribute to a better understanding. We showed that distinct groups of PSD scaffolds are associated with the MBS of KIF13B and with a homologous region on KIF1A (Table 1-2). DLG1 and DLG4 were previously reported to directly interact with KIF13B via its GUK domain (Hanada et al., 2000). Few studies have hypothesized that the DLG-KIF13B association is required for the correct loading and transport of proteins to the plasma membrane (Bolis et al., 2009; Marcello et al., 2007; Sans et al., 2001). Despite many indirect evidences, specific neuronal cargoes/proteins co-trafficked by the DLG1-KIF13B complex remain to be identified. In a similar way, the scaffolding protein liprin- α interacts with

a MBS-like region of KIF1A, and has been shown to be involved in cargo trafficking (Miller et al., 2005; Wagner et al., 2009; Wu et al., 2013). Also in this case, the putative role of liprin- α as adaptor protein linking KIF1A to vesicles still remains an open question. TANC2 and CASK are other PSD scaffolds with high affinity for the MBS of KIF1A, but they are also not part of the motile motor- vesicles complexes (Stucchi et al., 2018; Wu et al., 2016).

In this context, our results demonstrate that the KIF1A and KIF13B regions required for the interaction with these scaffolds are not necessary for KIF1A- and KIF13B-mediated transport of DCVs and TfR vesicles respectively. When using KIF1A(1105-1698) and KIF13B(883-1826) tails lacking these domains, we did register a reduction in the percentage of cells accumulating NPY and TfR at the tips (Figure 3E-F) compared to full length tails, but not a completely abolished transport as we would have expected in case these scaffolds had been required for transport. One reasonable explanation is that these proteins can work as signposts tethering vesicular trafficking proteins to the plasma membrane without directly affecting vesicle transport. We previously demonstrated that the synaptic scaffolds liprin- α 2 and TANC2 can affect the distribution of KIF1A-transported DCVs in spines but do not affecting their primary transport in the dendritic shaft (Stucchi et al., 2018). By using an analogous molecular mechanism, the scaffolding proteins DLGs can potentially recruit KIF13B-driven vesicles in different subset of spines (Kanai et al., 2014). Another explanation could be represented by an activating regulatory role for these proteins in respect to kinesin-3 family members. For example, DLG1/SAP-97 binds to KIF13B-MBS near a proposed auto-inhibitory region. It has been proposed that this association can relieve the auto-inhibitory mechanism of KIF13B, activating KIF13B motor activity (Yamada et al., 2007). Our data suggest that in absence of the MBS domain the accumulation of vesicles at the tips is only partial (50% reduction compared to FL) (Figure 4F) which could be explained by an incomplete activation of KIF13B. Also, in assays with KIF1A tails we showed that the accumulation at the tips is reduced in the construct missing the stalk domain compared to full length (Figure 4E). These findings suggest that DLG1 and liprin- α /TANC2 might act as molecular stimulators of KIF13B and KIF1A respectively, regulating the efficacy of the kinesin-mediated transport of vesicles. Future works are required to elucidate the accuracy of these proposed models.

Overall, these results also reveal new potential candidate proteins involved in trafficking. The C-terminal region (883-1826) of KIF13B could precipitate utrophin, syntrophin (Snt) and dystrobrevins (Dtn) (Table 2). KIF1A C-terminus (1105-1698) also shows high affinity for similar syntrophin (Snt) and dystrobrevins (Dtn) proteins (Table 1). These regions of both kinesins are also the minimal domains required for the vesicle transport. Based on these findings, we can hypothesize that a direct association between kinesin-3 members and Dystrophin

Associated Protein Complex (DAPC) might be an additional molecular event required for kinesin-driven transport. For a full understanding of the molecular dynamics behind the role of the DAPC complex in kinesin-mediated transport, future validations are necessary. Other kinesins such as KIF1B β , which possesses a C-terminal tail similar to KIF1A, or KIF16B, which has a C-terminal PX homology domain that binds PIP₃ on early endosomes (Hoepfner et al., 2005), could be subjected to similar molecular regulations. Summarizing, the data presented in this thesis chapter showed that a combination of proteomics techniques and imaging assays can be applied as a reliable approach to screen potential new adaptor proteins of different motor proteins and evaluate their contribution in cargo transport.

TABLES

Identified proteins			GFP		KIF1A (393-881)		KIF1A (657-1105)		KIF1A (657-1698)		KIF1A (950-1250)		KIF1A (1105-1698)	
Accession	gene name	Σ # Unique Peptides	# PSM	P-value	# PSM	P-value	# PSM	P-value	# PSM	P-value	# PSM	P-value	# PSM	P-value
F1MAA4	KIF1A	126	2	0	1096	1	803	1	1735	1	255	1	879	1
P82161	Calm1	13	0	0	7	1	47	1	51	1	1	0	0	0
Q6JLU4	Shank3	45	0	0	0	0	62	1	0	0	0	0	0	0
F1LSS0	Golga2	45	1	0	0	0	113	1	0	0	0	0	0	0
F1LTD	Tanc2	54	2	0	3	0.02	107	1	12	1	2	0	3	0.02
D3ZQJ3	Ggyl1	19	0	0	0	0	34	1	0	0	0	0	0	0
F1MAK3	Arhgap32	25	0	0	0	0	32	1	1	0	1	0	2	0.95
D3ZV3	Mad11	21	0	0	0	0	28	1	0	0	0	0	0	0
Q93Q74	Shank2	21	0	0	0	0	28	1	0	0	1	0	0	0
EP9L7	Ct	22	0	0	0	0	25	1	0	0	0	0	5	1
D3ZZ81	Ppf1a1	35	4	0	9	0.06	106	1	2	0	10	0.34	6	0
F1MB83	Ppf1a4	35	3	0	3	0	78	1	2	0	3	0	8	0.36
G3V917	Tanc1	1	0	0	0	0	18	1	0	0	0	0	0	0
Q9Z2X5	Homer3	11	0	0	0	0	15	1	0	0	0	0	0	0
Q55147	Utrn	14	0	0	0	0	15	1	1	0	0	0	0	0
Q9Z214	Homer1	23	1	0	0	0	30	1	2	0.19	0	0	0	0
D3ZDA2	Sema6d	11	0	0	0	0	13	1	0	0	0	0	0	0
Q62915	Cask	13	0	0	0	0	13	1	0	0	1	0	1	0
G3V8Q9	Apc	11	0	0	0	0	13	1	0	0	1	0	1	0
D3Z8E6	Camsap1	11	0	0	0	0	11	1	0	0	1	0	0	0
F1LS85	Sipa111	1	1	0	0	0	22	1	0	0	0	0	0	0
D4A7D3	Tbk1	18	2	0	0	0	30	1	1	0	0	0	2	0
Q4KMA0	Az12	5	0	0	0	0	9	1	0	0	0	0	0	0
F1MBA4	Ppf1a2	25	8	0	8	0	73	1	2	0	7	0	10	0
Q79Z0	Lin7c	4	0	0	0	0	6	1	1	0	0	0	0	0
F1M7S0	Mag3	6	0	0	0	0	6	1	0	0	2	0.97	0	0
Q99JD4	Casp2	18	3	0	3	0	27	1	12	0.99	0	0	1	0
F1LSE6	Ppf1a3	52	21	0	12	0	116	1	8	0	18	0	20	0
F1LQV9	Lin7a	1	0	0	0	0	4	1	1	0	1	0	0	0
D4AEC2	Camsap2	12	2	0	1	0	14	1	0	0	1	0	1	0
O8382	Mag2	3	0	0	0	0	3	1	0	0	0	0	0	0
Q9Z252	Lin7b	2	0	0	0	0	3	1	0	0	0	0	0	0
D3ZWC6	Smt1	16	0	0	0	0	22	1	10	1	0	0	0	0
F53678	App3nc	6	0	0	1	0	4	1	5	1	4	1	7	1
F53676	App3ml	6	0	0	1	0	4	1	5	1	6	1	4	1
D4AQH6	Dtna	15	2	0	1	0	30	1	17	1	1	0	1	0
O83377	Pp4k2b	8	3	0	1	0	0	0	22	1	2	0	0	0
F1LX22	Pp4k2a	2	2	0	1	0	0	0	10	0.99	1	0	0	0
F62280	Yw hae	19	8	0	12	0	16	0	23	0.93	18	0.03	56	1
D3Z2P2	Rab39a	1	0	0	2	0.94	3	1	4	1	5	1	5	1
F1LW77	Rab33b	2	0	0	1	0	4	1	4	1	4	1	5	1
B0BMW0	Rab14	1	0	0	1	0	4	1	3	0.99	4	1	4	1
F63102	Yw haz	18	14	0	24	0	22	0	25	0	27	0	45	1
F61983	Yw hag	12	12	0	16	0	17	0	22	0	19	0	38	1

Table 1. KIF1A interactors in brain extracts

Affinity purification mass spectrometry analyses (AP-MS) of bioGFP-KIF1A(393-881, 657-1105, 657-1698, 950-1250, 1105-1698) in rat brain protein extracts. Accession name = Uniprot accession code; gene name = corresponding gene name; Σ #Unique peptides = total number of unique peptides; #PSM= number of PSMs. Higher numbers of PSMs are highlighted in red, lower in green. P-value = probability score from SAINT analysis. $0 \leq p \leq 1$, the higher the score the higher the probability for a given interaction. Higher scores are highlighted in red, lower scores in green.

Identified proteins			GFP		KIF13B (442-832)		KIF13B (832-1826)		KIF13B (442-1826)	
Accession	gene name	Σ# Unique Peptides	# PSM	P-value	# PSM	P-value	# PSM	P-value	# PSM	P-value
Q70AM4	Kif13b	93	26	0	469	1	822	1	1136	1
Q63622	Dlg2	20	0	0	44	1	0	0	121	1
G3V7N0	Hs2st1	9	0	0	27	1	0	0	10	1
F1LNM0	Dlg1	42	2	0	75	1	4	0.12	154	1
Q62915	Cask	21	0	0	14	1	1	0	37	1
P31016	Dlg4	32	2	0	34	1	3	0.03	110	1
P0CG51	Ubb	2	11	0	133	1	24	0	16	0
Q5XI32	Capzb	7	0	0	6	1	5	1	4	1
D4A8M2	Cask	1	0	0	6	1	1	0	15	1
F1M863	Ppfia4	20	3	0	24	1	2	0	16	1
D3ZZ81	Ppfia1	10	4	0	19	1	2	0	10	0.36
F1MAK3	Arhgap32	5	0	0	5	1	1	0	0	0
G3V8Q9	Apc	3	0	0	4	1	0	0	0	0
P63170	Dynl1	3	0	0	4	1	7	1	4	1
Q9Z250	Lin7a	8	0	0	4	1	1	0	20	1
Q792D0	Lin7c	6	0	0	4	1	1	0	15	1
O55147	Utrn	121	0	0	1	0	171	1	112	1
O08679	Mark2	42	2	0	1	0	91	1	95	1
F1M836	Mark3	23	2	0	0	0	54	1	66	1
D3ZWC6	Sntb1	14	0	0	2	0.97	16	1	15	1
F1LNE7	Mark1	27	2	0	0	0	50	1	66	1
Q6XDA0	Sptb	13	0	0	3	1	14	1	11	1
B5DFL9	Sestd1	13	0	0	0	0	13	1	6	1
F1LW77	Rab33b	3	0	0	2	0.97	8	1	4	1
Q63357	Myo1d	6	0	0	0	0	6	1	5	1
P53678	Ap3m2	5	0	0	5	1	6	1	3	1
D3ZP2	Rab39a	1	0	0	3	1	6	1	4	1
D3ZMX6	Sntb2	15	1	0	1	0	13	1	19	1
D4A678	Spta1	14	1	0	0	0	12	1	13	1
P53676	Ap3m1	4	0	0	2	0.97	5	1	1	0
Q9WVB1	Rab6a	2	0	0	1	0	4	1	3	1
Q9QYF3	Myo5a	28	6	0	13	0.04	29	1	25	1
O88768	Adap1	19	0	0	2	0.97	0	0	32	1
D3ZHV2	Macf1	32	2	0	13	1	6	0.65	30	1
D3ZMX6	Sntb2	15	1	0	1	0	13	1	19	1
P35439	Grin1	7	0	0	0	0	0	0	7	1
P84060	Dtnb	2	0	0	0	0	3	1	5	1
Q9Z136	Tsc1	11	1	0	1	0	2	0.22	12	1
D4ACH6	Dtna	9	2	0	3	0.04	8	0.95	15	1

Table 2. KIF13B interactors in brain extracts

Affinity purification mass spectrometry analyses (AP-MS) of bioGFP-KIF13B(442-832, 832-1826, 442-1826) in rat brain protein extracts. Higher numbers of PSMs are highlighted in red, lower in green. Higher p-values are highlighted in red, lower in green.

Identified proteins			GFP		KIF1A (393-881)		KIF1A (657-1105)		KIF1A (657-1698)		KIF1A (950-1250)		KIF1A (1105-1698)	
Accession	gene name	Σ# Unique Peptides	# PSM	P-value	# PSM	P-value	# PSM	P-value	# PSM	P-value	# PSM	P-value	# PSM	P-value
Q12756	KIF1A	108	5	0	770	1	663	1	772	1	154	1	515	1
P62198	CALM1	15	0	0	10	1	66	1	70	1	0	0	0	0
Q9UHD2	TBK1	35	0	0	0	0	74	1	1	0	2	0.98	0	0
Q9H5S1	AZ2	17	0	0	0	0	24	1	0	0	0	0	0	0
Q13136	PFPA1	13	0	0	0	0	22	1	0	0	0	0	0	0
Q9Y330	ZBTB12	11	0	0	4	1	15	1	0	0	0	0	0	0
Q9ULW0	TPX2	10	0	0	0	0	12	1	0	0	0	0	0	0
Q9HW31	IMP3	7	0	0	2	0.93	11	1	0	0	0	0	0	0
Q98379	GOLGA2	9	0	0	0	0	9	1	0	0	0	0	0	0
Q43166	SPAL1L1	7	0	0	0	0	7	1	0	0	0	0	0	0
O15083	ERC2	1	0	0	3	0.99	7	1	3	1	0	0	0	0
Q14980	NUNA1	25	2	0	6	0.77	18	1	2	0.05	13	1	0	0
Q96FJ2	DYNLL2	2	0	0	1	0	6	1	1	0	2	0.98	2	0.96
O75334	PFPA2	0	0	0	0	0	4	1	0	0	0	0	0	0
Q4VC55	AMOT	8	1	0	0	0	5	0.99	0	0	7	1	0	0
O14578	CIT	1	0	0	0	0	3	0.99	0	0	0	0	0	0
O75335	PFPA4	0	0	0	0	0	3	0.99	0	0	0	0	0	0
Q01469	FABP5	9	0	0	0	0	0	0	22	1	0	0	0	0
P12883	MYH7	1	0	0	0	0	1	0	9	1	0	0	0	0
Q9Y623	MYH4	0	0	0	0	0	2	0.96	8	1	0	0	0	0
P13533	MYH6	0	0	0	0	0	1	0	8	1	0	0	0	0
P11055	MYH3	0	0	0	0	0	2	0.96	7	1	0	0	0	0
P12882	MYH1	0	0	0	0	0	2	0.96	6	1	0	0	0	0
Q9UKX3	MYH13	1	0	0	0	0	1	0	6	1	0	0	0	0
P61981	YWHA G	8	0	0	0	0	1	0	0	0	0	0	24	1
Q04917	YWHA H	7	0	0	0	0	1	0	0	0	0	0	21	1
P62258	YWHA E	18	0	0	0	0	2	0	0	0	0	0	63	1
P63104	YWHA Z	12	1	0	1	0	3	0	1	0	2	0	34	1
P31946	YWHA B	7	0	0	0	0	2	0	0	0	1	0	28	0.99

Table 3. KIF1A interactors in HEK293 cells

Affinity purification mass spectrometry analyses (AP-MS) of bioGFP-KIF1A(393-881, 657-1105, 657-1698, 950-1250, 1105-1698) in HEK293 cells protein extracts. Higher numbers of PSMs are highlighted in red, lower in green. Higher p-value scores are highlighted in red, lower in green.

Identified proteins			GFP		KIF13B (442-832)		KIF13B (832-1826)		KIF13B (442-1826)	
Accession	gene name	Σ# Unique Peptides	# PSM	P-value	# PSM	P-value	# PSM	P-value	# PSM	P-value
Q9NQ78	KIF13B	64	18	0	271	1	588	1	759	1
Q7LGA3	HS2ST1	18	0	0	57	1	1	0	18	1
Q15149	PLEC	16	1	0	16	1	0	0	0	0
Q12959	DLG1	6	0	0	4	1	0	0	6	1
Q9BST9	RTKN	2	0	0	3	0.99	0	0	0	0
P46779	RPL28	5	0	0	5	0.98	0	0	1	0
Q9Y3U8	RPL36	5	0	0	5	0.98	1	0	1	0
Q7KZ17	MARK2	13	0	0	0	0	18	1	15	1
P46939	UTRN	14	0	0	0	0	17	1	4	1
Q13425	SNTB2	12	0	0	0	0	12	1	9	1
P11182	DBT	8	0	0	2	0.95	11	1	3	0.99
Q9Y623	MYH4	0	0	0	0	0	8	1	0	0
Q9BTV4	TMEM43	7	0	0	3	0.99	8	1	0	0
P12882	MYH1	1	0	0	0	0	7	1	0	0
P11055	MYH3	1	0	0	0	0	7	1	0	0
Q9UKX2	MYH2	0	0	0	0	0	6	1	0	0
P13535	MYH8	0	0	0	0	0	6	1	0	0
Q9Y2T2	AP3M1	6	0	0	3	0.99	5	1	0	0
P13533	MYH6	0	0	0	0	0	4	1	0	0
P12883	MYH7	0	0	0	0	0	4	1	0	0
P04279	SEMG1	19	0	0	0	0	0	0	26	1
Q14331	FRG1	5	0	0	3	0.99	4	1	23	1
Q96CW1	AP2M1	17	0	0	3	0.99	2	0.98	20	1
Q9BZ01	FRG1B	0	0	0	0	0	1	0	14	1
Q02383	SEMG2	9	0	0	0	0	0	0	12	1
Q9Y297	BTRC	4	0	0	0	0	9	1	13	1
Q9UKB1	FBXW11	7	0	0	0	0	11	1	16	1
P61981	YWHA G	1	0	0	0	0	0	0	4	0.92
Q04917	YWHA H	2	0	0	0	0	1	0	4	0.92

Table 4. KIF13B interactors in HEK293 cells

Affinity purification mass spectrometry analyses (AP-MS) of bioGFP-KIF13B(442-832, 832-1826, 442-1826) in HEK293 cells protein extracts. Higher numbers of PSMs are highlighted in red, lower in green. Higher p-value scores are highlighted in red, lower in green.

EXPERIMENTAL PROCEDURES

Animals

All experiments were approved by the DEC Dutch Animal Experiments Committee (Dier Experimenten Commissie), performed in line with institutional guidelines of Utrecht University and were conducted in agreement with Dutch law (Wet op de Dierproeven, 1996) and European regulations (Directive 2010/63/EU).

Antibodies and reagents

The following primary and secondary antibodies were used in this study: GFP rabbit (Abcam), HA mouse (Covance), HA rabbit (Santa Cruz), liprin- α 1 rabbit, mCherry mouse (Clontech), myc mouse (Santa Cruz), Alexa405-, Alexa 488-, Alexa 568- and Alexa 594-conjugated secondary antibodies (Invitrogen). Other reagents used in this study include: Rapalog, Streptavidin Dynabeads M-280 (Thermo Scientific).

Hippocampal Neuron Cultures, Transfections, Treatments

Primary hippocampal cultures were prepared from embryonic day 18 rat brains. Cells were plated on coverslips coated with poly-L-lysine (30 μ g/ml) and laminin (2 μ g/ml) at a density of 100,000/well (Goslin and Banker, 1989). Hippocampal cultures were grown in Neurobasal medium (NB) supplemented with B27, 0.5 mM glutamine, 12.5 μ M glutamate and penicillin/streptomycin. Neurons were transfected using lipofectamine (Invitrogen). Neuron cultures were treated with Rapalog (100nM) and fixed 24h after addition of the drug.

Expression vectors and shRNA constructs

The following mammalian expression plasmids have been previously described: BirA coding vector, pebioGFP, pebioGFP-KIF1A(393-881, 657-1105, 657-1698, 950-1250, 1105-1698) and pGW2-HA-TANC2, pGW1-HA-liprin- α 2 (Stucchi et al., 2018). PebioGFP-KIF13B(442-832, 832-1826, 442-1826) constructs correspond to truncated version of the human KIF13B and were kindly given us by Gary Banker; mCherry-PSD-95 was a given us by Harold MacGillavry. PebioGFP-KIF1A(657-864) and pebioGFP-KIF1A(647-813) were produced by PCR using pebioGFP-KIF1A(657-1105) as template and cloned using BamHI and XbaI sites, pebioGFP-KIF13B(663-832) and pebioGFP-KIF13B(663-762) were produced by PCR using pebioGFP-KIF13B(442-832) as template and cloned using BamHI and XbaI sites. GW1-KIF5C(1-559)-mRFP-FKBP was produced by PCR using pBa-KIF5C(1-559)-GFP (Addgene) as template and cloned using HindIII and AgeI sites. GW1-FRB-3myc-KIF1A(395-1698) was produced using GW1-HA-KIF1A (Stucchi et al., 2018) as a template and cloned using AscI and Sall sites. GW1-FRB-3myc-KIF1A(395-752, 395-1105, 657-1698, 1106-1698, 1106-1559, 1560-1698) were produced using GW1-FRB-3myc-KIF1A(395-1698) as a template and cloned using AscI and Sall sites. GW1-FRB-3myc-KIF13B(443-1826) was produced using PebioGFP-KIF13B(443-1826) as a template and cloned using AscI and Sall sites. GW1-FRB-3myc-KIF13B(443-662, 443-832, 663-1826, 833-1826, 1160-1826, 833-1700, 1160-1700) were produced using GW1-FRB-3myc-KIF13B(443-1826) as a template and cloned using AscI and Sall sites.

Affinity Purification-Western Blot (AP-WB)

Human Embryonic Kidney 293 cells (HEK293) cells were cultured in DMEM/Ham's F10 (50%/50%) containing 10% Fetal Calf Serum (FCS) and 1% penicillin/streptomycin at 37°C and 5% CO₂. HEK293 cells were transfected with pebioGFP constructs in combination with BirA using polyethylenimine (PEI, Polysciences) according to the manufacturer instructions. Cells were lysed 48h later in lysis buffer (50mM TrisHCl (PH 7.4-7.8), 100mM NaCl, 0.5% TX-100, 5mM MgCl₂, protease inhibitors (Roche)), centrifuged at 13.000 rpm for 15 min. Supernatants were then incubated with Streptavidin Dynabeads M-280 (Thermo Scientific) for 1h at 4°C. Beads were separated using a magnet (Dyna, Invitrogen) and washed five times in washing buffer (20mM Tris HCl, 150mM KCl, 0.1% TritonX-100). Proteins were eluted from the beads by adding a 4x dilution of the sample buffer (8% SDS, 25% glycerol, 0.05M Tris pH 6.8, 400mM DTT and 40mg/l bromophenol blue). Samples were boiled at 99°C for 10 minutes before being analyzed by SDS PAGE.

Proteins were transferred on nitrocellulose membranes (Millipore) using a semi-dry blotting system. Membranes were blocked with 3% BSA in PBS-T (0.1% Tween-20) and incubated with primary antibodies (overnight at 4°C) in 3% BSA PBS-T. IRdye680 or IRdye800-conjugated secondary antibodies (Li-Cor) were diluted 1:20.000 in 3%BSA-PBST and applied for 1h at RT. Blots were acquired using a LICOR Odyssey scanner at 680nm or 800nm.

Affinity Purification-Mass Spectrometry (AP-MS) on rat brain extracts

Human Embryonic Kidney 293 cells (HEK293) cells were cultured in DMEM/Ham's F10 (50%/50%) containing 10% Fetal Calf Serum (FCS) and 1% penicillin/streptomycin at 37°C and 5% CO₂. HEK293 cells were transfected with pebio-GFP constructs in combination with BirA using polyethylenimine (PEI, Polysciences) according to the manufacturer instructions. Cells were lysed 48h later in RIPA lysis buffer (50mM TrisHCl pH 7.4-7.8, 150mM NaCl, 1%Triton X-100, 0.1% SDS, 0.5% Sodium Deoxycholate and Protease inhibitors (Roche)), centrifuged at 13.000 rpm for 15 min and the supernatants were incubated for 1h at 4°C with Streptavidin Dynabeads M-280 (Thermo Scientific) previously blocked in chicken egg albumin (Life Technologies). Beads were then separated using a magnet (Dyna, Invitrogen) washed twice in low salt washing buffer (20mM Tris-HCl pH 7.4-7.8, 100 mM KCl, 0.1% Triton X-100), followed by two washing steps in high salt wash buffer (20mM Tris-HCl pH 7.4-7.8, 500 mM KCl, 0.1% Triton X-100) and two final steps in low salt washing buffer (20mM Tris-HCl pH 7.4-7.8, 100 mM KCl, 0.1% Triton X-100) to remove binding proteins from HEK293 cells. Brains were obtained from female adult rats and homogenized in 10x volume/weight in tissue lysis buffer (50mM TrisHCl, 150mM NaCl, 0.1% SDS, 0.2% NP-40, and protease inhibitors). Brain lysates were centrifuged at 16.000 g for 15 min at 4°C and the supernatant was then incubated for 1h at 4°C with beads previously conjugated with either the biotinylated or the GFP-tagged proteins of interest. Beads were then separated using a magnet (Dyna; Invitrogen) and washed in normal washing buffer (20mM Tris HCl, 150mM KCl, 0.1% TritonX-100) for five times. Samples were processed as described in (Stucchi et al., 2018) and then analyzed by MS.

Affinity Purification-Mass Spectrometry (AP-MS)

Human Embryonic Kidney 293 cells (HEK293) cells were cultured in DMEM/Ham's F10 (50%/50%) containing 10% Fetal Calf Serum (FCS) and 1% penicillin/streptomycin at 37°C and 5% CO₂. HEK293 cells were transfected with pebio-GFP constructs in combination with BirA using polyethylenimine (PEI, Polysciences) according to the manufacturer instructions. Cells were lysed 48h later in RIPA lysis buffer (50mM TrisHCl pH 7.4-7.8, 150mM NaCl, 1%Triton X-100, 0.1% SDS, 0.5% Sodium Deoxycholate and Protease inhibitors (Roche)), centrifuged at 13.000 rpm for 15 min and the supernatants were incubated for 1h at 4°C with Streptavidin Dynabeads M-280 (Thermo Scientific) previously blocked in chicken egg albumin (Life Technologies). Beads were then separated using a magnet (Dyna, Invitrogen) washed in washing buffer (20mM Tris HCl, 150mM KCl, 0.1% TritonX-100) for four times and co-precipitated proteins were analyzed by MS.

Mass Spectrometry analysis

All samples were analyzed on an ETD enabled LTQ-Orbitrap Elite coupled to Proxeon EASY-nLC 1000 (Thermo Fisher Scientific, Odense, Denmark). Peptides were loaded onto a trap column (Reprosil pur C18, Dr. Maisch, 100 µm x 2 cm, 3 µm; constructed in-house) with solvent A (0.1% formic acid in water) at a maximum pressure of 800 bar and chromatographically separated over the analytical column (Poroshell 120 EC C18, Agilent Technologies, 50 µm x 50 cm, 2.7 µm) using 90 min linear gradient from 7-30% solvent B (0.1% formic acid in acetonitrile) at a flow rate of 150 nL/min. The mass spectrometers were used in a data-dependent mode, which automatically switched between MS and MS/MS. After a survey scan from 350-1500 m/z the 10 or 20 most abundant peptides were subjected to CID fragmentation. For data analysis, raw files were processed using Proteome Discoverer 1.4 (Thermo Scientific). Database search was performed using Uniprot rat database or Uniprot human database on Mascot (version 2.5.1, Matrix Science, UK) as the search engine. Carbamidomethylation of cysteines was set as a fixed modification and oxidation of methionine was set as a variable modification. Trypsin was set as cleavage specificity, allowing a maximum of 2 missed cleavages. Data filtering was performed using a percolator, resulting in 1% False Discovery Rate (FDR). Additional

filters were search engine rank 1 and mascot ion score >20.

Bioinformatic analysis

Statistical assessment of the AP-MS data was performed based on spectral counts using the SAINT (Significance Analysis of INteractome, version 2.3.2) algorithm (Choi et al., 2011). The SAINT parameters were set as follows: nburn=2000, niter=20.000, lowmode=0, minfold=0, and norm=1. Bait proteins with a SAINT probability score >0.95 were considered putative protein interaction partners.

Homology-based modeling (I-TASSER)

KIF1A(657-864) was superimposed to KIF13B-MBS structure (PDB: 5B64) using I-TASSER (Yang et al., 2015). Similarly, N-terminal-TANC2 and N-terminal-liprin- α 2 structures were predicted by using I-TASSER without constraint. Structure of the DLG4 GK/KIF13B MBS complex was previously obtained by (Zhu et al., 2016) using X-ray crystallography. The atomic coordinates of the DLG4 GK/KIF13B MBS complex are deposited in PDB under the accession code PDB: 5B64. The structural figures were prepared with PyMOL (www.pymol.org).

Split kinesin assay

KIF5C(1-559)-mRFP-FKBP was expressed together with a kinesin tail domain and NPY-GFP or TfR-GFP in hippocampal neurons (DIV7-9). Rapalogs were added at transfection. Neurons were fixed for 10 minutes with 4% formaldehyde/4% sucrose in phosphate-buffered saline (PBS) at room temperature, washed three times in PBS for 5 minutes, and then incubated with primary antibody diluted in GDB buffer (0.2% BSA, 0.8 M NaCl, 0.5% Triton X-100, 30 mM phosphate buffer, pH 7.4) at 4°C overnight. Neurons were then washed three times in PBS for 5 minutes and incubated with Alexa-conjugated secondary antibodies diluted in GDB buffer for 1h at room temperature. Neurons were then washed three times in PBS for 5 minutes and mounted on slides in Vectashield mounting medium (Vector Laboratories). Images were acquired on a Nikon Eclipse 80i upright widefield fluorescence microscope, equipped with a Photometrics CoolSNAP HQ2 CCD camera and Nikon NIS Br software, using a Plan Fluor 40x N.A. 1.30 oil objective. For quantification, cells that express all three constructs were counted and classified as cargo transporting, when all three constructs co-localized in axonal tips, or not transporting, when the cargo was not co-localizing with the other two constructs in axonal tips.

ACKNOWLEDGEMENTS

We thank Gary Banker for sharing bioGFP-KIF1A(393-881, 657-1105, 657-1698, 950-1250, 1105-1698) and bioGFP-KIF13B(442-832, 832-1826, 442-1826) constructs and Harold MacGillavry for sharing mCherry-PSD-95. This work was supported by the Netherlands Organization for Scientific Research (NWO-ALW-VICI, CCH), the Netherlands Organization for Health Research and Development (ZonMW-TOP, CCH) and the European Research Council (ERC) (ERC-consolidator, CCH).

REFERENCES

- Asaba, N., Hanada, T., Takeuchi, A., and Chishti, A.H. (2003). Direct interaction with a kinesin-related motor mediates transport of mammalian discs large tumor suppressor homologue in epithelial cells. *J Biol Chem* 278, 8395-8400.
- Barkus, R.V., Klyachko, O., Horiuchi, D., Dickson, B.J., and Saxton, W.M. (2008). Identification of an axonal kinesin-3 motor for fast anterograde vesicle transport that facilitates retrograde transport of neuropeptides. *Mol Biol Cell* 19, 274-283.
- Bendor, J., Lizardi-Ortiz, J.E., Westphalen, R.I., Brandstetter, M., Hemmings, H.C., Jr., Sulzer, D., Flajolet, M., and Greengard, P. (2010). AGAP1/AP-3-dependent endocytic recycling of M5 muscarinic receptors promotes dopamine release. *EMBO J* 29, 2813-2826.
- Bohl, J., Brimer, N., Lyons, C., and Vande Pol, S.B. (2007). The stardust family protein MPP7 forms a tripartite complex with LIN7 and DLG1 that regulates the stability and localization of DLG1 to cell junctions. *J Biol Chem* 282, 9392-9400.
- Bolis, A., Coviello, S., Visigalli, I., Taveggia, C., Bachi, A., Chishti, A.H., Hanada, T., Quattrini, A., Previtali, S.C., Biffi, A., and Bolino, A. (2009). Dlg1, Sec8, and Mtmr2 regulate membrane homeostasis in Schwann cell myelination. *J Neurosci* 29, 8858-8870.
- Choi, H., Larsen, B., Lin, Z.Y., Breikreutz, A., Mellacheruvu, D., Fermin, D., Qin, Z.S., Tyers, M., Gingras, A.C., and Nesvizhskii, A.I. (2011). SAINT: probabilistic scoring of affinity purification-mass spectrometry data. *Nat Methods* 8, 70-73.
- de Wit, J., Toonen, R.F., Verhaagen, J., and Verhage, M. (2006). Vesicular trafficking of semaphorin 3A is activity-dependent and differs between axons and dendrites. *Traffic* 7, 1060-1077.
- Goslin, K., and Banker, G. (1989). Experimental observations on the development of polarity by hippocampal neurons in culture. *J Cell Biol* 108, 1507-1516.
- Hall, D.H., and Hedgecock, E.M. (1991). Kinesin-related gene *unc-104* is required for axonal transport of synaptic vesicles in *C. elegans*. *Cell* 65, 837-847.
- Hammond, J.W., Cai, D., Blasius, T.L., Li, Z., Jiang, Y., Jih, G.T., Meyhofer, E., and Verhey, K.J. (2009). Mammalian Kinesin-3 motors are dimeric in vivo and move by processive motility upon release of autoinhibition. *PLoS Biol* 7, e72.
- Hanada, T., Lin, L., Tibaldi, E.V., Reinherz, E.L., and Chishti, A.H. (2000). GAKIN, a novel kinesin-like protein associates with the human homologue of the *Drosophila* discs large tumor suppressor in T lymphocytes. *J Biol Chem* 275, 28774-28784.
- Hirokawa, N., Niwa, S., and Tanaka, Y. (2010). Molecular motors in neurons: transport mechanisms and roles in brain function, development, and disease. *Neuron* 68, 610-638.
- Hoepfner, S., Severin, F., Cabezas, A., Habermann, B., Runge, A., Gillooly, D., Stenmark, H., and Zerial, M. (2005). Modulation of receptor recycling and degradation by the endosomal kinesin KIF16B. *Cell* 121, 437-450.
- Horiguchi, K., Hanada, T., Fukui, Y., and Chishti, A.H. (2006). Transport of PIP3 by GAKIN, a kinesin-3 family protein, regulates neuronal cell polarity. *J Cell Biol* 174, 425-436.
- Huo, L., Yue, Y., Ren, J., Yu, J., Liu, J., Yu, Y., Ye, F., Xu, T., Zhang, M., and Feng, W. (2012). The CC1-FHA tandem as a central hub for controlling the dimerization and activation of kinesin-3 KIF1A. *Structure* 20, 1550-1561.
- Jenkins, B., Decker, H., Bentley, M., Luisi, J., and Banker, G. (2012). A novel split kinesin assay identifies motor proteins that interact with distinct vesicle populations. *J Cell Biol* 198, 749-761.
- Kanai, Y., Wang, D., and Hirokawa, N. (2014). KIF13B enhances the endocytosis of LRP1 by recruiting LRP1 to caveolae. *J Cell Biol* 204, 395-408.
- Kapitein, L.C., Schlager, M.A., Kuijpers, M., Wulf, P.S., van Spronsen, M., MacKintosh, F.C., and Hoogenraad, C.C. (2010). Mixed microtubules steer dynein-driven cargo transport into dendrites. *Curr Biol* 20, 290-299.
- Karasmanis, E.P., Phan, C.T., Angelis, D., Kesisova, I.A., Hoogenraad, C.C., McKenney, R.J., and Spiliotis, E.T. (2018). Polarity of Neuronal Membrane Traffic Requires Sorting of Kinesin Motor Cargo during Entry into Dendrites by a Microtubule-Associated Septin. *Dev Cell* 46, 204-218 e207.
- Klopfenstein, D.R., Tomishige, M., Stuurman, N., and Vale, R.D. (2002). Role of phosphatidylinositol(4,5)bisphosphate organization in membrane transport by the *Unc104* kinesin motor. *Cell* 109, 347-358.
- Klopfenstein, D.R., and Vale, R.D. (2004). The lipid binding pleckstrin homology domain in UNC-

104 kinesin is necessary for synaptic vesicle transport in *Caenorhabditis elegans*. *Mol Biol Cell* 15, 3729-3739.

Kramarcy, N.R., Vidal, A., Froehner, S.C., and Sealock, R. (1994). Association of utrophin and multiple dystrophin short forms with the mammalian M(r) 58,000 dystrophin-associated protein (syntrophin). *J Biol Chem* 269, 2870-2876.

Lawrence, C.J., Dawe, R.K., Christie, K.R., Cleveland, D.W., Dawson, S.C., Endow, S.A., Goldstein, L.S., Goodson, H.V., Hirokawa, N., Howard, J., *et al.* (2004). A standardized kinesin nomenclature. *J Cell Biol* 167, 19-22.

Lee, S., Fan, S., Makarova, O., Straight, S., and Margolis, B. (2002). A novel and conserved protein-protein interaction domain of mammalian Lin-2/CASK binds and recruits SAP97 to the lateral surface of epithelia. *Mol Cell Biol* 22, 1778-1791.

Lipka, J., Kapitein, L.C., Jaworski, J., and Hoogenraad, C.C. (2016). Microtubule-binding protein doublecortin-like kinase 1 (DCLK1) guides kinesin-3-mediated cargo transport to dendrites. *EMBO J* 35, 302-318.

Lo, K.Y., Kuzmin, A., Unger, S.M., Petersen, J.D., and Silverman, M.A. (2011). KIF1A is the primary anterograde motor protein required for the axonal transport of dense-core vesicles in cultured hippocampal neurons. *Neurosci Lett* 491, 168-173.

Lochner, J.E., Spangler, E., Chavarha, M., Jacobs, C., McAllister, K., Schuttner, L.C., and Scalettar, B.A. (2008). Efficient copackaging and cotransport yields postsynaptic colocalization of neuromodulators associated with synaptic plasticity. *Dev Neurobiol* 68, 1243-1256.

Marcello, E., Gardoni, F., Mauceri, D., Romorini, S., Jeromin, A., Epis, R., Borroni, B., Cattabeni, F., Sala, C., Padovani, A., and Di Luca, M. (2007). Synapse-associated protein-97 mediates alpha-secretase ADAM10 trafficking and promotes its activity. *J Neurosci* 27, 1682-1691.

Mauceri, D., Gardoni, F., Marcello, E., and Di Luca, M. (2007). Dual role of CaMKII-dependent SAP97 phosphorylation in mediating trafficking and insertion of NMDA receptor subunit NR2A. *J Neurochem* 100, 1032-1046.

Miller, K.E., DeProto, J., Kaufmann, N., Patel, B.N., Duckworth, A., and Van Vactor, D. (2005). Direct observation demonstrates that Liprin-alpha is required for trafficking of synaptic vesicles. *Curr Biol* 15, 684-689.

Miyazaki, H., Yamazaki, M., Watanabe, H., Maehama, T., Yokozeki, T., and Kanaho, Y. (2005). The small GTPase ADP-ribosylation factor 6

negatively regulates dendritic spine formation. *FEBS Lett* 579, 6834-6838.

Mok, H., Shin, H., Kim, S., Lee, J.R., Yoon, J., and Kim, E. (2002). Association of the kinesin superfamily motor protein KIF1Balpha with postsynaptic density-95 (PSD-95), synapse-associated protein-97, and synaptic scaffolding molecule PSD-95/discs large/zona occludens-1 proteins. *J Neurosci* 22, 5253-5258.

Moore, C.D., Thacker, E.E., Larimore, J., Gaston, D., Underwood, A., Kearns, B., Patterson, S.I., Jackson, T., Chapleau, C., Pozzo-Miller, L., and Theibert, A. (2007). The neuronal Arf GAP centaurin alpha1 modulates dendritic differentiation. *J Cell Sci* 120, 2683-2693.

Nie, Z., and Randazzo, P.A. (2006). Arf GAPs and membrane traffic. *J Cell Sci* 119, 1203-1211.

Niwa, S., Tanaka, Y., and Hirokawa, N. (2008). KIF1Bbeta- and KIF1A-mediated axonal transport of presynaptic regulator Rab3 occurs in a GTP-dependent manner through DENN/MADD. *Nat Cell Biol* 10, 1269-1279.

Okada, Y., Yamazaki, H., Sekine-Aizawa, Y., and Hirokawa, N. (1995). The neuron-specific kinesin superfamily protein KIF1A is a unique monomeric motor for anterograde axonal transport of synaptic vesicle precursors. *Cell* 81, 769-780.

Osterweil, E., Wells, D.G., and Mooseker, M.S. (2005). A role for myosin VI in postsynaptic structure and glutamate receptor endocytosis. *J Cell Biol* 168, 329-338.

Peters, M.F., Adams, M.E., and Froehner, S.C. (1997). Differential association of syntrophin pairs with the dystrophin complex. *J Cell Biol* 138, 81-93.

Rumbaugh, G., Sia, G.M., Garner, C.C., and Huganir, R.L. (2003). Synapse-associated protein-97 isoform-specific regulation of surface AMPA receptors and synaptic function in cultured neurons. *J Neurosci* 23, 4567-4576.

Sans, N., Racca, C., Petralia, R.S., Wang, Y.X., McCallum, J., and Wenthold, R.J. (2001). Synapse-associated protein 97 selectively associates with a subset of AMPA receptors early in their biosynthetic pathway. *J Neurosci* 21, 7506-7516.

Schlager, M.A., and Hoogenraad, C.C. (2009). Basic mechanisms for recognition and transport of synaptic cargos. *Mol Brain* 2, 25.

Schluter, O.M., Xu, W., and Malenka, R.C. (2006). Alternative N-terminal domains of PSD-95 and SAP97 govern activity-dependent regulation of synaptic AMPA receptor function. *Neuron* 51, 99-111.

Shin, H., Wyszynski, M., Huh, K.H., Valtschanoff, J.G., Lee, J.R., Ko, J., Streuli, M.,

Weinberg, R.J., Sheng, M., and Kim, E. (2003). Association of the kinesin motor KIF1A with the multimodular protein liprin-alpha. *J Biol Chem* 278, 11393-11401.

Soppina, V., Norris, S.R., Dizaji, A.S., Kortus, M., Veatch, S., Peckham, M., and Verhey, K.J. (2014). Dimerization of mammalian kinesin-3 motors results in superprocessive motion. *Proc Natl Acad Sci U S A* 111, 5562-5567.

Stucchi, R., Plucinska, G., Hummel, J.J.A., Zahavi, E.E., Guerra San Juan, I., Klykov, O., Scheltema, R.A., Altelaar, A.F.M., and Hoogenraad, C.C. (2018). Regulation of KIF1A-Driven Dense Core Vesicle Transport: Ca(2+)/CaM Controls DCV Binding and Liprin-alpha/TANC2 Recruits DCVs to Postsynaptic Sites. *Cell Rep* 24, 685-700.

Tong, Y., Tempel, W., Wang, H., Yamada, K., Shen, L., Senisterra, G.A., MacKenzie, F., Chishti, A.H., and Park, H.W. (2010). Phosphorylation-independent dual-site binding of the FHA domain of KIF13 mediates phosphoinositide transport via centaurin alpha1. *Proc Natl Acad Sci U S A* 107, 20346-20351.

Venkateswarlu, K., Brandom, K.G., and Lawrence, J.L. (2004). Centaurin-alpha1 is an in vivo phosphatidylinositol 3,4,5-trisphosphate-dependent GTPase-activating protein for ARF6 that is involved in actin cytoskeleton organization. *J Biol Chem* 279, 6205-6208.

Venkateswarlu, K., Hanada, T., and Chishti, A.H. (2005). Centaurin-alpha1 interacts directly with kinesin motor protein KIF13B. *J Cell Sci* 118, 2471-2484.

Wagner, O.I., Esposito, A., Kohler, B., Chen, C.W., Shen, C.P., Wu, G.H., Butkevich, E., Mandalapu, S., Wenzel, D., Wouters, F.S., and Klopfenstein, D.R. (2009). Synaptic scaffolding protein SYD-2 clusters and activates kinesin-3 UNC-104 in *C. elegans*. *Proc Natl Acad Sci U S A* 106, 19605-19610.

Wu, G.H., Muthaiyan Shanmugam, M., Bhan, P., Huang, Y.H., and Wagner, O.I. (2016). Identification and Characterization of LIN-2(CASK) as a Regulator of Kinesin-3 UNC-104(KIF1A) Motility and Clustering in Neurons. *Traffic* 17, 891-907.

Wu, Y.E., Huo, L., Maeder, C.I., Feng, W., and Shen, K. (2013). The balance between capture and dissociation of presynaptic proteins controls the spatial distribution of synapses. *Neuron* 78, 994-1011.

Yamada, K.H., Hanada, T., and Chishti, A.H. (2007). The effector domain of human Dlg tumor suppressor acts as a switch that relieves autoinhibition of kinesin-3 motor GAKIN/KIF13B. *Biochemistry* 46, 10039-10045.

Yang, J., Yan, R., Roy, A., Xu, D., Poisson, J., and Zhang, Y. (2015). The I-TASSER Suite: protein structure and function prediction. *Nat Methods* 12, 7-8.

Zahn, T.R., Angleson, J.K., MacMorris, M.A., Domke, E., Hutton, J.F., Schwartz, C., and Hutton, J.C. (2004). Dense core vesicle dynamics in *Caenorhabditis elegans* neurons and the role of kinesin UNC-104. *Traffic* 5, 544-559.

Zhu, J., Shang, Y., Xia, Y., Zhang, R., and Zhang, M. (2016). An Atypical MAGUK GK Target Recognition Mode Revealed by the Interaction between DLG and KIF13B. *Structure* 24, 1876-1885.



CHAPTER 5

Fibril formation rewires interactome of the Alzheimer protein Tau by π -stacking

Luca Ferrari^{1,2}, **Riccardo Stucchi**^{2,3,5}, Katerina
Konstantoulea^{1,2}, Gerarda van de Kamp^{1,2},
Renate Kos^{1,2}, Willie J.C. Geert⁴, Friedrich
G. Förster⁴, Maarten AF Altelaar⁵, Casper
Hoogenraad^{2,3} and Stefan G. D. Rüdiger*^{1,2}

Submitted

¹Cellular Protein Chemistry, Bijvoet Center for Biomolecular Research, Utrecht University, Padualaan 8, 3584 CH Utrecht, The Netherlands

²Science for Life, Utrecht University, Padualaan 8, 3584 CH Utrecht, The Netherlands

³Cell Biology, Faculty of Science, Utrecht University

⁴Cryo Electron Microscopy, Bijvoet Center for Biomolecular Research, Utrecht University, Padualaan 8, 3584 CH Utrecht, The Netherlands

⁵Biomolecular Mass Spectrometry and Proteomics, Bijvoet Center for Biomolecular Research, Utrecht University, Padualaan 8, 3584 CH Utrecht, The Netherlands

ABSTRACT

Aggregation of the Tau protein defines progression of neurodegenerative diseases, including Alzheimer's Disease. Tau assembles into oligomers and fibrils. The molecular basis of their toxicity is poorly understood. Here we show that π -stacking by Arginine side chains rewires the interactome of Tau upon aggregation. Oligomeric nano-aggregates scavenge the COPI complex, fibrils attract proteins involved in microtubule binding, RNA binding and phosphorylation. The aberrant interactors have disordered regions with unusual sequence features. Arginines are crucial to initiate such aberrant interactions. Remarkably, substitution of Arginines by Lysines abolishes scavenging, which indicates a key role for the pi-stacking of the Arginine side chain. The molecular chaperone Hsp90 tames such re-arrangements, which suggests that the natural protein quality control system can suppress aberrant interactions. Together, our data present a molecular mode of action for derailment of protein-protein interaction in neurodegeneration.

INTRODUCTION

Protein aggregation is linked to a wide range of neurodegenerative disorders, including Alzheimer's, Parkinson's and Huntington's diseases (Hartl, 2017; Knowles et al., 2014). Protein fibrils are ubiquitous presence in patients' brains affected by neurodegeneration (Wilcock and Esiri, 1982). For all neurodegenerative disorders, protein aggregation proceeds in a step-wise fashion, from structurally heterogeneous oligomeric species to mature fibrils, the former considered to be the most toxic agents (Chiti and Dobson, 2017; Holtzman et al., 2016). Remarkably, it is unclear why protein aggregates are toxic and how they react within the cellular environment of the neuron (Goedert et al., 2017; Wang and Mandelkow, 2016). Intracellular aggregation of the protein Tau is hallmark of Alzheimer's disease and other fatal tauopathies. (Goedert et al., 2017; Sydow et al., 2011; Wilcock and Esiri, 1982). Several factors play a role in the origin of Alzheimer's, such as extracellular amyloid formation of the A β peptide (Lane et al., 2018). However, intracellular Tau aggregation is sufficient to induce neurodegeneration, correlates with cognitive impairment in humans and is necessary to mediate A β toxicity (Bejanin et al., 2017; Roberson et al., 2007; Wang and Mandelkow, 2016).

The mechanistic contribution to disease of Tau oligomers and fibrils remains largely elusive. Due to their structural heterogeneity and difficulties in isolation, it is difficult to point out which cellular processes they target (Holtzman et al., 2016; Wang and Mandelkow, 2016). However, non-physiological protein aggregates may result in new interactions within the cell, disturbing a variety of cellular processes and disrupting the protein quality control network, responsible for fibrils handling and disposal (Ciechanover and Kwon, 2017; Gidalevitz et al., 2006). Major components of this network are two conserved energy-driven chaperone systems, Hsp70 and Hsp90 (Morán Luengo et al., in the press). They both participate in Tau clearance in physiological condition (Blair et al., 2013; Fontaine et al., 2015), however their contribution to neurodegeneration is still elusive. Hsp70 can disaggregate Tau fibrils, while Hsp90 buffers aggregation prone stretches of Tau (Ferrari et al., 2018; Karagöz et al., 2014; Pratt et al., 2015). Hsp90 decreased efficiency during aging may contribute to Tau aggregation, which in turn may dictate further collapse of chaperones activity (Shelton et al., 2017).

Previous proteomics studies revealed that Tau fibrils establish new abnormal interactions with either the insoluble proteome (Donovan et al., 2012) or ER-associated protein complexes (Meier et al., 2015). We recently showed that toxicity of an aggregation-prone variant of the protein Axin is caused by aberrant interactions established by oligomeric nano-aggregates formed in the cytoplasm (Anvarian et al., 2016). Together, this made us wonder how Tau fibrils would interact with the soluble cytoplasmic component of the brain, where protein aggregation takes place. It is an open question whether common structural features govern the binding of interactors to

Tau fibrils. It is of great interest to understand which interactions are engaged by Tau fibrils and their binding mechanisms, as this would reveal which cellular processes are targeted by Tau-dependent neurodegeneration and would offer novel therapeutic strategies.

We set out to understand at molecular level how aggregation of Tau modulates interactions with proteins. Here we reveal that fibril formation rewires the interactome of Tau. Interestingly, the avidity properties gained upon fibril formation attract a defined, new set of interactors, which contains disordered regions with a unique amino acidic footprint. The key determinant for derailing the protein network is Arginine-driven π -stacking. This provides a molecular framework to understand aberrant interactions of neurotoxic fibrils. Interestingly, there is a cellular defence system suppressing Tau aggregation. We find that the Hsp90 chaperone stalls formation of Tau fibrils and reshapes their abnormal interactome. Thus, neurons are endowed with a powerful molecular machine that is able to counteract formation of Tau fibrils and their engagement with aberrant interactors.

RESULTS

Separation of Tau monomers, oligomers and fibrils

To analyse potential interactome changes upon aggregation of Tau, it is crucial to precisely control fibril formation over time. We set out to biochemically characterise the aggregation process, from monomeric Tau at the start to mature fibrils as end-point. To this mean, we recombinantly produced a pro-aggregating variant of Tau-RD (Tau-Q244-E372, DK280 (Gustke et al., 1994)), with a FLAG tag to facilitate detection (Tau-RD*). Tau-RD is an established Alzheimer model that aggregates more aggressively than the wildtype full length protein (Mocanu et al., 2008). We induced its aggregation via heparin following an established procedure (Goedert et al., 1996) and collected samples as aggregation proceeded. We then resolved these samples on density gradients spread over 12 fractions and detected them with a fluorescent antibody (Fig. 1A). At time 0, Tau-RD* sedimented on top of the gradient (Fractions 1 and 2, tube I), consistent with its expected monomeric nature at the start of the experiment. After 1 h (tube II), Tau-RD* sedimented further down until fraction 3, indicating the appearance of oligomeric, nanometer-scale aggregates (nano-aggregates). At 8 h (tube III), Tau-RD* spreaded until fractions 7, consistent with the growth of increasingly large aggregates. Finally, after 24 h (tube IV), we detected no Tau-RD* in fraction 1 anymore, indicating that all Tau-RD* aggregated into either oligomers or fibrils, reflected by the presence of aggregates from Electron Microscopy (TEM) characterised Tau-RD* fibrils at 24 h as negatively stained paired helical filaments with periodicity of 50-100 nm, consistent with previous observations (Wegmann et al., 2010) (Fig. 1B). Thus, our procedure generates the full spectrum of Tau species for aggregation-dependent

interactome analysis, representing monomers, oligomeric nano-aggregates and mature fibrils.

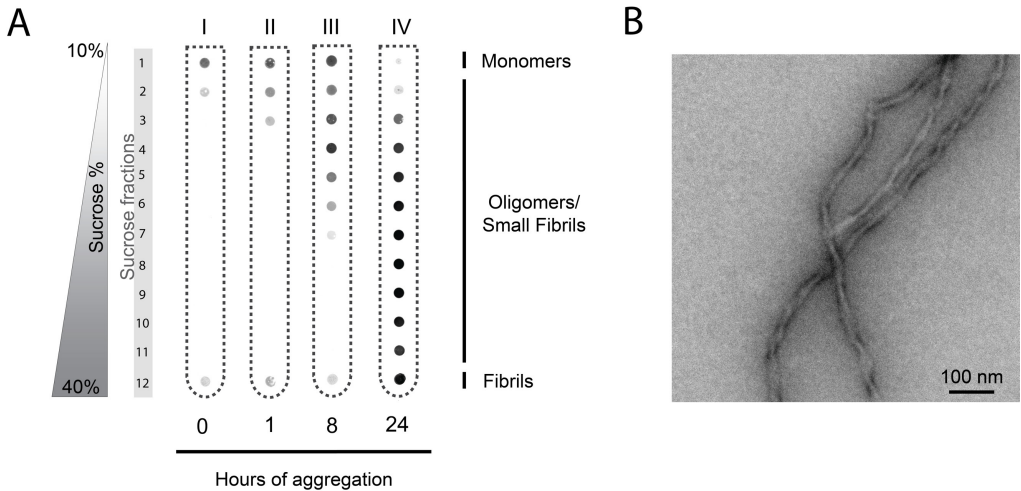


Figure 1. Precise control of Tau aggregation.

(A) Time course of Tau-RD* aggregation monitored by density gradients. Samples were centrifuged for 2.5 h at 200000g.

(B) Transmission Electron Microscopy of Tau-RD* fibrils, timepoint 24 h. Scalebar 100 nm.

Tau fibrils target specific protein families

Next, we wondered how Tau reacts at different aggregation stages with the soluble neuronal proteome. We exposed the FLAG-tagged Tau-RD* at different stages of aggregation during a 24 h period with rat brain lysates depleted of their insoluble components (Fig. 2A). We pulled down potential interactors with an anti-FLAG antibody and revealed their identity via mass spectrometry. For each protein, we determined the abundance by counting Peptide Spectrum Matches (PSMs) at each aggregation stage. We compared the protein spectrum at each timepoint (tx) to the one of monomeric Tau-RD* without heparin (t0-) and plotted changes as logarithmic function. This setup allowed us to monitor proteome changes. We uncovered striking interactome changes as Tau-RD* aggregation proceeds (Fig. 2B). A sub-group of interactors showed decreased levels compared to the monomeric reference values (Fig. 2B, purple box t24, blue interactors). Another sub-group of interactors showed binding levels similar for the fibril fractions as for the monomers. Remarkably, however, they bound stronger to early-stage Tau nanoaggregates (Fig. 2B, purple box t1). Finally, a sub-group of the proteome increasingly associated with Tau upon progression of fibril formation, reaching its maximum as mature fibrils appeared (Fig. 2B, purple box t24, red interactors). The time-dependent change in protein-protein interactions implies that fibrils and oligomers differ in binding properties to other proteins. Thus, progressive aggregation gradually rewires Tau interactome, with different aggregation species interacting with different

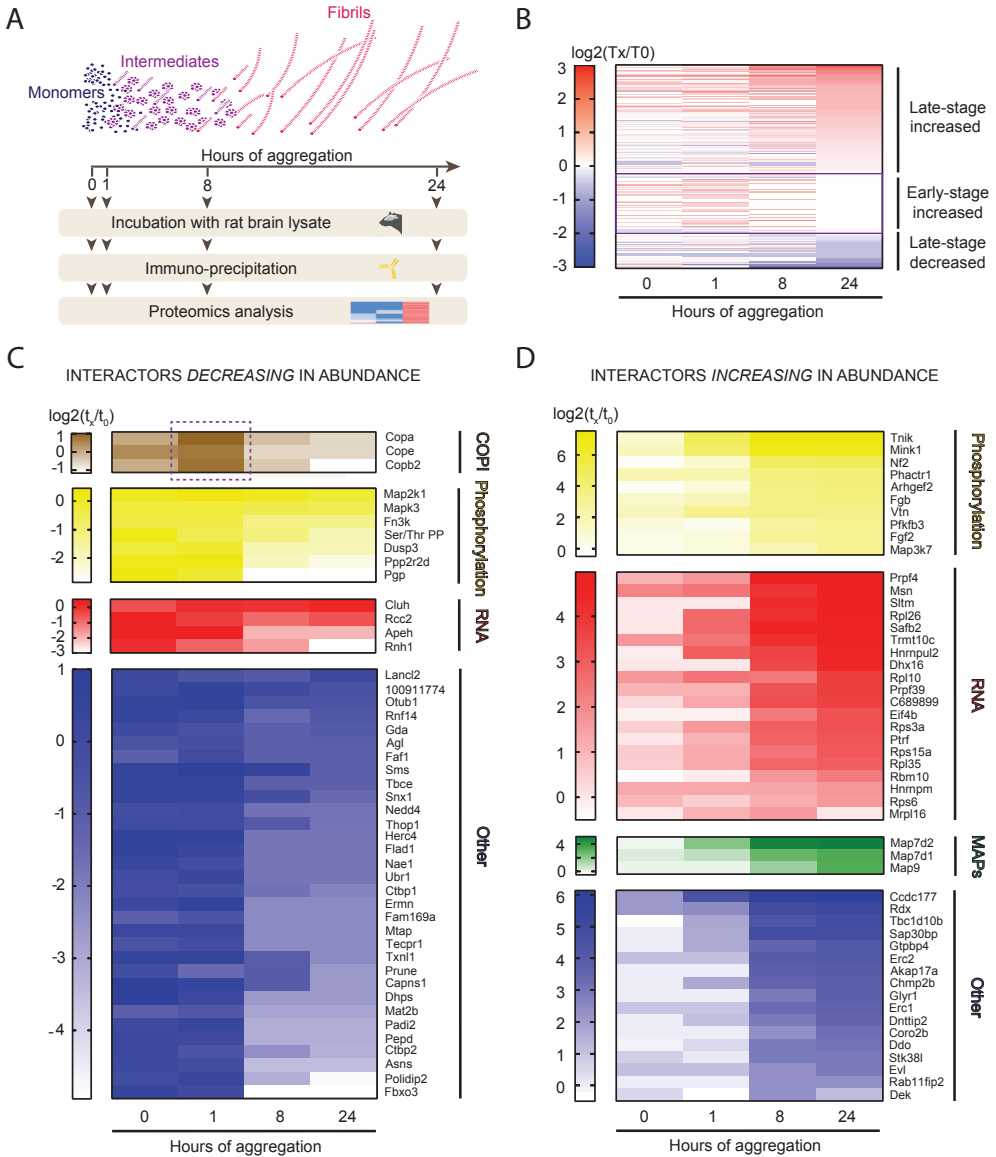


Figure 2. Tau interactome rewires during aggregation

(A) Experimental setup to highlight interactome changes upon Tau aggregation.

(B) Heat map of MS-identified proteins of Tau-RD* aggregates (0, 1, 8 and 24 h of aggregation). Colours show relative enrichment of different time points (tx) compared to monomeric Tau-RD* without heparin (t0-). Interactors are sorted by trend (late-stage decreased, early-stage increased, late-stage decreased).

(C) Heat map showing an unbiased selection of Tau-RD* lost proteins (decreasing in abundance) upon aggregation, sorted by functional clusters (GO-term analysis). Dashed purple box highlights interactors increasing in abundance at 1 hour, then decreasing as aggregation proceeds.

(D) Heat map showing an unbiased selection of Tau-RD* sequestered proteins (increasing in abundance) upon fibril formation, sorted as for (C).

molecular partners. We wondered whether the aberrant interactors of Tau aggregates share common functional properties by classifying them via Gene Ontology enrichment analysis, a tool to cluster proteins with similar biological functions (GO Consortium, 2017 (Ashburner et al., 2000)). We first focused on monomeric-specific interactor lost upon aggregation, with only 25% of interactors belonging to functional clusters, namely protein phosphorylation regulators (16%) or RNA binding proteins (9%) (Fig. 2C). Notably, members of the COPI complex are the most prominent interactor of nano-aggregates (t1). They neither bind to monomers nor fibrils, indicating that this complex prefers binding to Tau oligomeric species (Fig. 2C, dashed purple box). When analyzing the interactome of the Tau-RD* fibrils, remarkably 66% of the newly attracted interactors belong to only 3 major functional clusters (Fig. 2D), namely RNA Binding proteins (40% of the interactors), Regulators of Protein Phosphorylation (20%), Microtubule Associated Proteins (MAPs, 6%), with the rest of the proteins showing no GO enrichment (Various Proteins, 34%). Results were confirmed in 3 biological replicates (Fig. S1 for lost monomeric interactors and Fig. S2 for fibrillary interactors), allowing us to conclude that Tau aggregates attract proteins connected to a very limited set of biological processes, exchanging proteins connected to the same functional networks and increasing their relative abundance, whereas the rest of the cellular activity seems to not be disturbed by Tau fibrils. Strikingly, COPI preferentially interact with early stage aggregates and MAPs with late stage fibrils, suggesting that different types of aggregates may differ in their gain of function aberrant phenotypes.

Arginine side chains mediate fibril interactions

We hypothesized that shared biological activity may underline common sequence features. We noted that RNA and microtubule binding proteins and regulatory proteins often contain intrinsically disordered regions. Therefore, we determined the degree of disorder for each fibril-binding protein using the disorder predictor MetaDisorder, which particularly accurate because it is the consensus of 15 primary algorithms (Kozlowski and Bujnicki, 2012). We then plotted the disorder content per functional cluster. All functional clusters, even non-clustered fibrils binders, showed high disorder content, with medians at least 15% higher in absolute disorder than the average disordered percentage in the human proteome (Pentony and Jones, 2010) (Fig. 3A). Most dramatic is the MAP cluster, which is 95% disordered. We conclude that Tau fibrils attract proteins enriched in intrinsically disordered regions. It is unusual for intrinsically disordered proteins to directly interact with each other (van der Lee et al., 2014), therefore we can also conclude that fibrillation endows Tau with new properties to engage in protein-protein interactions.

We wondered whether disordered stretches captured by Tau fibrils showed specific sequence properties. To reveal such a bias, we compared the frequency of each amino acid in the disordered

regions of fibril interactors to the average frequency in the whole disordered proteome (Tompa, 2002). Remarkably, our analysis showed that chemical composition of disordered regions of fibril-specific interactors dramatically differed from that of typical disordered regions (Fig. 3B). In particular, Prolines and Valines were significantly depleted, whereas they are the most abundant components in the entire disordered proteome. Conversely, Arginine and Methionine stood out as the most significantly enriched amino acids ($p \leq 0.0001$, Wilcoxon paired non-parametric t-test). Arginines had higher frequency when compared to Methionines (5% of total residues in disordered regions for Arginine, 1.6% for Methionine, Fig. 3B). More than 85% of the interactors had at least 1 long disordered region (30+ residues), with 90% of these regions containing at least two Arginines. These numbers reveal that Arginines may have a predominant role in IDRs binding to Tau fibrils. When compared to the folded proteome, most of the amino acids were depleted, (Fig. 3C). Conversely, Arginine stood out again as the most significantly enriched amino acid ($p \leq 0.0001$, Wilcoxon paired non-parametric t-test), whereas Methionine had similar enrichment compared to globular proteins, suggesting that the footprint of Tau fibril-specific interactors is different from globular proteins too, and therefore a unique signature of proteins binding to Tau fibrils. Of note, aromatic amino acids, which can also engage in π -interactions but are less well tolerated in disordered stretches, were not enriched when compared with either folded or disordered proteome average frequencies, further highlighting the enrichment of Arginines in binders of Tau fibrils (Fig. 3B and Fig. 3C). Taken together, our bioinformatics analysis shows that Tau fibril-specific interactors have their own unique footprint, characterized by specific amino acid biases in Arginine-rich disordered regions that differ from the typical disordered segment and globular protein.

π - π interactions crucial for fibrils binding

Next, we aimed to reveal the molecular mechanism of interaction of Tau fibrils with IDRs. Tau-RD has a positive net charge at physiological pH ($pI = 9.7$ for Tau-RD, 9.3 for Tau-RD*), making us wonder why positively charged Arginines would be so enriched in Tau aggregation-specific interactors. Notably, next to charge-charge interactions, Arginine can also engage in protein-protein interactions via the delocalised π -system of sp^2 -hybridized atoms of its guanidinium group (Vernon et al., 2018). We also noted that there is no significant bias for the other positively charged residue, Lysine (Fig. 3B), whose side chains contain only sp^3 -hybridized atoms and are thus unable to engage in π - π interactions, suggesting that pi orbitals and not charge could be the determinant for binding to fibrils. We set out to test this hypothesis by analysing the impact of Arginine to Lysine exchanges in a fibril-binding protein, an established test to verify the contribution of π - π interactions (Vernon et al., 2018). We chose the N-terminal domain of the fibril-specific protein Map7 for this test (Fig. 4). This domain has extended disordered stretches

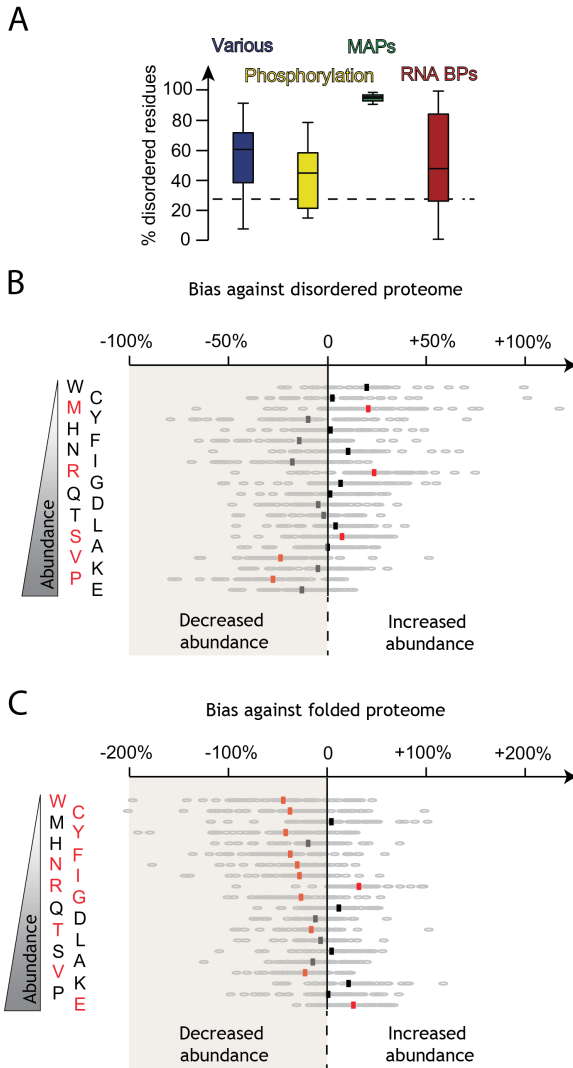


Figure 3. Tau aggregation-specific interactors are enriched in disordered sequences

(A) Prediction of percentage of disordered residues of Tau-RD* fibril-specific interactors (timepoint 24 h) using Meta-Disorder (Kozłowski and Bujnicki, 2012), sorted by functional clusters. Dashed line indicates the average disorder percentage for human proteome (Pentony and Jones, 2010).

(B) Amino-acidic footprint of disordered regions of Tau-RD* fibril-specific interactors, expressed in fold-changes against the abundance of each amino acid in the disordered regions of the whole human proteome (Tompa, 2002) (red: significantly increased; black: significantly decreased, $p \leq 0.0001$). Amino acids on the y-axis are sorted by abundance in the disordered proteome.

(C) As in B, but against folded regions of the whole human proteome (Tompa, 2002). Amino acids on the y-axis are sorted by abundance in the disordered proteome, for comparison with Fig. 3B.

enriched in Arginines (8.4% of disordered residues), next to a folded coiled coil domain, making it a valuable candidate to test Arginine-driven binding to fibrils. We designed and purified two HA-tagged truncations of Map7-M1-S227, wildtype and an R12K variant where we replaced all Arginines in the disordered regions of the protein with Lysines (Fig. 4A). The R12K substitution had no effect on the net charge of the protein (Fig. 4B). Moreover, the circular dichroism spectra of both proteins were identical and they both indicated the presence of α -helices and disordered stretches (Fig. 4C). Thus, exchanging Arginines to Lysines in the disordered segments of the N-terminal fragment of Map7 does neither alter its charge nor its secondary structure. Next, we set out to test whether the exchange of Arginines to Lysines would affect binding to fibrils. We subjected Tau-RD* fibrils to Map7 binding, with or without one of the two Map7 truncations. We resolved protein complexes via density gradients, using different antibodies to detect Tau-RD* and Map7. Map7 wt and R12K sedimented throughout the tube (Fig. 4D, anti-HA blot, Tube I and III), whereas Tau-RD* fibrils sedimented to the bottom half of the tube (Fig. 4D, anti-FLAG blot, tube II and IV, fractions 7-12). The homogenous spread of Map7 alone throughout the tube could be explained by the tendency of disordered regions to show higher apparent molecular mass compared to order structures (Receveur-Brechot et al., 2006). When Map7 wt and Tau-RD* fibrils reacted together, however, the entire Map7 population sedimented in the heaviest fraction, indicating its association with the largest fibrillary structures (Fig. 4D, anti-HA blot, tube II, fraction 12), consistent with the proteomics analysis (Fig. 2C). Conversely, when Map7 R12K and Tau-RD* fibrils reacted, only a part of Map7 population sedimented in the heaviest fraction, whereas another part distributed in the lightest fractions, indicating only partial association with largest fibrillar structures (Fig. 4D, anti-HA blot, tube IV, fractions 1-5 and 12). Since both constructs have same charge and structural properties but differ in their ability to engage in π - π interactions, we conclude that π - π interactions are key forces governing binding to fibrils.

Hsp90 stalls Tau aggregation

Aberrant interactome rewiring is linked to cellular toxicity (Anvarian et al., 2016). It would be therapeutically valuable to find endogenous proteins able to modulate such aberrant transition in interactome. We looked for such endogenous player in the protein quality control network, a pool of proteins that ensures the health of the proteome by removal of misfolded and aggregated proteins (Hartl, 2017). A key player in this network is the molecular chaperone Hsp90, which also controls Tau levels in the cell. Hsp90 forms a complex with Tau buffering its aggregation-prone regions (Karagöz et al., 2014) and controls the degradation of Tau monomers (Dickey et al., 2007). To understand the effect of Hsp90 on Tau aggregation dynamics, we wondered how this molecular chaperone would interfere with the formation of Tau fibrils. To monitor

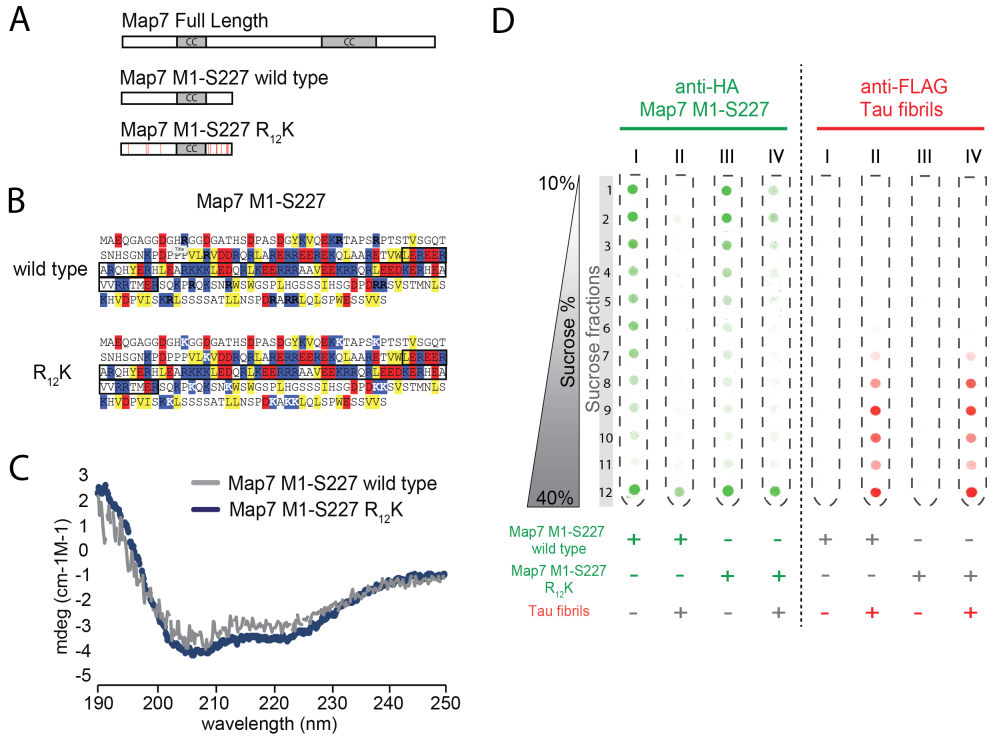


Figure 4. π stacking of Arginines drive binding to Tau fibrils

(A) Graphic scheme of Map7 Full Length and Map7 truncations used in this study. Red bars indicate R to K replacement. CC = coiled-coil domain.
 (B) Sequences of Map7 M1-S227 truncations colored by hydrophobicity (yellow boxes), negative charges (red boxes) and positive charges (blue boxes). White Ks indicate Arginines replaced with Lysines. Black boxes comprise coiled-coil domain.
 (C) Circular Dichroism of Map7 M1-S227 truncations.
 (D) Binding of Map7 1M-227S truncations to Tau-RD* fibrils, assessed by density gradients. Tubes (I to IV) were either blotted against HA tag against FLAG tag, targeting respectively Map7 truncations or Tau-RD* fibrils. Samples were centrifuged for 2.5 h at 200000g.

aggregation of Tau-RD* in the presence of increasing concentrations of Hsp90, we induced aggregation in the presence of Thioflavin T, a dye that recognizes amyloid structures (Fig. 5A). After aggregation reached plateau for all conditions, we resolved aggregating samples on density gradients (Fig. 5B). In a dose-dependent manner, Hsp90 suppressed Tau-RD* to form higher molecular weight species, decreased amyloid content and prevented fibril formation altogether. Hsp90 also altered morphology of the aggregates: instead of fibrils, only smaller structures were visible in the TEM images when aggregation was performed in the presence of Hsp90 (Fig. 5C). Thus, Hsp90 has a dramatic effect on Tau aggregation dynamics, derailing its aggregation toward non-fibrillar nano-aggregates with decreased amyloid content.

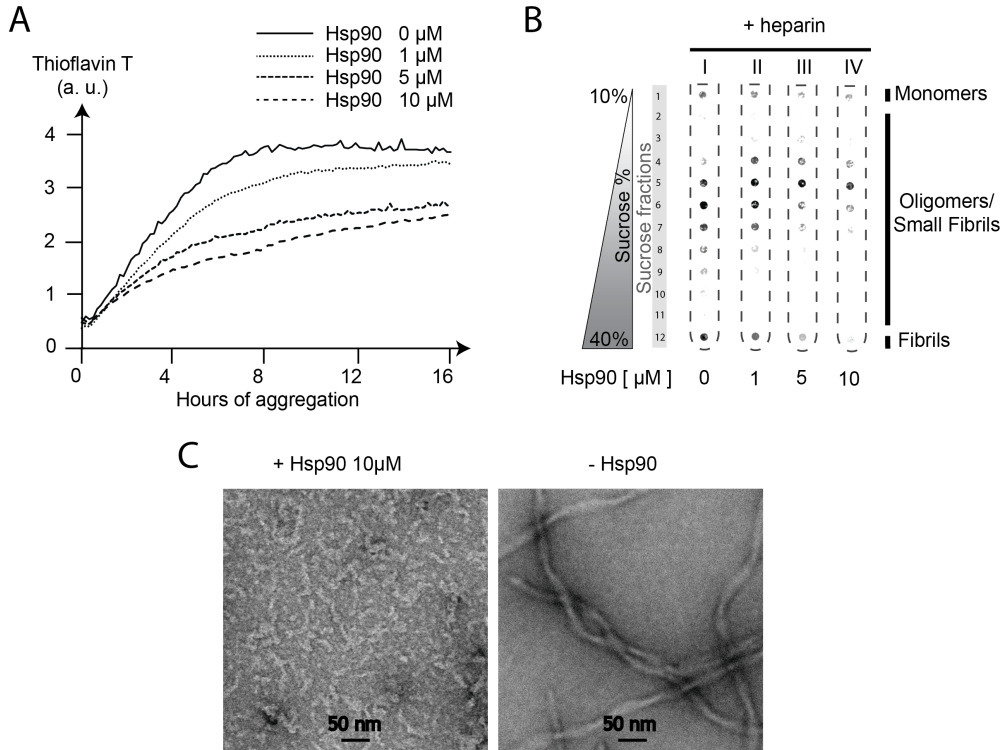


Figure 5. Hsp90 details Tau aggregation toward non-fibrillar nano-aggregates.

(A) Thioflavin T assay to detect decrease of amyloid content in the presence of increasing concentrations of Hsp90 (0, 1, 5, 10 μ M). Fluorescence is expressed as arbitrary unit (a. u.).

(B) Density gradients to detect inhibition of fibril formation in the presence of increasing concentrations of Hsp90 (0, 1, 5, 10 μ M). Samples from Fig. A at 16 h were loaded directly onto density gradients and resolved by centrifugation for 2.5 h at 200,000 g.

(C) Transmission Electron Microscopy of Tau-RD* aggregating samples in the presence or absence of 10 μ M Hsp90 after 2 days of aggregation.

Hsp90 modulates fibril interactome

Next, we wondered whether aggregates with different structural features should attract different binding partners. To address this question, we monitored Tau-RD* aggregation in the presence or absence of Hsp90 and described the changes in abundance of pulled-down interactors in these two conditions (Fig. 6A). Stunningly, none of the fibril-specific interactors were enriched, whereas many of them decreased in abundance for all functional clusters when Hsp90 modulated the aggregation (Fig. 6B). The only interactor that showed a significant enrichment was α -synuclein (SNCA), a well-known Hsp90 partner, suggesting that Hsp90 may co-aggregate with nanoaggregates. A subgroup of interactors, associated to Tau monomer but not to Tau fibrils (FBXO3, CTBP1, CTBP2 and POLDIP2, Fig. S1) appeared in the presence of Hsp90.

Also, the Hsp90-stalled nano-aggregates did not associate with COPI, in contrast to the ones formed in its absence. Taken together, these results suggest that Hsp90 drastically reshapes Tau aggregation-specific interactome, blocking the interactions associated to pathological Tau fibrils and moulding the interactome toward a more physiological state.

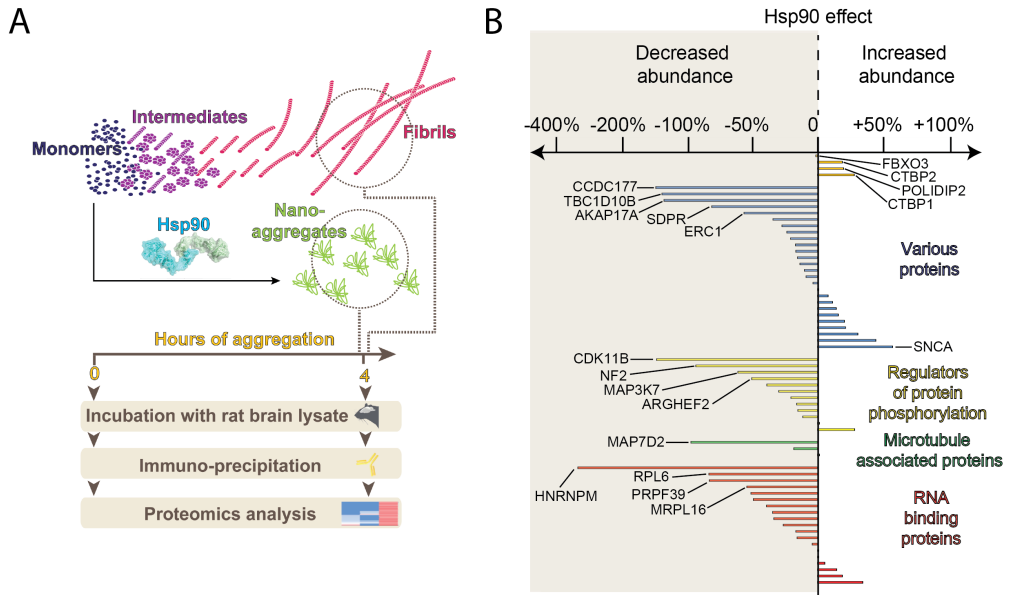


Figure 6. Hsp90 remodels Tau aggregation-specific interactome

(A) Experimental setup to compare interactome changes in the presence or absence of Hsp90.

(B) Bar graph showing Hsp90-dependent modulation of Tau-RD* aggregation reflected as differences enrichments for specific proteins sequestered by Tau-RD* fibrils in the presence/absence of Hsp90.

DISCUSSION

We tracked interactome changes associated to the formation of Tau fibrils, a hallmark of Alzheimer’s disease. Tau fibrils results from the aggregation of monomeric Tau, known to stabilize microtubules in neurons. As they form, Tau fibrils attract specific classes of abnormal interactors, mostly involved in RNA biology, regulation of protein phosphorylation and microtubule dynamics. Strikingly, these interactors share similar structural features, endowed with long disordered stretches with specific amino acidic bias. Arginine bias plays a crucial role, as Arginine-to-Lysine substitutions partially impairs the binding to Tau fibrils.

Tau fibrils target RNA, cytoskeletal and phosphorylation dynamics

Our experimental setup focuses on the soluble fraction of the cytoplasm, the environment where fibrils naturally accumulate during the progression of Alzheimer (Wang and Mandelkow,

2016). Proteomics studies concerning Tau fibrils reveal interactomes of insoluble membrane-enriched fractions co-pelleted with Tau fibrils and their ER-associated components (Donovan et al., 2012; Meier et al., 2015). Here we provide data sets revealing interactions of Tau fibrils with the soluble components of the brain, to which the protein is exposed when aggregating in disease. Our setup accelerates the process of Tau aggregation from years *in vivo* to hours *in vitro* and highlights proteomic rearrangements over time, adding a time dimension to proteomics studies. Thus, our study mimics the temporal dynamics of Tau aggregation spanning several decades from initial seeds to mature fibrils, with different aggregation stages having different reactivity with the cellular environment (Fig. 2B). We fractionated Tau aggregates over time to overcome the problem that the dynamic nature of the aggregation process would preclude us from obtaining a defined, monodisperse Tau nano-aggregate (Wang and Mandelkow, 2016). We show that early-stage aggregates specifically attract COPI components. These interactors decrease in abundance as fibrils form, highlighting the exchange of interactors as aggregation proceeds. Our data can explain Golgi fragmentation observed in neurons of Alzheimer brains without tangles (Stieber et al., 1996).

Our interactome data suggest that Tau fibrils may hijack three cellular processes: 1) RNA-related processes, 2) cytoskeletal dynamics via Microtubule Associated Proteins (MAPs) and 3) phosphorylation equilibria (Fig. 2C). Regarding RNA-related processes, the interactome of monomeric Tau is already highly enriched in components of the ribonucleoproteome (Gunawardana et al., 2015), and Tau fibrils have been shown to impair RNA translation (Meier et al., 2016). Our data suggest a mechanism where Tau fibrils attract additional proteins related to RNA processing, altering the balance between Tau and the ribonucleoproteome and thus impairing translation.

Tau fibrils target also MAPs, linked to cytoskeletal dynamics. MAPs have been shown to act together to regulate microtubule dynamics and cargo transport, with Map7-Tau imbalances disrupting axonal transport and neuronal growth (Monroy et al., 2018). Such imbalances in axonal transport are a common marker of Tau-related neurodegenerative disorders (Kneynsberg et al., 2017). Our data suggest a novel mechanism to explain such disorders, where Tau aggregation acts on two levels, first by promoting imbalances in the levels of different MAPs and second by actively sequestering other MAPs components, further exacerbating such imbalances.

Lastly, our data show how Tau fibrils attract a wide range of kinases and other protein phosphorylation regulators. Tau is hyperphosphorylated in Alzheimer, however the contribution of its phosphorylation to aggregation is yet to be understood (Goedert et al., 2017; Wang and Mandelkow, 2016). New structural insight proved that phosphorylated residues do not contribute significantly to assembly of mature fibrils (Fitzpatrick et al., 2017). Our data suggest

that the effect of Tau fibrils on phosphorylation dynamics may be subtler and not related to their hyperphosphorylation, once again disturbing levels and activity of a range of phosphoregulators as in the case of RNA binding proteins and MAPs.

To summarize, scattered experimental evidences support the targeting of RNA, microtubule and phosphorylation dynamics by Tau fibrils. Our work shows how these processes are coherently linked by interactome re-wiring of Tau from its monomeric, physiological protomer to its polymeric, toxic aggregate.

Analogies between mode-of binding of Tau fibrils and proteins involved in phase separation

The structural analysis of Tau fibril-specific interactome revealed an abundance of disordered stretches compared to average disorder propensity of the human proteome. Intriguingly, the abundance of disorder stretches is a characteristic of interactors binding to Huntingtin fibrils (Ripaud et al., 2014) or to artificial proteins with propensity to form amyloid fibrils (Olzscha et al., 2011), suggesting that the preference for highly disordered binders is a general feature of amyloids. We found a striking enrichment of Arginine and Methionine residues in disordered regions of Tau fibril binders, while Prolines and the hydrophobic residues Isoleucine, Valine and Phenylalanine were significantly depleted, highlighting a unique footprint of Tau fibrils binders. Lysine does not contribute to binding, despite their positive charge shared with Arginines, pointing to the role of Arginine as π -stacker (Vernon et al., 2018). Of note, also the other strongly enriched residue in Tau fibril interactors, Methionine, can establish π - π interactions with aromatic rings (Valley et al., 2012). However, Arginines increased abundance suggests a predominant role of this residues in driving the binding to Tau fibrils. Thus, our work describes interactome rearrangements not only in a qualitative manner but describe a key molecular component driving such re-arrangements, namely side chains of Arginines capable of engaging in π - π interactions. π -stacking in disordered regions is also the fundamental force driving Liquid Liquid Phase Separation, a process that forms membrane-less compartmentalization within a cell (Alberti, 2017; Qamar et al., 2018). The number of Arginines is a key factor for phase separation propensity (Wang et al., 2018). So far, the role of π -stacking was showed only for physiologically relevant proteins. We turned the table, using non-physiological aggregates to show that their interactions are based on the same chemical principles driving phase separation. Our paradigm explains recent phenomenological data, showing co-influence of aggregation dynamics between Tau and phase-separating proteins (Maziuk et al., 2018; Vanderweyde et al., 2016). Strikingly, Tau fibril-specific interactome is enriched in proteins from the Heteronuclear Ribonucleoparticle family (Fig. 2A and Fig. S2), whose protein architecture promotes phase separation (Harrison and Shorter, 2017). Thus, Tau fibrils can attract phase-separating

proteins, potentially increasing their local concentration and promoting their co-aggregation. Taken together, our data mechanistically support a tight cross-talk between physiological and pathological aggregates. In terms of fundamental chemical contacts, they are two sides of the same coin. Interestingly, Arginine is enriched in several chaperone binding motifs, including Hsp70, J-domain co-chaperones, SecB and trigger factor (Knoblauch et al., 1999; Patzelt et al., 2001; Rüdiger et al., 1997; Rüdiger et al., 2001). We speculate that Arginine may have specific but not yet understood implications for protein homeostasis and aggregation. In this context it is interesting that the abundant cytosolic Hsp90 chaperone (Picard, 2002) may have an upstream effect in avoiding the engagement of Tau fibrils with their abnormal interactors by buffering these exposed stretches in the cytoplasm. Hsp90 may therefore act on two levels in the fight against Alzheimer-related Tau fibrils, first by actively blocking their formation and second by preventing fibrils binding to their abnormal interactors. Understanding how the manipulation of Hsp90 affects the biology of Tau fibrils may grant us a new weapon to fight Alzheimer’s Disease.

SUPPLEMENTARY FIGURES

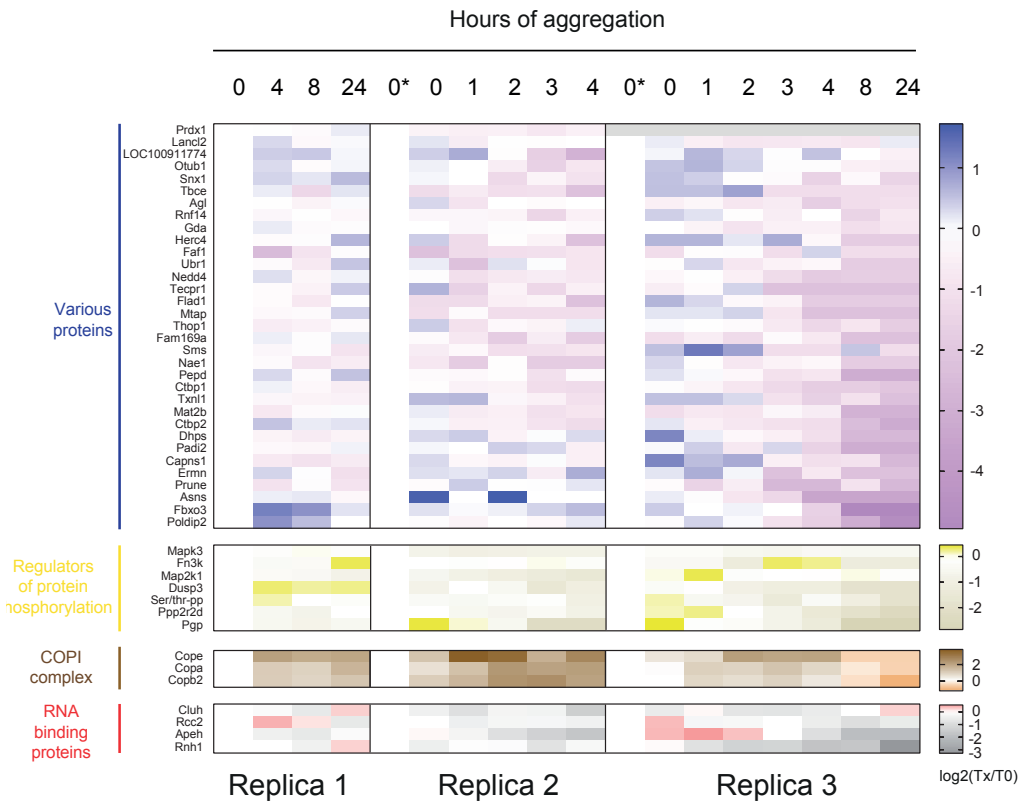


Figure S1. Interactome rewiring of monomeric-specific interactors, 3 independent biological replicas

Heat map showing an unbiased selection of Tau-RD* lost proteins upon aggregation. Only proteins with a Fold Change calculation > 2 (FC-A, Crapome; by averaging the spectral counts across the selected controls) were considered enriched in Tau-RD* monomers compared to control empty beads in the 3 different replicas.

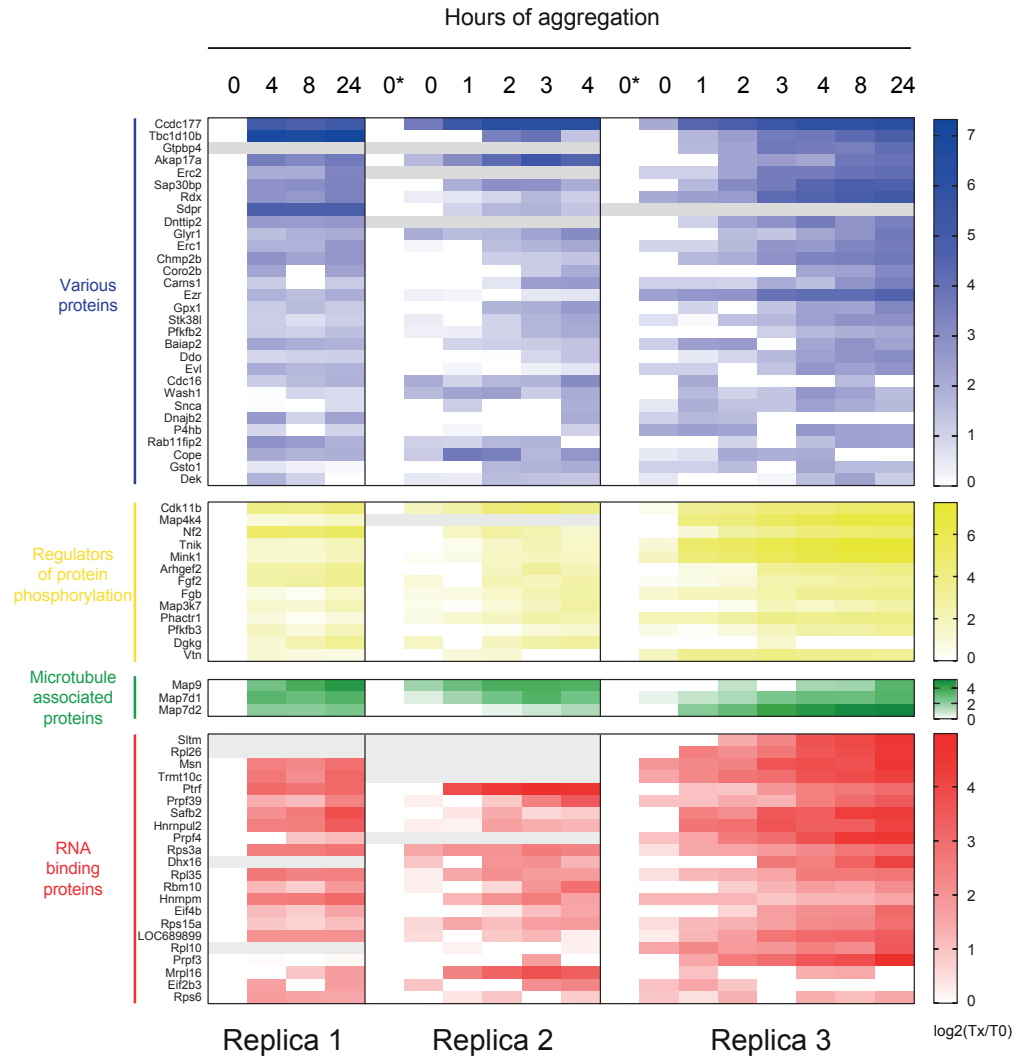
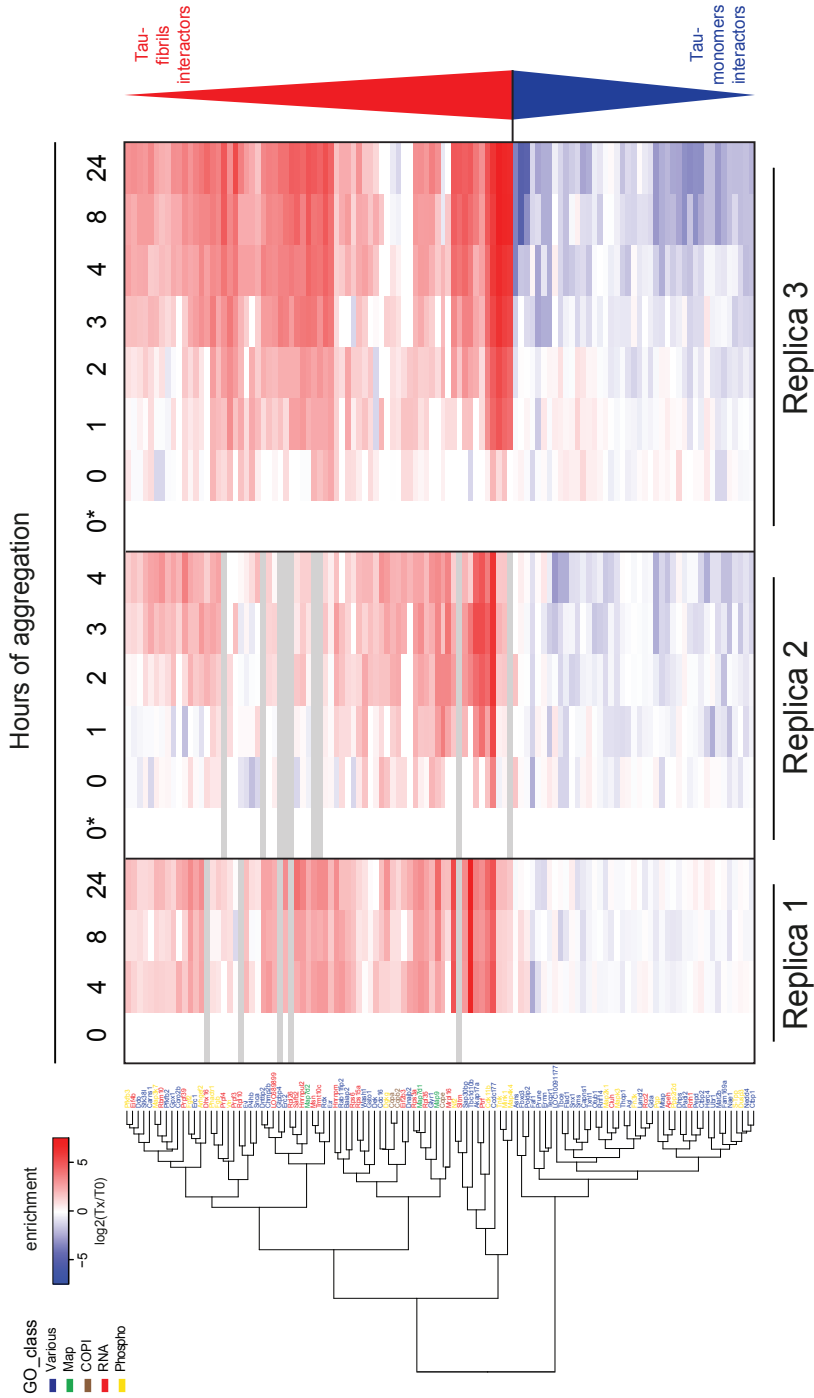


Figure S2. Interactome rewiring of fibrillar-specific interactors, 3 independent biological replicas

Heat map showing an unbiased selection of Tau-RD* sequestered proteins upon aggregation. Only proteins with a Fold Change calculation > 2 (FC-A, Crapome; by averaging the spectral counts across the selected controls) were considered enriched in Tau-RD* aggregates compared to Tau-RD* monomers in the 3 different replicas.

5



Tau interactome. 3 independent biological replicates.

Heat map showing significant proteins interacting with Tau fibrils or Tau momers.

KEY RESOURCES TABLE

Key resources table can be found with this article online at:

<https://www.biorxiv.org/content/early/2019/01/16/522284.full.pdf>

EXPERIMENTAL PROCEDURES

In Vitro Studies

Human Tau-RD* and rat HA-Map7 truncations (M1-S227, both wild type and R12K), were cloned in pET24a vectors and expressed in *E. coli* (BL21 Rosetta2). Human Hsp90b was cloned in pET23a vector and expressed in *E. coli* (BL21 Rosetta2).

Animals

All experiments were approved by the DEC Dutch Animal Experiments Committee (Dier Experimenten Commissie), performed in line with institutional guidelines of Utrecht University and were conducted in agreement with Dutch law (Wet op de Dierproeven, 1996) and European regulations (Directive 2010/63/EU). Female pregnant Wister rats were obtained from Janvier Laboratories.

Purification of Tau-RD*

We overproduced N-terminally FLAG-tagged (DYKDDDDK) Human Tau-RD (Q244-E372, also referred to as K18, with pro-aggregation mutation DK280) recombinantly in *E. coli* BL21 Rosetta 2 (Novagen), with additional removable N-terminal His6-Smt-tag.

(MGHHHHHHGSDSEVNQEAKPEVKPEVKPETHINLKVSDGSSEIFFKIKKTTPLRRLMEAFQKRGKEMDSL-RFLYDGIQADQTPEDLDMEDNDIIEAHREQIGG).

Cells were harvested, flash-frozen in liquid nitrogen and stored at -80°C until further usage. Pellets were thawed in a water bath at 37°C and resuspended in 50 mM HEPES-KOH pH 8.5 (Sigma-Aldrich), 50 mM KCl (Sigma-Aldrich), $\frac{1}{2}$ tablet/50 ml EDTA-free protease inhibitor (Roche), 5 mM β -mercaptoethanol (Sigma-Aldrich). Cells were disrupted by an EmulsiFlex-C5 cell disruptor (Avestin). Lysate was cleared by centrifugation, filtered with a $0.22\ \mu\text{m}$ polypropylene filter (VWR) and supernatant was purified using an ÄKTA Purifier chromatography system (GE Healthcare). First, protein was loaded onto a POROS 20MC (Thermo Fischer Scientific) affinity purification column in 50 mM HEPES-KOH pH 8.5, 50 mM KCl, 5 mM β -mercaptoethanol, eluted with a 0-100% linear gradient (5 Column Volumes, CV) of 1 M imidazole. Fractions of interest were collected and concentrated in a buffer concentrator (Vivaspin, cutoff 10 kDa) to final volume of 3 ml. The concentrated sample was desalted with a PD-10 desalting column (GE Healthcare) in 50 mM HEPES-KOH pH 8.5, $\frac{1}{2}$ tablet/50 ml Complete protease inhibitor (Roche) and 5 mM β -mercaptoethanol. The His6-Smt tag was removed by Ulp1 treatment, shaking at 4°C over night. Next day, protein was loaded onto a POROS 20HS (Thermo Fischer Scientific) cation exchange column equilibrated with 50 mM HEPES-KOH pH 8.5. Protein was eluted with a 0-100% linear gradient (15 CV) of 2 M KCl (Carl Roth). Fractions of interest were collected and loaded onto a HiLoad 26/60 Superdex 200 pg (GE Healthcare Life Sciences) size exclusion column equilibrated with aggregation buffer (25 mM HEPES-KOH pH 7.5, Complete Protease Inhibitors (1/2 tablet/50 ml), 75 mM KCl, 75 mM NaCl and 10 mM DTT). Fractions of interest were further concentrated to the desired final concentration using a concentrator (Vivaspin, cut-off 5 kDa). Protein concentration was measured using an ND-1000 UV/Vis spectrophotometer (Nanodrop Technologies) and purity was assessed with SDS-PAGE. Protein was aliquoted and stored at -80°C .

Purification of MAP7 truncations

We overproduced N-terminally HA-tagged (YPYDVPDYA) rat map 7 truncations (M1-S227, both wild type and R12K), recombinantly in *E. coli* BL21 Rosetta 2 (Novagen), with additional removable N-terminal His6-Smt-tag. Cells were harvested, flash-frozen in liquid nitrogen and stored at -80°C until further usage. Pellets were thawed in a water

bath at 37°C and resuspended in 50 mM phosphate buffer pH 8 (Sigma-Aldrich), 150 mM KCl (Sigma-Aldrich), ½ tablet/50 ml EDTA-free protease inhibitor (Roche), 5 mM β-mercaptoethanol (Sigma-Aldrich). Cells were disrupted by an EmulsiFlex-C5 cell disruptor (Avestin). Lysate was cleared by centrifugation, filtered with a 0.22 μm polypropylene filter (VWR) and supernatant was purified using an ÄKTA Purifier chromatography system (GE Healthcare). First, protein was loaded onto a column with Ni-IDA resin. Proteins were eluted by 250 mM imidazole (Sigmaaldrich) in phosphate buffer (150 mM, NaCl (Sigma-Aldrich), pH=8.0) in presence of Complete Protease Inhibitors (1 tablets/100 ml) (Roche) and 5 mM β-mercaptoethanol (Sigma-Aldrich). The His6-Smt tag was removed by Ulp1 treatment at 4°C over night, while dialyzed against 50mM phosphate buffer (pH=8.0) and 5 mM β-mercaptoethanol with a 6kDa cut-off membrane (SpectrumLaboratories). Next day, protein was loaded onto a POROS 20HS (Thermo Fischer Scientific) cation exchange column equilibrated with 50mM phosphate buffer (pH=8.0) and 5 mM βmercaptoethanol. Protein was eluted with a 0-100% linear gradient (15 CV) of 2 M KCl (Carl Roth). Fractions of interest were further buffer exchanged against 25 mM HEPES buffer (pH=7.5, salt: 75 mM KCl; 75 mM NaCl) Vivaspin, cut-off 6 kDa and further concentrated using a concentrator (Vivaspin, cut-off 5 kDa). Protein concentration was measured using an ND-1000 UV/Vis spectrophotometer (Nanodrop Technologies) and purity was assessed with SDS-PAGE. Protein was aliquoted and stored at -80°C.

Protein purification of Hsp90

Hsp90 was purified as previously described (Radli et al., 2017). We overproduced N-terminally His6-tagged human Hsp90b recombinantly in *E. coli* BL21 Rosetta 2 (Novagen). Cells were harvested, flash-frozen in liquid nitrogen and stored at -80°C until further usage. Pellets were thawed in a water bath at 37°C and resuspended in 12.5 mM sodium phosphate buffer pH 6.8 (Sigma-Aldrich), 75 mM KCl (Sigma-Aldrich), ½ tablet/50 ml EDTA-free protease inhibitor (Roche), 5 mM β-mercaptoethanol (Sigma-Aldrich). Cells were disrupted by an EmulsiFlex-C5 cell disruptor (Avestin). Lysate was cleared by centrifugation, filtered with a 0.22 μm polypropylene filter (VWR) and supernatant was purified using an ÄKTA Purifier chromatography system (GE Healthcare). First, protein was loaded onto a POROS 20MC (Thermo Fischer Scientific) affinity purification column in 50 mM sodium phosphate buffer pH 8.0, 400 mM KCl, 5 mM β-mercaptoethanol eluted with a 0-100% linear gradient (5 Column Volumes, CV) of 1 M imidazole. Peak was loaded onto a POROS 20HQ (Thermo Fischer Scientific) anion exchange column equilibrated with 25 mM sodium phosphate buffer pH 7.2 and 5 mM β-mercaptoethanol. Protein was eluted with a 0-100% linear gradient (15 CV) of 2 M KCl. Fractions of interest were then loaded onto a HiTrap heparin column High Performance (GE Healthcare) column equilibrated with 25 mM sodium phosphate buffer pH 7.2 and 5 mM β-mercaptoethanol. Protein was eluted with a 0-100% linear gradient (15 CV) of 2 M KCl and peak was buffer exchanged against 25 mM sodium phosphate buffer pH 7.2, 150 mM KCl, 150 mM NaCl and 5 mM βmercaptoethanol. Protein concentration was measured using an ND-1000 UV/Vis spectrophotometer (Nanodrop Technologies) and purity was assessed with SDS-PAGE. Protein was aliquoted and stored at -80°C.

Formation of Tau fibrils

Monomeric Tau-RD* aggregated in aggregation buffer and Heparin Low Molecular Weight (Santa Cruz Biotech), concentrations depending on the experiment and Tau:heparin ratio always kept 4:1. Aggregation was performed at 37°C, shaking at 180 rpm, and aliquots were flash frozen at timepoints indicated in the text. Aliquots were then thawed on ice for downstream applications.

Preparation of density gradients

Density gradients were prepared according to an established procedure (Stone, 1974). Gradients were formed by dissolving 10% and 40% sucrose (Sigma-Aldrich), in 25 mM HEPES pH 7.5, 75 mM KCl, 75 mM NaCl. Gradients were set up in polyallomer centrifuge tubes (Beckmann) by filling them to half hight with 40% sucrose and topping them up with an equal amount of 10% sucrose. Gradients were formed by tilting the tubes horizontally for 3 h at room temperature and then tilting them back to vertical position. Tubes were stored overnight at 4°C and samples were loaded

as described for each experiment.

Sample preparation for density gradients

Fig. 1A. 2.5 μ l of Tau-RD* aggregates (37 μ M of monomers) at different aggregation stages (time of aggregations: 0, 1, 8, 24 h) were loaded onto density tubes and subjected to centrifugation, 2.5 h at 200,000 g.

Fig. 4D. 2.5 μ l of Tau-RD* fibrils (20 μ M of monomers, timepoint 24 hours) reacted for 1 h at 37°C with either 7.5 μ l of aggregation buffer or 7.5 μ l of aggregation buffer plus 0.5 μ M rat HA-Map7 M1-S227, either wt or R12K. Samples were then entirely loaded onto density tubes and subjected to centrifugation, 2.5 h at 200000g.

Fig. 5B. 10 μ l of Tau-RD* (20 μ M of monomers), aggregated for 16 hours in the plate reader Spectramax i3 (Molecular Devices) in the presence of increasing concentration of Hsp90 (0, 1, 5 and 10 μ M) in aggregation buffer, were loaded completely onto density tubes and subjected to centrifugation, 2.5 h at 200000g.

Dot blot analysis of density gradients

Dot blot was performed using a dot blot apparatus (BioRad) and nitrocellulose membrane 0.1 μ M (Sigma-Aldrich) washed with PBS. Twelve fractions were manually collected for each tube into a 96-deep well (Thermo Fisher Scientific), and each dot-blot well was filled with 150 μ l of fraction using a multi-pipette which was pulled through by applying vacuum after 10 minutes of incubation with the membrane at room temperature. Nitrocellulose membranes were blocked with PBS blocking buffer (LI-COR) and incubated with primary antibody, either monoclonal anti-FLAG M2 (F3165, Sigma Aldrich, working dilution 1:1000) or anti-HA 12CA5 mouse hybridoma (produced in-house), at room temperature for 1 h. After three washes with PBS, secondary antibody Donkey anti Mouse IgG IR Dye 800 conjugated (610-732-002, Rockland, 1:5000) was added at room temperature for 45 minutes. After additional 2 washes with PBS-T and one final wash with PBS, detection was performed using Odyssey CLx (LI-COR). Imaging was performed via Image Studio Lite (LICOR).

Transmission Electron Microscopy

Specimens were prepared for Transmission Electron Microscopy using a negative staining procedure. Briefly, a 5 μ l drop of sample solution was adsorbed to a glow-discharged (twice for 20 s, on a Kensington carbon coater) pioloform-coated copper grid, washed five times on drops of deionized water, and stained with two drops of freshly prepared 2.0% Uranyl Acetate, for 1 and 5 minutes, respectively, and subsequently air dried. Samples were imaged at room temperature using a Tecnai T20 LaB6 electron microscope operated at an acceleration voltage of 200 kV and equipped with a slow-scan Gatan 4K x 4K CCD camera. Images were acquired at a defocus value of 1.5 μ m. Magnification/pixel size on specimen level: Fig. 1A 62.000 times/0.178 nm/pix; Fig. 5C right panel 62.000 times, 0.178 nm/pix; Fig. 5C right panel 100.000 times, 0.110 nm/pix

Rat brain extracts preparation

Rat brain extracts were obtained from female adult rats and homogenized in 10x volume/weight in tissue lysis buffer (50 mM Tris HCl, 150 mM NaCl, 0.1% SDS, 0.2% NP-40, and protease inhibitors). Brain lysates were centrifuged at 16.000 g for 15 min at 4°C, and the supernatant was used for the affinity purification-mass spectrometry experiments.

Affinity Purification-Mass spectrometry (AP-MS) using anti-FLAG beads on brain extracts

Tau-RD* monomers, oligomers or fibrils (37 μ M monomeric concentration, with or without 37 μ M Hsp90, depending on the experiment) were incubated for 1h at 4°C with FLAG beads (Sigma) previously blocked in chicken egg albumin (Sigma). Beads were then separated using a magnet (Dyna, Invitrogen) and washed three times with aggregation buffer to remove unbound Tau-RD* and excess of albumin. Beads conjugated with the Tau-RD* aggregated proteins were then incubated with brain extracts for 1h at 4°C. Beads were then washed in washing buffer (20 mM Tris HCl, 150 mM KCl, 0.1% TritonX-100) for five times to remove aspecific neuronal proteins. For MS analysis, beads were then resuspended in 15 μ l of 4x Laemmli Sample buffer (Biorad), boiled at 99°C for 10 minutes and supernatants were loaded on 4-12% Criterion XT Bis-Tris precast gel (Biorad). The gel was fixed with 40% methanol and 10% acetic acid

and then stained for 1h using colloidal coomassie dye G-250 (Gel Code Blue Stain, Thermo Scientific). Briefly, each lane from the gel was cut into three pieces and placed in 1.5-ml tubes. They were washed with 250 μ l of water, followed by 15-min dehydration in acetonitrile. Proteins were reduced (10 mM DTT, 1 h at 56°C), dehydrated and alkylated (55 mM iodoacetamide, 1 h in the dark). After two rounds of dehydration, trypsin was added to the samples (20 μ l of 0.1 g/l trypsin in 50 mM Ammoniumbicarbonate) and incubated overnight at 37°C. Peptides were extracted with acetonitrile, dried down and reconstituted in 10% formic acid prior to MS analysis.

Mass spectrometry analysis

All samples were analyzed on an Orbitrap Q-Exactive mass spectrometer (Thermo Fisher Scientific) coupled to an Agilent 1290 Infinity LC (Agilent Technologies). Peptides were loaded onto a trap column (Reprosil pur C18, Dr. Maisch, 100 μ m x 2 cm, 3 μ m; constructed in-house) with solvent A (0.1% formic acid in water) at a maximum pressure of 800 bar and chromatographically separated over the analytical column (Poroshell 120 EC C18, Agilent Technologies, 100 μ m x 50 cm, 2.7 μ m) using 90 min linear gradient from 7-30% solvent B (0.1% formic acid in acetonitrile) at a flow rate of 150 nl/min. The mass spectrometers were used in a data-dependent mode, which automatically switched between MS and MS/MS. After a survey scan from 350-1500 m/z the 10 or 20 most abundant peptides were subjected to HCD fragmentation. MS spectra were acquired in high-resolution mode ($R > 30,000$), whereas MS2 was in high-sensitivity mode ($R > 15,000$). For data analysis, the raw data files were converted to *.mgf files using Proteome Discoverer 1.4 software (Thermo Fisher Scientific). Database search was performed using the Uniprot rat database and Mascot (version 2.5.1, Matrix Science, UK) as the search engine. Carbamidomethylation of cysteines was set as a fixed modification and oxidation of methionine was set as a variable modification. Trypsin was set as cleavage specificity, allowing a maximum of 2 missed cleavages. Data filtering was performed using a percolator (Kall et al., 2007), resulting in 1% false discovery rate (FDR). Additional filters were search engine rank 1 and mascot ion score >20 .

Gene Ontology analysis

Proteins were classified using the enrichment analysis tool provided by Gene Ontology Consortium (GO Consortium, 2017 (Ashburner et al., 2000)).

Circular Dichroism

HA-tagged (YPYDVDPDYA) rat map 7 truncations (M1-S227, both wild type and R12K) were buffer exchanged against chloride-free phosphate buffer pH 7.5, 150 mM NaF (Sigma-Aldrich), to an estimated concentration of 0.05 mg/ml. Spectra were obtained on a Circular Dichroism Detector (JASCO), range from 180 nm to 250 nm, cut off at high tension over 700 V.

ThioflavinT aggregation assay

Aggregation of Tau-RD* (20 μ M stock) in aggregation buffer (total volume 100 μ l) was stimulated by 5 μ M heparin Low Molecular Weight in the presence of 60 μ M ThioflavinT (Sigma) in transparent, lidded Greiner 96-well plates (Sigma- Aldrich). To assess the impact of Hsp90, samples were supplied with 0, 1, 5 or 10 μ M of Hsp90. Fluorescent spectra were recorded every 10 minutes for 16 hours with a SpectraMax i3 (Molecular Devices).

QUANTIFICATION AND STATISTICAL ANALYSIS

Disorder prediction and Amino acidic bias

Disordered residues in Tau interactome protein were predicted using MetaDisorder predictor (Kozlowski and Bujnicki, 2012). We defined disorder percentage of each interactor as the amount of disordered amino acids divided by total amount of amino acids. To calculate aminoacidic biases in disordered regions, disordered regions of each aggregation-specific interactor were considered as a single string of amino acids. The frequency of each amino acid in each disordered string was then calculated and compared to its frequency in the disordered regions of the whole proteome (Pentony and

Jones, 2010). The ratio of calculated over predicted frequency was then computed and expressed as a log₂ function for the whole set of aggregation-specific interactors, sorted per amino acid, with residues ordered by their abundance in the human proteome.

Boxplot and graphs of Fig. 3 were created with SPSS. Statistical significance of Fig. 3B and Fig. 3C was tested using the Wilcoxon paired non-parametric t-test on measured paired to predicted data for each protein.

Mass spectrometry quantification

To infer protein abundance of each individual protein co-purified with Tau-RD*, we relied on total numbers of PSMs; PSMs of each identified protein were then normalized on the PSMs of the purified Tau-RD* in each condition. A ratio was then calculated between normalized PSMs of the protein co-purified with Tau-RD* at different time point of aggregation and normalized PSMs of the same protein at 0 h without heparin. Ratios were then transformed into log₂. Crapome (Mellacheruvu et al., 2013) was used to analyze Tau-RD* interacting binding proteins in three biological replicas. Proteins co-precipitated with Tau-RD* at 4 h were compared with proteins co-precipitated with Tau-RD* at 0 h without heparin. Proteins with a Fold Change calculation > 2 were considered significant proteins sequestered by Tau-RD* aggregates. This unbiased analysis for scoring AP-MS data generated a selection of proteins characterized by higher binding affinity for fibrillar species (Fig. 2D, Fig. S2). Same selected proteins are also shown in Fig. 6B to highlight how Tau-RD* interactomes change upon incubation with Hsp90. Proteins co-precipitated with Tau-RD* at 0h were compared with controls (FLAG-beads). Proteins with a Fold Change calculation > 2 were considered significant proteins sequestered by Tau-RD* monomers. This unbiased analysis for scoring AP-MS data, generated a selection of proteins characterized by higher binding affinity for monomeric species (Fig. 2C, Fig. S1). Data analysis was conducted using Perseus or R, hierarchical clustering was performed within Perseus using Euclidian distance. Fig. 2B: Quantifications of proteins detected at t = 0, 1, 8 and 24 h in replica 3 are represented in the heat map. Fig. 2C: Heat map shows an unbiased selection of proteins co-precipitating with Tau-RD* monomers without heparin (t0-) compared to control pull downs (empty FLAG-beads). Only proteins with a Fold Change calculation > 3 (FC, Crapome; by averaging the spectral counts across the selected controls) were considered enriched in Tau-RD* monomers without heparin (t0-) compared to controls in the 3 different biological replicas. Values shown in the heat map refer to time points t0, t1, t8 and t24 of replica 3. Fig. S1: Interactors of Tau-RD* monomers selected in Fig. 2C are shown with their relative quantifications across all time points in 3 biological replicas. Fig. 2D Heat map shows an unbiased selection of proteins specifically co-precipitating with Tau-RD* aggregates (t4) compared to Tau-RD* monomers without heparin (t0-). Only proteins with a Fold Change calculation > 2 (FC, Crapome; by averaging the spectral counts across the selected controls) were considered enriched in Tau-RD* monomers without heparin (t0-) compared to controls in the 3 different biological replicas. Values shown in the heat map refer to time points t0, t1, t8 and t24 of replica 3. Fig. S2: Full list of interactors of Tau-RD* oligomers and fibrils (t4) shown in Fig. 2D is shown with their relative quantifications across all time points in 3 biological replicas. Fig. 6B: Bar graph shows same selected proteins of Fig. S2 (significant proteins interacting with Tau-RD* aggregates, t4) and their average quantifications in Tau-RD* (t4) compared to Tau-RD* + Hsp90 (t4) across 3 different biological replicas. Ratios of normalized PSMs of interactors in Tau-RD* - Hsp90 / normalized PSMs of interactors in Tau-RD*+Hsp90 are graphically represented and shown as percentages. Negative values indicate a decreased binding affinity in presence of Hsp90 while positive ones indicate a higher affinity. Quantification of selected interactors of Tau-RD* monomers without heparin t0- (Fbxo3, Poldip2, Ctbp1, Ctbp2) is also included as additional control. Most of the interactors of Tau-RD* aggregates reduce their binding affinity in presence of Hsp90 whereas Fbxo3, Poldip2, Ctbp1 and Ctbp2 do not.

REFERENCES

- Alberti, S. (2017). Phase separation in biology. *Curr. Biol.* 27, R1097-R1102.
- Anvarian, Z., Nojima, H., van Kappel, E.C., Madl, T., Spit, M., Viertler, M., Jordens, I., Low, T.Y., van Scherpenzeel, R.C., Kuper, I., et al. (2016). Axin cancer mutants form nanoaggregates to rewire the Wnt signaling network. *Nat. Struct. Mol. Biol.* 23, 324-332.
- Ashburner, M., Ball, C.A., Blake, J.A., Botstein, D., Butler, H., Cherry, J.M., Davis, A.P., Dolinski, K., Dwight, S.S., Eppig, J.T., et al. (2000). Gene ontology: tool for the unification of biology. The Gene Ontology Consortium. *Nat. Genet.* 25, 25-29.
- Bejanin, A., Schonhaut, D.R., La Joie, R., Kramer, J.H., Baker, S.L., Sosa, N., Ayakta, N., Cantwell, A., Janabi, M., Lauriola, M., et al. (2017). Tau pathology and neurodegeneration contribute to cognitive impairment in Alzheimer's disease. *Brain* 140, 3286-3300.
- Blair, L.J., Nordhues, B.A., Hill, S.E., Scaglione, K.M., O'Leary, J.C., 3rd, Fontaine, S.N., Breydo, L., Zhang, B., Li, P., Wang, L., et al. (2013). Accelerated neurodegeneration through chaperone-mediated oligomerization of tau. *J. Clin. Invest.* 123, 4158-4169.
- Chiti, F., and Dobson, C.M. (2017). Protein Misfolding, Amyloid Formation, and Human Disease: A Summary of Progress Over the Last Decade. *Annu. Rev. Biochem.* 86, 27-68.
- Ciechanover, A., and Kwon, Y.T. (2017). Protein Quality Control by Molecular Chaperones in Neurodegeneration. *Front. Neurosci.* 11, 185.
- Dickey, C.A., Kamal, A., Lundgren, K., Klosak, N., Bailey, R.M., Dunmore, J., Ash, P., Shoraka, S., Zlatkovic, J., Eckman, C.B., et al. (2007). The high-affinity HSP90-CHIP complex recognizes and selectively degrades phosphorylated tau client proteins. *J. Clin. Invest.* 117, 648-658.
- Donovan, L.E., Higginbotham, L., Dammer, E.B., Gearing, M., Rees, H.D., Xia, Q., Duong, D.M., Seyfried, N.T., Lah, J.J., and Levey, A.I. (2012). Analysis of a membrane-enriched proteome from postmortem human brain tissue in Alzheimer's disease. *Proteomics Clin. Appl.* 6, 201-211.
- Ferrari, L., Geerts, W.J.C., van Wezel, M., Kos, R., Konstantoulea, A., van Bezouwen, L.S., Förster, F.G., and Rüdiger, S.G.D. (2018). Human chaperones untangle fibrils of the Alzheimer protein Tau. *Biorxiv*
- Fitzpatrick, A.W.P., Falcon, B., He, S., Murzin, A.G., Murshudov, G., Garringer, H.J., Crowther, R.A., Ghetti, B., Goedert, M., and Scheres, S.H.W. (2017). Cryo-EM structures of tau filaments from Alzheimer's disease. *Nature* 547, 185-190.
- Fontaine, S.N., Martin, M.D., Akoury, E., Assimon, V.A., Borysov, S., Nordhues, B.A., Sabbagh, J.J., Cockman, M., Gestwicki, J.E., Zweckstetter, M., and Dickey, C.A. (2015). The active Hsc70/tau complex can be exploited to enhance tau turnover without damaging microtubule dynamics. *Hum. Mol. Genet.* 24, 3971-3981.
- Gidalevitz, T., Ben-Zvi, A., Ho, K.H., Brignull, H.R., and Morimoto, R.I. (2006). Progressive disruption of cellular protein folding in models of polyglutamine diseases. *Science* 311, 1471-1474.
- Goedert, M., Eisenberg, D.S., and Crowther, R.A. (2017). Propagation of Tau Aggregates and Neurodegeneration. *Annu. Rev. Neurosci.* 40, 189-210.
- Goedert, M., Jakes, R., Spillantini, M.G., Hasegawa, M., Smith, M.J., and Crowther, R.A. (1996). Assembly of microtubule-associated protein tau into Alzheimer-like filaments induced by sulphated glycosaminoglycans. *Nature* 383, 550-553.
- Gunawardana, C.G., Mehrabian, M., Wang, X., Mueller, I., Lubambo, I.B., Jonkman, J.E., Wang, H., and Schmitt-Ulms, G. (2015). The Human Tau Interactome: Binding to the Ribonucleoproteome, and Impaired Binding of the Proline-to-Leucine Mutant at Position 301 (P301L) to Chaperones and the Proteasome. *Mol. Cell. Proteomics* 14, 3000-3014.
- Gustke, N., Trinczek, B., Biernat, J., Mandelkow, E.M., and Mandelkow, E. (1994). Domains of Tau-Protein and Interactions with Microtubules. *Biochemistry (N. Y.)* 33, 9511-9522.
- Harrison, A.F., and Shorter, J. (2017). RNA-binding proteins with prion-like domains in health and disease. *Biochem. J.* 474, 1417-1438.
- Hartl, F.U. (2017). Protein Misfolding Diseases. *Annu. Rev. Biochem.*
- Holtzman, D.M., Carrillo, M.C., Hendrix, J.A., Bain, L.J., Catafau, A.M., Gault, L.M., Goedert, M., Mandelkow, E., Mandelkow, E.M., Miller, D.S., et al. (2016). Tau: From research to clinical development. *Alzheimers Dement.* 12, 1033-1039.
- Karagöz, G.E., Duarte, A.M.S., Akoury, E.,

- Ippel, H., Biernat, J., Morán Luengo, T., Radli, M., Didenko, T., Nordhues, B.A., Vepintsev, D.B., et al. (2014). Hsp90-Tau complex reveals molecular basis for specificity in chaperone action. *Cell* 156, 963-974.
- Kneysberg, A., Combs, B., Christensen, K., Morfini, G., and Kanaan, N.M. (2017). Axonal Degeneration in Tauopathies: Disease Relevance and Underlying Mechanisms. *Front. Neurosci.* 11, 572.
- Knoblauch, N.T., Rüdiger, S., Schönfeld, H.J., Driessen, A.J., Schneider-Mergener, J., and Bukau, B. (1999). Substrate specificity of the SecB chaperone. *J Biol Chem* 274, 34219-25.
- Knowles, T.P., Vendruscolo, M., and Dobson, C.M. (2014). The amyloid state and its association with protein misfolding diseases. *Nat. Rev. Mol. Cell Biol.* 15, 384-396.
- Kozlowski, L.P., and Bujnicki, J.M. (2012). MetaDisorder: a meta-server for the prediction of intrinsic disorder in proteins. *BMC Bioinformatics* 13, 111-2105-13-111.
- Lane, C.A., Hardy, J., and Schott, J.M. (2018). Alzheimer's disease. *Eur. J. Neurol.* 25, 59-70.
- Maziuk, B.F., Apicco, D.J., Cruz, A.L., Jiang, L., Ash, P.E.A., da Rocha, E.L., Zhang, C., Yu, W.H., Leszyk, J., Abisambra, J.F., Li, H., and Wolozin, B. (2018). RNA binding proteins co-localize with small tau inclusions in tauopathy. *Acta Neuropathol. Commun.* 6, 71-018-0574-5.
- Meier, S., Bell, M., Lyons, D.N., Ingram, A., Chen, J., Gensel, J.C., Zhu, H., Nelson, P.T., and Abisambra, J.F. (2015). Identification of Novel Tau Interactions with Endoplasmic Reticulum Proteins in Alzheimer's Disease Brain. *J. Alzheimers Dis.* 48, 687-702.
- Meier, S., Bell, M., Lyons, D.N., Rodriguez-Rivera, J., Ingram, A., Fontaine, S.N., Mechas, E., Chen, J., Wolozin, B., LeVine, H., 3rd, Zhu, H., and Abisambra, J.F. (2016). Pathological Tau Promotes Neuronal Damage by Impairing Ribosomal Function and Decreasing Protein Synthesis. *J. Neurosci.* 36, 1001-1007.
- Mellacheruvu, D., Wright, Z., Couzens, A.L., Lambert, J.P., St-Denis, N.A., Li, T., Miteva, Y.V., Hauri, S., Sardi, M.E., Low, T.Y., et al. (2013). The CRAPome: a contaminant repository for affinity purification-mass spectrometry data. *Nat. Methods* 10, 730-736.
- Mocanu, M.M., Nissen, A., Eckermann, K., Khlistunova, I., Biernat, J., Drexler, D., Petrova, O., Schonig, K., Bujard, H., Mandelkow, E., et al. (2008). The potential for beta-structure in the repeat domain of Tau protein determines aggregation, synaptic decay, neuronal loss, and coassembly with endogenous Tau in inducible mouse models of tauopathy. *Journal of Neuroscience* 28, 737-748.
- Monroy, B.Y., Sawyer, D.L., Ackermann, B.E., Borden, M.M., Tan, T.C., and Ori-McKenney, K.M. (2018). Competition between microtubule-associated proteins directs motor transport. *Nat. Commun.* 9, 1487-018-03909-2.
- Morán Luengo, T., Mayer, M.P., and Rüdiger, S.G.D. (in the press). The Hsp70-Hsp90 chaperone cascade in protein folding. *Trends Cell Biol.*
- Olzscha, H., Schermann, S.M., Woerner, A.C., Pinkert, S., Hecht, M.H., Tartaglia, G.G., Vendruscolo, M., Hayer-Hartl, M., Hartl, F.U., and Vabulas, R.M. (2011). Amyloid-like aggregates sequester numerous metastable proteins with essential cellular functions. *Cell* 144, 67-78.
- Patzelt, H., Rüdiger, S., Brehmer, D., Kramer, G., Vorderwülbecke, S., Schaffitzel, E., Waitz, A., Hesterkamp, T., Dong, L., Schneider-Mergener, J., Bukau, B., and Deuerling, E. (2001). Binding specificity of Escherichia coli trigger factor. *Proc Natl Acad Sci U S A* 98, 14244-9.
- Pentony, M.M., and Jones, D.T. (2010). Modularity of intrinsic disorder in the human proteome. *Proteins* 78, 212-221.
- Picard, D. (2002). Heat-shock protein 90, a chaperone for folding and regulation. *Cell Mol Life Sci* 59, 1640-8.
- Pratt, W.B., Gestwicki, J.E., Osawa, Y., and Lieberman, A.P. (2015). Targeting Hsp90/Hsp70-based protein quality control for treatment of adult onset neurodegenerative diseases. *Annu. Rev. Pharmacol. Toxicol.* 55, 353-371.
- Qamar, S., Wang, G., Randle, S.J., Ruggeri, F.S., Varela, J.A., Lin, J.Q., Phillips, E.C., Miyashita, A., Williams, D., Strohl, F., et al. (2018). FUS Phase Separation Is Modulated by a Molecular Chaperone and Methylation of Arginine Cation- π Interactions. *Cell* 173, 720-734.e15.
- Radli, M., Vepintsev, D.B., and Rüdiger, S.G.D. (2017). Production and purification of human Hsp90beta in Escherichia coli. *PLoS One* 12, e0180047.
- Receveur-Brechot, V., Bourhis, J.M., Uversky, V.N., Canard, B., and Longhi, S. (2006). Assessing protein disorder and induced folding. *Proteins* 62, 24-45.
- Ripaud, L., Chumakova, V., Antonin, M., Hastie, A.R., Pinkert, S., Korner, R., Ruff, K.M., Pappu, R.V., Hornburg, D., Mann, M., Hartl, F.U., and Hipp, M.S. (2014). Overexpression of Q-rich prion-like proteins suppresses polyQ cytotoxicity

- and alters the polyQ interactome. *Proc. Natl. Acad. Sci. U. S. A.* 111, 18219-18224.
- Roberson, E.D., Searce-Levie, K., Palop, J.J., Yan, F., Cheng, I.H., Wu, T., Gerstein, H., Yu, G.Q., and Mucke, L. (2007). Reducing endogenous tau ameliorates amyloid beta-induced deficits in an Alzheimer's disease mouse model. *Science* 316, 750-754.
- Rüdiger, S., Germeroth, L., Schneider-Mergener, J., and Bukau, B. (1997). Substrate specificity of the DnaK chaperone determined by screening cellulose-bound peptide libraries. *Embo J* 16, 1501-7.
- Rüdiger, S., Schneider-Mergener, J., and Bukau, B. (2001). Its substrate specificity characterizes the DnaJ co-chaperone as a scanning factor for the DnaK chaperone. *Embo J* 20, 1042-50.
- Shelton, L.B., Koren, J., 3rd, and Blair, L.J. (2017). Imbalances in the Hsp90 Chaperone Machinery: Implications for Tauopathies. *Front. Neurosci.* 11, 724.
- Stieber, A., Mourelatos, Z., and Gonatas, N.K. (1996). In Alzheimer's disease the Golgi apparatus of a population of neurons without neurofibrillary tangles is fragmented and atrophic. *Am. J. Pathol.* 148, 415-426.
- Stone, A.B. (1974). A simplified method for preparing sucrose gradients. *Biochem. J.* 137, 117-118.
- Sydow, A., Van der Jeugd, A., Zheng, F., Ahmed, T., Balschun, D., Petrova, O., Drexler, D., Zhou, L., Rune, G., Mandelkow, E., et al. (2011). Reversibility of Tau-related cognitive defects in a regulatable FTD mouse model. *J. Mol. Neurosci.* 45, 432-437.
- Tomba, P. (2002). Intrinsically unstructured proteins. *Trends Biochem. Sci.* 27, 527-533.
- Valley, C.C., Cembran, A., Perlmutter, J.D., Lewis, A.K., Labello, N.P., Gao, J., and Sachs, J.N. (2012). The methionine-aromatic motif plays a unique role in stabilizing protein structure. *J. Biol. Chem.* 287, 34979-34991.
- van der Lee, R., Buljan, M., Lang, B., Weatheritt, R.J., Daughdrill, G.W., Dunker, A.K., Fuxreiter, M., Gough, J., Gsponer, J., Jones, D.T., et al. (2014). Classification of intrinsically disordered regions and proteins. *Chem. Rev.* 114, 6589-6631.
- Vanderweyde, T., Apicco, D.J., Youmans-Kidder, K., Ash, P.E., Cook, C., Lummertz da Rocha, E., Jansen-West, K., Frame, A.A., Citro, A., Leszyk, J.D., et al. (2016). Interaction of tau with the RNA-Binding Protein TIA1 Regulates tau Pathophysiology and Toxicity. *Cell. Rep.* 15, 1455-1466.
- Vernon, R.M., Chong, P.A., Tsang, B., Kim, T.H., Bah, A., Farber, P., Lin, H., and Forman-Kay, J.D. (2018). Pi-Pi contacts are an overlooked protein feature relevant to phase separation. *Elife* 7, 10.7554/eLife.31486.
- Wang, J., Choi, J.M., Holehouse, A.S., Lee, H.O., Zhang, X., Jahnel, M., Maharana, S., Lemaitre, R., Pozniakovsky, A., Drechsel, D., et al. (2018). A Molecular Grammar Governing the Driving Forces for Phase Separation of Prion-like RNA Binding Proteins. *Cell* 174, 688-699.e16.
- Wang, Y., and Mandelkow, E. (2016). Tau in physiology and pathology. *Nat. Rev. Neurosci.* 17, 5-21.
- Wegmann, S., Jung, Y.J., Chinnathambi, S., Mandelkow, E.M., Mandelkow, E., and Muller, D.J. (2010). Human Tau Isoforms Assemble into Ribbon-like Fibrils That Display Polymorphic Structure and Stability. *J. Biol. Chem.* 285, 27302-27313.
- Wilcock, G.K., and Esiri, M.M. (1982). Plaques, tangles and dementia. A quantitative study. *J. Neurol. Sci.* 56, 343-356.

CHAPTER 6

Proteomic-based approaches applied to investigate neuronal protein dynamics

This thesis chapter includes sections that have been published in the following works:

TRIM46 Controls Neuronal Polarity and Axon Specification by Driving the Formation of Parallel Microtubule Arrays. *Neuron*. 2015. 88(6):1208-1226.

van Beuningen SFB, Will L, Harterink M, Chazeau A, van Battum EY, Frias CP, Franker MAM, Katrukha EA, **Stucchi R**, Vocking K, Antunes AT, Slenders L, Doulkeridou S, Sillevius Smitt P, Altelaar AFM, Post JA, Akhmanova A, Pasterkamp RJ, Kapitein LC, de Graaff E, Hoogenraad CC.

The HAUS Complex Is a Key Regulator of Non-centrosomal Microtubule Organization during Neuronal Development.

Cell Rep. 2018. 24(4):791-800.

Cunha-Ferreira I, Chazeau A, Buijs RR, **Stucchi R**, Will L, Pan X, Adolfs Y, van der Meer C, Wolthuis JC, Kahn OI, Schätzle P, Altelaar AFM, Pasterkamp RJ, Kapitein LC, Hoogenraad CC.

Feedback-driven mechanisms between microtubules and the endoplasmic reticulum instruct neuronal polarity.

Neuron 2019.

Fariás GG, Fréal A, Tortosa E, **Stucchi R**, Pan X, Portegies S, Will L, Altelaar AFM, Hoogenraad CC.

VAP-SCRN1 interaction regulates dynamic endoplasmic reticulum remodeling and presynaptic function

EMBO journal. Under revision

Lindhout WF, Cao Y, Kevenaar TJ, Bodzeta A, **Stucchi R**, Boumpoutsari MM, Altelaar AFM, MacGillavry DH, Hoogenraad CC.

ABSTRACT

In this thesis chapter we selected a collection of works which exemplify the MS-based approaches we used to address specific neurobiological related questions. Quantitative proteomics was used to infer protein profiling in dissociated cortical neurons depleted for the axon initial segment (AIS) protein TRIM46 or depleted for selected endoplasmic reticulum (ER)-shaping proteins. In particular, dimethyl labeling (3plex) was applied to investigate changes in protein expression levels in neurons transfected with TRIM46_shRNA and TMT isobaric labelling (6plex) was used to quantify protein expression in neurons transfected with ER-shaping proteins_SHRNAs. Results greatly contributed to the validation of our knockdown (KD) approaches by providing accurate information about neuronal protein dynamics that will be followed up in future studies. Targeted proteomic approaches (Affinity Purification-Mass Spectrometry, AP-MS) were applied for the identification of proteins associated with HAUS/augmin and Secernin1 (SCRN1). The first one is a protein complex recently described to be involved in microtubule nucleation, while the latter is a protein with a potential new role in regulating the synaptic vesicle recycling at the pre-synapse.

INTRODUCTION

The use of differential stable isotopes allows accurate protein quantification thanks to their distinctive masses which can be distinguished in the MS-spectra. Several strategies have been developed to optimize the incorporation of stable isotopes. They mainly consist of metabolic labelling at the cellular or organism level or chemical labelling at the protein or peptide level (Altelaar et al., 2013). Chemical labelling has the advantage that can be applicable to almost any sample preserving accuracy, precision and reliability (Altelaar et al., 2013). A relatively cost-effective technique is dimethyl labelling, which typically achieves quantification at the MS level (Boersema et al., 2009). However, one major limitation of this approach relies in the limited amount of samples that can be analyzed simultaneously (dimethyl labeling is convenient for up to 3plex). Tandem Mass Tag (TMT) labeling on the other hand, using isobaric chemical labels, allows quantification based on MS/MS reporter ions therefore permitting the analysis of multiple conditions in parallel (up to 10plex) (Rauniyar and Yates, 2014). One of the major issues with isobaric labels has historically been the potential co-isolation of more than one peptide species, which could often lead to possible errors in the quantification results. Nowadays, the advent of new Mass Spectrometers allows analysis at higher resolution without affecting the speed of the MS analysis. Thanks to these technological advances, the issue of co-isolation and co-fragmentation of interfering ions with ions of interest is much more limited compared to the past. Here, we applied chemical isotope labeling LC-MS to efficiently measure protein expression levels in dissociated rat cortical neurons. Neurons, electroporated at DIV0 with specific sh_RNAs to deplete proteins of interest (TRIM46 or ER-shaping proteins) were harvested 4-7 days later and relative changes in their proteome dynamics were investigated by using high resolution MS.

Besides global investigation of protein profiling, proteomics can be used to investigate the precise composition of protein complexes. For example, here we applied AP-MS to get further insights into the role of the HAUS/augmin complex in neurons. Or in a similar experiment, we identified novel Scrn1 binding partners, therefore discovering possible molecular mechanisms by which Scrn1 affects the presynaptic vesicle cycle. The experimental workflow for the identification of specific brain interacting proteins has been already extensively described in the introduction of this thesis (Figure 3, Introduction). In this chapter, we make use of diverse MS-based technologies to obtain crucial data that would be otherwise more challenging to extrapolate with classical biochemical techniques. Up to now, the lack of reliable antibodies targeting rat proteins and the scarcity of material obtained from dissociated primary neuronal cultures have always represented the major limitations within the range of biochemical applications. Thankfully, recent advances in proteomics are now opening new exciting possibilities towards a more global

understanding of the biology of the neuron.

RESULTS

1. TRIM46 acts as microtubule (MT) bundler at the AIS

Axon formation, the initial step in establishing neuronal polarity, critically depends on local MT reorganization and is characterized by the formation of parallel MT bundles. The tripartite motif containing (TRIM) protein TRIM46 plays an instructive role in the initial polarization of neuronal cells. TRIM46 is specifically localized to the newly specified axon and, at later stages, partly overlaps with the axon initial segment (AIS). TRIM46 specifically forms closely spaced parallel microtubule bundles oriented with their plus-end out. Without TRIM46, all neurites have a dendrite-like mixed microtubule organization resulting in Tau missorting and altered cargo trafficking. By forming uniform microtubule bundles in the axon, TRIM46 is required for neuronal polarity and axon specification *in vitro* and *in vivo* (Figure 1A) (van Beuningen and Hoogenraad, 2016; van Beuningen et al., 2015). In this work, we applied dimethyl labelling (3plex) to TRIM46_shrRNA or pSuper (and untransfected) transfected neurons to validate the specificity of TRIM46-KD and to investigate neuronal protein dynamics upon TRIM46 depletion. Tryptic peptides from TRIM46-KD, pSuper and untransfected neurons were chemically labelled by using combinations of several isotopomers of formaldehyde and cyanoborohydride. TRIM46_shrRNA sample was labelled with heavy isotopes, pSuper with “medium” and untransfected with “light”. The efficiency of TRIM46 protein depletion was first tested by quantitative MS (Figure 1B-C) and then confirmed by Western blot analysis (Figure 1D-E). Quantifications obtained from both methods clearly indicate a significant reduction in the protein levels of TRIM46 by 80% (Figure 1C, 1E). These data, besides validating the efficacy of our produced shRNAs in depleting TRIM46 suggest that the shRNAs used in this study are specific for TRIM46 and do not affect any other member of the TRIM family (Figure 1C). Upon TRIM46 depletion one of the most striking effect that we observed was an increase in the total levels of TRIM36 (Figure 1C). This might underlie a feedback mechanism operated by the neurons which positively regulate the expression level of TRIM36 to compensate for TRIM46 reduction. TRIM36 shows quite high sequence homology compared to TRIM46 especially in their RING domains (Figure 1F). More interestingly, TRIM36 is the only other protein of the TRIM family which has MT bundling properties (Short and Cox, 2006) and labels the MT cytoskeleton in HeLa cells (Figure 1G). However, unlike TRIM46, TRIM36 does not localize at the AIS (van Beuningen et al., 2015) so it probably acts as MT bundler in other subcellular neuronal compartments. Map7d2 is another microtubule-associated protein whose expression is

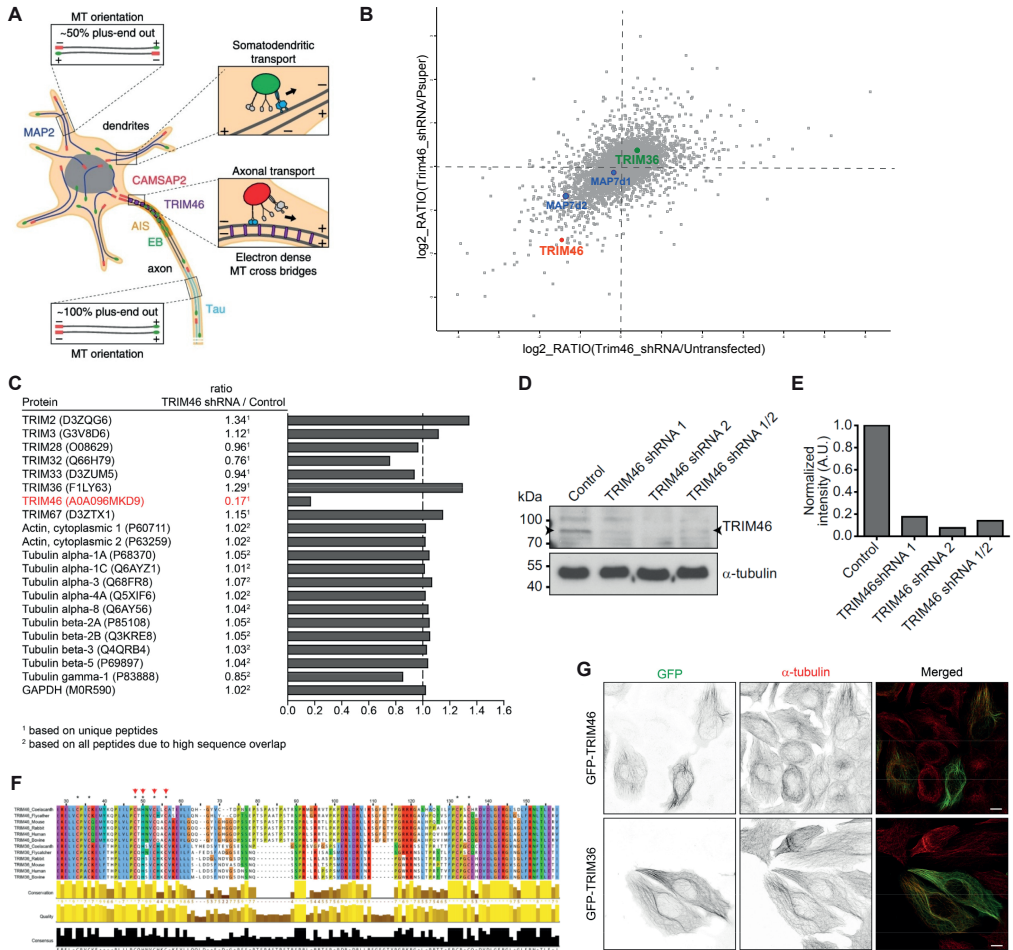


Figure 1. TRIM46 knockdown in neurons

(A) Microtubule organization at the axon initial segment (AIS). Tripartite motif-containing protein TRIM46 localizes to the proximal axon and forms parallel microtubule arrays. This uniform axonal microtubule organization is necessary for neuronal polarity and axon specification. The axonal microtubules are decorated by Tau, whereas MAP2 becomes enriched in the somatodendritic compartment. The microtubule minus-end binding protein CAMSAP2 stabilizes non-centrosomal microtubules and is enriched in the very first part of the axon, but absent from the AIS. (Adapted from Van Beugeningen & Hoogenraad, *Curr Opin in Neurobiol.* 2016)

(B) Scatter Plot showing protein expression levels calculated as $\log_2(\text{ratios})$ shRNA_TRIM46/PSuper and shRNA_TRIM46/untransfected.

(C) Diagram representing quantitative MS data of DIV4 cortical neurons electroporated with pSuper control (medium labeled) or TRIM46_shRNA#1/2 (heavy labeled). Protein names, Relative quantification is shown as ratio TRIM46_shRNA/pSuper.

(D-E) Western blot analysis (D) and quantifications of cortical neurons (DIV7) (E) expressing indicated constructs. Arrowheads indicate TRIM46 band.

(F) Clustal alignment of selected full-length TRIM46 and TRIM36 homologues from the animal kingdom. Alignment only shown for depicted residues. The essential cysteine and histidine residues of the RING domain are indicated with

asterisks and the mutated residues in the TRIM46 RING mutant are indicated by the red arrows.

(G) HeLa cells expressing either GFP-TRIM46 or GFP-TRIM36 (green) stained for alpha-tubulin (red). Scale bar, 10 μ m.

affected by TRIM46 depletion (Figure 1B), while its closely related homologous Map7d1 does not show any difference. Recent studies in our lab have successfully demonstrated that only Map7d2 but not Map7d1 plays an active role at the AIS (Pan et al., 2019). Altogether these data might suggest a synchronized action of Map7d2 and TRIM46 in regulating MTs dynamics at the AIS. Overall, these data further emphasize the accuracy of our proteomic based approach in providing in depth coverage of protein dynamics and in discovering new protein targets for future projects to come.

2. Role of the ER-shaping proteins (RTNs and DP1) in developing neurons

As described in the previous paragraph, the establishment of neuronal polarity strongly depends on local MT organization. Like MTs, also the endoplasmic reticulum (ER) forms an extensive network throughout the entire neuron. Cumulating evidence indicates that specific membrane proteins resident of the ER have the ability to directly bind and regulate MT organization and stability (Gurel et al., 2014). Our lab recently showed that the interplay between MTs and ER is also essential for neuronal polarity (Farias et al., 2019). ER-tubules localize within the axon, whereas ER-cisternae are retained in the somatodendritic domain. MTs are essential for axonal ER-tubule stabilization and reciprocally the ER is required for stabilizing and organizing axonal MTs. Recruitment of ER-tubules into one minor neurite initiates axon formation, while ER retention in the perinuclear area or disruption of ER-tubules prevents neuronal polarization. In light of these findings, this project describes for the first time a feedback-driven regulation between ER and MTs that is essential to establish neuronal polarity (Farias et al., 2019). Specific ER-resident transmembrane proteins control the shape of the ER. For instance, proteins such as reticulons (RTNs) and DP1 (REEP5) promote high curvature of ER-membranes to form ER-tubules (Voeltz et al., 2006). A preliminary MS analysis indicated the relative abundance of the major ER shaping proteins expressed in our dissociated rat neurons (Figure 2A). Next, a more precise MS-based quantification method was successfully applied to investigate the effects of the depletion of selected ER shaping proteins in cultured neurons. We tested the efficacy of our designed shRNA targeting RTNs 1-4 proteins (RTN1+RTN2+RTN3+RTN4), REEP1 and DP1 in nucleofected neurons at DIV4 (Figure 2B). The validation of these newly produced shRNAs, by using a quantitative proteomic approach (TMT labelling), was crucial for the outcome of this study considering: i) the large amount of imaging experiments performed in this project which relied on the use of these shRNAs, ii) the lack of effective antibodies targeting these proteins

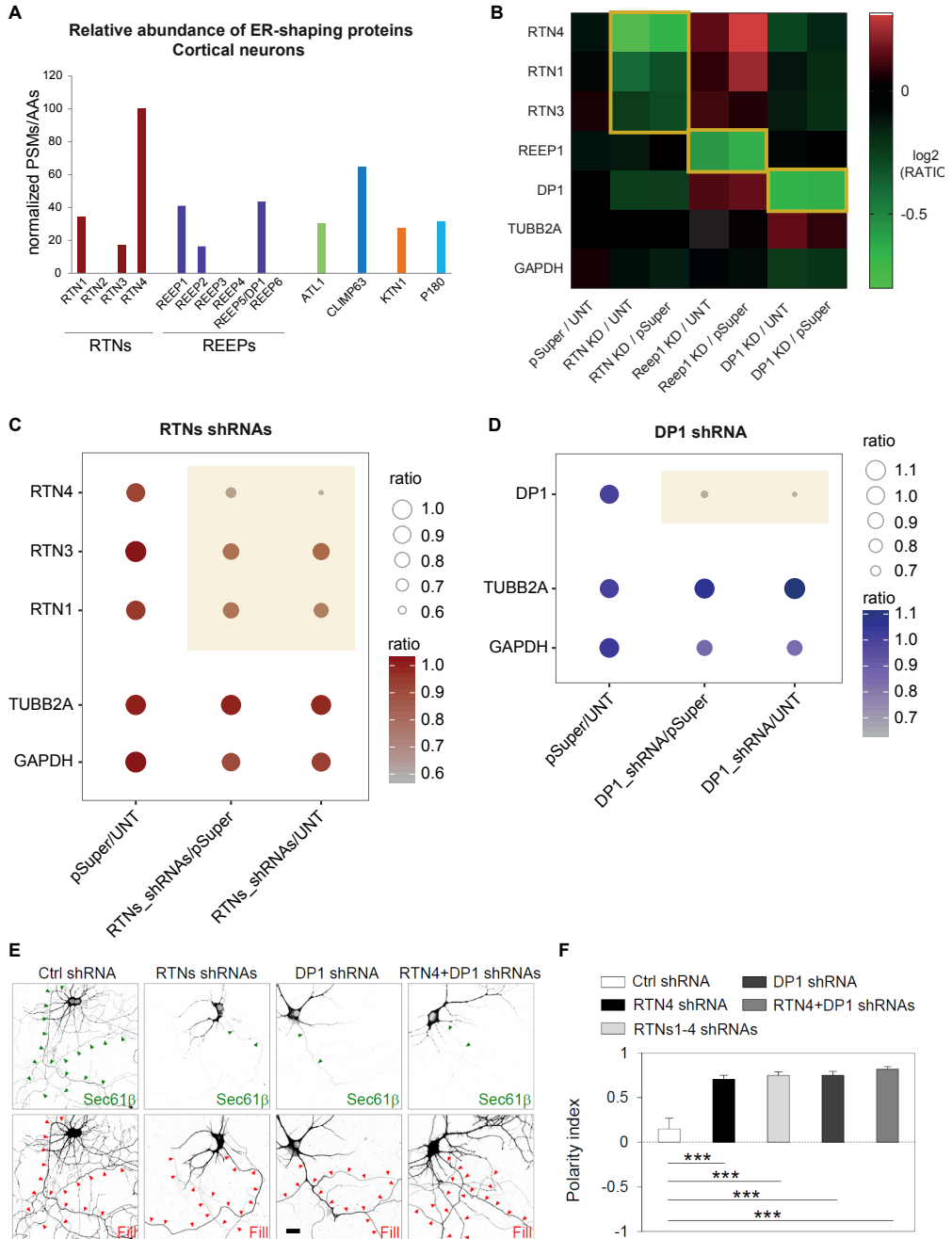


Figure 2. ER-shaping proteins knockdown in neurons

(A) Relative abundance of ER-shaping proteins calculated as total number of spectra (PSMs) normalized on the length of the protein (AAAs) in DIV4 cortical neurons.

(B) Heat map showing quantitative proteomics results of neurons (DIV4) transfected with pSuper, with RTNs_shRNAs, with REEP1_shRNA, with DP1(REEP5)_shRNA or untransfected (UNT). Graphical representations of these results

are shown in Figure 2C-D.

(C) Quantitative proteomics results of RTNs-KD neurons (DIV4). Average TMT ratios correspondent to the relative protein expression of RTN4, RTN3 and RTN1 proteins quantified in neurons untransfected (UNT), transfected with control shRNA (pSuper) or transfected with shRNAs for RTN1, RTN2, RTN3 and RTN4 and compared to control proteins (TUBB2A and GAPDH). Untreated neurons peptides were chemically labeled with TMT-126, pSuper neurons with TMT-127 and shRNAs for RTNs with TMT-128. RTN1, RTN4 and GAPDH quantifications were based on unique peptides. RTN3 and TUBB2A quantifications were based on total peptides due to high sequence overlap. RTN2 was not detected.

(D) Quantitative proteomics results of DP1-KD neurons (DIV4). Average TMT ratios correspondent to the relative protein expression of DP1 quantified in neurons untreated (UNT), transfected with control shRNA (pSuper) or transfected with shRNA for DP1 and compared to control proteins (TUBB2A and GAPDH). Untreated neurons peptides were chemically labeled with TMT-126, pSuper neurons with TMT-127 and shRNA for DP1 with TMT-131. DP1 and GAPDH quantifications were based on unique peptides. TUBB2A quantifications were based on total peptides due to high sequence overlap.

(E-F) Representative images of hippocampal neurons DIV7 co-transfected at DIV4 with GFP-Sec61 β (top panels) plus fill (bottom panels) together with control plasmid or shRNAs RTN1-4, DP1 and RTN4 plus DP1 (E). Polarity indexes of GFP-Sec61 β in neurons expressing shRNAs for RTN4, RTN1-4, DP1 or RTN4 plus DP1 in (F); n = 20 neurons per condition.

in biochemical assays. In order to achieve the quantification of 5 different conditions together (5plex), we used a MS2 based quantification using 5 different TMT isobaric tags. A scheme of the used isobaric tags is shown in the Experimental procedures and in Figure 2. Results clearly demonstrate that the designed shRNAs efficiently knocked down ER-shaping proteins without having any significant off target effect on other ER related proteins (Figure 2B). In particular, it was essential for us to demonstrate the efficacy and the specificity of the silencing of the RTN isoforms (Figure 2C) and of DP1 (Figure 2D) in neurons. The depletion of these specific ER-shaping proteins significantly affects the ER distribution, resulting in a imbalanced somatodendritic distribution of the ER marker Sec61 β (Figure 2E-F) and causes severe defects in neuronal polarization (Farias et al., 2019).

3. Characterization of the HAUS/augmin complex in neurons

The multisubunit protein HAUS/augmin complex is also required to establish and maintain neuronal polarity. HAUS/augmin was initially described to be required for mitotic spindle assembly in dividing cells (Goshima et al., 2008; Lawo et al., 2009; Liu et al., 2014). In our lab, we demonstrated that the HAUS complex is also essential in neurons (where the centrosome is inactivated early in development) by ensuring uniform microtubule polarity in axons and regulation of microtubule density in dendrites. Using imaging and high-resolution microscopy, we found that distinct HAUS clusters are distributed throughout neurons and colocalize with g-TuRC, suggesting local microtubule nucleation events. Based on these main findings this project describes how HAUS complex locally regulates microtubule nucleation events to

(C) Network analysis on HAUS2 and 6 putative binding partners associated with the microtubule (blue) and actin cytoskeleton (red). Edge color coding: blue, co-localization; orange, predicted interaction; green, shared protein domain; purple, co-expression.

(D-E) Selected putative binding partners of Bio-GFP-HAUS2 and HAUS6 identified in adult rat brains (D) and HEK293 (E) by AP-MS. Peptide counts are graphically represented by spheres, ratios of the spectral counts (PSMs) of the bait over the control are represented as colors (blue-microtubule binding proteins; red-actin binding proteins).

(F) Single molecule super-resolution reconstruction of a DIV4 hippocampal neuron transfected with GFP-HAUS2 (red), extracted and fixed with GA and PFA, and post-labelled with LifeAct-GFP (cyan) and DNA-PAINT (yellow) to visualize actin and α -Tubulin, respectively. Insets depict indicated areas. Scale bar 2 μ m in panel and 500 nm in insets.

(G) Percentage of GFP-HAUS2 clusters across 4 different categories: 1 – No co-localization, 2 – co-localization with microtubules, 3 – co-localization with actin and 4 – co-localization with microtubules and actin. (n=3, N=1). Data are presented as mean \pm SD.

control proper neuronal development (Figure 3A) (Cunha-Ferreira et al., 2018). In this work, the contribution of MS-based proteomics has been essential to gain further insight into the mechanism underlying HAUS localization and dynamics. Specifically, lysates of HEK293 cells co-expressing Bio-GFP-HAUS2 or HAUS6 and the biotin-protein ligase BirA were incubated with adult brain extracts, and isolated proteins were analyzed by affinity purification-mass spectrometry (AP-MS). As expected by pulling down HAUS2 or HAUS6 all the other subunits of the HAUS complex were successfully co-affinity-purified within the protein complex (Figure 3B). AP of HAUS2 and HAUS6 brought down various α and β -tubulin subunits and MT-associated proteins (Figure 3C–E), consistent with the association of the HAUS complex with the MT cytoskeleton. Interestingly, several actin-related proteins were also enriched in the list of proteins pulled down with HAUS6 (Figure 3C–E). Analysis of protein interaction networks (Cytoscape, GeneMANIA plugin) revealed how these proteins are interconnected with each other (Figure 3C). To better map the localization of the HAUS complex with respect to both actin and MTs, we performed three-color super-resolution imaging. In DIV4 neurons, GFP-HAUS2 clusters co-localized with the MT cytoskeleton. Surprisingly, GFP-HAUS2 clusters also localized with the actin cytoskeleton (Figures 3F-G). Although most clusters co-localized with both actin and MTs, some GFP-HAUS2 clusters localized exclusively with actin. These data helped us to understand how HAUS/augmin clusters associate both with the MT and the actin cytoskeleton.

4. SCRNI1-VAP1 interaction regulates dynamic endoplasmic reticulum remodeling and presynaptic function

Presynapses control the release and subsequent re-uptake of synaptic vesicles in neuronal cells. Numerous proteins that play important functions during the various phases of the synaptic vesicle cycle have been identified (Rizzoli, 2014; Sudhof, 2004, 2012). In our lab, we discovered novel proteins involved in presynaptic functioning. Using a knock-down screen approach, we

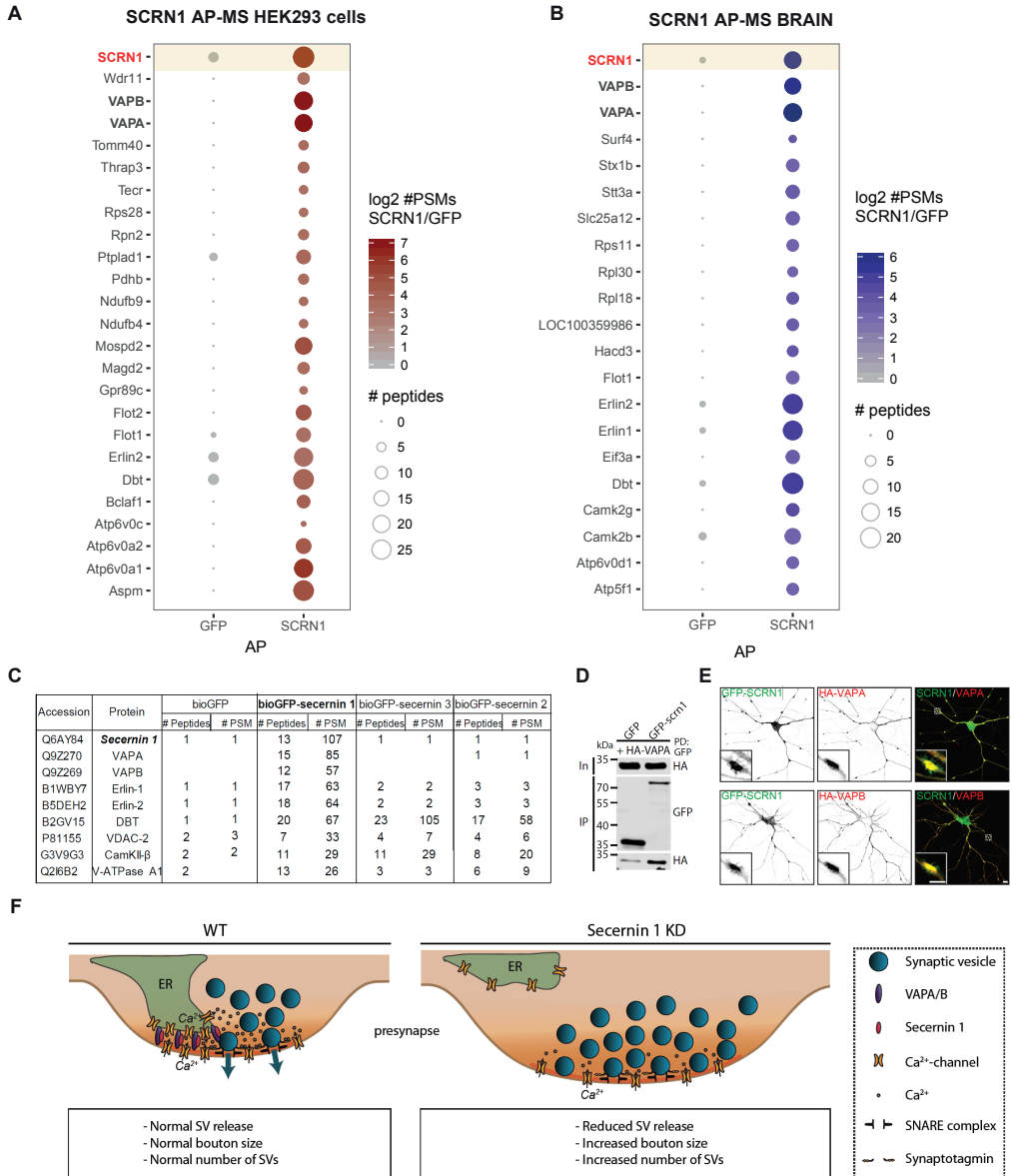


Figure 4. The pre-synaptic protein Secernin1 (SCRN1) interacts with the ER-membrane protein VAPA/VAPB (A-B) Significant binding partners of Bio-GFP-SCRN1 identified in rat brains (A) and HEK293 (B) by AP-MS. Only proteins with at least 10 fold change-enrichment compared to bio-GFP control are represented. Peptide counts are graphically represented by spheres, ratios of the spectral counts (PSMs) of the bait over the control are represented as colors (red-brains (A); blue-HEK293(B)).

(C) Table includes significant SCRN1 interactors with a >10 times enrichment compared to control (bioGFP alone) and with #PSM>25. Results of bio-GFP-SCRN2 and -SCRN3 are shown for comparison. For the extended list, see Figure A.

(D) AP-WB from extracts of HEK293 transfected with HA-VAPA and GFP-SCRN1 or GFP (control) and probed for

GFP and HA.

(E) Hippocampal neurons (DIV16) co-expressing GFP-SCRN1 with HA-VAPA or HA-VAPB. Scale bar (full size) = 10 μm , scale bar (zoom) = 5 μm .

(F) Model for Secernin1 function at presynaptic sites. SCRN1 may control the tethering of the ER to the presynaptic plasma membrane by interacting with the ER membrane protein VAPA/B. In this way, SCRN1 is able to control the localization of intracellular calcium (Ca^{2+}) stores to the presynapse and thus local Ca^{2+} concentrations.

identified Secernin1 (SCRN1) as an uncharacterized proteins involved in synaptic vesicle recycling. We showed that it promotes synaptic vesicle recycling and its depletion results in larger presynaptic sites and increased synaptic vesicle numbers (Lindhout et al., 2019, submitted). The application of AP-MS was crucial for understanding the possible mechanisms through which SCRN1 controls the presynaptic vesicle cycle. AP-MS experiments were performed in search for novel SCRN1 binding partners (Figure 4A-C). Secernin1 constructs were co-expressed with the biotin ligase BirA in HEK293 cells and cell extracts were used for pull-down assays with rat brain lysates. Interestingly, multiple ER-associated proteins were identified as the main SCRN1 interacting proteins, including VAPA/B and Erlin1/2 (Figure 4C). VAP and Erlin proteins showed a specific interaction with SCRN1 compared to SCRN2 and SCRN3 (Figure 4C). To further validate the interaction between SCRN1 and VAPA/B, subsequent pull-down experiments were conducted using extracts of HEK293 cells co-expressing with GFP-SCRN1 and HA-VAPA which confirmed the binding between Secernin1 and VAP (Figure 4D). Additionally, to further demonstrate the interaction between Secernin1 and VAP proteins, IF experiments were performed in neurons where co-expression of GFP-SCRN1 with either HA-VAPA or HA-VAPB resulted in the formation of dense VAP/SCRN1-positive clusters at neurites (Figure 4E). Altogether these results suggest that Secernin1 interacts with the ER protein VAPA/B. Based on these biochemical evidences and on other functional and imaging results from our lab (Lindhout et al., 2019, submitted), our conclusion is that this association is necessary to regulate the localization of the ER at the presynaptic site, thereby controlling local presynaptic calcium levels (Figure 4F). Our findings on SCRN1 will ultimately contribute to our growing understanding of presynaptic functioning.

EXPERIMENTAL PROCEDURES

Animals

All experiments were approved by the DEC Dutch Animal Experiments Committee (Dier experimenten Commissie), performed in line with institutional guidelines of Utrecht University and conducted in agreement with the Dutch law (Wet op de Dierproeven, 1996) and European regulations (Directive 2010/63/EU). Female pregnant Wister rats were obtained from Janvier Laboratories. Hippocampal neurons were obtained from embryos of both genders at E18 stage of development.

Antibodies and reagents

Rabbit anti-TRIM46 was made by injecting full length GST-TRIM46 (precipitated in PBS) together with adjuvant into New Zealand White rabbits (by BioGenes GmbH); rabbit anti-GFP (Abcam); mouse anti-HA (Covance). The following secondary antibodies were used: Alexa405-, Alexa488-, Alexa568-, Alexa647- (Invitrogen, 1:1000), IRDye 680LT (1:20.000) and IRDye 800CW (1:15.000) conjugated secondary antibodies. Streptavidin Dynabeads M-280 (Thermo Scientific).

Expression vectors and shRNA constructs

- The following shRNAs were created: rat TRIM46-shRNA 1 (5'-gttgctgacagagcttaac-3'), and rat/mouse TRIM46-shRNA 2 (5'-gaacatggagaaggaactg-3'), RTN1-shRNA (5'-gcagagcctgttaataata-3'), RTN2-shRNA (5'-tagcacagaccaatcagaa-3'), RTN3-shRNA (5'-ctgcaaatcagatgatttaa-3'), RTN4-shRNA (5'-gtccagatttcttaatta-3'), DP1-shRNA (5'-gacataaaagtccagaa-3'). The oligonucleotides were annealed and inserted into pSuper vector. Full-length mouse TRIM46 was generated in pGW1-GFP, full-length human TRIM36 was generated in pGW1-GFP (TRIM46 and TRIM36 clones were both kindly provided by Dr. T. Cox (Short and Cox, 2006).

- BirA vector was a kind gift from Dr. D. Meijer (Erasmus MC, Rotterdam, The Netherlands), Bio-GFP vector was previously described (Jaworski et al., 2009). Full length human HAUS2 was amplified by PCR from pEGFP-C1-HAUS2 (gift from Dr. Laurence Pelletier), full length HAUS6 was amplified by PCR from pEGFP-C1-HAUS6 (gift from Dr. Laurence Pelletier). Both fragments were inserted in *AscI*/*Sall* sites of pGW2-GFP expression vector to generate pGW2-GFP-HAUS2 and pGW2-GFP-HAUS6 respectively. To generate Bio-GFP-HAUS2 or HAUS6, HAUS2 and HAUS6 were recloned from pGW2-GFP-HAUS2/6 with *AscI*/*Sall* restriction enzymes and inserted in Bio-GFP vector.

- Secernin1-3 cDNA were obtained from a human cDNA library kindly provided by Mike Boxem. All N- and C-terminally HA and Bio-GFP tagged Secernin1-3 constructs were generated by PCR based strategies and cloned into Bio-GFP; HA-tagged; pGW1 and β -actin expression vectors (Jaworski et al., 2009; Kapitein et al., 2010; van der Vaart et al., 2013) using *AscI* and *Sall* restriction sites. HA- and myc-tagged VAPA and VAPB have been previously described (Teuling et al., 2007).

Primary hippocampal neuron cultures and transfection

Rat primary hippocampal cultures were prepared from embryonic day 18 rat brains. Cells were plated on coverslips coated with poly-L-lysine (30 μ g/ml) and laminin (2 μ g/ml) at a density of 100.000/well. Hippocampal cultures were grown in Neurobasal medium (NB) supplemented with B27, 0.5 μ M glutamine, 12.5 μ M glutamate and penicillin/streptomycin. Mouse primary hippocampal cultures were prepared from embryonic day 18 mouse brains then plated and cultured in the same conditions as rat primary neurons. Hippocampal neurons were transfected at DIV1 using Lipofectamine 2000 (Invitrogen). Briefly, DNA (1.8 μ g/well, for a 12 wells plate) was mixed with 3.3 μ l of Lipofectamine 2000 in 200 μ l NB, incubated for 30 min, and then added to the neurons in NB at 37°C in 5% CO₂ for 45 min. Next, neurons were washed with NB and transferred in their original medium at 37°C in 5% CO₂.

Primary cortical neuron nucleofection

Primary cortical neurons were isolated from E18 rat brain. Cells (1x10⁶) were transfected using the Amaxa Rat Neuron

Nucleofector kit (Lonza) with 3 µg of plasmid DNA and plated on coverslips coated with poly-L-lysine (37.5 µg/ml) and laminin (5 µg/ml) in 12-wells plates (2-6 x 10⁴ cells/well) containing DMEM supplemented with 10% FBS. Cells were allowed to recover and adhere to the surface at 37°C in 5% CO₂, after 4 hours the medium was replaced with Neurobasal medium supplemented with 2% B27, 0.5 mM glutamine, 15.6 µM glutamate, and 1% penicillin/streptomycin.

Mass spectrometry (dimethyl labelling)

Untreated, pSuper-transfected and TRIM46-shRNAs-transfected cortical neurons (DIV5) were washed 3 times with PBS and lysed with lysis buffer (8 M Urea, 50 mM triethylammonium bicarbonate (Sigma), EDTA-free protease inhibitor Cocktail (Roche)). 50 mg of proteins from each condition were reduced (5 mM DTT, 55°C, 30 min), alkylated (10 mM Iodoacetamide, 30 min in the dark) and sequentially digested by LysC (Protein-enzyme ratio 1:50, 37°C, 4 h) and trypsin (Protein-enzyme ratio 1:50, 37°C, overnight). Resulting peptides from each time point were desalted using C18 solid phase extraction cartridges (Waters) and subjected to stable isotope triplex dimethyl labeling on column (Boersema et al., 2009). For labeling the following scheme was used: untreated=light; pSuper=medium; shRNAs_TRIM46=heavy. Differentially labeled peptides were then mixed in a 1:1:1 ratio based on LC-MS base peak intensity of the separate channels, dried in a vacuum concentrator and reconstituted in 10% formic acid for subsequent fractionation. Peptides were fractionated using strong cation exchange chromatography (SCX) as previously described (Frese et al., 2017). Samples collected after fractionation were analyzed on a Q-Exactive mass spectrometer (Thermo Fisher Scientific, Bremen, Germany) coupled online to an Agilent UPLC 1290 system (Agilent Technologies). Peptides were loaded onto a trap column (Reprosil C18, 3 µm, 2 cm × 100 µm; Dr. Maisch) with solvent A (0.1% formic acid) and separated on an analytical column (Poroshell 120 EC C18, Agilent Technologies, 50 µm x 50 cm, 2.7 µm) using a 120 min linear gradient from 7-30% solvent B (0.1% formic acid in acetonitrile). For data analysis, raw files were processed using Proteome Discoverer 1.4 (version 1.4.1.14, Thermo Scientific, Bremen, Germany). Database search was performed using the Uniprot rat database and Mascot (version 2.5.1, Matrix Science, UK) as search engine. Carbamidomethylation of cysteines was set as a fixed modification. Oxidation of methionine and dimethylation (light, intermediate or heavy) of lysine residues and the peptide N-termini, respectively, were set as variable modifications. Trypsin was set as cleavage specificity, allowing a maximum of 2 missed cleavages. Data filtering was performed using percolator, resulting in 1% false discovery rate (FDR). Additional filters were search engine rank 1 and mascot ion score >20. Unique peptides or total peptides were used for quantification and the obtained ratios were normalized to the median.

Mass spectrometry (TMT labelling)

Untreated, pSuper-transfected and shRNAs-transfected (RTNs; REEP1, DPI) cortical neurons (DIV5) were washed 3 times with PBS and lysed with lysis buffer (8 M Urea, 50 mM triethylammonium bicarbonate (Sigma), EDTA-free protease inhibitor Cocktail (Roche)). 50 mg of proteins from each condition were reduced (5 mM DTT, 55°C, 30 min), alkylated (10 mM Iodoacetamide, 30 min in the dark) and sequentially digested by LysC (Protein-enzyme ratio 1:50, 37°C, 4 h) and trypsin (Protein-enzyme ratio 1:50, 37°C, overnight). Resulting peptides were then desalted using C18 solid phase extraction cartridges (Waters) and subjected to stable isotope TMT-6plex labeling according to manufacturer's instruction (Thermo Scientific). For labeling the following scheme was used: untreated=TMT-126; pSuper=TMT-127; shRNAs_RTNs=TMT-128; shRNA_REEP1=TMT-130; shRNA_DPI=TMT-131. Differentially labeled peptides were mixed in a 1:1:1:1:1 ratio based on LC-MS/MS base peak intensity of the separate channels, dried in a vacuum concentrator and reconstituted in 10% formic acid for subsequent fractionation. Peptides were fractionated using off-line high pH (basic) reversed-phase chromatography prior to MS analysis. Samples collected after fractionation were analyzed on a Q-Exactive mass spectrometer (Thermo Fisher Scientific) coupled online to an Agilent UPLC 1290 system (Agilent Technologies). Peptides were loaded onto a trap column (Reprosil C18, 3 µm, 2 cm × 100 µm; Dr. Maisch) with solvent A (0.1% formic acid) and separated on an analytical column (Poroshell 120 EC C18, Agilent Technologies, 50 µm x 50 cm, 2.7 µm) using a 120 min linear gradient from 7-30% solvent B (0.1% formic acid in acetonitrile). For data analysis, raw files were processed using Proteome Discoverer 1.4 (version 1.4.1.14, Thermo Scientific). Database search was performed using the Uniprot rat database and Mascot (version 2.5.1, Matrix Science,

UK) as search engine. Carbamidomethylation of cysteines was set as a fixed modification. Oxidation of methionine and TMT-6plex of lysine residues and peptide N-terminus, were set as variable modifications. Trypsin was set as cleavage specificity, allowing a maximum of 2 missed cleavages. Data filtering was performed using percolator, resulting in 1% false discovery rate (FDR). Additional filters were search engine rank 1 and mascot ion score >20. Unique peptides or total peptides were used for quantification and the obtained ratios were normalized to the median.

Affinity Purification-Mass Spectrometry (AP-MS)

Streptavidin beads pull-down assays were performed with HEK293 cells transfected with BirA and Bio-GFP-HAUS2, Bio-GFP-HAUS6 and Bio-GFP using polyethylenimine (PEI, Polysciences); or with BirA and Bio-GFP-Scrn1, Bio-GFP-Scrn2, Bio-GFP-Scrn3 and Bio-GFP for 48h according to the manufacturer's instructions. AP, MS-sample preparation, and MS-analysis were performed as previously described (Stucchi et al., 2018) (Introduction, Figure 3).

Map of interactions analysis

Selected HAUS2 and HAUS6 interactors linked to microtubule cytoskeleton or actin cytoskeleton were used for the generation of protein-protein interaction networks in Figure 3. Network analyses were performed using the GeneMania plugin (Montejo et al., 2010) within Cytoscape (Shannon et al., 2003).

Live imaging

Three color SMLM was performed on a Nikon Ti microscope equipped with a 100× N.A. 1.49 Apo TIRF oil objective, a Perfect Focus System and an additional 2.5× Optovar to achieve an effective pixel size of 64 nm. After immunocytochemistry, samples were first incubated for 15 minutes with Tetraspeck™ 100 nm-beads (Invitrogen). High laser power induced blinking of GFP-HAUS2 was first imaged for 1000-2000 frames, after which it was completely bleached. LifeAct-GFP and fluorescently labelled DNA complementary strand, I2-650 (binding to anti-mouse-D2) were then added and diluted to obtain single molecule binding events. DNAPaint imaging was performed according to Ultime™-2 super-resolution 2-plex kit protocol. Subsequently, LifeAct-GFP was imaged as previously described (Janssen et al., 2017). Between 20,000 and 30,000 frames were recorded per acquisition with exposure time of 100 ms.

SUPPLEMENTAL INFORMATION

Supplemental Experimental Procedures and additional data can be found online at:

- [https://www.cell.com/neuron/fulltext/S0896-6273\(15\)01018-1](https://www.cell.com/neuron/fulltext/S0896-6273(15)01018-1)
- [https://www.cell.com/neuron/pdf/S0896-6273\(19\)30057-1.pdf](https://www.cell.com/neuron/pdf/S0896-6273(19)30057-1.pdf)
- [https://www.cell.com/cell-reports/fulltext/S2211-1247\(18\)31035-0](https://www.cell.com/cell-reports/fulltext/S2211-1247(18)31035-0)

REFERENCES

- Altelaar, A.F., Frese, C.K., Preisinger, C., Hennrich, M.L., Schram, A.W., Timmers, H.T., Heck, A.J., and Mohammed, S. (2013). Benchmarking stable isotope labeling based quantitative proteomics. *J Proteomics* 88, 14-26.
- Boersema, P.J., Raijmakers, R., Lemeer, S., Mohammed, S., and Heck, A.J. (2009). Multiplex peptide stable isotope dimethyl labeling for quantitative proteomics. *Nat Protoc* 4, 484-494.
- Cunha-Ferreira, I., Chazeau, A., Buijs, R.R., Stucchi, R., Will, L., Pan, X., Adolfs, Y., van der Meer, C., Wolhuis, J.C., Kahn, O.I., *et al.* (2018). The HAUS Complex Is a Key Regulator of Non-centrosomal Microtubule Organization during Neuronal Development. *Cell Rep* 24, 791-800.
- Frese, C.K., Mikhaylova, M., Stucchi, R., Gautier, V., Liu, Q., Mohammed, S., Heck, A.J.R., Altelaar, A.F.M., and Hoogenraad, C.C. (2017). Quantitative Map of Proteome Dynamics during Neuronal Differentiation. *Cell Rep* 18, 1527-1542.

- Goshima, G., Mayer, M., Zhang, N., Stuurman, N., and Vale, R.D. (2008). Augmin: a protein complex required for centrosome-independent microtubule generation within the spindle. *J Cell Biol* 181, 421-429.
- Gurel, P.S., Hatch, A.L., and Higgs, H.N. (2014). Connecting the cytoskeleton to the endoplasmic reticulum and Golgi. *Curr Biol* 24, R660-R672.
- Janssen, A.F.J., Tas, R.P., van Bergeijk, P., Oost, R., Hoogenraad, C.C., and Kapitein, L.C. (2017). Myosin-V Induces Cargo Immobilization and Clustering at the Axon Initial Segment. *Front Cell Neurosci* 11, 260.
- Jaworski, J., Kapitein, L.C., Gouveia, S.M., Dortland, B.R., Wulf, P.S., Grigoriev, I., Camera, P., Spangler, S.A., Di Stefano, P., Demmers, J., *et al.* (2009). Dynamic microtubules regulate dendritic spine morphology and synaptic plasticity. *Neuron* 61, 85-100.
- Kapitein, L.C., Schlager, M.A., Kuijpers, M., Wulf, P.S., van Spronsen, M., MacKintosh, F.C., and Hoogenraad, C.C. (2010). Mixed microtubules steer dynein-driven cargo transport into dendrites. *Curr Biol* 20, 290-299.
- Lawo, S., Bashkurov, M., Mullin, M., Ferreria, M.G., Kittler, R., Habermann, B., Tagliaferro, A., Poser, I., Hutchins, J.R., Hegemann, B., *et al.* (2009). HAUS, the 8-subunit human Augmin complex, regulates centrosome and spindle integrity. *Curr Biol* 19, 816-826.
- Liu, T., Tian, J., Wang, G., Yu, Y., Wang, C., Ma, Y., Zhang, X., Xia, G., Liu, B., and Kong, Z. (2014). Augmin triggers microtubule-dependent microtubule nucleation in interphase plant cells. *Curr Biol* 24, 2708-2713.
- Pan, X., Cao, Y., Stucchi, R., Hooikaas, P.J., Portegies, S., Will, L., Martin, M., Akhmanova, A., Harterink, M., and Hoogenraad, C.C. (2019). MAP7D2 Localizes to the Proximal Axon and Locally Promotes Kinesin-1-Mediated Cargo Transport into the Axon. *Cell Rep* 26, 1988-1999 e1986.
- Rauniyar, N., and Yates, J.R., 3rd (2014). Isobaric labeling-based relative quantification in shotgun proteomics. *J Proteome Res* 13, 5293-5309.
- Rizzoli, S.O. (2014). Synaptic vesicle recycling: steps and principles. *EMBO J* 33, 788-822.
- Short, K.M., and Cox, T.C. (2006). Subclassification of the RBCC/TRIM superfamily reveals a novel motif necessary for microtubule binding. *J Biol Chem* 281, 8970-8980.
- Stucchi, R., Plucinska, G., Hummel, J.J.A., Zakhavi, E.E., Guerra San Juan, I., Klykov, O., Scheltema, R.A., Altelaar, A.F.M., and Hoogenraad, C.C. (2018). Regulation of KIF1A-Driven Dense Core Vesicle Transport: Ca(2+)/CaM Controls DCV Binding and Liprin-alpha/TANC2 Recruits DCVs to Postsynaptic Sites. *Cell Rep* 24, 685-700.
- Sudhof, T.C. (2004). The synaptic vesicle cycle. *Annu Rev Neurosci* 27, 509-547.
- Sudhof, T.C. (2012). The presynaptic active zone. *Neuron* 75, 11-25.
- Teuling, E., Ahmed, S., Haasdijk, E., Demmers, J., Steinmetz, M.O., Akhmanova, A., Jaarsma, D., and Hoogenraad, C.C. (2007). Motor neuron disease-associated mutant vesicle-associated membrane protein-associated protein (VAP) B recruits wild-type VAPs into endoplasmic reticulum-derived tubular aggregates. *J Neurosci* 27, 9801-9815.
- van Beuningen, S.F., and Hoogenraad, C.C. (2016). Neuronal polarity: remodeling microtubule organization. *Curr Opin Neurobiol* 39, 1-7.
- van Beuningen, S.F.B., Will, L., Harterink, M., Chazeau, A., van Battum, E.Y., Frias, C.P., Franker, M.A.M., Katrukha, E.A., Stucchi, R., Vocking, K., *et al.* (2015). TRIM46 Controls Neuronal Polarity and Axon Specification by Driving the Formation of Parallel Microtubule Arrays. *Neuron* 88, 1208-1226.
- van der Vaart, B., van Riel, W.E., Doodhi, H., Kevenaar, J.T., Katrukha, E.A., Gumy, L., Bouchet, B.P., Grigoriev, I., Spangler, S.A., Yu, K.L., *et al.* (2013). CFEOM1-associated kinesin KIF21A is a cortical microtubule growth inhibitor. *Dev Cell* 27, 145-160.
- Voeltz, G.K., Prinz, W.A., Shibata, Y., Rist, J.M., and Rapoport, T.A. (2006). A class of membrane proteins shaping the tubular endoplasmic reticulum. *Cell* 124, 573-586.

CHAPTER 7

General Discussion

Riccardo Stucchi^{1,2}

¹Cell Biology, Department of Biology, Faculty of Science, Utrecht University, Padualaan 8, 3584 Utrecht, the Netherlands

²Biomolecular Mass Spectrometry and Proteomics, Bijvoet Center for Biomolecular Research and Utrecht Institute for Pharmaceutical Sciences, Utrecht University, Padualaan 8, 3584 Utrecht, the Netherlands

In contrast to genomics, transcriptomics and imaging approaches, proteomics is still one step behind in the field of neurobiology. Therefore, the overall aim of this work was to use mass spectrometry (MS)-based technologies to provide important insights into the complex architecture and the molecular mechanisms underlying the biology of the neuron. This thesis is composed by a collection of neurobiological studies that combine targeted and/or quantitative proteomics for the identifications of protein-protein interactions and/or for the investigation of protein profiling with advanced imaging techniques. Specifically, we sought to investigate the changes in the proteome occurring during neurodevelopment (*Chapter 2*) or in response to specific stimuli (*Chapter 6*) and to understand the mechanisms underlying cargo transport by microtubule motors (*Chapters 3, 4*). Furthermore we optimized an affinity purification (AP)-MS based technique that allowed us to distinguish the aberrant neuronal interactors of Tau in its pathological fibrillary conformation (*Chapter 5*). These multidisciplinary approaches successfully contributed to unravel new molecular mechanisms regulating neuronal protein dynamics and to explore novel intracellular pathways which might be fundamental for future research in the field.

1. Neurodevelopment of hippocampal neurons *in vitro*

Neurons are highly specialized cells that can be distinguished from any other type of cells of the human body because of their intrinsic capability of using electrical and chemical signals to transfer information to surrounding cells. Synapses are the specialized compartments used by the neurons to contact and communicate with each other. The mature human brain is composed of approximately 100 billion neurons, all generated from a relative small population of precursor cells. During maturation, neurons undergo well-defined developmental stages. Our ability to generate *in vitro* cultures of primary neuronal cells has been fundamental to our understanding of the development and functioning of the nervous system. Primary cultures of rat or mouse hippocampal neurons at the moment represent the best experimental model for the investigation of neuronal differentiation and synaptic plasticity (Kaech and Banker, 2006). Hippocampal neurons undergo well-defined developmental stages, characterized by crucial steps: after initial neurites outgrowth neurons polarize, which means that one of the several neurites develops into an axon, next dendrites start to develop from the minor neurites and later (after one week in culture) synaptogenesis begins (Dotti et al., 1988; Fletcher and Banker, 1989). A quantitative proteomic based approach has allowed us to analyze proteome dynamics during these stages of differentiation (*in vitro* hippocampal neurons at DIV1, DIV5, DIV14) (Figure 1). About one third of the neuronal proteins measured by this MS-based analysis revealed substantial changes in protein expression, clearly highlighting an extensive reprogramming of the proteome throughout the neuronal differentiation. In our analysis, we mainly focused our attention and

validated proteins that undergo increased expression from DIV1 to DIV5. This cluster included several transmembrane receptor kinases involved in cell adhesion, migration, axon guidance and dendrite formation. In total, 82 cell adhesion proteins were quantified in our data set and most of them, including Cntn1, NrCAM, Nrxa2, NCAM1 and NCAM2 were allocated to this cluster (Chapter 2). These data indicate that their major expression increase proceeds during an “early neuronal maturation” therefore supporting an important role for neuronal cell adhesion proteins in dendrite formation. Neural cell adhesion molecule 1 (NCAM1) is a prominent member of the cell adhesion proteins that perfectly resembles the expression profile of cluster 3 (Chapter2). By using a combination of biochemical and imaging techniques we unraveled a previously uncharacterized role for NCAM1 in stimulating dendritic arbor development by promoting actin filament stabilization at the dendritic growth cone. We provided proof of concept by applying this strategy to identify and characterize the role of NCAM1 during dendritic outgrowth but this quantitative map of neuronal proteome constitutes a fundamental tool for the understanding of any other specific molecular mechanism involved in neurodevelopment (Figure 1).

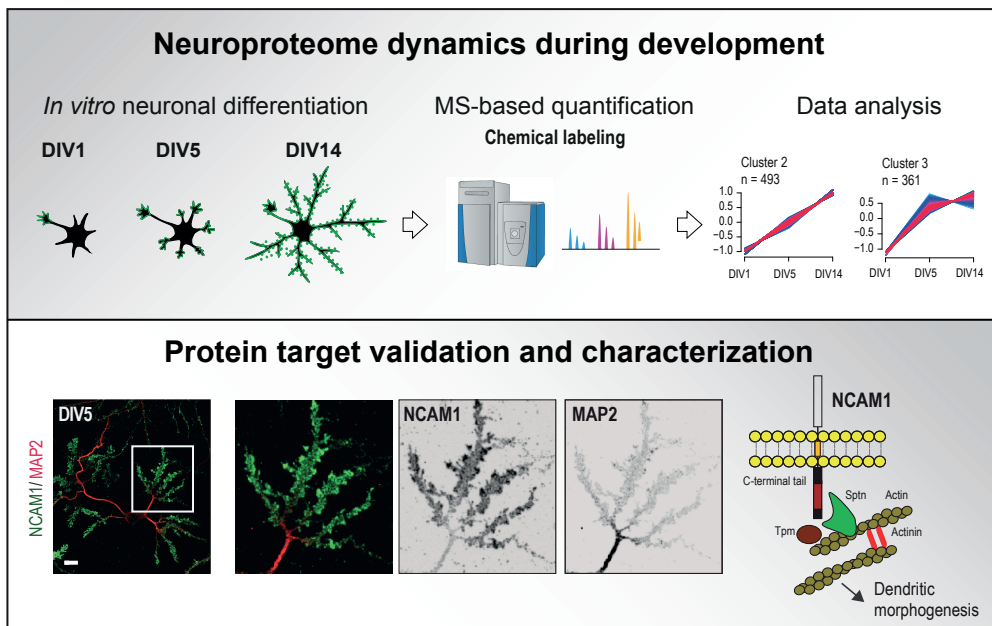


Figure 1. Protein profiling of hippocampal neurons throughout *in vitro* development

Quantitative-MS (dimethyl labeling) was applied to hippocampal neurons in culture at different stages of differentiation to systematically profile proteome dynamics (chapter 2). Approximately 1,800 proteins show significant expression changes during differentiation. Proteins are classified into six expression profile clusters, each one describing a stage-specific pattern of protein dynamics (top panel). This database helps to identify new neurodevelopment mechanisms; for example in this study we unravel a novel role for the neural cell adhesion molecule 1 (NCAM1) in stimulating dendritogenesis (bottom panel)(Adapted from(Frese et al., 2017)).

For example, this research clearly indicated that specific proteins involved in transport, such as adaptor complex subunits of AP2 and AP3 showed a significant coordinated up-regulation throughout differentiation, following the expression profile of most synaptic proteins (Chapter 2). AP complexes are involved in intracellular vesicular transport and cargo selection by binding to sorting signals. The AP2 complex mainly plays a role in endocytosis from the plasma membrane, whereas AP3 is important for trans-Golgi sorting events (Boehm and Bonifacino, 2001). Similar observations were made for synaptic proteins, in fact the majority of them were characterized by a steady increase in their protein levels throughout neuronal maturation (Chapter 2). Nevertheless, our data set demonstrates substantial up-regulation of many synaptic proteins already at early developmental stages, even before synaptogenesis takes place. This group included important presynaptic proteins involved in vesicle trafficking (Syp, Syt1), protein anchoring (Cask, Pclo, Bsn), neurotransmitter release (Syn1, Vamp2, Snap25, Sv2a, Sv2b) alongside with postsynaptic scaffolds (Shank, PSD95, Grip1, Homer1) and several glutamate and GABA receptors (Chapter 2). This quantitative map clearly indicates that drastic changes in intracellular transport machinery are essential to ensure proper delivery of cargos and synaptic materials from the cell body to the forming synapses and to efficiently sustain neuronal differentiation.

2. The role of kinesin-dependent transport in neurons, the study of KIF1A

As discussed in the previous paragraph, transport components are among the group of proteins undergoing major expression changes during neuronal development and dynamic remodeling of the trafficking machinery is essential to sustain neuron capability of modifying its synaptic content throughout differentiation (Holtmaat and Svoboda, 2009). Movements of vesicular cargos play important roles in synapse formation as well as in homeostatic maintenance of mature synapses. Bidirectional movement of these cargos is mediated by cytoskeletal-based molecular motors. Kinesins are the main motor proteins able to drive cargo transport along the plus end of the microtubules and therefore they are implicated in a diverse range of critical neuronal processes (Vale, 2003). Numerous neurodegenerative disorders are associated with mutations in genes encoding kinesin motor proteins or other components of the trafficking machinery in human patients, strongly supports the view that cargo transport is essential for neurodevelopment and proper neuron functioning (Millecamps and Julien, 2013). One of the most critical aspects in kinesin-mediated transport is to ensure that correct cargos are attached and transported by the correct motor protein to the correct location. Kinesin-mediated transport is of major relevance in neurons where essential building blocks that determine their polarity have to be distributed from the cell body to distal compartments either in the axon or in dendrites (Hirokawa et al., 2010). Different mechanisms mediate cargo-motor recruitment and cargo delivery at distal sites.

Adaptor proteins play a major role in these processes (Hirokawa et al., 2009). In neurons, calcium is a regulatory factor for multiple elements of the trafficking machinery. In chapter 3 we described the role of calcium in KIF1A-dependent vesicle trafficking. Our data for the first time reveal the existence of a Ca^{2+} /CaM (calmodulin) dependent mechanism acting on a kinesin motor, that directly regulates KIF1A tail conformation thereby resulting in increased binding to cargos in response to calcium. Calcium allows activation of specific myosins, such as myosin Va (Krementsov et al., 2004), myosin VI (Batters et al., 2016), myosin 1C (Lu et al., 2015) through a similar CaM-dependent mechanism. Our results indicate that at low calcium concentrations the tail domain of KIF1A does not bind to DCVs (Dense Core Vesicles), whereas at high calcium concentrations, CaM binds KIF1A allowing for subsequent DCV motility (Figure 2).

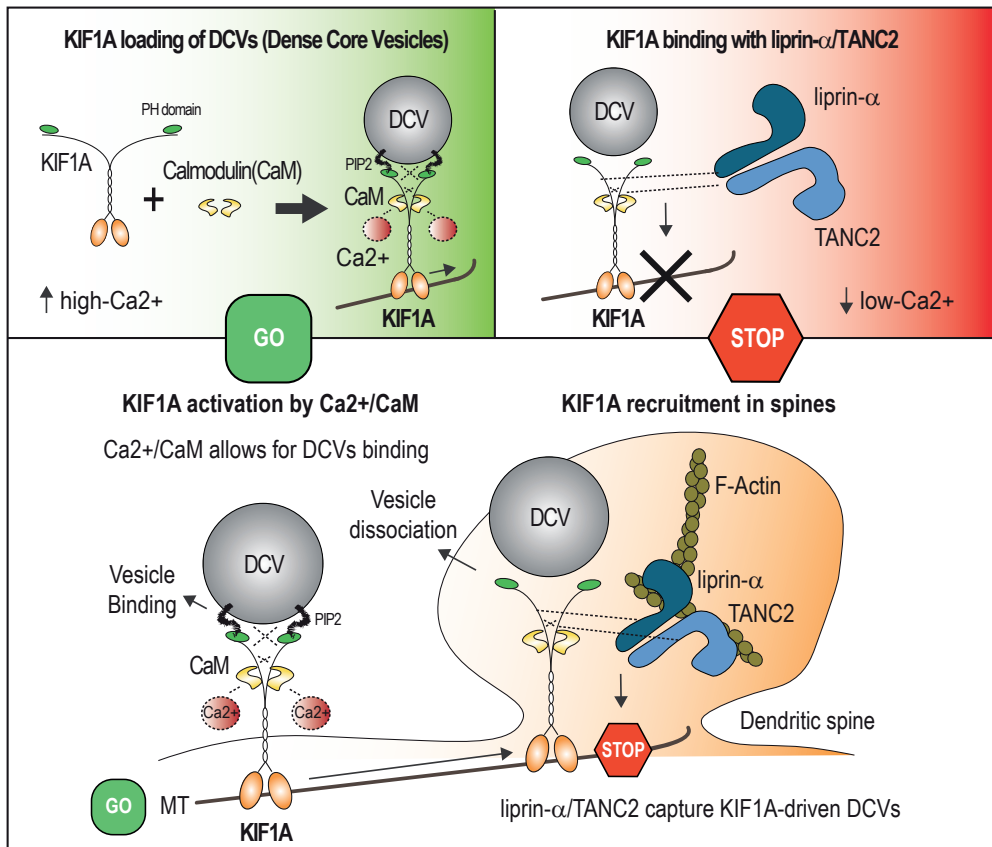


Figure 2 – Regulation of KIF1A-dependent transport

A Ca^{2+} /CaM molecular mechanism directly regulates the conformation of KIF1A tail and the binding between KIF1A and DCVs. At high local Ca^{2+} concentrations, CaM efficiently binds to KIF1A, allowing for DCV loading and motility. On the contrary, at low Ca^{2+} concentrations, Liprin- α and TANC2, acting as synaptic posts, tether KIF1A-driven DCVs into dendritic spines (chapter 3) (adapted from (Stucchi et al., 2018)).

We demonstrated that calcium, by modulating CaM binding affinity to KIF1A, regulates KIF1A-binding to vesicular cargos. Interestingly it has been recently shown that calcium and synaptic activity are required for an efficient KIF1A-dependent transport of DCVs into dendritic spines (McVicker et al., 2016). Based on these findings, our model could potentially represent a direct link between local intracellular calcium concentrations (and neuronal activity) and KIF1A-dependent cargo transport (Figure 2). KIF1A is normally in auto-inhibited state, and it gets activated upon cargo binding which releases this self-autoinhibition (Hammond et al., 2009; Niwa et al., 2016). At the same time KIF1A exists as monomer but it works as a processive motor mainly when in its dimeric state (Al-Bassam et al., 2003; Tomishige et al., 2002). Consequently, it will be interesting to further investigate whether KIF1A conformational changes induced by Ca^{2+} /CaM are also directly connected to a switch from monomer to dimer. These complex layers of regulation acting on the motor would be necessary to directly connect neuronal activity, motor processivity, release of autoinhibition and consequent cargo-binding. Other kinesins are also directly or indirectly regulated by calcium (Guillaud et al., 2008; Macaskill et al., 2009; Wang and Schwarz, 2009) indicating that coupling “ Ca^{2+} sensors” on motors is essential for neuronal cargo trafficking.

3. Cargo trafficking into dendritic spines

In hippocampal neurons, excitatory synapses are typically located on dendritic spines. In dendritic spines, actin filaments are predominantly present in the spine neck, whereas short, branched actin filaments are found in the spine head in proximity of the post synaptic density (PSD) (Hotulainen and Hoogenraad, 2010; Matus, 2000). Actin primary role in spines is to stabilize PSD proteins (Kuriu et al., 2006; Renner et al., 2009) and to modulate spine head structure in response to postsynaptic stimulation (Fischer et al., 2000; Star et al., 2002). On the contrary, microtubules (MTs) are enriched in dendritic shaft and almost absent in dendritic spines (Conde and Caceres, 2009). Despite this clear spatial segregation, live-cell experiments revealed that microtubules can transiently enter into dendritic spines (Hu et al., 2008; Jaworski et al., 2009; Merriam et al., 2013; Schatzle et al., 2018). Recent findings have also demonstrated that MTs are steered into spines through mechanical action of actin at the base of the spines (Schatzle et al., 2018) and that microtubule-based motors by walking along polymerizing MTs into spines can directly deliver cargos to the PSD (Esteves da Silva et al., 2015; McVicker et al., 2016). Nevertheless, the importance of this type of transport into spines has not been fully elucidated yet, due to the difficulties of studying such an infrequent event, like MT invasions of spines. As previously discussed in chapters 3-4, specific kinesin-3 family members, such as KIF1A and KIF13B are required for transporting vesicles in dendrites and have been hypothesized to

enter dendritic spines along MT tracks (Jenkins et al., 2012; McVicker et al., 2016; Stucchi et al., 2018). Our group and others showed that the middle stalk region of KIF1A interacts with a restricted subgroup of post synaptic density (PSD) proteins, such as liprin- α and TANC2 (chapter 3-4) (Shin et al., 2003; Stucchi et al., 2018), while an homologous MBS (MAGUK binding site) on KIF13B mediates the binding with other class of PSD proteins, such as SAP-97 and PD-95 (Mok et al., 2002) (chapter 4). It is therefore tempting to speculate that these different biochemical properties are at the base of their selectivity for different spines. Different composition of PSD proteins in spines could explain why certain spines are preferentially targeted by a specific motor and could dictate the precise locations where kinesin-transported cargos are targeted and consequently released.

4. The role of KIF1A and KIF13B in vesicle transport into spines

As explained in the previous paragraph, our model postulates that specific PSD proteins, such as liprin- α and TANC2, act as immobile synaptic posts tethering KIF1A-transported DCVs into spines (Stucchi et al., 2018). Consistent with these findings, depletion of KIF1A in neurons (as well as liprin- α and TANC2 depletion) negatively affects dendritic spines density (mainly mushroom shape spines) (McVicker et al., 2016; Stucchi et al., 2018), indicating that KIF1A is a crucial motor protein essential for the MT-based transport of cargos (DCVs) in protrusions. An analogous role could be played by SAP-97 and PSD-95 in respect to KIF13B dependent transport (chapter 4).

From a biochemical point of view, this situation has numerous similarities with the molecular model which describes how microtubules interact with plasma membrane sites surrounding Focal Adhesions (FA) in cells (van der Vaart et al., 2013). At the cell plasma membrane, KANK proteins, a class of proteins with high structural similarity with the neuronal TANC proteins (Kakinuma et al., 2009; Zhu et al., 2008), initiate a cortical platform assembly by recruiting and clustering the kinesin KIF21A, liprins, CLASP and other scaffolding proteins around FA (Bouchet et al., 2016; van der Vaart et al., 2013). In neurons, similar recruitment mechanisms have been already postulated in the axonal compartment where static clusters of liprin- α cause immobilization of KIF1A-transported SVs (Olsen et al., 2005; Wu et al., 2016), or actin pre-synaptic pools can capture KIF1A-transported Syt4-positives DCVs (Bharat et al., 2017).

Despite these evidences, we can not entirely rule out that myosin motors can also control DCV transport in spines. Myosin V modulates transport, maturation and exocytosis of DCVs in the axon (Bittins et al., 2009; Bittins et al., 2010) and it is also involved in several processes in dendritic spines such as actin based-transport of GKAP (Shin et al., 2012) or trafficking of AMPA receptors and recycling endosomes (Hales et al., 2002; Wang et al., 2008). One hypothesis would be that KIF1A and myosin are both bound to the same DCV, but kinesin

acts as predominant motor along MTs in dendrites whereas in proximity of microtubule-actin intersection, in the dendritic shaft, myosin gets activated and would take over cargo delivery, transporting DCVs along actin filaments into spines. Interestingly, the processive movements of KIF1A on MTs and of myosin V on f-actin are both modulated by similar conformational changes induced by calcium concentration (Lu et al., 2006; Nguyen and Higuchi, 2005; Stucchi et al., 2018), suggesting that local calcium concentrations can trigger the shift between kinesin-mediated transport and myosin-mediated transport. In an alternative model, KIF1A (walking on invading MTs) would be responsible of the anterograde transport into the spines while myosin would only play a role in the retrograde transport of DCVs from the spines.

5. The importance of LBS and MBS domains in KIF1A and KIF13B regulation respectively

In chapter 4 we explore the biochemical properties of the Liprin Binding Site (LBS, 657-854) on KIF1A and of the MAGUK Binding Site (MBS, 663-832) on KIF13B. By using a cell-imaging approach we could also demonstrate that both domains are not directly required for the binding of the vesicles on the kinesin tails. As we mentioned in the previous paragraph our conclusion is that these regions and their associated adaptor proteins might mainly play regulatory roles on the motors, for example by influencing the recruitment of these kinesin-3 members at distal sites. Interestingly both LBS and MBS regions, apart from being homologous with each other, contain well defined coiled-coil motifs which seem to mediate the association between motors and PSD proteins. However, for the time being it is not clear which are the molecular mechanisms underlying this protein-protein interaction.

In chapter 3 and chapter 4 we showed that a short motif within LBS of KIF1A is the minimal binding region for liprin/TANC2 and this interaction might act as a stop signal for the motor protein. Based on these data, our hypothesis is that, in presence of an active and processive kinesin, this motif must not be accessible to its substrates otherwise the kinesin would be always clustered by these scaffolds, and thus inactive. Moreover, our data suggest that the activity of KIF1A and its capability of transporting cargos are strongly dependent on the conformation of its tail. It is plausible that this strong regulation on KIF1A tail is directly translated into facilitated formation of KIF1A dimers. Indeed, our hypothesis is that a dimeric state of the motor is necessary for the formation of a stable allosteric binding between two pleckstrin homology (PH) domains (each one from each KIF1A molecule) and phosphatidylinositol 4,5-bisphosphate (PIP₂) micro-clusters on cargo vesicle membranes (Klopfenstein et al., 2002). Based on these points, our assumption is that in presence of an active KIF1A, this coiled coil region within the LBS must be sterically covered or not accessible. This might be caused for example by the presence of coiled-coil intermolecular interactions with the other KIF1A molecule of

the dimer, which might help in stabilizing KIF1A-dimer, preventing the association with the PSD scaffolds. Contrarily, when KIF1A is inactive (and in its monomeric conformation) this specific coiled-coil domain is exposed and then able to bind specific PSD proteins, resulting in KIF1A recruitment at synaptic sites. Local calcium concentration would determine activation or inactivation of the motor by modulating conformation of KIF1A tail and consequently the position of this critical CC motif. We explained in the previous paragraph the importance of a Ca^{2+} /CaM regulatory mechanism acting downstream of this region in modulating the structure of KIF1A-tail (Figure 2). This calcium dependent mechanism is essential for kinesin-activation and for cargo loading. In agreement with this model, KIF1A-binding to PSD proteins is favored by low calcium concentrations, thereby working as an opposite mechanism counteracting the KIF1A-vesicle mobilization stimulated by high calcium (Figure 2).

In the case of KIF13B, the scenario would be similar but with few significant differences. KIF13B interactome was extensively described in chapter 4. Dimerization of KIF13B, as in the case of KIF1A, results in super-processive movement (Soppina et al., 2014), however unlike KIF1A, KIF13B is not subjected to Ca^{2+} /CaM regulation. A defined coiled-coil region (CC3) in the MBS of KIF13B, is likely to mediate the recruitment of the motor to PSD-95 at synaptic sites but it is not directly required for the vesicle loading and transport (as in the case of KIF1A) (chapter 4). Unlike KIF1A, KIF13B tail does not contain a PH domain, so this kinesin can bind phosphoinositides (PIP) on vesicle membranes only through an adaptor. Centaurin- α 1 (ADAP1) represents the ideal candidate (chapter 4), due to its double capability of binding both KIF13B and PIP_3 on cargo vesicles, through its PH domain (Horiguchi et al., 2006; Tong et al., 2010). In disagreement with literature, our data suggest that the entire kinesin tail is necessary for centaurin- α 1 binding and not only the forkhead-associated (FHA) domain, as was previously reported (chapter 4). Our idea is that the CC3 of KIF13B could interact with another coiled-coil motif (CC4) located at the c-terminal of the tail, and this CC-CC binding would be essential to facilitate centaurin- α 1 association. Our hypothesis is that the motor needs to be in a compact conformation to stabilize centaurin- α 1 binding and to ensure an efficient vesicle binding (Figure 3). In agreement with this model, recent data from our lab indicate that in presence of a KIF13B carrying a point mutation in the CC4, the association with centaurin- α 1 is abolished.

Our model implies that KIF13B binding to centaurin- α 1 is directly linked to vesicle transport while binding to PSD-95/SAP-97 is associated with recruitment of the motor at distal sites (Figure 3). It is also logic to speculate about a competitive binding of these proteins for the motor, so that kinesin properties would be tightly controlled by the type of adaptor bound. CC3 would be exposed only in absence of vesicle binding and therefore available for the interaction with scaffolding proteins PSD-95/SAP-97. In a similar pattern of regulation, the CC3 of KIF1A

seems to alternatively regulate either kinesin-dimerization or binding to liprin- α /TANC2 resulting in vesicle transport or vesicle recruitment respectively (chapter 3 and 5; (Stucchi et al., 2018)).

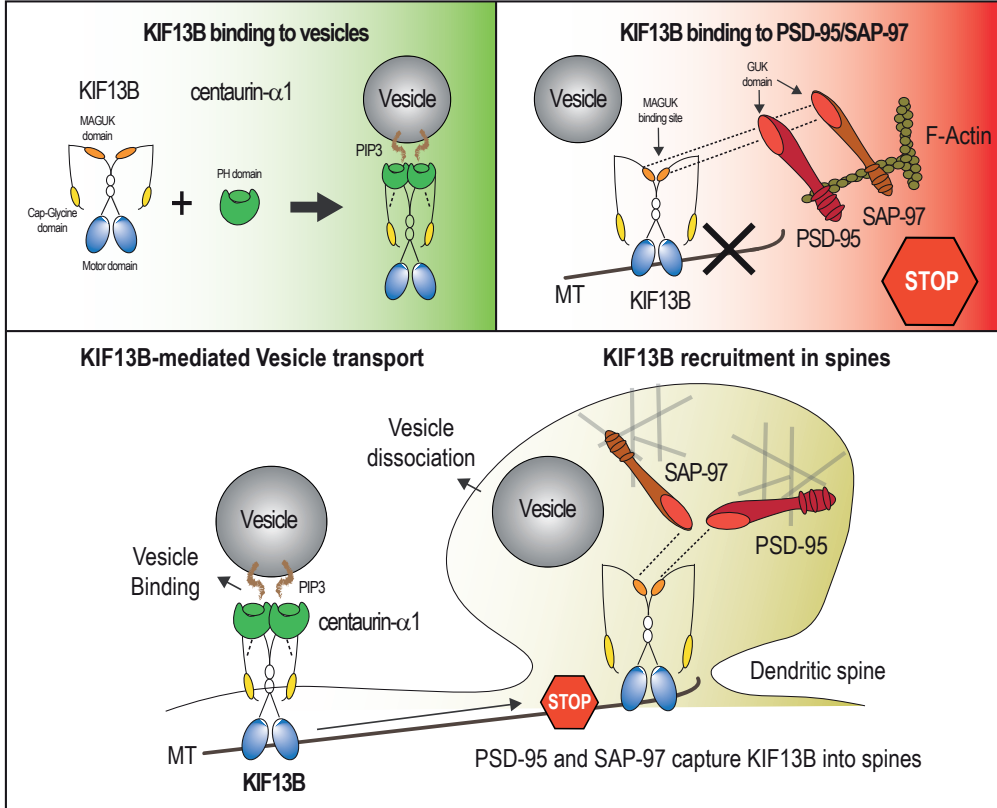


Figure 3. Regulation of KIF13B-dependent transport

KIF13B binding to centaurin- α 1 is required for the association and the transport of vesicles. PSD-95 and SAP-97, working as immobile scaffolds in spines, recruit KIF13B-driven vesicles at distal sites. Kinesin behavior is tightly controlled by the type of adaptor bound. Our data suggest that a specific coiled-coil motif on the MBS of KIF13B alternatively regulates tail back-folding and its consequent association with centaurin- α 1, or binding to PSD-95 and the consequent kinesin recruitment in spines.

A similar example of autoinhibition mechanism mediated by an antiparallel coiled coil motif has been recently described for the kinesin-4 family members KIF21A and KIF21B (Bianchi et al., 2016). Although autoinhibition through intramolecular interactions is a general principle for the regulation of kinesin motors in the absence of cargo (Akhmanova and Hammer, 2010; Schlager and Hoogenraad, 2009), here we pinpoint specific coiled coil motifs that could play double roles in controlling autoinhibition and in tethering motors to their final destination. To sum up these concepts, our data highlight the importance of specific coiled coil motifs in regulating kinesin-3

activation, monomer-to-dimer transition and processive transport of cargoes; as well as in the motor recruitment mediated by PSD scaffolds at distal sites (Figure 4).

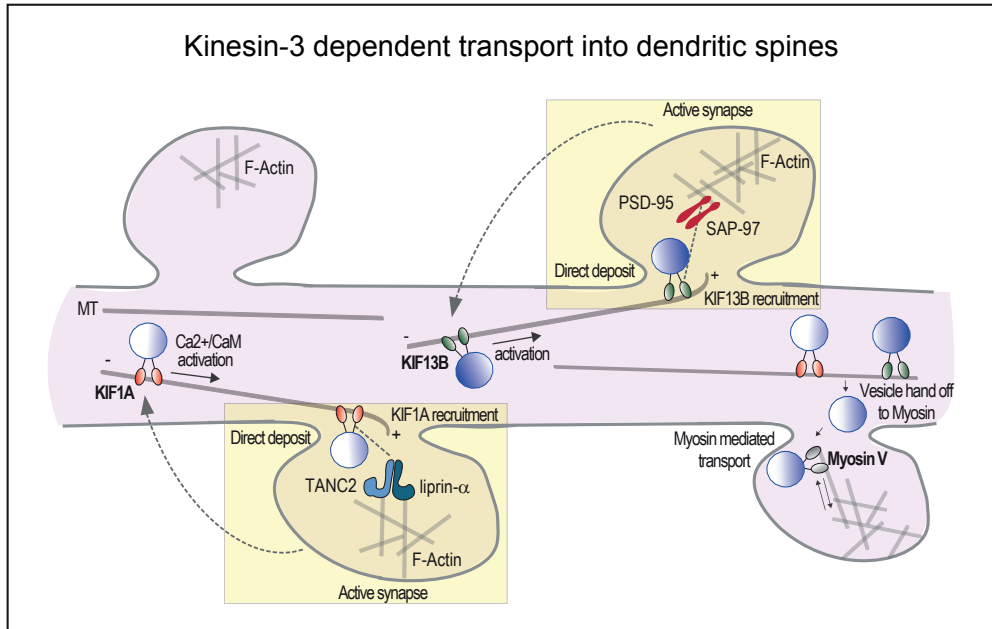


Figure 4. Hypothetical model of kinesin-3 dependent transport of vesicles in dendrites and spines

KIF1A and KIF13B recruitment into dendritic spines is controlled by specific synaptic posts which bind the middle regions (LBS and MBS) of these kinesin-3 members. Kinesin-3 activation might be linked to synaptic activity and consequent calcium influxes, which directly relieve kinesin auto-inhibition and increase MT invasions into spines. Vesicle delivery is also controlled by Myosin V that can receive cargoes transported by kinesin-3 members in the dendritic shaft and transports them along actin filaments into the spine head.

6. Open questions about kinesin-3 mediated transport

Different types of PH domains show different specificities for phosphoinositides (PIPs) and interactions between PH domains and PIPs in the membranes are essential to localize proteins to specific membrane domains (Lemmon and Ferguson, 2001). Interestingly, in addition to lipids, PH domains can also bind directly the adaptor protein (AP) complexes (Lemmon, 2003). AP proteins, through association with clathrin, contributes to the formation of vesicles by membrane deformation and connect cargo proteins and lipids. The kinesin-3 family members KIF1A and KIF13B can directly or indirectly bind to PIP and consequently AP proteins (chapter 2, chapter 4). However, how motifs are precisely recognized by these motor proteins and how the specificity for different vesicles is ensured remain still unclear. It is therefore essential to deeply investigate the molecular mechanisms regulating kinesin-cargo interaction. Up to now

multiple efforts have been made in order to identify new adaptor proteins possibly involved in this process. Our hypothesis is that the conformation of the kinesin tail is the real determinant factor triggering vesicle transport. In the case of KIF1A we showed that tail conformation (and consequently of its PH domain) is directly regulated by a Ca^{2+} /CaM mechanism. We speculate that structural changes in the tail directly promote vesicle binding by affecting the position of the PH domain. KIF13B does not bind CaM and does not have a PH domain in its tail. For this motor, the binding with vesicles is ensured by the formation of a hetero-tetrameric complex with the adaptor protein centaurin- α 1 (Tong et al., 2010). Motor-vesicle binding in this case is indirect and is mediated by the PH domain located on centaurin- α 1. Predicted phospho-residues (Y633, S732) located within the MBS of KIF13B could selectively modulate its binding affinity with centaurin- α 1 and/or with PSD-95/SAP-97. Interestingly KIF13B can be phosphorylated by the kinase Par1, leading to a reduction in PIP_3 transportation (Yoshimura et al., 2010). On the contrary, no phosphorylated residues are present within the KIF1A homologous LBS. These evidences lead us to hypothesize that KIF13B tail conformation, centaurin- α 1 binding and consequent vesicle association might be potentially regulated by a phosphorylation-dependent mechanism at the MBS. The spatial position of the PH domains in relationship with the position of PIP microdomains and AP protein clusters on vesicles can be the determining factors ultimately leading to cargo binding and transport. Further investigation in this direction is required to fully understand these regulatory mechanisms connecting cellular signaling and kinesin-3 trafficking processes.

Moreover, the scaffolding protein TANC2, apart from binding and recruiting KIF1A into spines (chapter 3, (Stucchi et al., 2018)), is also able to strongly interact with centaurin- γ 2 (AGAP1) and centaurin- γ 1 (AGAP3) in brains (chapter 3, (Stucchi et al., 2018)), suggesting that specific centaurins and PIP domains at the plasma membranes could also control the trafficking of KIF1A-directed secretory vesicles in spines. A recent study indicates that centaurin- γ 2 is expressed in dendritic spines, where it regulates endosomal trafficking and dendritic spine morphology (Arnold et al., 2016), therefore supporting a role for this GTPase in KIF1A-dependent membrane trafficking in spines.

Although the functional consequence of the interaction between PSD-scaffolds and kinesin-3 members has been debated for long time, up to now there is not clear consensus about the complex role of PSD-95/SAP-97 and liprin- α /TANC2 in respect to KIF13B and KIF1A mediated transport respectively. Despite our data suggesting these scaffolds targeting and recruiting kinesin-3-driven vesicles into spines, they do not necessarily exclude a parallel role in activating kinesin-3 by relieving of their auto-inhibition (Wagner et al., 2009; Yamada et al., 2007). Similarly, we cannot completely rule out the possibility that PSD-proteins are

transported by the kinesin-3 members KIF1A and KIF13B as preformed mobile clusters of scaffolding proteins, acting as postsynaptic hotspots for the formation of new synapses (Gerrow et al., 2006). Alternatively, PSD proteins can also act as adaptors facilitating kinesin-mediated transport of specific proteins; for example in hippocampal neurons, KIF17 forms a protein complex with SAP-97 and other PDZ scaffolds (CASK, MALS, Mint) which contributes to the MT-mediated transport of NMDA receptor subunits (Jeyifous et al., 2009; Setou et al., 2000). Another aspect that requires further investigation is the calcium dependent coupling of KIF1A with its transported vesicles (chapter 3). For a full understanding of this mechanism it would be optimal to test whether KIF1A-driven vesicle transport stimulated by calcium is also connected to synaptic activity. Future works should help understanding whether local synaptic stimulation at single spine level might be locally translated into an increased KIF1A-mediated transport of vesicles at the dendritic shaft and/or into dendritic spines (Figure 4). In line with this hypothesis, a recent study from our lab showed that local calcium-influx in an activated dendritic spine directly leads to an increase in the number of MT invasions into the same spine (Schatzle et al., 2018). Moreover it was previously shown that KIF1A-driven transport of DCVs into spines along MT tracks is stimulated in response to neuronal activity (McVicker et al., 2016). Altogether these evidences indicate that neuronal activity dramatically increases the number of MTs invading dendritic spines and the consequent number of KIF1A-vesicle complexes targeting spines. In parallel, our data might point to an activity-dependent stimulation of KIF1A, which would be the result of a direct Ca^{2+} /CaM-dependent mechanism acting on the kinesin tail. If this true, the calcium sensor CaM would represent the molecular link coupling neuronal activity and KIF1A-mediated transport.

7. Tau fibrils promote co-aggregation of aberrant interactors leading to loss of function mechanisms in Alzheimer's Disease (AD)

In chapter 5 we used a combined *in vitro*/MS approach to biochemically characterize Tau aggregates and their brain interactors, providing a time-resolved description of interactome re-arrangements occurring upon Tau pathological aggregation. Tau amyloid aggregates are one of the major landmarks of Alzheimer's Disease (AD) and their accumulation in the brain correlates with the severity of the disease (Goedert et al., 2017). Unfortunately, despite extensive biochemical and biophysical characterization of these toxic species in Alzheimer patients' brain, it is still unclear how they interact with other components in neurons and their real contribution to AD pathology. This proteomics-based application, allows us to follow interactome re-wiring of Tau at different steps of aggregation from its monomeric, physiological species to its polymeric, toxic aggregate. Our data suggest that the appearance of Tau aggregates directly results in the formation of new abnormal interactions within the neuron, ultimately disturbing a

variety of cellular processes. Specifically, Tau fibrils sequester a defined set of interactors, mainly targeting RNA Binding Proteins, Microtubule Associated Proteins and Protein Phosphorylation Regulators. Almost all of these identified proteins are enriched in disordered regions and possess specific aminoacidic footprint, with a significant overrepresentation of Arginine residues, thus uncovering a mechanism where Arginines in disordered regions drive binding to Tau fibrils via π - π stacking (Vernon et al., 2018). Our data also show that the chaperone Hsp90, by forming a complex with Tau, blocks the formation of Tau fibrils, therefore preventing their detrimental engagement with aberrant interactors. Overall, the precise characterization of Tau aberrant interactome upon aggregation might have a huge impact on our current understanding of the loss of function mechanisms that are directly related to Tau fibrils formation and to the severe neurodegeneration linked to Alzheimer pathology. Moreover, understanding how the manipulation of Hsp90 affects the biology of Tau fibrils may grant us a new molecular weapon that could be finely tuned to contrast AD.

8. Future perspectives

In this thesis, we have used a combination of proteomics, biochemical and live cell imaging techniques to study neurodevelopment and to explore the role of specific motor proteins in MT-based transport. In particular, we have provided strong biological evidence for the importance of specific cell adhesion molecules (NCAM1) in dendritogenesis and of two kinesin-3 family members (KIF1A and KIF13B) in dendritic transport. Moreover we also used a semi-quantitative MS-based approach to understand which abnormal interactions are engaged by Tau fibrils in the brain. These generated data led to follow-up works that will probably unravel other important principles, specifically on active transport and microtubule dynamics in neurons. Understanding how different vesicles, different adaptors and different motor proteins cooperate with each other to ensure an accurate temporal and spatial targeting of cargos is a central question for the neuroscientific community. The addressing of this question will require a multidisciplinary approach similar to what we used in this thesis. We also envision that high throughput techniques will play a dominant role in this complex scenario. Therefore, the combination of advanced MS techniques, structural studies and high resolution live cell microscopy applied in this work might represent a general scheme for future studies to come.

A great amount of studies has enormously contributed to our current knowledge about the function of neuronal cytoskeleton and its components. Nevertheless, the recruitment and delivery of protein cargos to synapses have always represented a particularly challenging aspect. In this thesis we show that different mechanisms regulate the affinity of motors to cargos and motor ability to walk along the cytoskeletal tracks. Furthermore we shed light on several aspects of synaptic transport, in particular on the role of motor proteins in transporting cargos into

dendritic spines. Understanding how synapses work is fundamental to unravel how information is processed in the brain and to elucidate the neuropathological mechanisms underlying different neurological disorders. Despite several advances, our knowledge is still incomplete and key aspects still require further investigations. For a more global comprehension of synaptic function it is crucial to identify which components are cycled to the membrane or added to the PSD in response to LTP stimulation and discover which other motor proteins, besides KIF1A, are able to couple neural activity to synaptic membrane trafficking. In an ideal future scenario, neuroscientists would be able to perform proteomics on specific neuronal compartments, such as dendritic spines or axonal terminals, in order to understand how neurons precisely change their local protein content upon stimulation and to unravel the secrets behind synaptic scaling. Furthermore, recent advances in MS combined with proximity-based approaches will finally allow the detection of transient and dynamic protein-protein interaction directly in neurons, providing a better picture of the biochemical properties of neuronal transport. Similar techniques could be also applied for an accurate biochemical characterization of the different components contained in membrane compartmentalized structures, such as for instance synaptic vesicles (SVs) or DCVs. A precise identification of the transmembrane proteins decorating their surface and of the transported cargos contained in their lumen, could open new fascinating perspectives in the study of neuronal transport, providing vesicle specific protein markers to be effectively visualized by advanced microscopy.

REFERENCES

- Akhmanova, A., and Hammer, J.A., 3rd (2010). Linking molecular motors to membrane cargo. *Curr Opin Cell Biol* 22, 479-487.
- Al-Bassam, J., Cui, Y., Klopfenstein, D., Carragher, B.O., Vale, R.D., and Milligan, R.A. (2003). Distinct conformations of the kinesin Unc104 neck regulate a monomer to dimer motor transition. *J Cell Biol* 163, 743-753.
- Arnold, M., Cross, R., Singleton, K.S., Zlatic, S., Chapleau, C., Mullin, A.P., Rolle, I., Moore, C.C., Theibert, A., Pozzo-Miller, L., *et al.* (2016). The Endosome Localized Arf-GAP AGAP1 Modulates Dendritic Spine Morphology Downstream of the Neurodevelopmental Disorder Factor Dysbindin. *Front Cell Neurosci* 10, 218.
- Batters, C., Brack, D., Ellrich, H., Aeverbeck, B., and Veigel, C. (2016). Calcium can mobilize and activate myosin-VI. *Proc Natl Acad Sci U S A* 113, E1162-1169.
- Bharat, V., Siebrecht, M., Burk, K., Ahmed, S., Reissner, C., Kohansal-Nodehi, M., Steubler, V., Zweckstetter, M., Ting, J.T., and Dean, C. (2017). Capture of Dense Core Vesicles at Synapses by JNK-Dependent Phosphorylation of Synaptotagmin-4. *Cell Rep* 21, 2118-2133.
- Bianchi, S., van Riel, W.E., Kraatz, S.H., Olieric, N., Frey, D., Katrukha, E.A., Jaussi, R., Missimer, J., Grigoriev, I., Olieric, V., *et al.* (2016). Structural basis for misregulation of kinesin KIF21A autoinhibition by CFEOM1 disease mutations. *Sci Rep* 6, 30668.
- Bittins, C.M., Eichler, T.W., and Gerdes, H.H.

- (2009). Expression of the dominant-negative tail of myosin Va enhances exocytosis of large dense core vesicles in neurons. *Cell Mol Neurobiol* 29, 597-608.
- Bittins, C.M., Eichler, T.W., Hammer, J.A., 3rd, and Gerdes, H.H. (2010). Dominant-negative myosin Va impairs retrograde but not anterograde axonal transport of large dense core vesicles. *Cell Mol Neurobiol* 30, 369-379.
- Boehm, M., and Bonifacino, J.S. (2001). Adaptins: the final recount. *Mol Biol Cell* 12, 2907-2920.
- Bouchet, B.P., Gough, R.E., Ammon, Y.C., van de Willige, D., Post, H., Jacquemet, G., Altelaar, A.M., Heck, A.J., Goult, B.T., and Akhmanova, A. (2016). Talin-KANK1 interaction controls the recruitment of cortical microtubule stabilizing complexes to focal adhesions. *Elife* 5.
- Conde, C., and Caceres, A. (2009). Microtubule assembly, organization and dynamics in axons and dendrites. *Nat Rev Neurosci* 10, 319-332.
- Dotti, C.G., Sullivan, C.A., and Banker, G.A. (1988). The establishment of polarity by hippocampal neurons in culture. *J Neurosci* 8, 1454-1468.
- Esteves da Silva, M., Adrian, M., Schatzle, P., Lipka, J., Watanabe, T., Cho, S., Futai, K., Wierenga, C.J., Kapitein, L.C., and Hoogenraad, C.C. (2015). Positioning of AMPA Receptor-Containing Endosomes Regulates Synapse Architecture. *Cell Rep* 13, 933-943.
- Fischer, M., Kaech, S., Wagner, U., Brinkhaus, H., and Matus, A. (2000). Glutamate receptors regulate actin-based plasticity in dendritic spines. *Nat Neurosci* 3, 887-894.
- Fletcher, T.L., and Banker, G.A. (1989). The establishment of polarity by hippocampal neurons: the relationship between the stage of a cell's development in situ and its subsequent development in culture. *Dev Biol* 136, 446-454.
- Frese, C.K., Mikhaylova, M., Stucchi, R., Gautier, V., Liu, Q., Mohammed, S., Heck, A.J.R., Altelaar, A.F.M., and Hoogenraad, C.C. (2017). Quantitative Map of Proteome Dynamics during Neuronal Differentiation. *Cell Rep* 18, 1527-1542.
- Gerrow, K., Romorini, S., Nabi, S.M., Colicos, M.A., Sala, C., and El-Husseini, A. (2006). A preformed complex of postsynaptic proteins is involved in excitatory synapse development. *Neuron* 49, 547-562.
- Goedert, M., Eisenberg, D.S., and Crowther, R.A. (2017). Propagation of Tau Aggregates and Neurodegeneration. *Annu Rev Neurosci* 40, 189-210.
- Guillaud, L., Wong, R., and Hirokawa, N. (2008). Disruption of KIF17-Mint1 interaction by CaMKII-dependent phosphorylation: a molecular model of kinesin-cargo release. *Nat Cell Biol* 10, 19-29.
- Hales, C.M., Vaerman, J.P., and Goldenring, J.R. (2002). Rab11 family interacting protein 2 associates with Myosin Vb and regulates plasma membrane recycling. *J Biol Chem* 277, 50415-50421.
- Hammond, J.W., Cai, D., Blasius, T.L., Li, Z., Jiang, Y., Jih, G.T., Meyhofer, E., and Verhey, K.J. (2009). Mammalian Kinesin-3 motors are dimeric in vivo and move by processive motility upon release of autoinhibition. *PLoS Biol* 7, e72.
- Hirokawa, N., Niwa, S., and Tanaka, Y. (2010). Molecular motors in neurons: transport mechanisms and roles in brain function, development, and disease. *Neuron* 68, 610-638.
- Hirokawa, N., Noda, Y., Tanaka, Y., and Niwa, S. (2009). Kinesin superfamily motor proteins and intracellular transport. *Nat Rev Mol Cell Biol* 10, 682-696.
- Holtmaat, A., and Svoboda, K. (2009). Experience-dependent structural synaptic plasticity in the mammalian brain. *Nat Rev Neurosci* 10, 647-658.
- Horiguchi, K., Hanada, T., Fukui, Y., and Chishti, A.H. (2006). Transport of PIP3 by GAKIN, a kinesin-3 family protein, regulates neuronal cell polarity. *J Cell Biol* 174, 425-436.
- Hotulainen, P., and Hoogenraad, C.C. (2010). Actin in dendritic spines: connecting dynamics to function. *J Cell Biol* 189, 619-629.
- Hu, X., Viesselmann, C., Nam, S., Merriam, E., and Dent, E.W. (2008). Activity-dependent dynamic

microtubule invasion of dendritic spines. *J Neurosci* 28, 13094-13105.

Jaworski, J., Kapitein, L.C., Gouveia, S.M., Dortmund, B.R., Wulf, P.S., Grigoriev, I., Camera, P., Spangler, S.A., Di Stefano, P., Demmers, J., *et al.* (2009). Dynamic microtubules regulate dendritic spine morphology and synaptic plasticity. *Neuron* 61, 85-100.

Jenkins, B., Decker, H., Bentley, M., Luisi, J., and Banker, G. (2012). A novel split kinesin assay identifies motor proteins that interact with distinct vesicle populations. *J Cell Biol* 198, 749-761.

Jeyifous, O., Waites, C.L., Specht, C.G., Fujisawa, S., Schubert, M., Lin, E.I., Marshall, J., Aoki, C., de Silva, T., Montgomery, J.M., *et al.* (2009). SAP97 and CASK mediate sorting of NMDA receptors through a previously unknown secretory pathway. *Nat Neurosci* 12, 1011-1019.

Kaech, S., and Banker, G. (2006). Culturing hippocampal neurons. *Nat Protoc* 1, 2406-2415.

Kakinuma, N., Zhu, Y., Wang, Y., Roy, B.C., and Kiyama, R. (2009). Kank proteins: structure, functions and diseases. *Cell Mol Life Sci* 66, 2651-2659.

Klopfenstein, D.R., Tomishige, M., Stuurman, N., and Vale, R.D. (2002). Role of phosphatidylinositol(4,5)bisphosphate organization in membrane transport by the Unc104 kinesin motor. *Cell* 109, 347-358.

Krementsov, D.N., Kremntsova, E.B., and Trybus, K.M. (2004). Myosin V: regulation by calcium, calmodulin, and the tail domain. *J Cell Biol* 164, 877-886.

Kuriu, T., Inoue, A., Bito, H., Sobue, K., and Okabe, S. (2006). Differential control of postsynaptic density scaffolds via actin-dependent and -independent mechanisms. *J Neurosci* 26, 7693-7706.

Lemmon, M.A. (2003). Phosphoinositide recognition domains. *Traffic* 4, 201-213.

Lemmon, M.A., and Ferguson, K.M. (2001). Molecular determinants in pleckstrin homology domains that allow specific recognition of phosphoinositides. *Biochem Soc Trans* 29, 377-384.

Lu, H., Kremntsova, E.B., and Trybus, K.M. (2006). Regulation of myosin V processivity by calcium at the single molecule level. *J Biol Chem* 281, 31987-31994.

Lu, Q., Li, J., Ye, F., and Zhang, M. (2015). Structure of myosin-1c tail bound to calmodulin provides insights into calcium-mediated conformational coupling. *Nat Struct Mol Biol* 22, 81-88.

Macaskill, A.F., Rinholm, J.E., Twelvetrees, A.E., Arancibia-Carcamo, I.L., Muir, J., Fransson, A., Aspenstrom, P., Attwell, D., and Kittler, J.T. (2009). Miro1 is a calcium sensor for glutamate receptor-dependent localization of mitochondria at synapses. *Neuron* 61, 541-555.

Matus, A. (2000). Actin-based plasticity in dendritic spines. *Science* 290, 754-758.

McVicker, D.P., Awe, A.M., Richters, K.E., Wilson, R.L., Cowdrey, D.A., Hu, X., Chapman, E.R., and Dent, E.W. (2016). Transport of a kinesin-cargo pair along microtubules into dendritic spines undergoing synaptic plasticity. *Nat Commun* 7, 12741.

Merriam, E.B., Millette, M., Lombard, D.C., Saengsawang, W., Fothergill, T., Hu, X., Ferhat, L., and Dent, E.W. (2013). Synaptic regulation of microtubule dynamics in dendritic spines by calcium, F-actin, and drebrin. *J Neurosci* 33, 16471-16482.

Millecamps, S., and Julien, J.P. (2013). Axonal transport deficits and neurodegenerative diseases. *Nat Rev Neurosci* 14, 161-176.

Mok, H., Shin, H., Kim, S., Lee, J.R., Yoon, J., and Kim, E. (2002). Association of the kinesin superfamily motor protein KIF1B α with postsynaptic density-95 (PSD-95), synapse-associated protein-97, and synaptic scaffolding molecule PSD-95/discs large/zona occludens-1 proteins. *J Neurosci* 22, 5253-5258.

Nguyen, H., and Higuchi, H. (2005). Motility of myosin V regulated by the dissociation of single calmodulin. *Nat Struct Mol Biol* 12, 127-132.

Niwa, S., Lipton, D.M., Morikawa, M., Zhao, C., Hirokawa, N., Lu, H., and Shen, K. (2016). Autoinhibition of a Neuronal Kinesin UNC-104/

KIF1A Regulates the Size and Density of Synapses. *Cell Rep* 16, 2129-2141.

Olsen, O., Moore, K.A., Fukata, M., Kazuta, T., Trinidad, J.C., Kauer, F.W., Streuli, M., Misawa, H., Burlingame, A.L., Nicoll, R.A., and Brecht, D.S. (2005). Neurotransmitter release regulated by a MALS-liprin-alpha presynaptic complex. *J Cell Biol* 170, 1127-1134.

Renner, M., Choquet, D., and Triller, A. (2009). Control of the postsynaptic membrane viscosity. *J Neurosci* 29, 2926-2937.

Schatzle, P., Esteves da Silva, M., Tas, R.P., Katrukha, E.A., Hu, H.Y., Wierenga, C.J., Kapitein, L.C., and Hoogenraad, C.C. (2018). Activity-Dependent Actin Remodeling at the Base of Dendritic Spines Promotes Microtubule Entry. *Curr Biol* 28, 2081-2093 e2086.

Schlager, M.A., and Hoogenraad, C.C. (2009). Basic mechanisms for recognition and transport of synaptic cargos. *Mol Brain* 2, 25.

Setou, M., Nakagawa, T., Seog, D.H., and Hirokawa, N. (2000). Kinesin superfamily motor protein KIF17 and mLin-10 in NMDA receptor-containing vesicle transport. *Science* 288, 1796-1802.

Shin, H., Wyszynski, M., Huh, K.H., Valtschanoff, J.G., Lee, J.R., Ko, J., Streuli, M., Weinberg, R.J., Sheng, M., and Kim, E. (2003). Association of the kinesin motor KIF1A with the multimodular protein liprin-alpha. *J Biol Chem* 278, 11393-11401.

Shin, S.M., Zhang, N., Hansen, J., Gerges, N.Z., Pak, D.T., Sheng, M., and Lee, S.H. (2012). GKAP orchestrates activity-dependent postsynaptic protein remodeling and homeostatic scaling. *Nat Neurosci* 15, 1655-1666.

Soppina, V., Norris, S.R., Dizaji, A.S., Kortus, M., Veatch, S., Peckham, M., and Verhey, K.J. (2014). Dimerization of mammalian kinesin-3 motors results in superprocessive motion. *Proc Natl Acad Sci U S A* 111, 5562-5567.

Star, E.N., Kwiatkowski, D.J., and Murthy, V.N. (2002). Rapid turnover of actin in dendritic spines and its regulation by activity. *Nat Neurosci* 5, 239-246.

Stucchi, R., Plucinska, G., Hummel, J.J.A., Zahavi, E.E., Guerra San Juan, I., Klykov, O., Scheltema, R.A., Altelaar, A.F.M., and Hoogenraad, C.C. (2018). Regulation of KIF1A-Driven Dense Core Vesicle Transport: Ca(2+)/CaM Controls DCV Binding and Liprin-alpha/TANC2 Recruits DCVs to Postsynaptic Sites. *Cell Rep* 24, 685-700.

Tomishige, M., Klopfenstein, D.R., and Vale, R.D. (2002). Conversion of Unc104/KIF1A kinesin into a processive motor after dimerization. *Science* 297, 2263-2267.

Tong, Y., Tempel, W., Wang, H., Yamada, K., Shen, L., Senisterra, G.A., MacKenzie, F., Chishti, A.H., and Park, H.W. (2010). Phosphorylation-independent dual-site binding of the FHA domain of KIF13 mediates phosphoinositide transport via centaurin alpha1. *Proc Natl Acad Sci U S A* 107, 20346-20351.

Vale, R.D. (2003). The molecular motor toolbox for intracellular transport. *Cell* 112, 467-480.

van der Vaart, B., van Riel, W.E., Doodhi, H., Kevenaer, J.T., Katrukha, E.A., Gumy, L., Bouchet, B.P., Grigoriev, I., Spangler, S.A., Yu, K.L., *et al.* (2013). CFEOM1-associated kinesin KIF21A is a cortical microtubule growth inhibitor. *Dev Cell* 27, 145-160.

Vernon, R.M., Chong, P.A., Tsang, B., Kim, T.H., Bah, A., Farber, P., Lin, H., and Forman-Kay, J.D. (2018). Pi-Pi contacts are an overlooked protein feature relevant to phase separation. *Elife* 7.

Wagner, O.I., Esposito, A., Kohler, B., Chen, C.W., Shen, C.P., Wu, G.H., Butkevich, E., Mandalapu, S., Wenzel, D., Wouters, F.S., and Klopfenstein, D.R. (2009). Synaptic scaffolding protein SYD-2 clusters and activates kinesin-3 UNC-104 in *C. elegans*. *Proc Natl Acad Sci U S A* 106, 19605-19610.

Wang, X., and Schwarz, T.L. (2009). The mechanism of Ca²⁺-dependent regulation of kinesin-mediated mitochondrial motility. *Cell* 136, 163-174.

Wang, Z., Edwards, J.G., Riley, N., Provance, D.W., Jr., Karcher, R., Li, X.D., Davison, I.G., Ikebe, M., Mercer, J.A., Kauer, J.A., and Ehlers, M.D. (2008). Myosin Vb mobilizes recycling endosomes

and AMPA receptors for postsynaptic plasticity. *Cell* 135, 535-548.

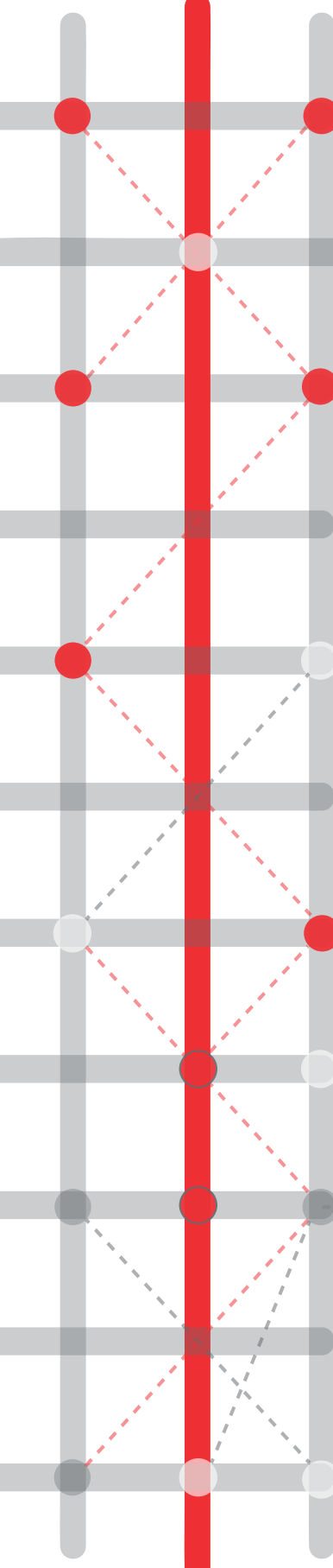
Wu, G.H., Muthaiyan Shanmugam, M., Bhan, P., Huang, Y.H., and Wagner, O.I. (2016). Identification and Characterization of LIN-2(CASK) as a Regulator of Kinesin-3 UNC-104(KIF1A) Motility and Clustering in Neurons. *Traffic* 17, 891-907.

Yamada, K.H., Hanada, T., and Chishti, A.H. (2007). The effector domain of human Dlg tumor suppressor acts as a switch that relieves autoinhibition of kinesin-3 motor GAKIN/KIF13B. *Biochemistry* 46, 10039-10045.

Yoshimura, Y., Terabayashi, T., and Miki, H. (2010). Par1b/MARK2 phosphorylates kinesin-like motor protein GAKIN/KIF13B to regulate axon formation. *Mol Cell Biol* 30, 2206-2219.

Zhu, Y., Kakinuma, N., Wang, Y., and Kiyama, R. (2008). Kank proteins: a new family of ankyrin-repeat domain-containing proteins. *Biochim Biophys Acta* 1780, 128-133.





&

Addendum

Summary

Samenvatting

Curriculum Vitae

List of Publications

Acknowledgements

SUMMARY

Similarly to the amazon rainforest which is formed by a multitude of different trees, many of them growing around and on top of each other with their branches and roots tightly interconnected, the human brain is composed by approximately 100 billion neurons organized into a complex matrix of connections and packed into highly specialized layers. The tridimensional organization of the neurons within the human brain is what makes the human brain so unique. In fact, it is now universally accepted that our capability of thinking, moving and performing the most difficult tasks (like writing this thesis) is only partially explained by the high numbers of neuronal cells contained in the human brain and mainly relies in their infinite multitude of dynamic connections. The peculiar cellular shape and the precise subcellular organization of the neuron, characterized by one long axon, generating output signals, and multiple dendrites, receiving chemical inputs, confer to this specific cell the capability of transmitting electro-chemical information. The connection sites where communication takes place are called synapses. Each synapse has a very defined and specialized composition of proteins. In order to establish and maintain neuronal polarity and to build functional synapses, neuronal cells must be able to sort and deliver proteins and other components to the pre- (axon) and post-synaptic compartments (dendritic spines) with extreme precision. In fact, the protein composition of each single neuronal compartment not only determines its unique architectural morphology and function but has also a more profound effect on the formation of the neuronal network which is the essence of our brain. In this perspective, it is essential to study the primary building blocks of life, the proteins, alongside with their interactions and the molecular mechanisms regulating their functions. Only by studying these primary components we can fully understand the elaborate architecture of branches and roots, ultimately getting one step closer to the immense complexity of the rainforest. Unfortunately science is not “an easy thing” and a reductionist approach that aims to simplistically explain one phenomenon as caused by one single protein, roughly translated into the paradigm “one protein, one function”, has already shown huge limitations in modern biology. In line with these observations, a key concept of modern biology is that proteins participate in complex, interconnected networks, rather than linear pathways. In recent years the rapid adoption of high-throughput -omics approaches (genomics, transcriptomics, proteomics) has created new exciting possibilities for the investigation of the brain and its cellular entities, the neurons. In the field of neurobiology, proteomics has recently started to showcase its full potential as a powerful methodology able to outperform classical biochemical approaches by allowing a more global understanding of protein dynamics and a more detailed characterization of intracellular protein networks and complexes. This thesis describes our efforts in advancing

the understanding of selected mechanisms in neurons by using Mass Spectrometry (MS)-based proteomics applications. Latest MS techniques have been widely used to investigate neuronal differentiation, kinesin-mediated neuronal transport and protein-interaction networks in physiological or pathological condition.

In Chapter 2, we used stable isotope labeling MS to perform a systematic and in-depth analysis of proteome dynamics in cultured hippocampal neurons at various stages of development. This technique allowed us to precisely map neuronal proteins undergoing extensive up-regulation or down-regulation throughout differentiation. By using a combination of biochemical and imaging techniques we then revealed unappreciated roles for protein candidates which we selected from this analysis.

In Chapter 3, we focused our study on neuronal transport and on the crucial role played by the kinesin-3 family member KIF1A in transporting dense core vesicles (DCVs). By performing a systematic affinity purification (AP)-MS approach we mapped the physical interactions of KIF1A. We next focused on three binding partners, the calcium binding protein Calmodulin (CaM) and two synaptic scaffolding proteins: liprin- α and TANC2. Our findings revealed that calcium, acting via CaM, enhances KIF1A binding to DCVs and increases vesicle motility in dendrites. In addition we showed that the scaffolding proteins liprin- α and TANC2 work by tethering KIF1A-driven DCVs into synapses.

In Chapter 4, we further extended our analysis on Kinesin-3 mediated transport. After identifying the specific KIF1A and KIF13B domains involved with the binding with specific neuronal adaptor proteins we systematically tested their role in mediating vesicle transport. These data shed light on the precise function of the Maguk Binding Site (MBS) of KIF13B and the Liprin Binding Domain (LBD) of KIF1A.

Chapter 5 is focused on the aggregation of the microtubule-binding protein Tau. Tau pathological species (oligomers and fibrils) are investigated using an *in vitro* approach combined with MS. We showed that Tau aggregation completely rewires the “physiological” interactome of Tau. Our data mechanistically demonstrated that Tau aberrant interactors have disordered regions with unusual sequence features and that the chaperone protein Hsp90, by stalling fibrils formation, suppresses aberrant interactions. This molecular basis for derailment of protein-protein interactions can explain the toxicity of these aggregates during neurodegeneration.

Finally in Chapter 6, we reported a selection of quantitative MS-applications and targeted MS methods that were used in different projects to address specific neurobiological questions.

The aforementioned results of this thesis, obtained by integrating multiple techniques ranging from proteomics and bioinformatics to cell biology, imaging and microscopy, will contribute to

provide a more detailed picture of the biology of the neuron and lay the foundation for further studies in the field. Our vision is that high-throughput studies and multidisciplinary approaches will be fundamental for the future of neuroscience, by helping scientists to unravel the deeper secrets of the brain forest.

SAMENVATTING

Zoals het Amazoneregenwoud bestaat uit vele verschillende bomen die, met hun takken en wortels vervlochten, om en over elkaar heen groeien, bestaat het menselijk brein uit circa 100 miljard neuronen die zijn georganiseerd in een complexe matrix van verbindingen en gerangschikt zijn in gespecialiseerde lagen. Deze driedimensionale organisatie van neuronen is wat het menselijk brein zo uniek maakt. Het is tegenwoordig zelfs algemeen geaccepteerd dat onze bekwaamheid om te denken, bewegen, en het volbrengen van allerlei zeer uitdagende taken (zoals het schrijven van deze thesis), slechts gedeeltelijk kan worden verklaard door het grote aantal neuronale cellen in het menselijk brein, maar voornamelijk afhangt van de ontelbare dynamische connecties. De uitzonderlijke vorm en de exacte intracellulaire organisatie van het neuron, gekenmerkt door één lang axon - dat uitgaande signalen genereert - en meerdere dendrieten - die chemische signalen ontvangen - geven deze specifieke cellen de mogelijkheid om elektrochemische informatie over te dragen. De verbindingen waar communicatie plaatsvindt heten synapsen. Iedere synaps heeft een bepaalde en gespecialiseerde samenstelling van eiwitten. Om neuronale polariteit te bewerkstelligen en behouden, en om functionele synapsen te maken, moeten neuronen in staat zijn om met uiterste nauwkeurigheid eiwitten en andere bestanddelen te sorteren en bezorgen naar de pre- en post- synaptische compartimenten (het axon en de dendritische spines). De samenstelling van eiwitten in ieder neuronale onderdeel bepaalt niet alleen diens unieke morfologische opbouw en functie, maar heeft ook een fundamenteel effect op de formatie van het neuronale netwerk, die de essentie van ons brein is. In het licht daarvan is onderzoek naar eiwitten, de elementaire bouwstenen van het leven, en de interacties en moleculaire mechanismen die hun functies reguleren essentieel. Door het bestuderen van deze primaire elementen kunnen we de uitgebreide architectuur van de takken en de wortels begrijpen, om uiteindelijk een stapje dichterbij de immense complexiteit van het regenwoud te komen. Wetenschap is helaas geen gemakkelijke zaak, en een minimalistische benadering die streeft om een fenomeen simpelweg te verklaren als zijnde veroorzaakt door een enkel eiwit, ruwweg vertaald als het paradigma 'één eiwit, één functie', blijkt ernstige beperkingen te hebben in de huidige biologie. Deze observaties passen beter bij een ander concept, dat steeds meer aanhang krijgt binnen de huidige biologie. Binnen dit concept worden eiwitten bekeken als onderdeel van complexe netwerken die onderling verbonden zijn in plaats van als schakels in lineaire cascades. De ontwikkeling van high-throughput technieken (op het gebied van genomica, transcriptomica en proteomica) brengt interessante nieuwe mogelijkheden met zich mee om het brein en zijn cellulaire eenheden, de neuronen, te onderzoeken. Binnen de neurobiologie begint de proteomica pas recentelijk tot zijn recht te komen als onderzoekstechniek. Het blijkt een

krachtige methode die in staat is om de klassieke biochemische technieken te overtreffen, doordat proteomica zowel een meer integraal begrip geeft van eiwitdynamica als een gedetailleerde beschrijving van intracellulaire eiwitnetwerken en -complexen. Met behulp van verschillende proteomica methodes die gebaseerd zijn op massaspectrometrie (MS) beschrijven we in dit proefschrift onze inspanningen en resultaten in het bevorderen van het begrip van neuronale mechanismen. De nieuwste MS-technieken zijn gebruikt om neuronale differentiatie, kinesine-gemedieerd transport in neuronen, en interactie-netwerken van eiwitten - in fysiologische of pathologische toestand - te onderzoeken.

In Hoofdstuk 2 hebben we stabiele isotoop-labeling MS gebruikt om een systematische en diepgaande analyse uit te voeren van de proteoom-dynamica in gekweekte hippocampale neuronen tijdens verschillende stadia van ontwikkeling. Met deze techniek konden we nauwkeurig in kaart brengen hoe de expressie van bepaalde eiwitten sterk veranderd tijdens de neuronale differentiatie. Door een combinatie van biochemische en microscopie-technieken te gebruiken, onthulden we vervolgens ondergewaardeerde rollen voor eiwitkandidaten die we uit deze analyse selecteerden.

In Hoofdstuk 3 hebben we gekeken naar het cellulaire transport in neuronen en de cruciale rol van KIF1A, welke behoort tot de kinesine-3 familie, in het transport van specifieke blaasjes, zogeheten Dense Core Vesicles (DCV's). Met behulp van affiniteits-zuivering MS brachten we op een systematische manier de fysieke interacties van KIF1A in kaart. Vervolgens hebben we ons gefocust op drie bindingspartners, het calciumbindende eiwit Calmodulin (CaM) en twee synaptische scaffold-eiwitten: liprin-a en TANC2. Onze resultaten tonen aan dat calcium via CaM de binding van KIF1A aan DCV's versterkt en de beweeglijkheid van de blaasjes in dendrieten verhoogt. Daarnaast laten we zien dat de scaffold-eiwitten liprin-a en TANC2 de KIF1A-aangestuurde DCV's vasthouden in synapsen.

In Hoofdstuk 4 hebben we onze analyse van Kinesine-3 gemedieerd transport verder uitgebreid. Na identificatie van de specifieke KIF1A en KIF13B domeinen die betrokken zijn bij de binding met specifieke neuronale adapter eiwitten, hebben we hun rol in het mediëren van blaasjestransport systematisch getest. Onze bevindingen werpen licht op de precieze functie van de Maguk Binding Site (MBS) van KIF13B en het Liprin Binding Domain (LBD) van KIF1A.

Hoofdstuk 5 richt zich op de aggregatie van het microtubulus-bindende eiwit Tau. Met behulp van een in vitro benadering gecombineerd met MS worden pathologische soorten van Tau (oligomeren en vezels) onderzocht. We laten zien dat Tau aggregatie het "fysiologische" interactoom van Tau compleet herschrijft. Onze gegevens laten mechanistisch zien dat afwijkende interactoren van Tau verstoorde regio's met ongewone sequentie kenmerken hebben en dat het chaperone eiwit Hsp90, door vezel formatie te vertragen, afwijkende interacties onderdrukt.

Deze moleculaire basis voor het ontsporen van eiwit-eiwit interacties kan de toxiciteit van deze aggregaten tijdens neurodegeneratie verklaren.

Tot slot rapporteren we in Hoofdstuk 6 een selectie van kwantitatieve MS-applicaties en gerichte MS methoden die gebruikt zijn om de specifieke neurobiologische vragen om de verschillende projecten te adresseren.

De bovengenoemde resultaten van deze thesis zijn verkregen door meerdere technieken, variërend van proteomica en bioinformatica tot cel biologie en microscopie, te integreren. Ze zullen bijdragen aan een gedetailleerder beeld van de biologie van het neuron, en de basis leggen voor verdere studies in het veld. Onze visie is dat high-throughput studies en multidisciplinaire benaderingen fundamenteel zijn voor de toekomst van neurowetenschappen, door wetenschappers te helpen de diepere geheimen van het hersenwoud te ontrafelen.

CURRICULUM VITAE

Riccardo Stucchi was born on 24th April 1985 in Vimercate (Milan), Italy. After obtaining his high school diploma in 2004 (Scientific Lyceum A. Banfi, Vimercate) he started studying Biotechnology at the University of Milano-Bicocca. He finalized his bachelor's studies in 2007 with a research internship at the department of experimental medicine under the supervision of Prof. Massimo Masserini. During these years as bachelor's student, he realized that he was mainly fascinated by the molecular aspects underlying the functioning of cells. Therefore, he continued his academic education with a Master program specialized in molecular biotechnology (University of Milano-Bicocca). The main research project of his master was performed at the department of Molecular Biochemistry and Pharmacology at the Mario Negri Institute for Pharmacological research (IRFMN, Milan) under the supervision of Dr. Valentina Bonetto. The main topic of his research was to identify early protein biomarkers in ALS disease and investigate their mechanism of action. In 2011, Riccardo obtained his Master's degree in Biotechnology and decided to continue his studies at the IRFMN by working as research assistant in the Laboratory of Translational biomarkers. During this period he extended his knowledge in Mass Spectrometry-based proteomics and few years later, driven by growing interest in the molecular mechanisms of protein dynamics in neurons, he decided to join the Laboratory of Prof. dr. Casper Hoogenraad (Cell Biology, Utrecht University) as a PhD candidate. In September 2013, Riccardo started his PhD and for the next years he worked in close collaboration with the Mass Spectrometry and Proteomics department (under the co-supervision of Dr. Maarten Altelaar and Prof. Dr. Alert Heck). The main results of this research are described in this current dissertation.

LIST OF PUBLICATIONS

Regulation of KIF1A-Driven Dense Core Vesicle Transport: Ca²⁺/CaM Controls DCV Binding and Liprin- α /TANC2 Recruits DCVs to Postsynaptic Sites

Stucchi R, Plucińska G, Hummel JJA, Zahavi EE, Guerra San Juan I, Klykov O, Scheltema RA, Altelaar AFM, Hoogenraad CC.
Cell Rep. (2018) 24(3):685-700.

Quantitative Map of Proteome Dynamics during Neuronal Differentiation

Frese CK*, Mikhaylova M*, **Stucchi R***, Gautier V, Liu Q, Mohammed S, Heck AJR, Altelaar AFM, Hoogenraad CC.

Cell Rep. (2017) 18(6):1527-1542.

*equal contribution

Fibril formation rewires interactome of the Alzheimer protein Tau by π -stacking

Ferrari L, **Stucchi R**, Konstantoulea A, van de Kamp G, Kos R, Geerts WJC, Förster FG, Altelaar AFM, Hoogenraad CC, Rüdiger SGD.

Submitted

The HAUS Complex Is a Key Regulator of Non-centrosomal Microtubule Organization during Neuronal Development

Cunha-Ferreira I, Chazeau A, Buijs RR, **Stucchi R**, Will L, Pan X, Adolfs Y, van der Meer C, Wolthuis JC, Kahn OI, Schätzle P, Altelaar M, Pasterkamp RJ, Kapitein LC, Hoogenraad CC.

Cell Rep. (2018) 24(4):791-800.

TRIM46 Controls Neuronal Polarity and Axon Specification by Driving the Formation of Parallel Microtubule Arrays

van Beuningen SFB, Will L, Harterink M, Chazeau A, van Battum EY, Frias CP, Franker MAM, Katrukha EA, **Stucchi R**, Vocking K, Antunes AT, Slenders L, Doulkeridou S, Sillevius Smitt P, Altelaar AFM, Post JA, Akhmanova A, Pasterkamp RJ, Kapitein LC, de Graaff E, Hoogenraad CC.

Neuron (2015) 88(6):1208-1226.

Feedback-driven mechanisms between microtubules and the endoplasmic reticulum instruct neuronal polarity

Fariás GG, Fréal A, Tortosa E, **Stucchi R**, Pan X, Portegies S, Will L, Altelaar AFM, Hoogenraad CC.

Neuron (2019) pii: S0896-6273(19)30057-1.

VAP-SCRN1 interaction regulates dynamic endoplasmic reticulum remodeling and presynaptic function

Lindhout FW, Kevenaer JT, Bodzeta A, Cao Y, **Stucchi R**, Boumpoutsari MM, Altelaar AFM, MacGillavry HD, Hoogenraad CC.

EMBO J. Under revision.

MAP7D2 localizes to the proximal axon and locally promotes kinesin-1 mediated cargo transport into the axon

Pan X, Cao Y, **Stucchi R**, Hooikaas PJ, Portegies S, Will L, Martin M, Akhmanova A, Harterink M, Hoogenraad CC.

Cell Rep. (2019) 26(8):1988-1999.e6.

Feedback-driven assembly of the axon initial segment

Freal A, Rai D, Tas R, van de Willige D, **Stucchi R**, Aher A, Yang C, Altelaar M, Vocking M, Post JP, Harterink M, Kapitein LC, Akhmanova A, Hoogenraad CC.

Neuron (2019) Under revision.

MAP7 family proteins regulate kinesin-1 recruitment and activation

Hooikaas PJ, Martin M, Kuijntjes GJ, Peeters C, Katrukha EA, Ferrari L, **Stucchi R**, Verhagen DGF, van Riel WE, Altelaar AFM, Hoogenraad CC, Rüdiger SGD, Kapitein LC, Akhmanova A.

Journal of Cell Biology (2019) pii: jcb.201808065.

Peptidylprolyl isomerase A governs TARDBP function and assembly in heterogeneous nuclear ribonucleoprotein complexes

Lauranzano E, Pozzi S, Pasetto L, **Stucchi R**, Massignan T, Paoletta K, Mombrini M, Nardo G, Lunetta C, Corbo M, Mora G, Bendotti C, Bonetto V.

Brain (2015) 138(Pt 4):974-91.

A possible role of transglutaminase 2 in the nucleus of INS-1E and of cells of human pancreatic islets

Sileno S, D'Oria V, **Stucchi R**, Alessio M, Petrini S, Bonetto V, Maechler P, Bertuzzi F, Grasso V, Paoletta K, Barbetti F, Massa O.

J Proteomics (2014) 96:314-27.

ACKNOWLEDGMENTS

As all nice things in life have to come to an end, also my PhD is now approaching to its final act. I truly considered this journey as one of the most positives and rewarding experiences that I have ever had. When I started, I did not know exactly what to expect, but now that it is almost over I can look back at it and clearly observe my transformation and maturation from the professional point of view but more importantly as individual. Coming to the Netherlands has been a challenge but I could not have hoped anything better. In fact, I am so grateful to have discovered an open-minded country, a wonderful city, a new cozy home, and so many people supporting me over these years. So let's start with a "short" recap of all of those involved in this long and fulfilling ride.

First of all I would like to express my sincere gratitude to **Casper**, my supervisor and promotor. I will be always thankful for the opportunity you gave me to join your lab and for your mentorship during these years. I can still vividly remember your enthusiasm and passion when you described me possible projects and ideas during the first personal chat with you and in the subsequent meetings. I have always admired your positivity and your innate capability of transferring this sentiment to people surrounding you. For me personally, that boost of positivity was exactly the type of support needed to complete this journey and that was exactly what you were able to provide every single time during our regular work-meetings. I really admire your relaxed attitude even in stressful situations, the nice atmosphere that you contributed creating in the lab by using your peculiar skills in managing people and the freedom you gave me to do my own mistakes, to develop my own ideas, to elaborate my own projects. But most of all I loved your scientific creativity, your rational way of connecting data into new convincing scientific theories or models, and your intuitive way of making them visible by simply drawing them. You filled that gap of creativity that has always been one of my main limitations. I learnt a lot from your knowledge and experience and I'll try not to waste any single suggestion you gave me throughout these years because these will be the most crucial things that will help me in the future as an independent scientist. Finally I want to thank you for having fully supported and trusted me, and I wish you will continue having fun doing science for the next "n" years (n=numbers of replicates necessary to have a p-value < 0.000001).

Secondly I have to deeply thank my promotor **Albert** and my co-promotor **Maarten**. I will always be grateful to you, Albert, for the fact that you were the first one who took into consideration my motivation letter and my CV when years ago I expressed my will to join your lab and for your invitation in Utrecht as potential PhD candidate. I feel it has been a privilege and a wonderful opportunity for my scientific career to actively work in your group and to be

able to use the best MS instruments and the best expertise and technical support a scientist could ever dream of. Maarten, it was great to have you as co-promotor for my PhD. I could learn a lot from the advanced proteomics expertise that is present in your research group and I sincerely appreciate the advices you gave me to complete different proteomic-based projects and to complete this thesis. It has been a great professional experience collaborating and doing science in the Mass-Spectrometry and Proteomics department, I really loved it.

I would also like to thank all the group leaders of the Cell Biology, Biophysics and the Developmental Biology departments. **Anna** and **Lukas**, thanks for the inputs and suggestions during the work discussions and for being members of my reading committee. **Sander**, **Mike**, **Sabrina**, **Paul** thanks for the discussions in seminars, the nice chats at the coffee machine and the good times we shared during the social events. **Corette**, thanks for your positive attitude, smiles and enthusiasm, **Esther**, thank for your useful comments and help, and for being an example of strength and determination, **Harold**, thanks for the nice period we spent in the lab together and for the help and support. **Ginny**, thank you for all the nice moments we spent together in the office and for the fruitful collaborations we did together. I wish you all the best with the new career as young PI in the department, your passion for science will bring you very far. **Laurens** thanks for your help and your kindness.

And a big thank to all the group leaders of the MS and Proteomic department, in particular **Richard**, thanks for letting me use your XL-MS expertise and **Wei** for giving me advices and offering technical/scientific support when needed. To **Jeroen Pasterkamp**, **Guus Smit**, **Hendrik Korswagen** and **Stefan Rüdiger**, thank you for being members of my reading committee and assessing my final PhD thesis.

Moreover I would also like to extend my gratitude to all the people that directly or indirectly contributed to the projects I have been involved during these years; it has been a pleasure to collaborate with so many different people, with different backgrounds and different scientific ideas. In nature as in science, diversity and heterogeneity always give rise to the best final products.

Over these years spent in between the 5th and 6th floor of the Kruytbuilding I had the opportunity to meet so many talented and interesting people that I ll probably forget a lot of them in the next pages, but anyway I would like to express my gratitude to everyone that decided to dedicate a tiny fraction of his/her busy working time to spend few words with me. I have always liked connecting with people, and making connections is what life is all about.. so thank you because every single minute, hour or day spent together will be always part of me, imprinted somewhere in one of the infinite neuronal connections of my brain.

I want to first thank a special colleague and friend for her help, support and for the wonderful periods we enjoy together at the university and in life, an enormous hug to you, **Qingyang**. Thanks for helping me with everything in the first period of my PhD, for being my first friend in the NL and for being my MS partner at 5th floor. I have always enjoyed our sarcastic conversations and I truly missed them now that you are gone. I wish you and Stefan (your new fresh husband and my cycling partner) a happy life together, and thank you two for all the nice dinners and funny/relaxing times. I know we will always be in contact wherever we will be and ours will always be a robust and solid friendship.

I cannot avoid mentioning my dear office mates. N505 has always been a friendly and loud room throughout all these years. **Hai Yin**, we started our PhD journey approximately at the same time and we are happily concluding it together. We got to know each other day after day, in the good and bad times. I admired your work-attitude, your strength, your being reserved but also talkative and your outstanding capability of analyzing data. Good luck for your future career and we will meet at Griftpark to play with Kaiba. **Lena**, I admire a lot your dedication and precision both at work when performing experiments as well as in the kitchen when preparing professional cakes. Thanks for all the tips, the nice chats, the homemade cookies, the moments we shared together and for being always here over these years. You are a prepared and beloved teacher and I hope you'll be teaching for a long time. **Ines** what can I say, you have been a real example of perseverance and organization. I have always been envious of your strength in overcoming obstacles and your energy. You were a constant source of portugese sparkles in the office and outside (what a happy time we had in Crete!!), I wish all the best to you and Roland in Germany, maybe I will join you in a near future. **Olga**, I miss you a lot but I am glad to hear that you are now happily settled down in San Francisco. You have always represented an example of super-woman able to nicely combine family and science, and I am sure you'll continue doing that in the outstanding way you are capable of. Thanks for being so genuinely nice with me and I am looking forward to meeting you and Maja. **Phil** thanks for the precious help with cloning, for being a volcano of brilliant ideas in the field of neuroscience and for your constant presence always in front of me.

Marina thanks for introducing me to the lab, to the group and for teaching me a tiny portion of your vast scientific knowledge, you have been a real example of a true scientist, full of energy and joy. **Sam, Max, Kah Wai, Michael, Marta, Elena, Mariella, Marleen, Joanna, Josta, Laura, Petra** thanks for having been nice lab mates and for the fun we had in&out the university. **Catia**, thanks for supporting me at the beginning when I needed it the most and for being always the funniest girl of the lab. **Dieudonnee** thanks for sharing your PhD time with me, you have been a nice lab mate and the best scientific storyteller I have ever met. **Martin** thanks

for all the suggestions and useful inputs, I truly admire for your dedication and passion for science, I hope you'll have your own group very soon, you really deserve it. **Xingxiu** and **Yujie**, thanks for all the moments spent together, I wish you two good luck with finishing your PhD and for your new future adventures. **Amelie**, I admired your calm and relaxation even in stressful situations, your social and scientific skills and your character, which is very similar to mine, being born on the same day of the year. **Robin**, thanks for all the nice moments we lived together, they will always be part of my young life, I hope we will replicate them soon and good luck with finishing your project. **Sybrein**, thanks for those nights we happily slept together sharing the same bed and for all the laughs we had in these years, last efforts before finishing... **Robbelien** and **Feline**, thanks for your smiles and positivity in the lab and for introducing me to hiPSCs, you'll have fun with them. **Liu**, it was nice working with you and I wish you good luck with the *C.elegans* proteins. **Gabi**, getting to know you and have you around in the lab was great. I felt very privileged to have you actively involved in my project. Thanks for your precious experience with microscopy, yours was a priceless contribution to my PhD and I will always thank you for that. I wish you all the best with your new exciting career. **Jessica**, I truly admire your work attitude and I greatly appreciated the huge contribution you gave me for the revision experiments, without you I would have spent months getting those results. Good luck in finishing up the nice project you successfully started. **Bart**, thanks for your funny jokes that always bring smiles all over the lab and for the positive and relaxed attitude. **Phebe**, you are really the pulsing heart and the inner soul of Casper lab and an extraordinary example of organization and efficiency. Thanks for taking care of every aspect of the lab, for simplifying our complicated PhD lives and for always being nice and caring with me.

Irene, you have been the best Master student I could have ever imagined, apart from being an energetic and joyful person, you showed real motivation and scientific initiative which resulted in a valuable contribution to my project. We had a lot of fun together in&out of the lab and I am glad I had the opportunity to know the great person you are. I wish you all the best for your PhD and I know we will keep on staying in contact. **Eliana** thanks for all the never-ending chats we had, for the Italian dinners in Gouda and for being much more than a colleague. I hope to meet you and Mark many other times in the coming years. **Eitan**, it has been a real pleasure to have shared a lot of experiences with you in these last few years. You have been an unforgettable colleague who helped me a lot when mostly needed and a trustable friend who has always provided unconditional support. Your hospitality and capability of connecting with people are qualities that make you so unique. I wish you and Zlil all the best either it will be here in the Netherlands or somewhere else.

I would also like to thank everyone in the lab of Anna, Corette, Harold, Sabrina, Sander and

Mike, **Rene, Anna, Lisa, Nicky, Boris, Dennis, Ankit, Jingchao, Maud, Lars, Helma, Ate, Lotte, Marjin, Klara, Carlijn, Milena, Joyce, Dipti, Cynthia, Funso, Andrea, Sanne** and all the other members of the department with whom I used to have late lunch breaks or with whom I spent unforgettable moments at parties, cycling and/or drinking beers. To **Amol and Ivar**, despite being on the opposite sides of the world now, you together have represented an essential component of the department and I will always bring with me the nice memories of the partying/cycling/chatting moments together. **Fangrui**, thanks a lot for your advices and for our conversations, I wish all the best to you and your family; **Jian**, your politeness and empathy are rare qualities, **Chao**, good luck for your career and with football. **York**, thanks for all the nice football conversation, those really made my days, **Peter-Jan**, thanks for your kindness every time I bother you in the office. To **Eugene and Desiree**, thanks for the housewarming parties and for all the times we had good times together, all the best with your “adult” life together in Utrecht. **Bas**, thanks “old man” for showing me that age is only a relative concept, for the nice experiences we shared at parties and for always be the happy version of yourself. **Ruddi**, I got to know you little by little but I truly discovered one of the warmest and most enjoyable person of my dutch life. I truly appreciated your and Aline’s hospitality and your Cuban-latin personality. By getting closer it was impossible for me not to be impressed by your big heart. I truly hope you will find your place in the world, either here or somewhere else in Europe (but for sure not in France).

Sofia, Katerina, Sara, Rachid thanks for being extraordinary colleagues and thanks to all the past and present members of Paul group. **Alessia and Michele**, I wish you would have stayed longer in Utrecht. **Wilco, Roderick, Anna, Mithila, Chiung-Yi**, thanks for all the ordinary/boring/funny/serious/discussing/ moments and for creating a nice atmosphere in the lab and to all the members of Lukas group.

Having actively collaborated with the MS and proteomics department meant I spent quite some time bothering a lot of people at the 6th floor. First of all I want to thank all the technicians, PhD students and Post-docs for the great support with MS, LC, protocols and consumables. **Harm**, good luck with your projects and in organizing the proteomics part of the lab, **Mirjam**, I can still remember your first trainings in the wet lab and I ll miss a lot our never-ending cycling discussions. **Christian**, thanks for the help and the constant support you gave me to conclude the quantitative proteomics project. **Oleg**, thanks for the help with XL-MS, but more important thank you for the nice chats about music, projects and future. Good luck for the next step in your career. **Fabio, Eleonora, Piero, Domenico, Riccardo, Gianluca, Anna**, it was wonderful to meet all of you and thanks for recreating a little Italy at 6th floor. **Matina, Suzy and Charlotte**, we shared our PhD tracks and it was nice condividng with you the same feelings/frustrations/

hopes.

I had the chance of knowing a lot of motivated young scientists within the IB PhD students and I wish all of them to follow their PhD dreams. A particular mention to **Luca**, with whom we nicely collaborated together to characterize Tau interactome, all the best with your future professional and private adventures.

Nicky thanks for being a good party mate and for introducing me to dutch parties (however I am still not fully convinced about your taste for music), **Irene**, wherever you are, and **Jasmine**. My ex housemates (**Dora&Shima**), in particular **Stavroula**, which is a genuine person and an essential member of my dutch family, I know we will stay in contact for a very long time, wherever we will be. **Lianne**, which is much more than a simple neighbor for us and **Cecilia&Benno** which have always been friendly and supportive. My tennis-partners **Yang** and **Rob**, thanks for playing sports together and for the nice conversations whenever I needed to refresh my mind. **Teo&Dzemila** I wish you a great time in Utrecht.

To all my friends and relatives in Italy, few pages would not be enough to express my gratitude to all of them, to the guys and girls from Depo, we have grown up together and that is something that will stay forever. I have always felt strong support throughout all these years by receiving your visits, by partying together, by every single phone call or Skype, or simply every time we had the opportunity to meet again back home. I know my real friends will be always here, so there is no need to express my gratitude in these acknowledgements.

The biggest thank goes to my family, to my parents **Fausto&Luisa**, who have always put absolute trust in me by giving me all sort of support I needed in every step of my life and to my “little” sister **Martina** who has always been the best among us and as expected she is actually doing great in her adult life.

And finally to you **Isabella**, the love of my life, that made me a happy guy, a happy man and a happy dad and that everyday shape me into the best version of myself. And to you **Sven**, with whom, many pages and chapters have still to be written.



